Perylene Diimide-Based Nanoparticles for Tracking Cells and their Encapsulating Hydrogels

Thesis submitted in accordance with the requirements of the
University of Liverpool for the degree of Doctor in Philosophy

by

Claudia Alexandra Fryer

June 2021

Acknowledgements

This work has been supported by an EPSRC CASE Studentship in collaboration with Element Six Ltd.

Firstly, I would like to extend my thanks to my supervisors, Dr Haifei Zhang and Prof. Patricia Murray, for creating such an interesting project and seeing the potential in me to fulfil it. Thank you both for the guidance and a particular thank you to Trish for the extra support.

I am grateful for the many people I have met and worked with over the last 3.5 years, particularly members of the Stem Cell Group and Zhang Group. Thank you to Chris Hill, Arthur Taylor and Jack Sharkey for teaching a chemist how to culture cells. A huge thank you to Meg Smith and Tamiris Borges da Silva for being my go-to cell experts and amazing supportive friends. Furthermore, thank you to O2 and Café Nero for supplying us with weekly free coffees. I would also like to thank the team at the Materials Innovation Factory for their technical support.

Lastly, I would like to thank all of my wonderful family and friends who have been there for me throughout this project. Thank you to my parents, my sister and my best friends for being the greatest support network I could ask for. A special thank you to Lee who has been my rock; your continued support and confidence in me has gotten me through.

Abstract

Cell-based regenerative medicine therapies (RMTs) hold great potential for the treatment of a wide range of injuries and disease. There are several concerns which hinder the translation of RMTs to the clinic, an important one being our lack of understanding of how the cells behave following administration. To address this, we need to be able to track the cells using non-invasive imaging techniques. A further problem is that in some applications, a large proportion of the implanted cell population will die shortly after delivery, reducing the efficacy of the therapy. A potential solution is to encapsulate the cells in hydrogels that provide a supportive environment for cell survival, and that help to protect the cells from the host's immune system. However, before using this approach in the clinic, it is necessary to be able to monitor the behaviour of the hydrogels in animal models to ensure their safety and monitor their rate of degradation.

In this study, novel contrast agents have been explored for the *in vivo* tracking of mesenchymal stromal cells (MSCs) and encapsulating hydrogels with fluorescence and photoacoustic imaging techniques. The two types of contrast agents that have been assessed in the project are polymer-stabilised nanoparticles prepared by nanoprecipitation and nanodiamonds. These nanoparticles have been prepared with perylene diimide (PDI) derivatives, a class of organic dyes with high absorptivity and photostability.

For cell-tracking with photoacoustic imaging, a near-infrared (NIR) absorbing PDI derivative was prepared with absorption at ~710 nm. PDI nanoparticles were prepared by nanoprecipitation with our novel star hyperbranched block copolymer stabiliser ($DEAMA_{50}$-*c*-$DEGDMA_2$)-*b*-($OEGMA_{80}$). These nanoparticles were shown to be effective contrast agents for photoacoustic imaging whilst also having limited cytotoxicity and good cellular uptake in MSCs. The NIR-absorbing PDI nanoparticles were also investigated for their ability to label cell-encapsulating hydrogels. MSCs were seeded in collagen hydrogel constructs that had been labelled with PDI nanoparticles. The labelled hydrogels could be visualised with both fluorescence and photoacoustic imaging and the nanoparticles had limited cytotoxicity. However, further work is required to prevent nanoparticles leaching out of the hydrogels over time.

Nanodiamonds (NDs) have been investigated for cell tracking with fluorescence imaging techniques due to their high biocompatibility. PDI-NDs were prepared and compared with commercial fluorescent NDs with nitrogen-vacancy (NV) defects, and it was found that particle aggregation hindered the efficacy of PDI-NDs. NV NDs with a particle size of 90 nm appeared as superior contrast agents for the labelling of MSCs, exhibiting high fluorescence intensity, limited aggregation and excellent cellular uptake.

The experiments conducted herein have highlighted 90 nm NV NDs as effective contrast agents for cell tracking with fluorescence imaging. Additionally, polymer stabilised NIR-absorbing PDI nanoparticles can be effectively visualised in MSCs with photoacoustic imaging techniques. These probes can be used to determine the mechanism of action of cells expressing the firefly luciferase reporter, to simultaneously monitor the viability of administered cells using bioluminescence imaging in order to aid the design of safe and efficacious cell-based RMTs. Furthermore, preliminary work herein has highlighted the potential of using PDI nanoparticles to track the fate of cell-encapsulating hydrogels *in vivo*.

Publications

Perylene Diimide Nanoprobes for *In Vivo* Tracking of Mesenchymal Stromal Cells Using Photoacoustic Imaging - Y. Yang, C. Fryer, J. Sharkey, A. Thomas, U. Wais, A. W. Jackson, B. Wilm, P. Murray and H. Zhang, *ACS Appl. Mater. Interfaces*, 2020, **12**, 27930-27939.

Polymers and Nanostructured Materials for Drug Nanoparticles, Bioimaging and Cell Delivery - C. Fryer, Y. Yang, T. Wang, P. Murray and H. Zhang, in *Materials Science and Technology*, ed R.W. Cahn, P. Haasen and E.J. Kramer, Wiley, New Jersey, 2020.

Conferences

Perylene Diimide-Based Nanoparticles as Photoacoustic Contrast Agents for *In Vivo* Cell Tracking - Oral Presentation at Virtual European Molecular Imaging Meeting, 2020.

NIR-Absorbing Nanoparticles for Cell Tracking – Oral Presentation at Centre for Preclinical Imaging Symposium, University of Liverpool, 2019.

Nanodiamonds for Stem Cell Tracking – Best Poster Prize at University of Liverpool/Unilever Careers Event, University of Liverpool, 2019.

Nanoparticles for Stem Cell Tracking - Poster Presentation at Future Investigators in Regenerative Medicine, Costa Brava, Spain, 2018.

Nanoparticles for Stem Cell Tracking - Poster Presentation at Chemistry PhD Symposium, University of Liverpool, 2018.

Contents

List of Figures

List of Tables

List of Equations

Abbreviations

^{18}FDG	^{18}F-fluorodeoxyglucose
3D	3-dimensional
5DI	Pentarylene diimide
ATP	Adenosine triphosphate
AuNP	Gold nanoparticle
BLI	Bioluminescence imaging
CNS	Central nervous system
CNT	Carbon nanotubes
CT	Computed Tomography
CVD	Chemical vapour deposition
DAPI	4′,6-Diamidino-2-phenylindole
DBU	1,8-Diazabicyclo[5.4.0]undec-7-ene
DCM	Dichloromethane
DEAE	diethylaminoethyl
DLS	Dynamic light scattering
DMEM	Dulbecco’s modified eagle medium
DMSO	Dimethyl sulfoxide

DOTA	1,4,7,10-Tetraazacyclododecane-1,4,7,10-tetraacetic acid
DOX	Doxorubicin
ε	Extinction coefficient
ECM	Extracellular matrix
EDC	1-Ethyl-3-(3-dimethylaminopropyl)carbodiimide
FACS	Fluorescence-activated cell sorting
FBS	Fetal bovine serum
FDA	Food and Drug Administration
FLS	Fluorescence Lifetime Spectrometer
FSC	Front scatter
FTIR	Fourier-Transform Infrared
GelMA	Gelatin methacryloyl
GRP	Green fluorescent protein
HDI	Hexarylene diimide
hESC	Human embryonic stem cell
HPHT	High-pressure high-temperature
ICG	Indocyanine green
MRI	Magnetic resonance imaging

MSC	Mesenchymal stromal cell
MSN	Meseoporous silica nanoparticle
MSOT	Multispectral Optoacoustic Tomography
MWCNT	Multi-walled carbon nanotubes
NDs	Nanodiamonds
NIR	Near-infrared
NMR	Nuclear magnetic resonance
NV	Nitrogen-vacancy
NVD	Nitrogen vacancy defect
ODA	Octadecylamine
OFET	Organic field-effect transistor
OPV	Organic photovoltaic cell
OTFT	Organic thin-film transistor
PAAm	Polyacrylamide
PA	Photoacoustic
PAI	Photoacoustic imaging
PBS	Phosphate buffered saline
PDI	Perylene diimide

PEBBLE	Photonic explorers for biomedical use by biologically localised embedding
PEG	Poly(ethylene glycol)
PET	Positron emission tomography
PFA	Paraformaldehyde
PFC	Perfluorocarbon
PFCE	Perfluoro-15-crown-5-ether
PFOB	Perfluorooctylbromide
PFPE	Perfluoropolyether
PLA	Poly(lactic acid)
PLGA	Poly(lactic-co-glycolic acid)
PTCDA	Perylene-3,4,9,10-tetracarboxylic dianhydride
PTT	Photothermal therapy
PTX	Paclitaxel
PVA	Poly(vinyl alcohol)
QD	Quantum dot
QDI	Quarterrylene diimide
RFP	Red fluorescent protein
RGD	Arg-Gly-Asp

RMTs	Regenerative medicine therapies
ROS	Reactive oxidative species
SBM	Solomon, Bloembergen and Morgan
SCI	Spinal cord injury
SEM	Scanning Electron Microscopy
SHBP	Star hyperbranched block copolymer
SiV	Silicon-vacancy
SPECT	Single photon emission computed tomography
SPION	Superparamagnetic iron oxide nanoparticles
SPN	Semiconducting polymer nanoparticle
SPR	Surface plasmon resonance
SSC	Side scatter
Sulfo-NHS	N-Hydroxysulfosuccinimide sodium salt
T_1	Longitudinal relaxation
$T_{1/2}$	Half-life
T_2	Transverse relaxation
TDI	Terrylene diimide
TEM	Transmission Electron Microscopy
TMS	Tetramethylsilane

TPEG	Isopentyl poly(ethylene glycol)
UV-vis	Ultraviolet-visible

Chapter 1: Introduction

1.1 Regenerative Medicine Therapies

In recent years, cell-based regenerative medicine therapies (RMTs) have been extensively explored for their ability to restore cells/tissue/organs which have been damaged by disease or trauma.[1] Broadly, cell-based RMTs include stem cells, progenitor cells and stromal cells; however, the definition has been extended to any cell-based therapy which has the capacity to regenerate.[2] Stem cells have two specific properties: the capacity to self-renew through cell division, and the ability to differentiate into specialised cell types.[3, 4] They can be categorised based on their ability to differentiate, where unipotent, multipotent and pluripotent stem cells are able to differentiate into one, multiple or all cell types within a mature organism, respectively.

RMTs could offer a solution to the problems associated with organ and tissue transplants, such as limited donor supply and organ rejection.[1, 5] Although significant advances have been made to reduce the rejection of organs by immunosuppression, this is not always effective and can cause detrimental side effects. Therefore, if successful, RMTs could avoid the reliance on donors, and by using autologous cells it could be possible to circumvent rejection issues.

One of the most widely-used and successful RMTs are hematopoietic stem cells from bone marrow or umbilical cord blood, used for the treatment of leukaemia and other blood disorders.[6] Many advances in the regenerative medicine field have looked at exploring cell-based treatments for renal, cardiovascular and neurodegenerative diseases.[7-10] Although bone marrow transplants have been used for over 50 years, it was not until the first human embryonic stem cell line (hESC) was established in 1998 that the stem cell field began to rapidly expand.[11] The derivation of the first hESC line gave rise to much optimism because these cells are pluripotent and have the ability to generate all cell types in the adult human.[12] However, there are several ethical concerns around the use of ESCs, namely because their procurement requires the destruction of the human embryo, and also undifferentiated ESCs pose a risk of tumour formation.[13] Hence, this stimulated research into RMTs derived from adult sources, such as mesenchymal stromal cells (MSC) which is a type of multipotent progenitor cell that can be derived from bone marrow and other tissues, including adipose tissue and umbilical cord.[14]

MSCs have an ability to differentiate into different cell types, including fat, bone and cartilage, and have promising immunomodulatory properties.[15] Although at first it was thought that administered MSCs could differentiate *in vivo* to replace injured cells, it is now widely thought that their main therapeutic effect is *via* paracrine factors that stimulate immunomodulation and other repair processes.[16] MSCs are of particular interest due to their potential use as an autologous treatment. Despite this, there is a high variation in clinical outcomes, possibly due to factors such as age and weight, and so allogenic therapies from young, healthy donors are also being explored.[17]

1.1.1 Limitations and Safety Concerns

Despite the high volume of research into RMTs, there are many safety concerns which hinder their clinical translation. Unlike pharmacological therapies, cell-based RMTs are capable of persisting and proliferating in the body, with the potential to migrate to other organs.[18] As previously mentioned, some administered RMTs have resulted in tumour formation, inherent of their rapid cell division, particularly for ESCs.[13, 19] In addition to this, there are adverse side effects reported relating to immunogenicity.[20] These risks, combined with inconsistency in therapeutic outcomes based on demographic factors, mean that while many cell-based RMTs have been tested in clinical trials, only a few have been found to be effective.

Aside from safety concerns, there are many questions around the efficacy of RMTs. The lack of safety and efficacy data for RMTs can be attributed to a lack of understanding of their mechanism of action. The ability to track the fate and biodistribution of administered cells *in vivo* will aid the translation of RMTs by providing invaluable information on cell survival, migration and mechanism of action, as well as addressing the aforementioned safety concerns.

1.1.2 Cell Delivery

Encapsulation of RMTs within protective polymer matrices, such as hydrogels, has been found to increase cell survival.[21, 22] The polymer matrix offers novel benefits, such as limiting immunogenicity by protecting the cells from immune system components, whilst allowing the diffusion of nutrients.[23, 24] Furthermore, constructs can be designed to mimic the extracellular matrix (ECM) to enable 3D cell growth and regulate differentiation.[25] Hydrogels are defined as swollen 3D networks of polymers held together by physical or chemical crosslinking.[26] The polymers can be either natural or synthetic, although the former is preferred for cell encapsulation due to biocompatibility.[27]

Hydrogel scaffolds are of particular interest for cell delivery in spinal cord injury (SCI). RMTs have been widely explored as treatments for SCI and early clinical trial data has demonstrated some regenerative effects through increased sensory and locomotor function.[28-31] Despite this, trials associated with SCI are still in their infancy as optimisation of the cell administration process is required to increase cell viability.[32] For instance, improved methods are needed to enable precise delivery of cells to the required location and to prevent adhesion to the spinal surface and cell sedimentation; these problems could potentially be addressed through encapsulating the cells in hydrogels.[33, 34] Furthermore, the mouldable structure can easily adapt to fit the space, and injectable hydrogels can facilitate a less invasive route of administration compared to surgical treatments.[35, 36]

There are many different materials being explored as hydrogel constructs for SCI.[37] Alginate hydrogels have been investigated for cell delivery in SCI and it has been found that the addition of fibronectin, a component of the ECM, enhanced the regenerative effect of administered schwann cells.[38] Hence, hydrogels that are able to mimic the ECM are of great significance for cell delivery in SCI.[39, 40] Collagen is a major component of the ECM and has been employed in hydrogel development for cell delivery and tissue engineering applications.[41, 42] Moreover, collagen hydrogel constructs were used to encapsulate neural cells for the treatment of SCI where the collagen matrix enabled astrocyte growth over an extended time frame.[32]

There are several factors to consider when selecting suitable materials and designing hydrogel constructs for cell delivery including: (i) cell migration, (ii) cell survival, (iii) cell proliferation and (iii) the degradation rate of the hydrogel material. Hence, the ability to monitor cell release and hydrogel fate *in vivo* will aid the design of encapsulated RMTs.

1.1.3 Tracking of RMTs

Animal models help researchers obtain more information on the safety and efficacy of RMTs. *Ex vivo* imaging strategies have been developed together with histological analyses in order to confirm the biodistribution of MSCs in post-mortem samples.[43] However, this method does not allow tracking of administered cells with time, and hence, non-invasive preclinical imaging technologies are preferred because they provide the capacity for researchers to monitor the same animal at various time points.[44]

In order to track cells *in vivo*, they must either be engineered to contain reporter genes that code for proteins which exhibit a traceable signal, or labelled with probes. Using genetically engineered cells can be advantageous as it circumvents some of the problems associated with probes, such as signal dilution; i.e. when cells are labelled with probes, the signal is diluted 50% with each cell division. Furthermore, as it is the probe that is being imaged, there is a risk that the probe could be released from the cell and taken up by host cells, leading to false positive results.

Despite this, there are several limitations to the reporter gene approach, including the complex genetic engineering protocols with related safety concerns and the potential immunological response.[45, 46] Furthermore, there have been significant advances in probe chemistry over recent years which has seen the development of a wide range of biocompatible nanoparticles ideal for cell tracking.[47] Both the reporter gene and probe approaches are useful in different applications and can also be used simultaneously for dual imaging capabilities.[48]

When encapsulating cells in protective matrices, it is important to be able to track cell release in order to optimise the construct material and cell delivery process. In addition to this, it is also useful to be able to monitor the integrity of the hydrogel constructs *in vivo* to observe fragmentation and degradation.[27] Hydrogels can be engineered to provide contrast with bioimaging techniques, either by chemical modification of the polymers used to prepare the gel or by incorporation of contrast agents upon gel assembly.[49-51] Furthermore, being able to distinguish between the labels of the cells and hydrogel would enable simultaneous tracking of cell release and gel integrity *in vivo*.

1.2 Bioimaging Techniques and Probes

The five main types of pre-clinical imaging techniques include nuclear imaging, magnetic resonance imaging (MRI), optical (including fluorescence and bioluminescence), ultrasound and photoacoustic imaging (PAI). A summary of the imaging capabilities of each technique can be found in Table 1.1. Furthermore, significant developments have been made to design contrast agents for each of the bioimaging techniques. Some of the contrast agents used for the tracking of cell-based RMTs are shown in Figure 1.1.

Table 1.1: A summary of the five main bioimaging techniques used in preclinical research.[44, 52]

Imaging Technique	Spatial Resolution	Temporal Resolution	Penetration Depth
Nuclear Imaging	1-2 mm	Seconds-minutes	No limit
MRI	40-100 µm	Minutes-hours	No limit
Optical Imaging	2-5 mm	Seconds-minutes	<1 cm (fluorescence) 1-2 cm (bioluminescence)
Ultrasonography	>30 µm	Seconds-minutes	3-4 cm
PAI	20-300 µm	Seconds-minutes	4-5 cm

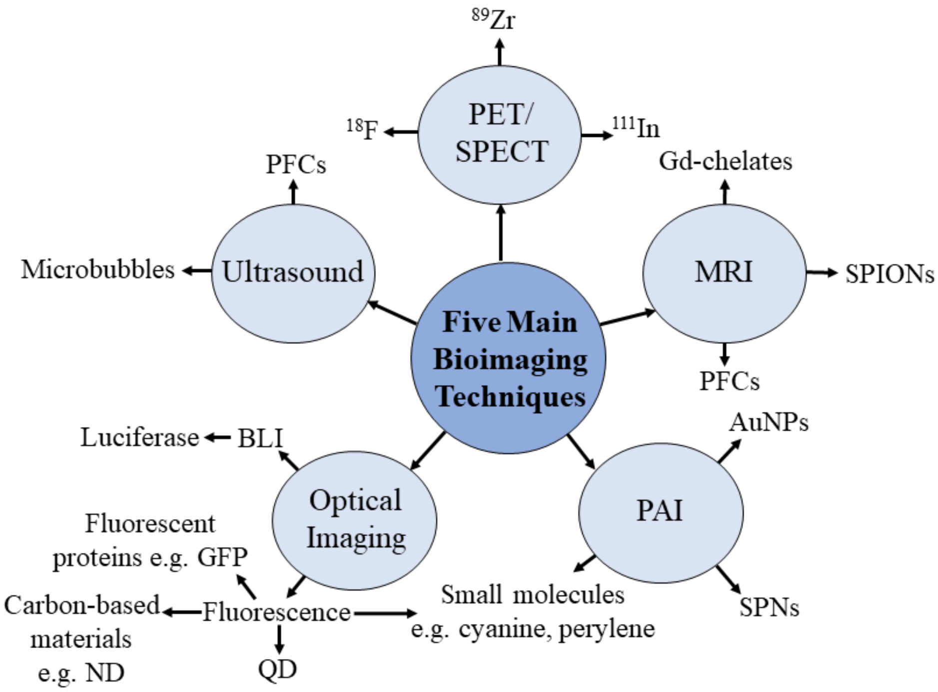

Figure 1.1: Summary of the five main bioimaging techniques utilised for cell tracking and the common contrast agents employed. Nuclear imaging modalities include positron emission tomography (PET) and single photon emission computed tomography (SPECT) with associated radionucleotide metal contrast agents. Magnetic Resonance Imaging (MRI) contrast agents are gadolinium chelates, superparamagnetic iron oxide nanoparticles (SPION) and perfluorocarbons (PFC). Photoacoustic (PA) probes include gold nanoparticles (AuNP), semiconducting polymer nanoparticles (SPN) and small molecules. Bioluminescence imaging (BLI) utilises luciferase enzymes and fluorescence imaging probes include fluorescent proteins, carbon-based materials, such as nanodiamonds (ND) and quantum dots (QD). Probes capable of providing ultrasound contrast are microbubbles and perfluorocarbons (PFC).

1.2.1 Nuclear Imaging

Nuclear imaging includes positron emission tomography (PET) and single photon emission computed tomography (SPECT), where the signal comes from measuring the decay of a radionucleotide. Contrast agents for PET/SPECT include unstable atoms which release particles through radioactive decay to reach a more stable form. For PET, a positron is emitted which collides with a free electron to form a positronium; this decays by annihilation to form a pair of gamma rays which are detected by the scanner.[53] In contrast, SPECT tracers emit gamma radiation directly and are detected using rotating gamma cameras and a collimator; hence SPECT has lower sensitivity.[54]

Contrast agents for PET are based upon unstable isotopes, where the most common PET tracers contain fluorine-18 or zirconium-89. PET has been widely used in the clinic for imaging tumours using the ^{18}F-fluorodeoxyglucose (^{18}FDG) radiotracer.[55, 56] The glucose aspect of ^{18}FDG enables accumulation at tumour sites which is thought to be due to the high metabolic rate of cancer cells, making ^{18}FDG an excellent marker for tumours. The half-life of ^{18}F ($t_{1/2}$ = 110 min) is significantly longer than other common radioactive isotopes such as ^{13}C ($t_{1/2}$ = 20 min); however, ^{89}Zr is the most suitable for cell tracking, with a half-life of 78 hr.[57, 58]

PET/^{18}FDG can be a useful tool for assessing the biodistribution and homing of stem cells within the early phase of administration, thus enabling optimisation of the dosing and delivery method.[59] In one study, PET/^{18}FDG was specifically used to quantify myocardial retention and evaluate the possible different delivery methods when administering cardiac-derived stem cells in a rodent models.[60] The widespread use of ^{18}FDG makes it the obvious choice for cell labelling; however, the short half-life limits its utility and hence more recent research has focussed on other isotopes, such as ^{89}Zr- ($t_{1/2}$ = 78 hr) and ^{111}In-based radiotracers ($t_{1/2}$ = 2.8 d).[61-64]

Nuclear imaging has also been used for monitoring hydrogel delivery and retention in mice.[51] Alginate-based hydrogels have been prepared by utilising the SPECT tracer, ^{111}In, as an ionic crosslinker. MSCs were encapsulated in the hydrogels for cardiac repair which could be visualised with SPECT, thus demonstrating the feasibility of monitoring hydrogel retention *in vivo* with nuclear imaging.

The main benefits of PET/SPECT are the high sensitivity and unlimited penetration depth. However, the imaging time window is limited to the half-life of the radionucleotide and the spatial resolution is poor without co-localisation with computed tomography (CT) or magnetic resonance imaging (MRI).[45] In addition to this, there are safety concerns associated with over-exposure to radiation.[65]

1.2.2 Magnetic Resonance Imaging

One of the main advantages of MRI in bioimaging is the lack of ionising radiation. MRI works by monitoring the spin alignment of water protons in the direction of an applied magnetic field. Hydrogen nuclei precess at a particular frequency which is disturbed upon introduction of a perpendicular radio frequency pulse.[66] When this pulse is removed, protons return to their aligned state through equilibration of the net magnetisation and this process is called relaxation. Protons in different tissues/fats/organs relax to different extents resulting in the complex greyscale images observed in MRI.[67] The high sensitivity of the technique to soft tissue has seen the use of MRI in imaging the brain and spinal cord, as well as assessing cardiac function and tumour detection.[68-70]

There are two mechanisms of proton relaxation: longitudinal (T_1) and transverse (T_2) and hence there are two types of contrast agent for MRI. T_1 contrast agents are commonly based on gadolinium (III) ions, a paramagnetic lanthanide species with 7 unpaired electrons.[71] Gd alters relaxation properties of protons through an interaction with the protons in local water molecules. This mechanism is thought to involve changes in the water exchange rate in the gadolinium coordination sphere and water diffusional correlation time, as described by Solomon, Bloembergen and Morgan (SBM) theory.[72, 73] Gd-based contrast agents are used in the clinic; however, as elemental Gd is toxic, organic multidentate ligands are required to reduce transmetallation. An example of this is FDA-approved Dotarem® where the DOTA macrocycle (1,4,7,10-Tetraazacyclododecane-1,4,7,10-tetraacetic acid) chelates the Gd(III) ions.[74]

Significant efforts have been made to develop Gd-based probes for cell tracking as the Gd-chelates alone have unfavourable cellular uptake and cytotoxicity. One approach was to incorporate Gd complexes into mesoporous silica nanoparticles (MSN) for the tracking of human MSCs.[75] The probes showed excellent cellular internalisation and a sufficient loading of Gd was achieved which enabled *in vivo* MRI for 14 days. Another approach linked a Gd-chelate to rhodamine particles using a dextran polymer for the tracking of neural stem cells.[76] A Gd-chelate has also been covalently attached to chitosan hydrogels for monitoring gel degradation with MRI.[77]

Superparamagnetic iron oxide nanoparticles (SPION) are T_2 contrast agents which are more widely used for biomedical applications due to their low cytotoxicity and ease of synthesis.[78, 79] Particularly for cell tracking applications, their superior cellular uptake and biocompatibility has meant they are more widely investigated compared to Gd-based tracers. SPIONs are colloidal suspensions of magnetite (Fe_3O_4) or maghemite (γ-Fe_2O_3), usually with a polymeric coating to prevent aggregation.[80, 81] Dextran is the most common coating for SPIONs, where it has been shown that the surface charge can be tailored, by incorporating the diethylaminoethyl (DEAE) group, to improve cellular uptake and negate the need for transfection agents.[82] These DEAE-Dextran-SPIONs could effectively be used to label macrophages where hepatic localisation was observed *in vivo*.[83] Furthermore, SPIONs have been used to label cellulose/silk fibroin hybrid hydrogels;[84] this enabled monitoring of hydrogel integrity with MRI without affecting the proliferation rate of encapsulated MSCs for applications in cartilage regeneration.

1.2.2.1 Fluorine-19 MRI

There are several advantages of ^{19}F which make it suitable as an MRI contrast agent, including relatively high sensitivity (83% of ^{1}H), 100% natural abundance and there is relatively low amount of ^{19}F in biological tissue; hence, ^{19}F MRI essentially allows background-free visualisation of ^{19}F probes.[85-87] Furthermore, the most common contrast agent, perfluorocarbons (PFC) have been extensively explored as blood substitutes and now many are available as ^{19}F probes, for example commercially available CelSense.[88-90]

PFCs are linear or cyclic carbon molecules where all of the protons have been substituted by fluorine atoms and the strong C-F bond renders PFCs chemically inert. They are extremely hydrophobic and hence PFC nanoemulsions have been developed.[91] Surfactants are used to stabilise the nanoemulsion which can also impart desirable surface properties to promote cellular uptake.[86]

Examples of PFCs used in cell tracking include perfluoropolyether (PFPE), perfluorooctylbromide (PFOB) and perfluoro-15-crown-5-ether (PFCE).[92] PFCs has been encapsulated in poly(lactic-co-glycolic acid) (PLGA) nanoparticles as efficient ^{19}F probes for dendritic cell tracking.[93] Furthermore, the manipulation of the nanoparticle ultrastructure enabled control over the *in vivo* clearance rate, where multi-core particles produced fast-clearing highly sensitive ^{19}F probes thus minimising local retention time and associated safety concerns.[94] Fluorinated PLGA nanoparticles have also been developed as multimodal probes;[95, 96] the particles can be tracked with ^{19}F MRI and could also be loaded with dyes for optical or photoacoustic contrast.

MRI techniques are widely used in the clinic due to unlimited penetration depth and minimal safety concerns associated with the lack of ionising radiation. However, the high temporal resolution means that image acquisition takes much longer which is intensive work in preclinical studies where multiple animals are required.

1.2.3 Optical Imaging

The two main types of optical imaging used for the tracking of cell-based RMTs in small animals are bioluminescence and fluorescence.[44] Both techniques involve the detection of light emitted from a cell which expresses a reporter gene or has been labelled with a probe. The widespread use of optical imaging techniques in cell tracking is owed to their high sensitivity and low cost.

1.2.3.1 Bioluminescence Imaging

In BLI, the light detected has been biochemically emitted by a luciferase enzyme. The enzyme can be found in a variety of organisms where the North American firefly (*Photinus pyralis*) has been most extensively studied, however luciferase is also found in certain bacteria, insects and fish.[97, 98] BLI is therefore particularly useful for monitoring the biodistribution of luciferase-expressing cells in rodent tissues and organs, as it generates a high signal-to-noise ratio and hence high sensitivity.[99] One of the main factors which prevents the clinical translation of this technique, is the need for a substrate such as luciferin (the substrate for Firefly luciferase).[100] BLI also suffers from poor spatial resolution and a limited penetration depth, as well as an inability to visualise particular organs due to light scattering.[101]

Live animal imaging can be non-invasively carried out by engineering cells with bioluminescent reporter genes that encode a luciferase. Luciferase is the generic term for a group of enzymes which catalyse the oxidation of a substrate. In the case of Firefly luciferase, which is the luciferase most commonly used for small animal imaging, the substrate is luciferin, which emits light in the presence of oxygen, Mg^{2+} and ATP.[102] Firefly luciferase converts D-luciferin into oxyluciferin, resulting in light emissions at 562 nm (Figure 1.2).

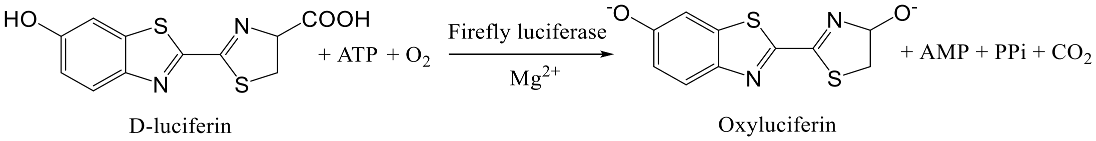

Figure 1.2: The conversion of D-luciferin to oxyluciferin by firefly luciferase in the presence of oxygen and ATP

BLI has been a useful tool for tracking the fate of administered cells *in vivo* to monitor cell migration and survival.[101] Generally, cells are first genetically engineered to express luciferase before being administered into rodent models.[103] The dependence of luciferase on oxygen and ATP metabolism means that BLI will only detect cells which are alive, where other techniques may show both alive and dead cells.[44] BLI has been used for the tracking of neural progenitor cells to assess engraftment and migration in order to optimise the timing of administration after spinal cord injury in mice.[104] Similar studies have been carried out to assess cell survival and migration in rodents of a wide variety of administered cells including cardiac progenitor cells, MSCs, and ESCs.[105-107] In most cases, BLI could be corroborated by *ex vivo* histological analysis.

1.2.3.2 Fluorescence Imaging

Fluorescence imaging can be carried out on cells modified with reporter genes to code for fluorescent proteins, or cells which have been labelled with fluorescent probes. The proteins/probes absorb light of a particular wavelength and emit light, typically of a longer wavelength.[108] The excitation and emission wavelengths are specific to a particular protein/probe and the difference between them is known as the Stoke's shift. The efficiency of a fluorophore is described by the quantum yield (Φ), as shown in Equation 1.1.[109]

$$\Phi = \frac{photons\ emitted}{photons\ absorbed} \quad \text{(Equation 1.1)}$$

Similar to BLI, fluorescence imaging has high sensitivity; however, the spatial resolution and penetration depth inhibits routine use in the clinic and makes it difficult to image internal organs in rodents. One of the many advantages of fluorescence imaging is the capabilities for high contrast. There is an optical window at 700-900 nm where the light-absorbing molecules in tissue, such as fat, water, melanin and haemoglobin, have the lowest absorption coefficient.[110] Hence contrast agents can be designed to absorb within the optical window to enable deeper light penetration as less light is absorbed by endogenous absorbers.

Cells can be transfected with fluorescent reporter genes which encode for fluorescent proteins. Common examples include green fluorescent protein (GFP) and red fluorescent protein (RFP) which fluoresce at 509 nm and 618 nm, respectively.[47] Significant progress in genetic engineering has enabled the development of GFPs with improved properties, such as enhanced brightness and stability, as well as the development of GFP-like proteins of different colours.[111] Far-red and near-infrared (NIR) fluorescent proteins have been developed, such as Katushka2S which enabled small animal whole body imaging with minimal background signal due to its absorbance peak being within the optical window.[112]

Fluorescent probes have been widely explored for cell tracking applications, in particular quantum dots (QDs). QDs are semiconducting nanoparticles which have interesting optical and electronic properties owing to quantum confinement. Hence, their properties are dependent upon particle size, shape and surface chemistry.[113, 114] QDs have many advantages including resistance to photobleaching, high molar extinction coefficient, broad spectrum absorbance, and high resistance to degradation.[115] Furthermore, QDs have been prepared with absorption/fluorescence in the NIR region to increase signal-to-noise ratio.[116]

QDs have been made from a variety of materials including CdSe, CdS, CdTe, InP, carbon and silicon nanoparticles.[117-120] One of the hurdles in the development of QD for cell tracking is cytotoxicity, and hence it is common for QDs to be coated to improve biocompatibility. CdSe QDs were found to be cytotoxic due to surface oxidation leading to the release of Cd^{2+} ions.[121] It was found that the cytotoxic effect was significantly reduced when CdSe QDs were coated with ZnO or bovine serum albumin. Furthermore, the circulation lifetime of core-shell CdSe-ZnS QDs can be increased by surface modification with long poly(ethylene glycol) (PEG) chains for whole body fluorescence imaging of mice.[122]

Organic dyes have also been developed as fluorescent probes for cell and gel tracking, in particular cyanine dyes. IRDye 800CW is a cyanine derivative which has been incorporated into hyaluronan hydrogels to monitor hydrogel integrity *in vivo* with fluorescence imaging techniques.[123] IRDye 800CW was covalently attached to thiol groups included in the modified hyaluronan macromolecules. By monitoring the fluorescent signal of the dye, hydrogel degradation could be assessed and it was found that the rate of degradation could be controlled by changing hydrogel concentration.

Indocyanine green (ICG) is a tricarbocyanine dye with emission around 800 nm, well within the optical window. In addition to this, ICG has the significant advantage of already being FDA-approved for use in humans with only a few rare cases of adverse side effects.[124] ICG has been successfully used for tracking MSCs with both NIR fluorescence and photoacoustic imaging.[125] Despite this, there are a number of disadvantages to the use of ICG in cell tracking; it has relatively weak fluorescence and low photostability so must be imaged within 10 hours.[126] Hence, rylene derivatives, in particular perylene diimides (PDI), are another class of organic dyes which have emerged as fluorescent probes due to their bright fluorescence, high quantum yield and high photostability.[127, 128]

Carbon-based materials, including graphene, carbon nanotubes (CNTs), fullerenes, carbon dots and nanodiamonds (NDs), have more recently been investigated due to their interesting optical properties which are can be exploited for cell tracking. Generally, graphene and CNTs require a surface coating in order to improve biocompatibility, and fullerene derivatives have issues with solubility.[129-132] Carbon dots are a relatively new class of material which are being explored for cell and organelle tracking.[133, 134]

NDs have been shown to have high fluorescence intensity and also extremely low cytotoxicity, thus offering an advantage over other carbon-based materials and QDs.[135-137] NDs are defined as a dense network of sp^3 hybridised carbon atoms which give a rigid structure thus resulting in high chemical inertness. Defects can be introduced to the diamond structure which can alter the optical properties of the NDs, where the most common are nitrogen-vacancy defects, NV^0 and NV^-.[138] Furthermore, the surface chemistry of the NDs can be exploited for the attachment of targeting ligands, drug molecules and dyes thus rendering NDs ideal candidates for theranostic applications.[139-141]

Although there are examples of cell tracking with fluorescence imaging, the utility of the technique is hampered due to photon scattering in biological tissue, limiting the penetration depth. Despite this, fluorescent imaging can still provide useful information in cell tracking experiments; for instance, the intra-organ distribution of administered cells can be quickly and easily confirmed after *in vivo* experiments by imaging the dissected organs after animal sacrifice. NDs have been shown to be excellent candidates for this due to their high stability under physiological conditions, which was confirmed by fluorescence imaging in mice after 37 days.[142] Moreover, NDs could be detected during *ex vivo* histological analysis where it was also shown that high doses (up to 75 mg/kg body weight) did not cause toxicity.

1.2.4 Ultrasound Imaging

Ultrasound imaging is another bioimaging technique that does not require ionising radiation and has other advantages, including excellent spatial and temporal resolution.[52] Furthermore, ultrasound can be used at the bedside and hence is one of the most wide-spread and cost efficient imaging modalities. Images are generated as sound waves are attenuated/reflected/scattered by tissue and ultrasound has been a useful tool for guided stem cell delivery.[143] The most common ultrasound contrast agent is a gas-filled microbubble.[52, 144, 145] Microbubbles are most commonly used in diagnostics, in particular for contrast enhancement during echocardiograms; however, they are also being explored as drug carriers for therapeutic applications.[146, 147]

Many studies have focussed on improving the efficacy of microbubbles by stabilising the gas-liquid interface with lipids, polymers and proteins.[148] The use of PFCs as the internal gas phase has also been shown to stabilise microbubbles and hence many of the commercially available microbubbles have a fluorinated gas core.[149, 150] This research has opened up opportunities to explore the use of ultrasound for cell tracking;[151-153] this field had previously been hindered by microbubble instability making long-term imaging a challenge. More recently, PLGA particles containing liquid PFCs have been shown to enable ultrasound contrast for long-term imaging of dendritic cells with ultrasound and ^{19}F MRI.[154]

1.2.5 Photoacoustic Imaging

Photoacoustic imaging (PAI) combines the advantages of optical imaging with ultrasound, whereby light is converted to sound waves *via* the photoacoustic effect, as demonstrated in Figure 1.3. A laser is irradiated on a sample and photon absorption causes an increase in the transient temperature, resulting in thermoelastic expansion and ensuing relaxation. This produces sound pressure waves which are detected by an ultrasound transducer. An image can then be reconstructed based on the amplitude of the wave and the time it takes to hit the detector.[155] The conversion of light to sound waves presents a significant advantage in terms of penetration depth as phonons are scattered approximately three orders of magnitude less than photons.[156]

PAI has a penetration depth of up to 4-5 cm in biological tissue which is significantly deeper than optical imaging (Table 1.1). Furthermore, PAI has other advantages, such as higher spatial resolution and the capacity for tomographic imaging means that it is easier to locate cells in the body; therefore, PAI is suited to imaging internal organs of intact small animals.[44] One drawback of the technique is that it is difficult to image the lungs due to the presence of air.[18]

Different biological tissues have different absorption, thermal and elastic properties and hence the resultant sound waves have different amplitudes and reach the detector at different times, thus giving information on depth and tissue characteristics. As with optical imaging, strong absorbers, such as lipids, melanin and haemoglobin, have a strong photoacoustic signal and thus exogenous absorbers, including gold nanoparticles and organic dyes, are designed to absorb in the NIR region to improve sensitivity.

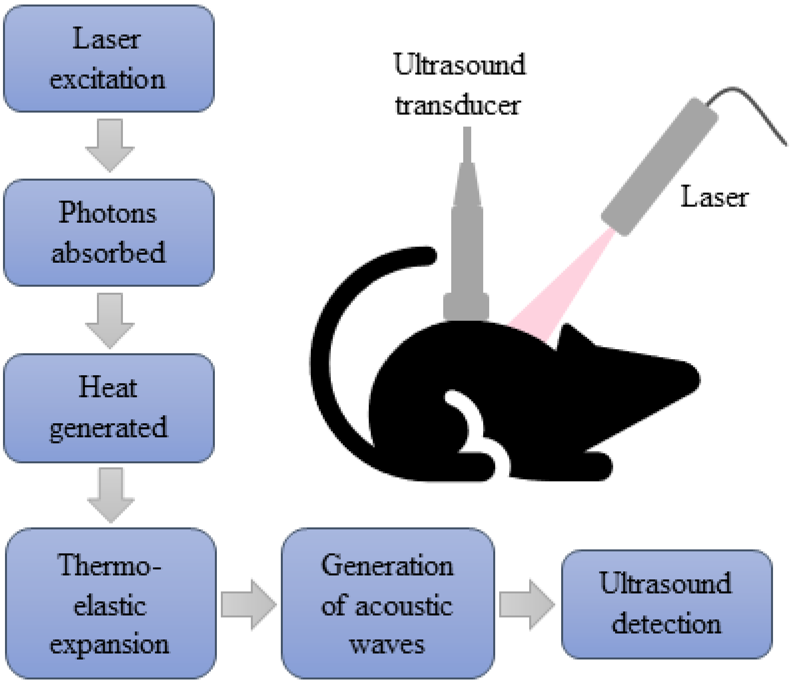

Figure 1.3: Schematic representation of the principles of the photoacoustic effect.

1.2.5.1 Multispectral Optoacoustic Tomography (MSOT)

MSOT is a type of PAI where tissues can be excited at multiple wavelengths.[157] Images can then be spectrally unmixed so that different absorbers in the tissue can be detected and visualised separately. One example of this is using PAI to monitor blood oxygenation; haemoglobin and oxyhaemoglobin are endogenous absorbers with different spectral absorption which can be distinguished by MSOT.[158] Furthermore, as well as endogenous absorbers, MSOT can simultaneously detect and spectrally unmix exogenous absorbers, such as reporter genes, NIR dyes and gold nanoparticles.[159, 160]

MSOT can be used for small animal imaging; multiple cross-sectional images can be acquired in sequential steps which can then be used to build up a 3D image of animal or target tissue/organ. In cell tracking, this enables an understanding of the biodistribution of labelled cells across the whole body. MSOT can also be used for real-time tracking of pharmacokinetics, for example to analyse the accumulation or clearance of an exogenous absorber in a specific location.[18] MSOT has been used for dynamic imaging of mice to assess the biodistribution of multiple exogenous absorbers;[161] the clearance of indocyanine green from systemic circulation was observed along with the uptake of IRDye 800CW carboxylate in separate regions of the kidney. This demonstrated the high-resolution *in vivo* imaging capabilities of MSOT for tracking the fate of multiple exogenous absorbers in real-time.

The multispectral unmixing capabilities of MSOT are ideal for cell tracking applications in order to distinguish the absorption of labelled cells from endogenous absorbers. Furthermore, a study was carried out where cells were administered and tracked by simultaneously detecting multiple exogenous absorbers: gold nanorods and reporter genes.[48] MSCs co-expressing BLI reporter luciferase and NIR fluorescent protein iRGP720 were labelled with gold nanorods; the nanorods highlighted the immediate distribution of the cells and were cleared after 15 days, whereas the NIR reporter gene could be detected up to day 40. The absorbance of each of the exogenous absorbers could be distinguished enabling effective short- and long-term biodistribution studies.

Distinguishing between multiple absorbers is useful for tracking and distinguishing between multiple cell types. Furthermore, different exogenous absorbers could be used to label cells and encapsulating hydrogels, enabling the simultaneous tracking of cell and hydrogel fate *in vivo*, thus making MSOT the ideal imaging modality for the present study.

1.2.5.2 Photothermal Therapy (PTT)

Another significant application of the photoacoustic effect is PTT. In this case, light is converted to heat in order to cause cell death.[162] Hence, PTT shows strong promise as a non-invasive treatment for cancer as photothermal absorbers can be designed to target and enhance the generation of heat at tumour sites.[163] The careful design of photothermal probes can minimise the effect on healthy tissue, thus limiting side effects. Advances in the progress of photothermal absorbers are extremely relevant when considering photoacoustic (PA) probes for cell tracking, as they share a common goal to develop particles capable of high photoacoustic efficiency.

1.3 Photoacoustic Probes

Exogeneous PA contrast agents include NIR reporter genes and nanoparticles, the latter of which can be categorised based on how they interact with light.[159] Some nanoparticles absorb light *via* surface plasmon resonance (SPR), where optical absorption is dependent on the physical dimensions of the material, for example, gold nanorods. The second type of PA nanoprobes involve light absorbing organic dyes, such as cyanine or perylene dyes.

1.3.1 Reporter Genes

Genetically encoded florescent proteins which absorb in the far-red and NIR region of the spectrum can also been utilised in PAI due to their strong light absorption.[164-166] For example, iRFP can be used as a PA probe as it has an extremely high molar extinction coefficient (105,000 M^{-1} cm^{-1}) and low quantum yield (6%), with excitation and emission spectra in the NIR region.[167] Furthermore, the fluorescent properties provide additional capacity for *ex vivo* fluorescence imaging.[168]

The genetically encoded enzyme, tyrosinase, has also been investigated for generating PA contrast.[169, 170] Tyrosinase catalyses the reaction of cellular tyrosine into the pigment eumelanin, which has broad absorption and high photostability.[171] A study was carried out where mammalian cells encoded with the tyrosine reporter gene could be detected with PAI for up to 7 weeks, thus suggesting the potential for these probes in longitudinal studies.[172] Despite these advances, overall reporter genes tend to have relatively low PA contrast and hence nanoparticle probes have been much more widely explored.[44]

1.3.2 Gold Nanoparticles

Gold nanoparticles (AuNP) absorb light due to surface plasmon resonance (SPR); SPR is a phenomenon which describes the collective oscillation of conduction electrons on the surface of a metal due to propagation of an electromagnetic wave when photons are absorbed.[173] This results in an enhanced magnetic field at the surface, which is extremely sensitive to changes in the surrounding environment and hence AuNPs have been widely utilised in biosensing and diagnostics.[174, 175] Spherical 5 nm AuNPs are red (λ_{max}= 520 nm); however this is highly dependent on the composition, size, shape, inter-particle distance and surrounding environment.[176] Hence these properties can be tailored to the desired application, i.e. to absorb in the optical window to create a highly sensitive PA probes.

Spherical AuNPs have limited use for PAI due to weak NIR absorbance, and hence, other morphologies have been investigated, including Au nanorods, nanoshells and nanocages (Figure 1.4).[177] Modifications in the size, shape, dimensions and surrounding environment of such nanoparticles causes a shift in the SPR, which in turn alters the absorption profile.[178]

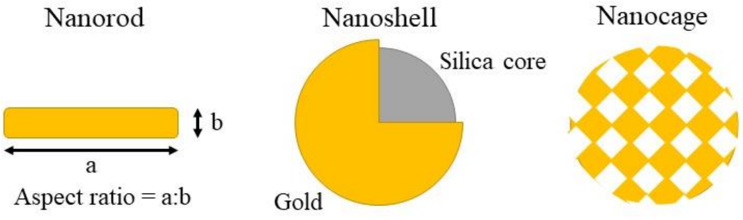

Figure 1.4: The most common AuNP shapes and morphologies.

Au nanoshells comprise a dielectric silica core with a surrounding conductive, gold shell where the absorption and scattering properties can be controlled by altering both the core and shell size.[179] The nanoshells have high NIR absorbance and photostability and the gold surfaces of the nanoshell can be exploited for anchoring of polymers to increase uptake and biocompatibility.[180] Nanoshells have been widely explored in cancer imaging and PTT.[181-183]

Au nanorods are another class of AuNP which have seen wider use in targeting cellular receptors due to their smaller particle sizes (>100 nm).[177] They are prepared by seed mediated growth methods which have been developed to enable control over the size and aspect ratio (i.e. ratio of length to width).[184] For example, nanorods were synthesized with dimensions of 45 nm x 15 nm which resulted in an absorption peak at 810 nm. The relevant antibody was then conjugated to the surface for targeting of prostate cancer cells.[185] The Au nanorods enabled effective detection of selected tumour cells using PAI with high sensitivity compared to non-tumour cells *in vitro*.

Au nanorods have been used for the tracking of cells *in vivo* using PAI.[186] As previously mentioned, AuNP properties are dependent on the inter-particle distance and hence it has been found that endocytosis results in the tight packing of nanorods, leading to plasmon coupling.[187, 188] Coating Au nanorods with silica has provided a solution to his problem by sterically hindering the close proximity of the particle without affecting the optical absorption.[189] This enabled the successful tracking of MSCs *in vivo* with MSOT to give high sensitivity without affecting MSC viability or differentiation properties. It has also been found that coating Au nanorods with silica can increase cellular uptake 5-fold with limited effect on the viability, proliferation or pluripotency of MSCs.[190]

Au nanocages consist of porous, hollow structures of cuboidal symmetry where their intense signal can be attributed to their large absorption cross-section.[191] Au nanocages are prepared by the galvanic replacement of $HAuCl_4$ with Ag templates where altering the molar ratio Ag:Au enables the peak absorption to be tuned within the visible-NIR region.[192] Au nanocages have made significant advances as probes for PTT, for example in targeting breast cancer.[193, 194] As well as this, the hollow structure can be exploited for drug delivery and cancer therapeutics.[195] PEG-coated nanocages effectively enhanced the contrast of blood for PAI of the cerebral cortex of mice.[196] Human MSCs labelled with Au nanocages could be effectively detected in a glioblastoma mouse model using PAI.[197] Dual wavelength scanning enabled simultaneous imaging of the MSCs and endogenous absorbers in the tumour vasculature.

The surface chemistry of AuNPs is widely explored which has hence further expanded their biomedical applications. Commonly, thiol groups have been attached to the surface of AuNP for the anchoring of a wide variety of molecules. For example, functional thiolates have been shown to be effective in stabilising gold nanoparticles by incorporating groups such as PEG.[198] As well as this, surface functionalisation has enabled applications of AuNPs in gene and drug delivery to be explored.[199]

1.3.3 Quantum Dots

QDs have previously been discussed as fluorescent probes however the optical properties have also been explored for PAI. For example, copper selenide and copper sulphide have absorbance in the NIR region and have been used for sentinel lymph node mapping in mice with PAI.[200, 201] Despite this, the PA detection limit is much better for AuNPs, as QDs generally have much lower absorption in the NIR region.[202] Several methods have been explored to improve the PA sensitivity of QDs, where one idea is to design integrated QD-Au nanoprobes.[203] Although the PAI signal is not as high as AuNPs, QDs could be used as hybrid contrast agents enabling both PAI and fluorescence imaging.[204]

1.3.4 Carbon-Based Materials

Nanosized reduced graphene oxide sheets have been shown to have high NIR absorption for PTT and PAI.[205] NIR absorbance was increased 6-fold when the reduced graphene oxide sheets were functionalised with PEGylated polymer chains, which also improved the stability of the contrast agents in biological medium.[206] Similarly, reduced graphene oxide nanosheets have been functionalised with bovine serum album (BSA) which were found to be effective theranostic contrast agents for PAI/PTT in mice.[207] Several studies have shown that coating Au nanorods with reduced graphene oxide layers can strongly amplify the photoacoustic signal compared to non-coated and silica coated Au nanorods.[208, 209]

CNTs have also been widely explored as photoacoustic probes.[210, 211] Similarly to graphene, most of the literature has focussed on the design of photoacoustic probes for targeting applications or PTT.[212] This can be attributed to the large surface area and ease of functionalisation of graphene and CNTs.[209] Despite the high NIR absorption, CNTs often require a coating to reduce toxicity. Gold-plated CNTs provide a novel solution to this problem whilst also providing high contrast.[213] CNTs were prepared with a diameter of 1.5-2 nm and a thin gold layer (4-8 nm) was deposited on the surface; changes in both the dimensions of the CNTs and the thickness of the gold enabled control over the absorbance properties. Small molecule dyes, such as ICG, can also be conjugated to the surface to enhance photoacoustic signal.[214]

There are few examples of NDs in photoacoustic imaging, possibly due to their high quantum yield. NDs can be engineered with structural defects which alter the absorption properties. Nitrogen-vacancy (NV) defects are the most common defects which result in high fluorescence across the visible spectrum however more recently silicon-vacancy (SiV) defects have demonstrated NIR absorbance.[215, 216] A more common approach to obtain a ND-based PA probe is to attach NIR-absorbing moieties to the surface. Examples include attaching small molecules such as cyanine dyes to the surface; however, Au-ND nanocomposites have also been explored.[217] It has been hypothesized that combining NDs with Au enables energy transfer from the NDs to the Au clusters resulting in increased PA signal compared to AuNPs.[218]

1.3.5 Semiconducting Polymer Nanoparticles

Semiconducting polymer nanoparticles (SPN) are made up of electronically and optically active semi-conducting polymers and have been explored in electronic devices, photovoltaics and sensors.[219-221] The unique semi-conducting properties come from the π-conjugated backbone of the polymers where a decrease in hydrophobicity is achieved through formulating into nanoparticles.[222] One of the key advantages of SPNs is that they are organic and biologically inert thus making them ideal for biomedical applications.[223] This together with their high brightness, excellent photostability and versatile surface modification have propelled research into applications of SPNs in biological sensing applications, therapeutics and bioimaging.[224-227]

In PAI, two NIR-absorbing SPNs developed for photovoltaic applications were assessed for contrast enhancement in mice and their performance was compared with gold nanorods.[228] It was found that amplitude of the PA signal was much higher than for gold nanorods of the same concentration, thus suggesting dose levels could be reduced. SPNs have also been shown to be effective probes for tracking stem cells with PAI. Furthermore, the structural versatility of the SPNs opens the door to activatable probes for real-time monitoring of stem cell behaviours i.e. cell differentiation.[229]

1.3.6 Cyanine Dyes

Cyanine dyes have been previously discussed as fluorescent probes however they have also been explored as PA contrast agents. One example is IRDye 800CW carboxylate which has been used to visualise renal clearance in mice with MSOT.[161] The NIR-absorbing dye is water soluble and hence its capacity for monitoring renal function has been further developed for assessing the efficacy of kidney therapies *in vivo* with MSOT.[230]

More commonly, indocyanine green (ICG) has been utilised for PAI due to its absorption in the NIR region (Figure 1.5). Furthermore, ICG has limitations for fluorescence imaging due to having a low quantum yield which is ideal for PAI where light energy is converted to acoustic waves.[209] An extra benefit of ICG is that it is already approved by the FDA for use in clinical applications.

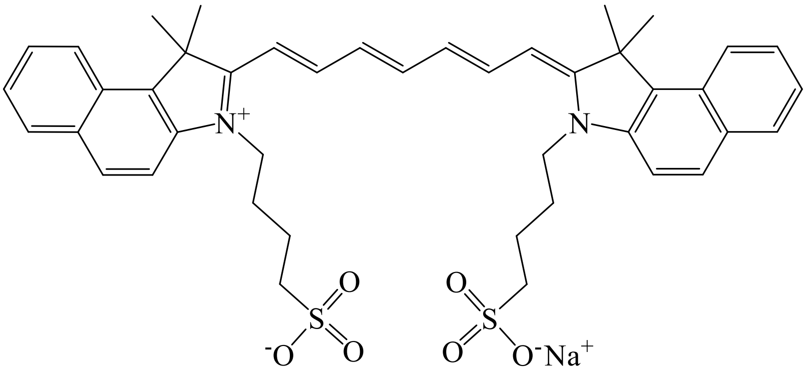

Figure 1.5: Chemical structure of ICG.

One of the drawbacks of ICG is low photostability; the half-life of ICG in the blood stream is only several minutes and hence research efforts have focussed on trying to improve this. One approach looked at trapping ICG in MSNs which improved the stability of the dye and performances as a PA probe.[231, 232] Photonic explorers for biomedical use by biologically localized embedding (PEBBLE) technology has also been explored for tackling the problems associated with ICG.[177] The technology was originally utilised in sensing and therapeutic applications however entrapment of ICG in an organically modified silicate matrix was shown to stabilise the dye against aggregation, whilst retaining the high absorption.[233] Furthermore, encapsulation of ICG in nanoparticles opens up opportunities for surface functionalisation with targeting moieties.

ICG has also been encapsulated in PFC-loaded PLGA nanoparticles.[95] PFC-based particles have been investigated as contrast agents for ^{19}F MRI however the incorporation of ICG opens up opportunities for multimodal imaging. The probe combined the ease and sensitivity of PAI with the penetration depth and quantitative analysis of ^{19}F MRI for applications in cell tracking and lymph node detection. Moreover, these particles are approved for a clinical cell tracking trial hence demonstrating the feasibility for clinical translation.

1.3.7 Perylene Diimide

Rylene dyes have also been exploited for the high absorption properties, where perylene diimide (PDI) derivatives have gained traction in PAI due to absorption in the NIR region (Figure 1.6).[234] Whilst the majority of research has focussed on photovoltaic and electronic applications, their high stability (thermal and photo) and unique electronic and optical properties are of great interest for bioimaging applications.[235, 236]

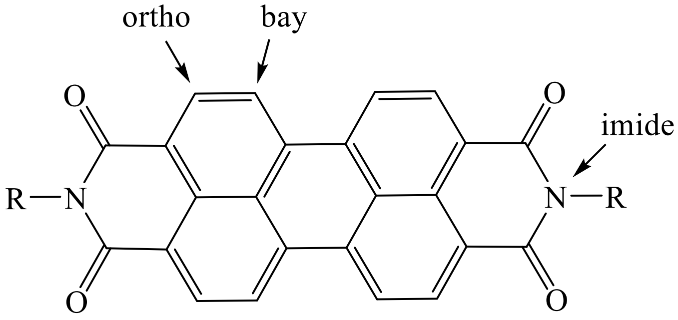

Figure 1.6: General structure of PDI.

The high molar extinction coefficient and photostability makes PDI stand out from other probes for PAI applications.[159] PDI dyes also have strong fluorescence and have been used in fluorescence sensing applications.[237, 238] Despite this, the high absorptivity of PDI derivatives means that they can still provide effective PA contrast. Furthermore, for cell tracking applications, the fluorescence properties provide additional capacity for *ex vivo* fluorescence imaging.

The strong absorbance is derived from the electron dense perylene core where core expansion causes a red-shift in absorbance, albeit at the expense of solubility.[239] Furthermore, PDI is highly versatile compound where modification of the perylene core or imide groups can alter the physical properties (Figure 1.6). Modification at the bay and ortho positions have a significant effect on the wavelength of absorbance, where electron-donating groups, such as pyrrolidine and pyrrolidinone, shift the absorption to the NIR region.[240] However, modification at the imide position has a greater effect on solubility.

The synthesis of PDI derivatives has been widely explored in the literature. Starting from commercially available PTCDA, multiple PDI derivatives can be synthesized with a range of absorption profiles.[236, 237] The tunability of PDI is highly beneficial for MSOT, where spectral unmixing capabilities can be utilised. In principle, two PDI derivatives with different peak absorption could be detected and distinguished with MSOT, opening up opportunities for tracking of multiple PDI-based probes in one experiment.

A drawback of PDI derivatives is that they suffer from poor solubility and hence PDI nanoparticles offer a novel advantage.[241] Nanoparticles have been extensively explored in drug formulation where nano-sizing provides an effective way to improve water solubility.[242, 243] Particle sizes of 10-1000 nm result in a high surface/volume ratio meaning that the properties of the material are defined by the surface. As a result, surface moieties are usually introduced to stabilise nanoparticles, preventing aggregation and improving bioavailability.[244]

PDI nanoparticles have been explored as PA probes for deep tumour imaging in mice;[245] the unique properties, including extraordinarily high photostability, low cost and ease of modification highlighted the potential of PDI-based probes for PAI. Further to this, the same group demonstrated the capabilities of PDI-based probes for identifying early thrombus and targeted PTT.[246, 247] Throughout all of these studies, the probes were found to have limited cytotoxicity thus demonstrating the potential for PDI-based probes in cell tracking.

PDI nanoparticles have also been developed as dual PAI and PET imaging probes by labelling the nanoparticles with ^{64}Cu.[248] These particles were coating in PEG to increase biocompatibility and effectively used for lymph node mapping and cancer imaging. Further to this, another study developed theranostic PDI nanoparticles containing an anticancer drug, to enhance the generation of reactive oxidative species (ROS), and a ROS activatable near-infrared dye (IR790s). The probe was able to have a chemotherapeutic effect whilst also allowing for real-time monitoring of ROS generation through ratiometric PAI, at excitation wavelengths of 680 nm and 790 nm for PDI and IR790s dye, respectively.[249]

1.4 PDI Nanoparticles for Tracking of Encapsulated RMTs

PDI-based probes stand out as excellent PA contrast agents due to their high molar extinction coefficient and photostability. The versatile chemistry of PDI allows for tuneable optical properties and hence multiple PDI derivatives can be prepared with different peak absorption wavelengths. In principle, these derivatives could be employed to prepare two different sets of nanoparticles; these nanoparticles can then be used to label cells and hydrogels separately for the simultaneous tracking of cell biodistribution and hydrogel integrity with MSOT. The spectral absorbance of the two sets of nanoparticles could be unmixed enabling distinction between the labelled cells and labelled hydrogel *in vivo*.

PDI derivatives also exhibit strong fluorescence which is a useful property for designing cell and gel tracking probes. For *in vitro* cell studies, it is important to be able to assess the cellular uptake of the nanoparticles, in particular flow cytometry is a useful tool for detecting labelled cells based on their fluorescence properties.

Furthermore, fluorescence microscopy of labelled cells can provide qualitative data on labelling efficiency and the ability to visualise labelled gels with *in vitro* fluorescence imaging is also of great importance.

In preclinical studies, the fluorescence properties of the probes could be utilised for *ex vivo* imaging and histology, which are commonly carried out post-mortem to corroborate *in vivo* imaging data. It is worth noting that in some cases, it can be difficult to detect probes *ex vivo* due to signal dilution over the timescale of the experiment. Hence, high doses of nanoparticles could circumvent this problem which may be achieved by using particles with extremely low cytotoxicity. Hence, honing the high biocompatibility of nanodiamonds (NDs) by combining them with PDI could be the ideal solution.

When designing probes for labelling encapsulated RMTs, there are several factors which must be considered. The probes must exhibit high signal so that imaging can be carried out at depth *in vivo* and the signal can still be detected even with dilution from cell proliferation. Furthermore, probes must be biocompatible and have limited cytotoxicity. For cell labelling, it is important to optimise parameters such as cellular uptake and retention. When designing probes to label gels, considerations include the interaction between the gel and the probe, as well as the effect the probe has on gel formation.

1.5 Aims

The purpose of this work is to investigate the performance of perylene diimide-based nanoprobes for the *in vivo* tracking of administered mesenchymal stromal cells and encapsulating collagen hydrogels with multispectral optoacoustic tomography and fluorescent imaging. The aims are as follows:

1. To synthesize a near-infrared absorbing perylene diimide derivative that can be prepared into nanoparticles to efficiently label cells and enable their detection with multispectral optoacoustic tomography.
2. To assess whether near-infrared absorbing perylene diimide nanoparticles can efficiently label cell-encapsulating hydrogels to enable their detection with multispectral optoacoustic tomography.
3. To develop nanoprobes comprising a perylene diimide derivative and nanodiamonds for cell labelling to enable cells to be visualised with fluorescence imaging.

The probes investigated herein will be assessed for their photoacoustic and fluorescent signal, cellular uptake and biocompatibility in *in vitro* models.

Chapter 2: Synthesis of Near-Infrared Absorbing Perylene Diimide Nanoparticles for Cell Labelling

2.1 Introduction

Rylene dyes are characterised as a framework of naphthalene units linked at the peri-positions, where perylene, terrylene and quarterrylene are the first in the series (Figure 2.1). Rylene diimides are a novel class of materials which consist of a rylene core with a π-accepting six-membered dicarboxylic imide at each end.[250] These dyes have been investigated for their intense light absorption properties, owed to their highly aromatic and electron dense core, particularly in the dye and pigment, electronic and photovoltaic industries.[239, 251, 252] Rylene diimide derivatives, particularly naphthalene diimide and perylene diimide, have gained significant interest due to their ease of modification, low cost, high chemical and thermal stability and high absorption.[234]

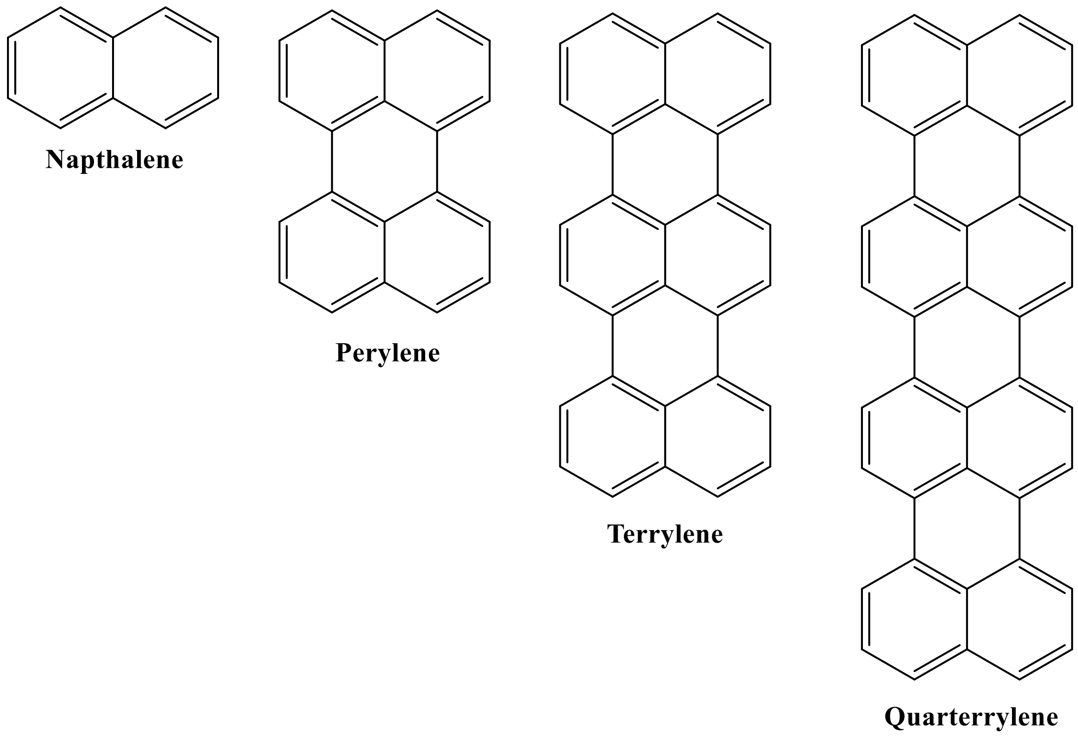

Figure 2.1: Chemical structure of rylene dyes.

2.1.1 Perylene Diimide

Perylene-3,4,9,10-tetracarboxylic dianhydride (PTCDA, Figure 2.2) is a commercially available, low-cost starting material which can be easily modified into various PDI derivatives.[253] PTCDA is a red dye with poor solubility in water and other common solvents; however, chemical modification can alter both absorption maxima and solubility properties. Functionalisation at the bay position predominantly affects the optical properties whereas forming the diimide and exploring different imide substituents generally has a greater effect on solubility.[239]

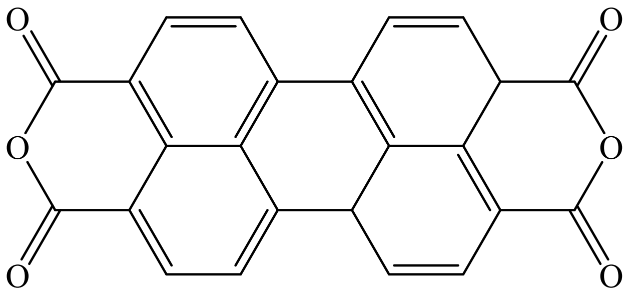

Figure 2.2: Chemical structure of perylene-3,4,9,10-tetracarboxylic dianhydride (PTCDA).

2.1.2 Synthesis of Near-Infrared Absorbing Perylene Diimide Derivatives

2.1.2.1 Core Expansion

Core expansion of the perylene core has shown to cause a bathochromic shift in peak absorption, albeit at the expense of reducing solubility.[254, 255] Terrylene, quarterrylene, pentarylene and hexarylene diimide derivatives have been synthesized where an absorption shift of around 100 nm is seen as the core size is increased by one naphthaline unit.[254] An increase in molar extinction coefficient (ε) was also observed with larger rylene diimide derivatives.

The synthesis of terrylene and quarterrylene diimides is usually carried out *via* a coupling reaction from the monoimide, followed by dehydrogenation, or an alternative route is a one-pot fusion from the respective monoimides.[254] Higher rylene diimide derivatives are much less common due to their more complex synthesis and their lower solubility arising from strong π-π stacking.[256]

2.1.2.2 Imidization

Reactions of PTCDA with aliphatic amines and anilines at the imide position have been carried out with high yield in the dye and pigment industry for some time.[257] The simple condensation reaction is commonly carried out under reflux and inert atmosphere in *N*-methyl-2-pyrrolidinone with acetic acid for 6 hours.[258, 259] More recently, a green chemistry approach has been adopted where the imidization process can be carried out under hydrothermal conditions, without the need for organic solvents or catalysts.[260]

Many PDI derivatives suffer from poor solubility due to their planar aromatic structure resulting in strong π-π stacking. Hence it was found that attaching bulky alkyl or aryl groups to the imide position can increase solubility by disrupting the planarity of PDI, in particular *tert*-butyl groups or long-chain secondary alkyl groups (swallow-tail substituent).[257, 261] *N*-substituted PDI derivatives such as these, have good solubility in chlorinated solvents; however, more hydrophilic groups are required to obtain water-soluble PDI derivatives. Imidization with sulfonic acid moieties, crown ethers, cyclodextrin and polyglycerol dendrons have been reported although these PDI derivatives do not exhibit NIR absorbance.[128, 257]

2.1.2.3 Bay Functionalisation

Bay modification can allow for extension of the perylene π-system, which in turn affects the peak absorption. Hence, the bromination of PDI derivatives at the bay position was a crucial building block for the development of NIR-absorbing PDI derivatives.[236, 237] Typically, bromination of the perylene core has been carried out under harsh conditions using concentrated sulfuric acid with heating producing a mixture of the 1,6- and 1,7-isomers, where consequent recrystallisation or column chromatography has been used to obtain a pure yield.[262]

Alternative routes to bromination of PDI derivatives have been explored in order to avoid the use of concentrated acids. Mild conditions of PDI bromination have been reported using excess bromine in dichloromethane however it was found that the imide groups affect the reactivity at the bay position.[263] Bulkier groups disrupt π-π stacking of PDI derivatives, thus increasing reactivity. Therefore, when dimethyl pentyl groups were at the imide position, the reaction proceeded after 2 days at 22-24 °C; however, the reaction of a PDI derivative containing cyclohexyl imide groups required 4 days under reflux. Milder conditions result in a mixture of mono- and disubstituted brominated PDI derivatives. Indirect routes to bromination have also been explored to avoid harsh conditions and have been employed herein.[236, 237]

Modifying the bay positions at the perylene core with hydrophilic substituents, such as poly(ethylene glycol) or peptide chains, can also increase the solubility albeit at the expense of NIR absorption.[264] Thus it was found that attaching electron-donating amines, such as pyrrolidinyl or piperidinyl groups, to the perylene core causes a red shift towards the NIR region.[127, 236] The red-shift is much more pronounced in disubstituted derivatives.[263, 265] It was found that there was a greater red shift with pyridinyl groups compared to piperidinyl due to short C-N bond length and greater sp^2 character of the nitrogen hybrid orbital.[240]

2.1.2.4 *Recent Advances in Perylene Diimide Synthesis*

More recent methods have investigated attachment of substituent groups at two positions in the perylene core, which has shown to cause a large red-shift. A facile, metal-free approach to annulation of 1,8-diazabicyclo[5.4.0]undec-7-ene (DBU) to PDI has been established whereby DBU can act as both a reactant and catalyst to yield a derivative with absorbance at 750-800 nm.[266] Another recent approach has involved thionation of the carboxylic acid groups causing a red-shift of approximately 50-100 nm.[267]

2.1.3 Applications of Perylene Diimide

PDI derivatives, as well as other rylene dyes, have been historically used in the dye and pigment industry and played a significant part in the industrial revolution.[252] They have predominantly been used as dyes in the industrial textile colourants, in red/black shades, but more recently, they have been developed as pigments, e.g. Pigment Violet 29.[235, 254, 268] The high stability, particularly photostability and stability against the weather, makes PDI derivatives ideal materials for coatings.

More recent times has seen the evolution of these materials into ‘functional dyes.’ In particular, the electron-accepting character of PDI derivatives has led to interest for electronic and photonic applications, such as organic field-effect transistors (OFET), organic thin-film transistors (OTFT) and organic photovoltaic cells (OPV).[235, 251, 269, 270] The ease of modification and versatility of PDI derivatives, combined with control of stacking in the solid state, is advantageous compared to fullerenes which are predominantly used as n-type semiconductors in solar cells.[257, 262] Hence, PDI derivatives offer greater ease and ability of tuning the band gap.

2.1.3.1 Biomedical Applications

One of the key properties of PDI derivatives for biomedical applications, which is the focus of the present study, is the ease of modification to tune the absorption wavelength to the near-infrared (NIR) region (700-1000 nm). This is ideal for biomedical applications as NIR attenuation in tissues is relatively low,[166, 271] and so suggests that PDI-based probes could be efficiently detected when administered *in vivo*, with minimal background signal from the body or endogenous fluorophores. Hence, PDI-based probes are being explored for applications in cell tracking.

Photoacoustic imaging (PAI) is a useful imaging tool for tracking the fate and biodistribution of administered cells (stem cells, progenitor cells and other types of therapeutic cells), in order to aid the design of regenerative medicine therapies.[189, 190] Contrast agents for PAI have been designed to absorb >650 nm to increase signal-to-noise and also to enable them to be distinguished from endogenous absorbers such as haemoglobin and water.[166] Gold and cyanine dyes have previously been investigated as PAI contrast agents, as discussed in Chapter 1. [174, 189, 190, 233] PDI exhibits high photostability compared to cyanine dyes and greater ease of tunability in optical absorbance compared to gold nanoparticles. Therefore, these significant advantages have prompted research into PDI-based probes for PAI.

In parallel with PDI-based probes for PAI, there is also reason to suggest that PDI could be utilised in photothermal therapies (PTT). Also based on the photoacoustic effect, PTT has been exploited for the treatment of cancer where tumour ablation can be caused by thermal stress induced by laser excitation. NIR-absorbing agents are ideal for selective targeting, thus minimising the effect on healthy cells.[163] At present, research into this area has involved gold nanoparticles or carbon-based materials, such as carbon nanotubes;[193, 272, 273] however, there is clear potential for NIR-absorbing probes in these type of applications, particularly with increasing interest in so-called theranostics (agents capable of therapeutic and diagnostic effects).

2.1.4 PDI-Based Probes

PDI-based nanoparticles offer superior properties which can improve the bioavailability, stability and signal intensity when compared to the free PDI dye.[178] PDI-based nanoparticles have previously enabled deep brain tumour photoacoustic imaging in mice.[245] We have published a study investigating the use of PDI-based nanoparticles for tracking the fate and biodistribution of mesenchymal stromal cells (MSC) *in vivo* with multispectral optoacoustic tomography (MSOT).[274]

MSOT is a form of PAI imaging whereby multiple wavelengths can be scanned and unmixed. This allows the effective detection of various light absorbing molecules to be distinguished. Hence, the ability to control the absorption wavelength of PDI derivatives opens up the capacity of multiple PDI-based contrast agents to be imaged simultaneously with MSOT. This would be particularly useful in cell tracking if more than one cell type was used, e.g. MSC and macrophages, or for tracking cells and encapsulating hydrogels simultaneously.

2.1.5 Aims

The present study will investigate the potential of perylene diimide nanoparticles as probes for tracking administered regenerative medicine therapies with multispectral optoacoustic tomography. The aims are as follows:

1. To synthesize an near-infrared absorbing perylene diimide derivative, *N,N’*-dicyclohexyl-1,7-di(pyrrolidinyl)perylene-3,4,9,10-tetracarboxy diimide,

using a multistep synthesis from commercially available perylene-3,4,9,10-tetrecarboxylic dianhydride (PTDCA).

2. To prepare near-infrared absorbing perylene diimide nanoparticles *via* nanoprecipitation with our novel star hyperbranched block copolymer (SHBP)[275] or poly(vinyl alcohol) (PVA) as a stabiliser.
3. To label mesenchymal stromal cells with perylene diimide nanoparticles and assess the biocompatibility, cellular uptake and photoacoustic signal of the probes.

2.2 Experimental

2.2.1 Materials

All reagents were used as received from the manufacturer. Perylene-3,4,9,10-tetrecarboxylic dianhydride (PTDCA, 97%), bromobutane (99%), butanol (99.8%, 1,8-diazabicyclo[5.4.0]undec-7-ene (DBU, 98%), potassium hydroxide (≥85%), sodium bisulfite (≥99%), sodium sulfate (≥99%), p-toluenesulfonic acid monohydrate (99%), cyclohexylamine (≥99%), *N*-methyl-2-pyrrolidinone (99.5%), pyrrolidine (≥99%) and poly(vinyl alcohol) (MW 9-10K, 80% hydrolysed) were purchased from Sigma Aldrich. All solvents were HPLC grade VWR. Bromine (99.6%) was from Acros chemicals. The star hyperbranched block copolymer ($DEAMA_{50}$-*c*-$DEGDMA_2$)-*b*-($OEGMA_{80}$) was prepared by Dr Ulrike Wais.[275]

2.2.2 Characterisation Methods

^1H NMR spectra were recorded using a Bruker Fourier 300HD NMR spectrometer (400 MHz) and spectroscopic data was obtained using a Vertex 70 Fourier Transform Infrared (FTIR) Spectrometer (Bruker). A Cary 5000 UV-Vis-NIR Spectrometer (Agilent) was used to measure absorption spectra of PDI derivatives in CH_2Cl_2 or $CHCl_3$ (50 µg/ml) and PDI nanoparticles in water (0.15 mg/ml PDI). A Malvern Zetasizer Nano and associated Zetasizer software were used to determine information about the particles in aqueous suspension using dynamic light scattering (DLS). This included (i) the hydrodynamic diameter of the particles, which is the effective diameter of a particle calculated from the diffusion coefficient, (ii) the polydispersity index, which is a measure of the heterogeneity of sizes of particles, and (iii) zeta potential, which measures the electrical potential at the slipping plane. Samples were first diluted (25 µg/ml PDI) and consequently sonicated for 10 minutes prior to DLS analysis. Images of particles were acquired with a Hitachi S4800 Scanning Electron Microscope

(5 kV). One drop of nanosuspension was placed on SEM stub and left for the liquid to evaporate before coating with chromium.

2.2.3 Synthesis of Perylene Diimide Derivatives

2.2.3.1 Synthesis of Perylene-3,4,9,10-tetrabutylester (compound 1a)

Brominated PTCDA (compound 2) was prepared following an established route by Sengupta *et al*. with small modifications. Briefly, perylenetetracarboxylic dianhydride (PTCDA, 4 g, 10 mmol), bromobutane (20 g, 0.146 mol), BuOH (13 g, 0.175 mol), DBU (15 g, 0.100 mol) and acetonitrile (ACN, 160 ml) were refluxed at 100 °C for 18hr. The cooled reaction was then filtered, washed with methanol and purified by recrystallization in boiling BuOH. The pure orange compound 1a was isolated in 93% yield. ^{1}H NMR ($CDCl_3$, TMS): δ: 8.36 (d, 4H), 8.08 (d, 4H), 4.33 (t, 8H), 1.80-1.77 (m, 8H), 1.50-1.47 (m, 8H), 0.99 (t, 12H). UV-vis (DMSO): 448 nm, 470 nm.

2.2.3.2 Synthesis of 1,7-Dibromoperylene-3,4,9,10-tetracarboxytetrabutylester (compound 1b)

Compound 1a (4 g, 6.13 mmol) and KOH (2 g, 14 mmol) were stirred in CH_2Cl_2 (50 ml). Bromine (4 ml) was added dropwise and the reaction was stirred at room temperature for 24hr. A saturated aqueous solution of $NaHSO_3$ was then added dropwise with stirring. The organic layer was then washed three times with water and dried over sodium sulfate. The crude orange product was a mixture of two isomers: compounds 1b and 1b(i). Compound 1b was isolated *via* double solvent recrystallisation from dichloromethane and acetonitrile (64% yield). ^{1}H NMR ($CDCl_3$, TMS): δ: 8.96 (d, 2H), 8.30 (s, 2H), 8.10 (d, 2H), 4.34 (t, 8H), 1.80-1.77 (m, 8H), 1.51-1.44 (m, 8H), 0.99 (t, 12H). UV-vis (DMSO): 448 nm, 470 nm.

2.2.3.3 Synthesis of 1,7-Dibromoperylene-3,4,9,10-tetracarboxylic dianhydride (compound 2)

Compound 1b (3 g, 3.75 mmol), *p*-toluenesulfonic acid monohydrate (3.6 g, 19 mmol) and toluene (105 ml) were refluxed at 100 °C for 30hr. The reaction was then cooled, filtered and washed with methanol and water. The dried product was then refluxed at 75 °C in $CHCl_3$ (150 ml) for 3hr to obtain the pure product in 83% yield. ^1H NMR could not be measured due to the extremely low solubility of compound 1b. UV-vis (DMSO): 495 nm, 524 nm.

2.2.3.4 Synthesis of N,N'*-Dicyclohexyl-1,7-dibromoperylene-3,4,9,10-tetracarboxy diimide (compound 3)*

Compound 2 (1.5 g, 2.78 mmol), cyclohexylamine (0.8 g, 8.1 mmol), acetic acid (0.9 g, 15.0 mmol) and *N*-methyl-2-pyrrolidinone (30 ml) were refluxed at 85 °C under a N_2 atmosphere for 6hr. The resulting red precipitate (compound 3) was filtered, washed with methanol and dried in an oven. The final yield was 42%. ^1H NMR ($CDCl_3$, TMS): δ: 9.48 (d, 2H), 8.85 (s, 2H), 8.67 (d, 2H), 5.05-4.99 (m, 2H), 2.59-2.53 (d, 8H), 1.93-1.25 (m, 12H). UV-vis (CH_2Cl_2): 492 nm, 525 nm

2.2.3.5 Synthesis of N,N'*-Dicyclohexyl-1,7-di(pyrrolidinyl)perylene-3,4,9,10-tetracarboxy diimide (compound 4)*

Compound 3 (500 mg, 0.71 mmol) was dissolved in pyrrolidine (26 ml, 317 mmol) and stirred a 70 °C under an Ar atmosphere for 48hr. The reaction mixture was then poured into 10% hydrochloric acid solution (25 ml) before liquid extraction in dichloromethane was carried out three times. The blue-green product (compound 4) was dried over magnesium sulfate, filtered and dried in a vacuum oven. The resulting product was purified by silica gel column chromatography (CH_2Cl_2/hexane, 40/1, v/v) giving a final yield of 14.2%. ^{1}H NMR ($CDCl_3$, TMS): δ: 8.47 (s, 2H), 8.41 (d, 2H), 7.74 (d, 2H), 5.13-5.00 (m, 2H), 3.83-3.71 (m, 4H), 2.89-2.77 (m, 4H), 2.66-2.54 (m, 4H), 2.12-1.86 (m, 8H), 1.76-1.70 (m, 4H), 1.57-1.25 (m, 12H). UV-vis (CH_2CL_2): 448 nm, 650 nm, 710 nm.

2.2.4 Preparation of PDI Nanoparticles *via* Nanoprecipitation

2.2.4.1 Star Hyperbranched Block Copolymer (SHBP) Stabiliser

A solution of NIR PDI (compound 4) in acetone was prepared at a concentration of 1 mg/ml. A second solution was the prepared with SHBP ($DEAMA_{50}$-*c*-$DEGDMA_2$)-*b*-($OEGMA_{80}$) in acetone (2 mg/ml). In some cases, the polymer solution was diluted further with acetone so that PDI:polymer ratios of 1:1, 2:1 and 3:1 were achieved. The PDI and polymer solutions (2 ml of each) were added dropwise to water (8 ml) with stirring. The reaction was stirred for 24hr to allow the acetone to evaporate, yielding a clear, blue-green aqueous nanoparticle suspension.

2.2.4.2 Poly(vinyl alcohol) Stabiliser (PVA)

Nanoparticles were also prepared with PVA as a stabiliser using a slightly different method as PVA is soluble in water. PVA (80 mg) was dissolved in 8 ml water, where consequently 2 ml of PDI/acetone solution (1 mg/ml) was added. The reaction was also stirred for 24hr to yield a clear, green aqueous nanoparticle suspension.

2.2.5 Cell Culture

The murine mesenchymal stromal cell line (MSC) D1 (ATCC) was used for all *in vitro* cell studies. MSCs had previously been modified by a member of our group (Dr Taylor, Murray Lab) to express firefly luciferase and ZsGreen under the control of the constitutive promoter, EF1α.[276, 277] MSCs were cultured in 6 cm or 10 cm tissue culture dishes (Greiner CELLSTAR®) in high glucose Dulbecco’s Modified Eagle Medium

(DMEM, Sigma Aldrich) containing 10% fetal bovine serum (FBS, Sigma Aldrich), 1% non-essential amino acids (Sigma Aldrich) and 2 mM L-glutamine (Gibco). Cells were incubated at 37°C and 5% v/v CO_2 and passaged with 1% trypsin-EDTA (Sigma Aldrich) when they reached 90% confluence.

2.2.6 *In Vitro* Cell Studies

2.2.6.1 Cell Viability

CellTiter-Glo® Luminescent Cell Viability Assay (Promega) was used according to the manufacturer’s guidelines. MSCs were seeded in triplicate at a density of $2x10^4$ cells/well in a 96-well plate and left to attach and grow for 24hr. After this, the medium was replaced with 200 µl fresh medium containing various concentrations of PDI nanoparticles (PDI concentration 0-40 µg/ml). Cells were incubated for a further 24hr before carrying out the assay. The principle is based on the detection of ATP released from lysed cells which reacts with luciferin/luciferase, leading to light emission at 562 nm. Cell viability was measured as the amount of ATP released from treated cells as a percentage of the ATP released from the control. Luminescence measurements were taken with a µ–Quant Microplate reader (BioTek).

2.2.6.2 Flow Cytometry

Flow cytometry was used to assess the cellular uptake and fluorescence properties of the PDI nanoparticles. MSCs were seeded at a density of $2x10^5$ cells/well (24-well plate) and incubated for 24hr. After this, the medium was aspirated and replaced with fresh medium containing nanoparticles of varying concentrations (0-25 µg/ml). After a further 24hr, cells were resuspended in PBS (1x) and kept on ice ahead of analysis. Flow cytometry was carried out using a BD FACSCalibur™ (BD Biosciences) with a 488 nm laser wavelength and a long pass FL3 filter (670 nm). When appropriate, threshold values for side scatter (SSC), front scatter (FSC) and FL3 were altered relative to the control to exclude unwanted events. 10,000 events were counted and the data was analysed with Flowing Software 2.5.1 (Turku Bioscience Centre).

2.2.6.3 Confocal Fluorescence Microscopy

Confocal fluorescence microscopy was employed to visualise and determine the location of PDI nanoparticles in MSCs. MSCs were seeded in 8-well chamber slides (Ibidi µ-Slide 8-well) at a density of 2×10^4 cells/well. After 24hr labelling with nanoparticles (25 µg/ml), samples were fixed with 4% paraformaldehyde (PFA, Sigma Aldrich). Cells were permeabilised with Triton-X (0.1 %v/v, Sigma Aldrich) and stained with 4′,6-diamidino-2-phenylindole (DAPI, 1:1000, Thermo Fisher) and Alexa Fluor™ 488 phalloidin (1:50, Invitrogen). Images were acquired with a Zeiss LSM 800 Airyscan confocal using 405 nm, 488 nm and 640 nm diode lasers and 63x oil objective. Z-stack images were obtained using a step size of 0.34 µm and the master gain of the PMT was set to 700 mV. Images were analysed in ImageJ (FIJI).

2.2.7 Multispectral Optoacoustic Tomography

2.2.7.1 Preparation of Phantoms

Agar phantoms were prepared for imaging with multispectral optoacoustic tomography (MSOT). 20 ml syringes were used as moulds by removing the end and pulling the plunger out. With the handle of the plunger taped to a surface, a straw (ends sealed) was suspended in the middle of the syringe and secured with tape in order to create a hole in the phantom for loading samples. Next, intralipid (1.03 ml, Sigma Aldrich) was heated in a water bath whilst agar (0.75 g, Sigma Aldrich) was added to 50 ml of water and heated in a microwave. The solution was shaken and intralipid was added. The agar mixture was then poured into the syringe moulds and left to set for 30 minutes. Once set, the straws were removed and phantoms were stored in a small amount of water in the fridge to be used the following day.

2.2.7.2 Imaging

The nanoparticle suspensions were put in clear plastic straws and sealed at either end. The straws were then inserted into agar phantoms, covered in ultrasound gel and placed in the water bath (25°C) of the MSOT inVision System (iThera). A single slice was imaged at 660-1000 nm in 5 nm intervals. The following reconstruction parameters were utilised: backprojection 25mm(res:75μm), 50 kHz-6.5 MHz-IR and images were analysed using viewMSOT software (iThera).

2.3 Results

NIR-absorbing PDI was prepared from the commercially available starting material, perylenetetracarboxylic dianhydride (PTCDA, compound 1), as shown in Figure 2.3. Firstly, PTCDA was brominated at the C1 and C7 positions of the aromatic core to form compound 2, following a slightly modified version of a method reported by Sengupta *et al.*[237] Consequently, imide substitution resulted in compound 3 and then the bromine atoms were substituted by pyrrolidine groups to cause a red-shift in absorption to the NIR region (compound 4), based upon a protocol developed by Sukul *et al.*[236]

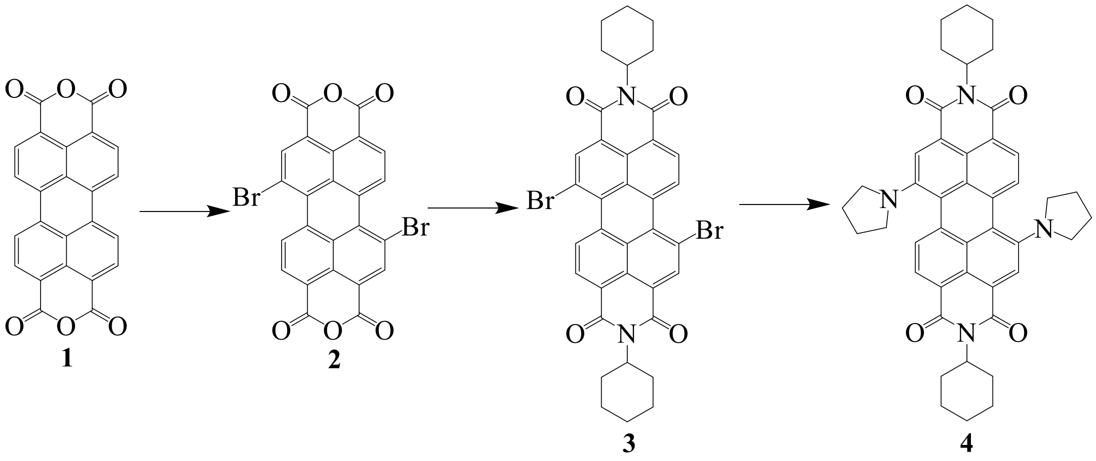

Figure 2.3: Synthetic scheme to produce NIR-absorbing PDI from PTDCA.[236, 237]

2.3.1 Synthesis of brominated PTCDA

The bromination of PTCDA has been reported in several publications.[235, 259, 263] The method used in this study was carried out *via* a 3-step process to yield the regioisomerically pure brominated PTCDA, whilst avoiding harsh conditions and minimising safety risks. Firstly, the anhydride groups were opened to produce a tetraester derivative (compound 1a) followed by bromination at the bay area (compound 1b). The dianhydride was then reformed under acidic condition to yield brominated PTCDA (compound 2), as depicted in Figure 2.4.

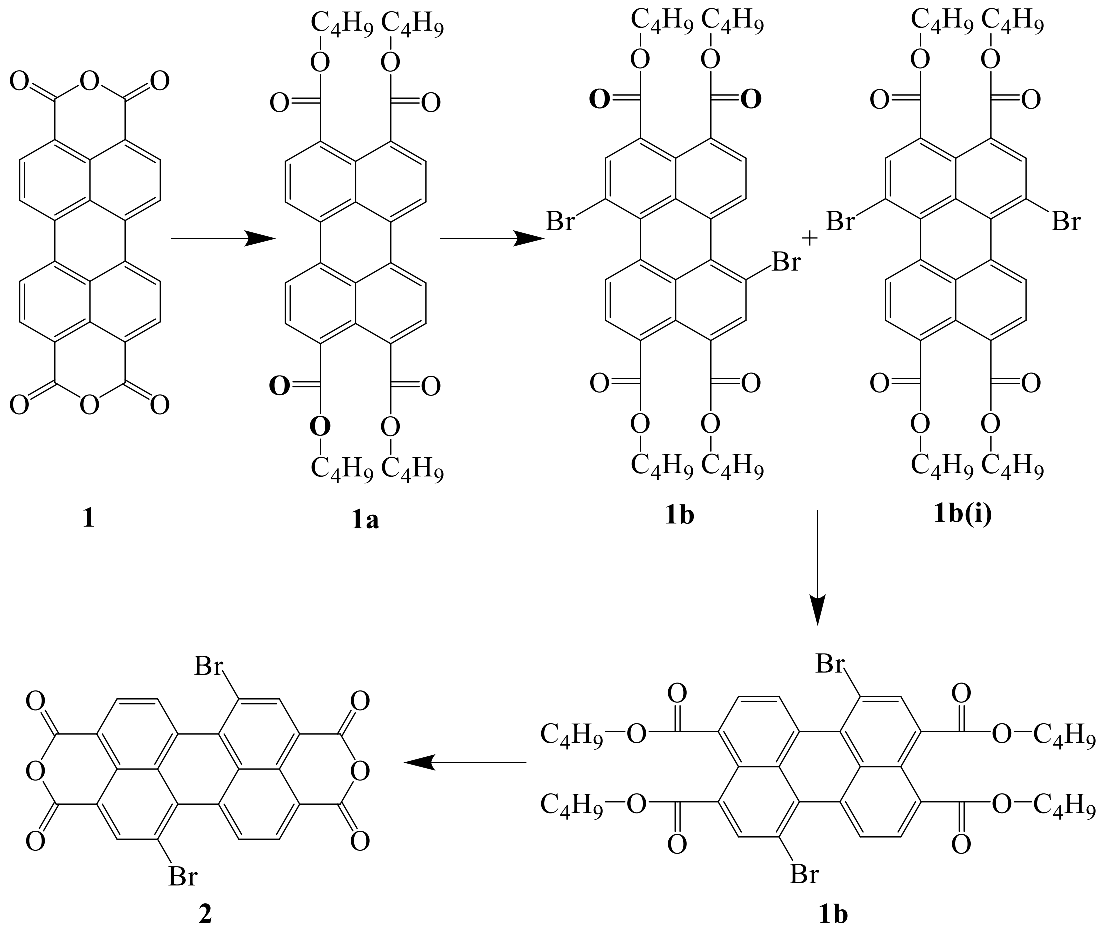

Figure 2.4: Synthesis of brominated PTCDA.[237]

2.3.1.1 *Synthesis of Perylene-3,4,9,10-tetrabutylester (compound 1a)*

The synthesis of compound 1a proceeded under ambient conditions with 1,8-diazabicyclo(5.4.0)undec-7-ene (DBU) acting as a catalyst to give a 93% yield. The ^{1}H NMR spectra confirmed the presence of the alkyl chains with new upfield peaks; 1.80-1.77 ppm, indicated the methylene group attached to the oxygen atom, 1.50-1.47 ppm for the methylene chain and 0.99 ppm was the terminal methyl group (Figure 2.5). The downfield peaks can be attributed to the proton environments at the perylene core. FTIR also confirmed the transformation from anhydride to ester functionality with a shift in wavenumber from 1756 to 1720 cm^{-1} and the occurrence of a new stretch at 2867 cm^{-1} indicating the methylene groups (Figure 2.6).

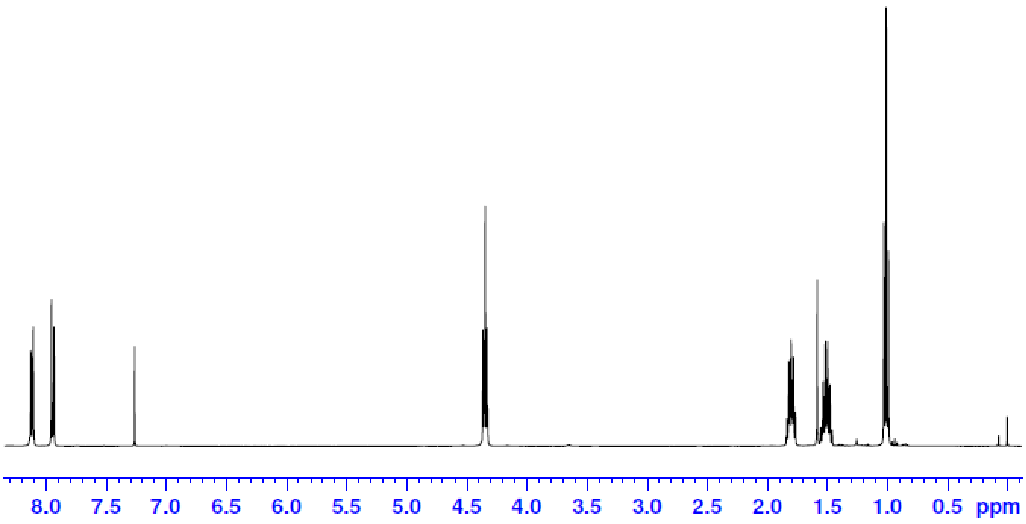

Figure 2.5: ^{1}H NMR of perylene-3,4,9,10-tetrabutylester (compound 1a) in $CDCl_3$.

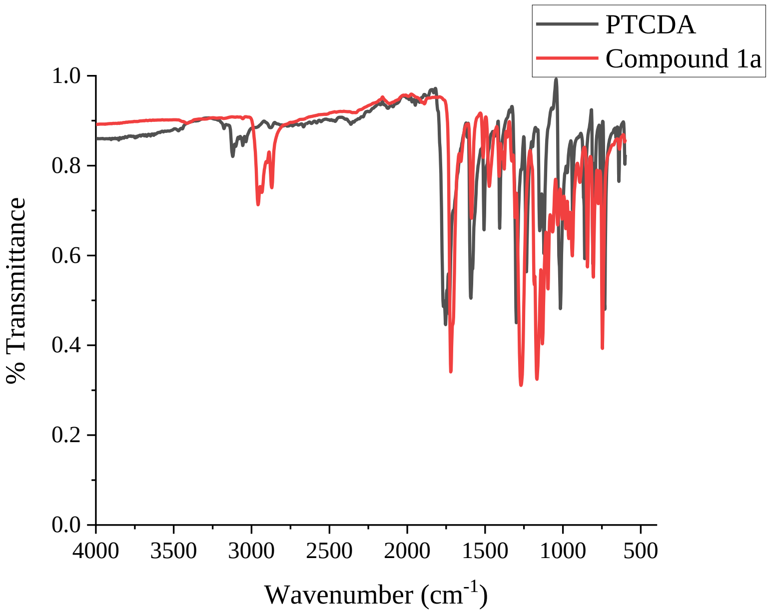

Figure 2.6: FTIR spectra of starting material, PTCDA and perylene-3,4,9,10-tetrabutylester (compound 1a).

An increase in solubility was also observed with the addition of the alkyl chains; PTCDA has extremely low solubility however compound 1a was soluble in chlorinated solvents. Compound 1a is orange in colour, compared to red PTCDA, which corresponded to peaks at 448 and 470 nm in the UV-vis spectrum, shown in Figure 2.7.

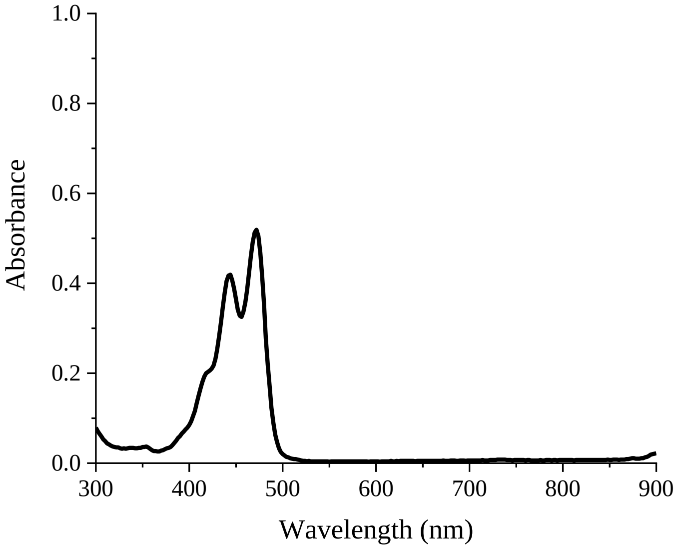

Figure 2.7: UV-vis spectrum of perylene-3,4,9,10-tetrabutylester (compound 1a) (0.05 mg/ml DMSO).

2.3.1.2 Synthesis of 1,7-Dibromoperylene-3,4,9,10-tetracarboxytetrabutylester (compound 1b)

The formation of compound 1b involved the addition of excess pure bromine to compound 1a dissolved in dichloromethane in the presence of potassium carbonate. The reaction proceeded at room temperature over 24hr, before quenching with sodium bisulfite. Bromination of the bay region of PDI generally resulted in the formation of the 1,6- and 1,7-regioisomers in a 2:1 ratio. The regioisomers were separated by double-solvent recrystallisation in dichloromethane/acetonitrile over 3 days.

The success of the reaction was confirmed by ^{1}H NMR, where peaks associated with aromatic hydrogen atoms, at 8.96 and 8.10 ppm were shifted downfield (Figure 2.8). A new singlet peak at 8.30 ppm indicated the hydrogen atoms next to the bromine. The NMR indicated there was some of the 1,6-regioisomer even after recrystallisation; the peaks at 8.96 and 8.30 ppm have smaller peaks which were slightly downfield.[237] This was not considered to be a problem for the current application as the regioisomers have the same absorbance maxima (Figure 2.9).

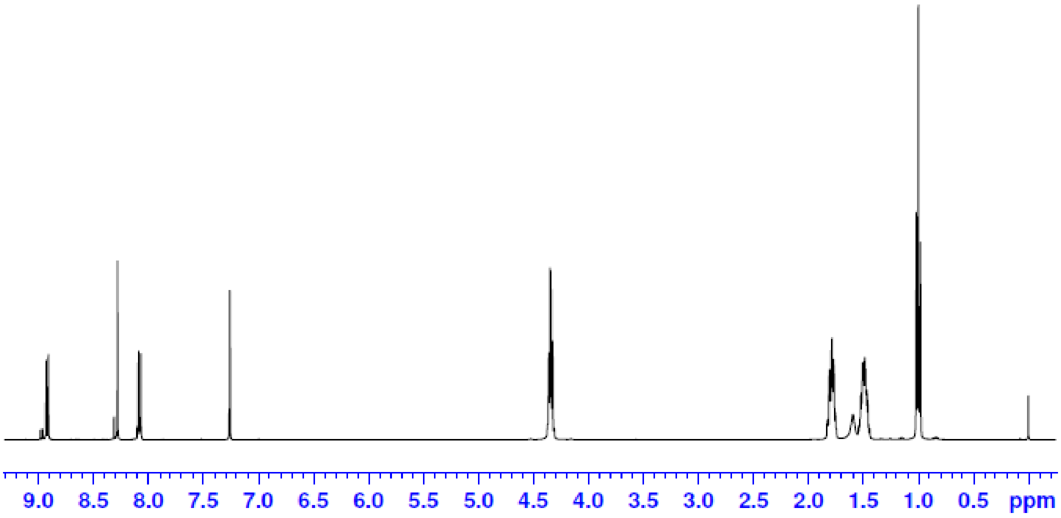

Figure 2.8: ^{1}H NMR of 1,7-dibromoperylene-3,4,9,10-tetracarboxytetrabutylester (compound 1b) in $CDCl_3$.

There was little change in the FTIR spectrum however the presence of new stretches within the fingerprint region agreed that a C-Br bond had been introduced (Figure A1, Appendix).

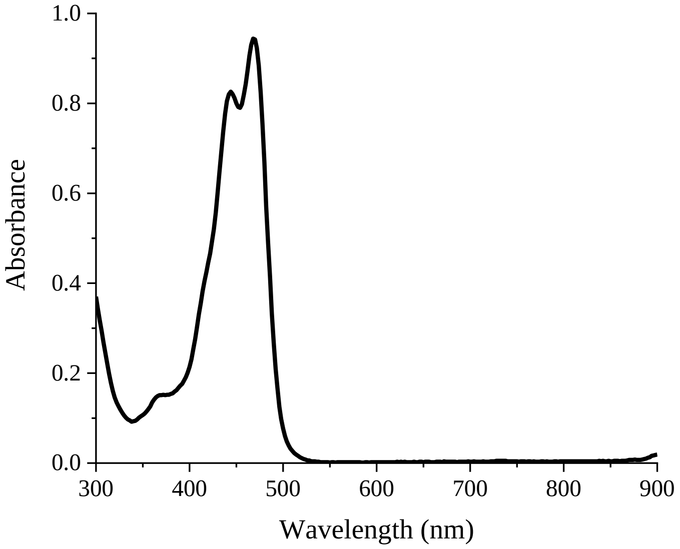

Figure 2.9: UV-vis spectrum of 1,7-dibromoperylene-3,4,9,10-tetracarboxy tetrabutylester (compound 1b) in DMSO (0.05 mg/ml).

2.3.1.3 Synthesis of 1,7-Dibromoperylene-3,4,9,10-tetracarboxylic dianhydride (compound 2)

The anhydride groups were reintroduced under acidic conditions to yield brominated PTCDA (compound 2) with an 83% yield. The solubility of compound 2 is extremely low (as for PTCDA) and hence an NMR spectrum could not be obtained. The FTIR spectrum confirmed the reformation of the anhydride from the ester with a shift in the carboxyl peak from 1718 to 1764 cm^{-1} (Figure 2.10). Additionally, there is no longer a stretch at 2867 cm^{-1} for the methylene groups.

The low solubility and deep red colour of brominated PTCDA (compound 2), similar to that of PTCDA, suggested the reaction had been successful. This was confirmed with UV-vis analysis with peaks at 495 and 524 nm (Figure 2.11); this was possible as compound 2 was partially soluble in dimethyl sulfoxide (DMSO) at extremely low concentrations.

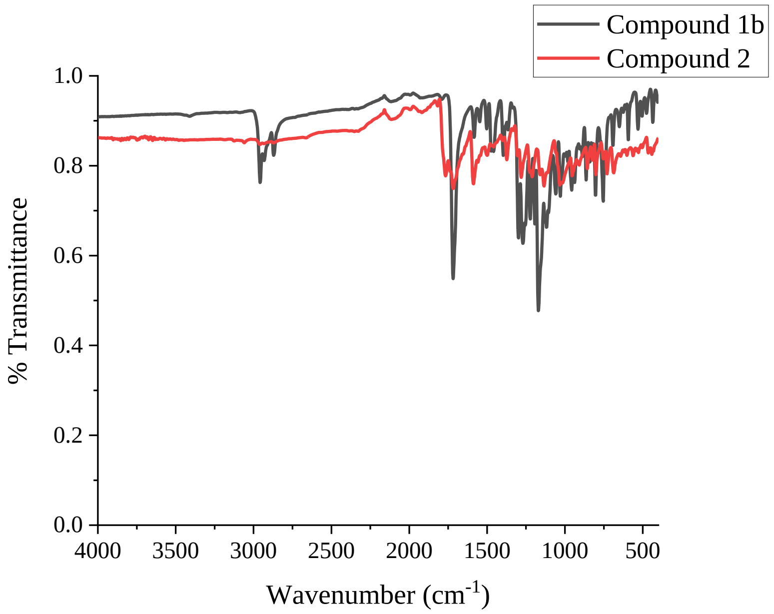

Figure 2.10: FTIR spectra of 1,7-dibromoperylene-3,4,9,10-tetracarboxy tetrabutylester (compound 1b) and brominated PTCDA (compound 2).

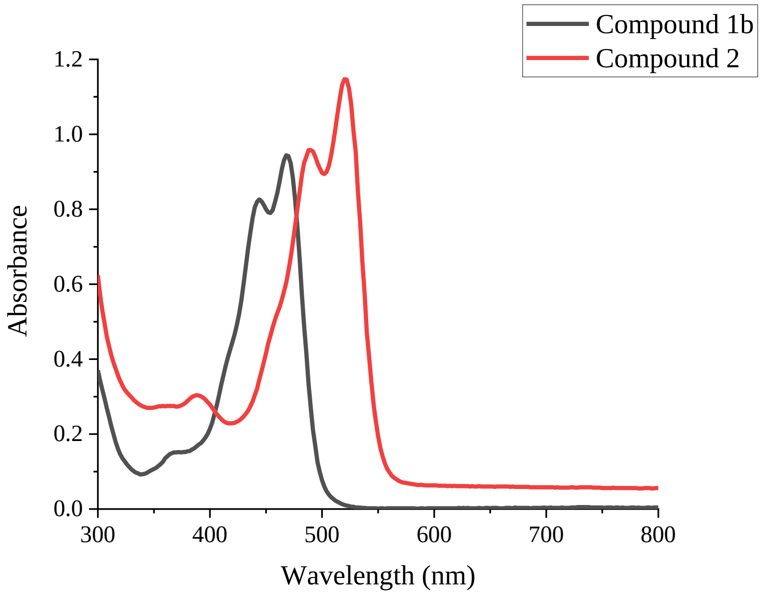

Figure 2.11: UV-visible spectra of 1,7-dibromoperylene-3,4,9,10-tetracarboxy tetrabutylester (compound 1b) and brominated PTCDA (compound 2) in DMSO (0.05 mg/ml).

2.3.2 Synthesis of NIR-absorbing PDI

N,N'-Dicyclohexyl-1,7-di(pyrrolidinyl)perylene-3,4,9,10-tetracarboxy diimide was synthesized from brominated PTCDA, following the scheme in Figure 2.4.[236] Firstly, the dianhydride was converted to a diimide group with cyclohexyl substituent (compound 3). Following this, the bromine atoms at the bay position were substituted for pyrrolidine groups to increase electron density in the perylene core, resulting in a red shift in absorption to the NIR region (compound 4).

2.3.2.1 Synthesis of N,N'-Dicyclohexyl-1,7-dibromoperylene-3,4,9,10-tetracarboxy diimide (compound 3)

The anhydride groups were first converted to imides with cyclohexyl substituents. ^{1}H NMR identified a small new peak at 5.05-4.99 ppm indicating the two hydrogen atoms bond to C1 of each cyclohexyl ring, which each have four adjacent hydrogen atoms resulting in the multiplet splitting (Figure 2.12). The doublet peak at 2.59-2.53 ppm and the multiplet at 1.93-1.25 ppm correspond to the other hydrogen atoms in the cyclohexyl ring.

FTIR was again a good indicator of the success of the reaction as stretches reappeared around 2800-3000 cm^{-1} due to the presence of methylene groups in the cyclohexyl ring, shown in Figure 2.13. Additionally, the carboxyl peak is shifted to a lower wavenumber of 1650 cm^{-1}, characteristic of the imide compared to the previous anhydride group. The UV-vis profile was similar to that of brominated PTCDA (compound 2), thus further iterating the limited impact of imide substitution on the optical properties of PDI derivatives (Figure 2.14).

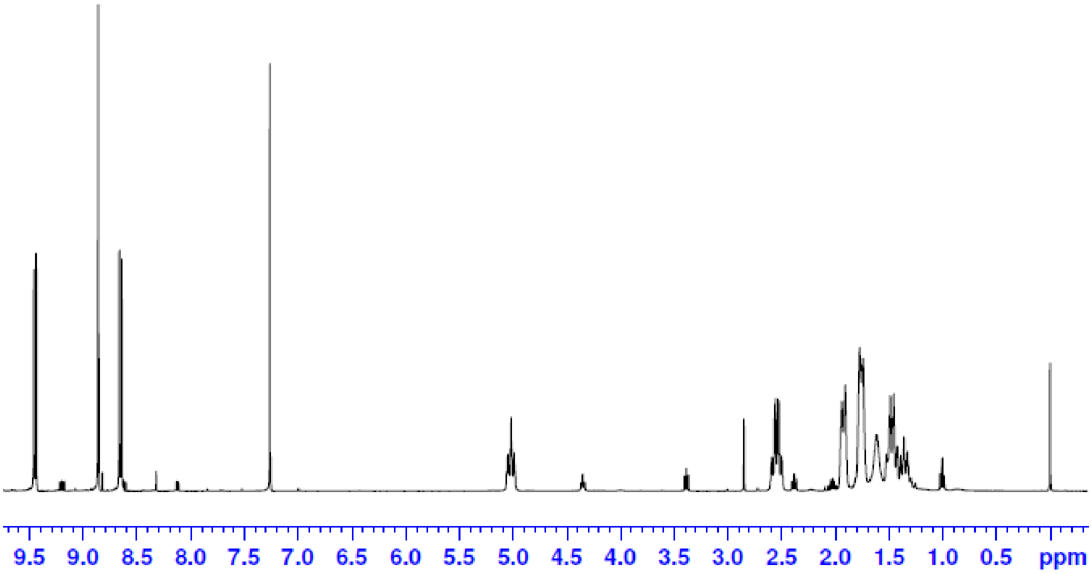

Figure 2.12: ^{1}H NMR of *N,N'*-dicyclohexyl-1,7-dibromoperylene-3,4,9,10-tetracarboxy diimide (compound 3) in $CDCl_3$.

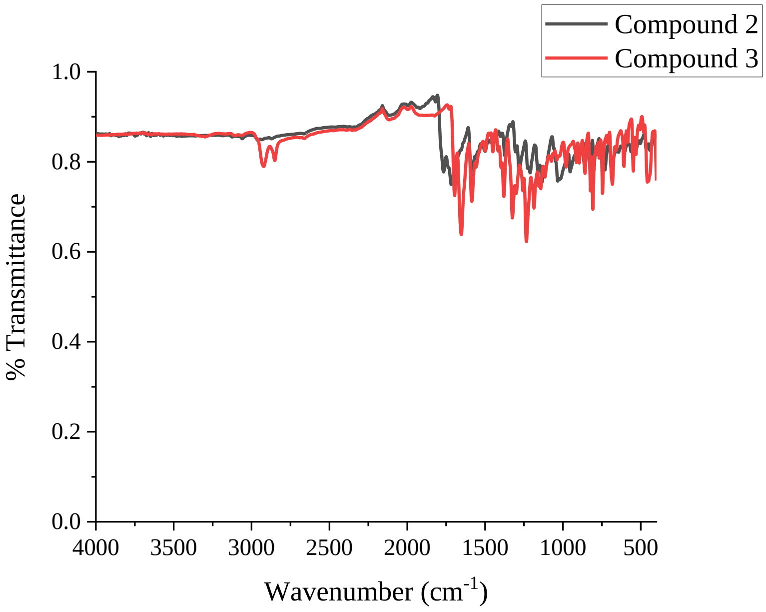

Figure 2.13: FTIR spectra of brominated PTCDA (compound 2) and the *N,N'*-dicyclohexyl-1,7-dibromoperylene-3,4,9,10-tetracarboxy diimide (compound 3).

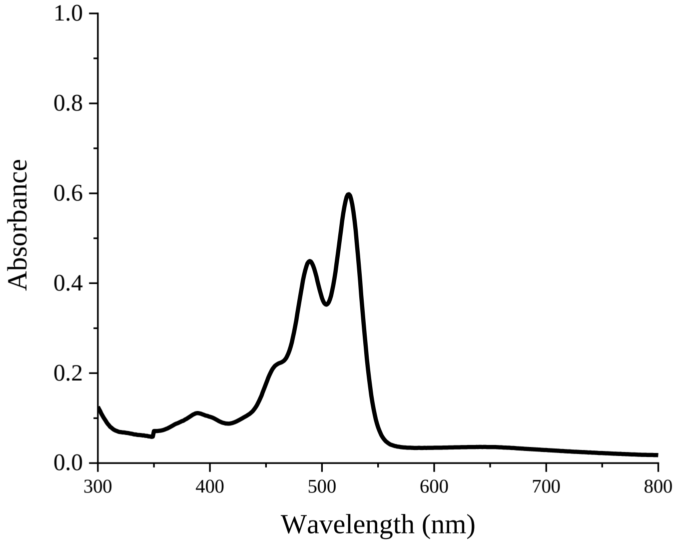

Figure 2.14: UV-vis spectrum of *N,N'*-dicyclohexyl-1,7-dibromoperylene-3,4,9,10-tetracarboxy diimide (compound 3) in DCM (0.05 mg/ml).

2.3.2.2 Synthesis of N,N'*-Dicyclohexyl-1,7-di(pyrrolidinyl)perylene-3,4,9,10-tetracarboxy diimide (compound 4)*

The next stage of the reaction was the critical step to attain NIR absorption by substituting the bay functionalised bromine atoms for pyrrolidine groups. The ^{1}H NMR showed new multiplet peaks at 3.83-3.71 ppm and 2.89-2.77 ppm which can be attributed to the proton environments in the pyrrolidine ring (Figure 2.15). There was very little change in the FTIR spectrum other than in the fingerprint region, which suggested the C-Br bond was no longer present (Figure A2, Appendix).

Ultimately, the success of the reaction was confirmed with UV-vis, where a peak at 700 nm was observed, as shown in Figure 2.16, and colour of compound was dark green/blue. The substitution of bromine for pyrrolidine groups resulted in a red shift of 175 nm into the NIR region, making PDI derivative 4 ideal for *in vivo* imaging, as tissue attenuation is low at this wavelength.

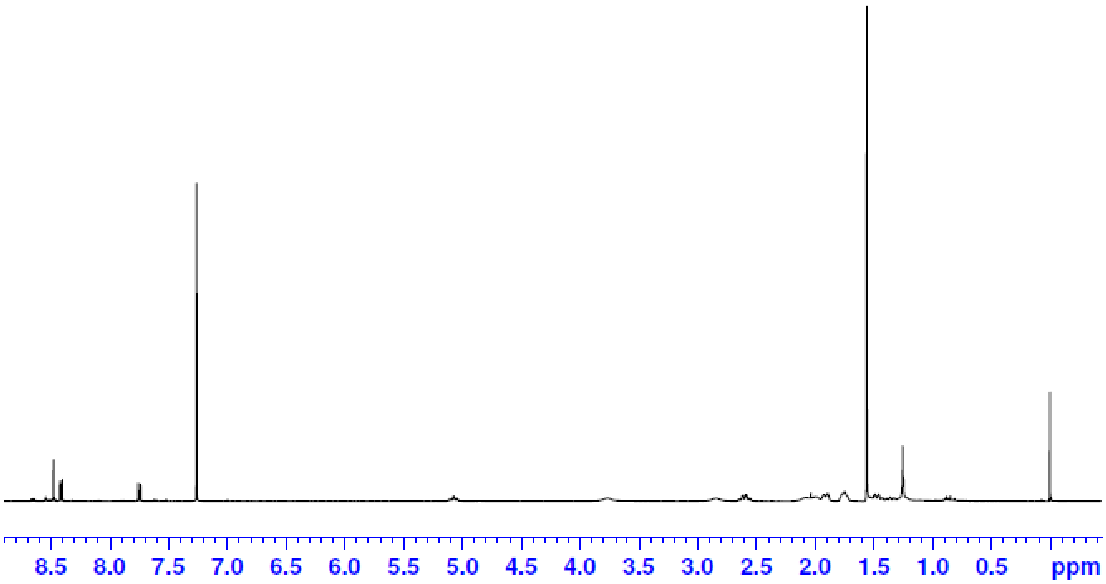

Figure 2.15: ^{1}H NMR of *N,N'*-Dicyclohexyl-1,7-di(pyrrolidinyl)perylene-3,4,9,10-tetracarboxy diimide (compound 4) in $CDCl_3$.

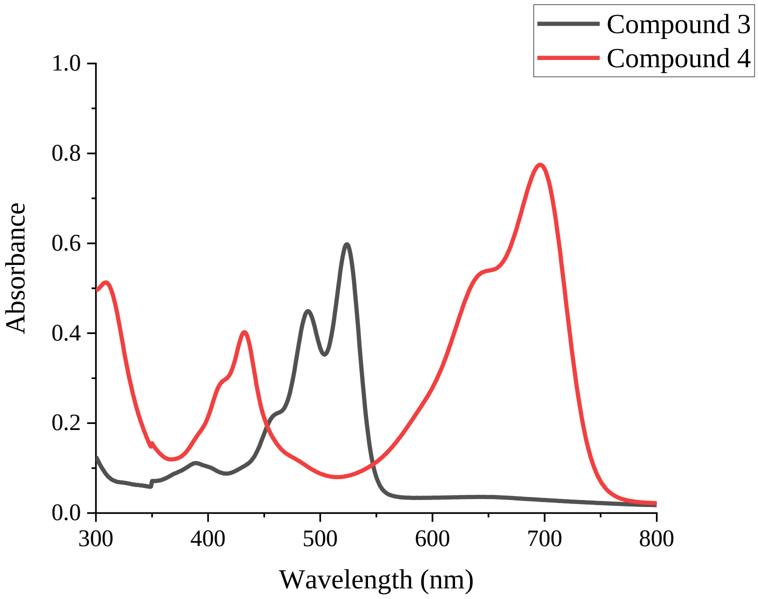

Figure 2.16: UV-vis spectra of *N,N'*-dicyclohexyl-1,7-dibromoperylene-3,4,9,10-tetracarboxy diimide (compound 3) and *N,N'*-dicyclohexyl-1,7-di(pyrrolidinyl)perylene-3,4,9,10-tetracarboxy diimide (compound 4) in DCM (0.05 mg/ml).

2.3.3 Preparation of PDI Nanoparticles *via* Nanoprecipitation with Star Hyperbranched Block Copolymer Stabiliser

PDI derivative 4 (*N,N'*-dicyclohexyl-1,7-di(pyrrolidinyl)perylene-3,4,9,10-tetracarboxy diimide) was formulated into nanoparticles because of the NIR absorbance and the improved solubility afforded by the cyclohexyl group at the imide position. A nanoprecipitation method was used as it is a facile way to prepare stable nanoparticles using various stabilisers. The stabiliser used in this method is a novel star hyperbranched block copolymer (SHBP), (DEAMA$_{50}$-*c*-DEGDMA$_2$)-*b*-(OEGMA$_{80}$), which was previously developed by our group as a pH sensitive stabiliser to prepare hydrophobic drug nanoparticles (Figure 2.17).[275]

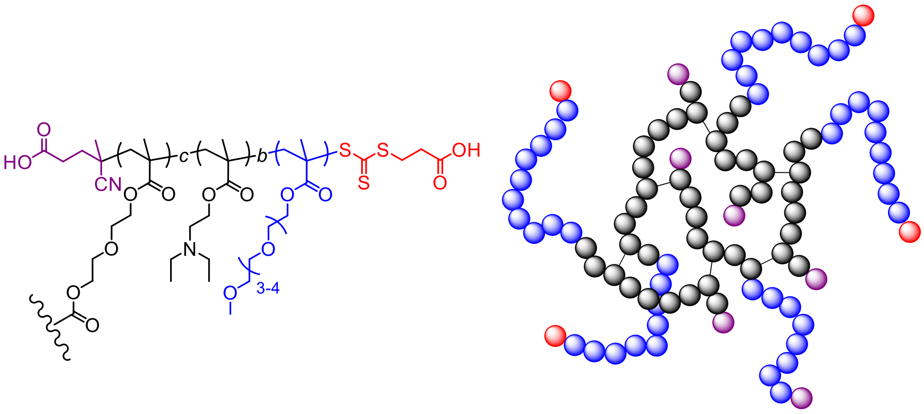

Figure 2.17: Structure of the star hyperbranched block copolymer (DEAMA$_{50}$-*c*-DEGDMA$_2$)-*b*-(OEGMA$_{80}$).[275]

PDI 4, referred to as PDI from here onwards, and SHBP were first dissolved in acetone, as it is miscible with water. Each solution was then added dropwise to water and the reaction was left overnight for the acetone to evaporate, as shown in Figure 2.18. This yielded a green-blue aqueous nanosuspension.

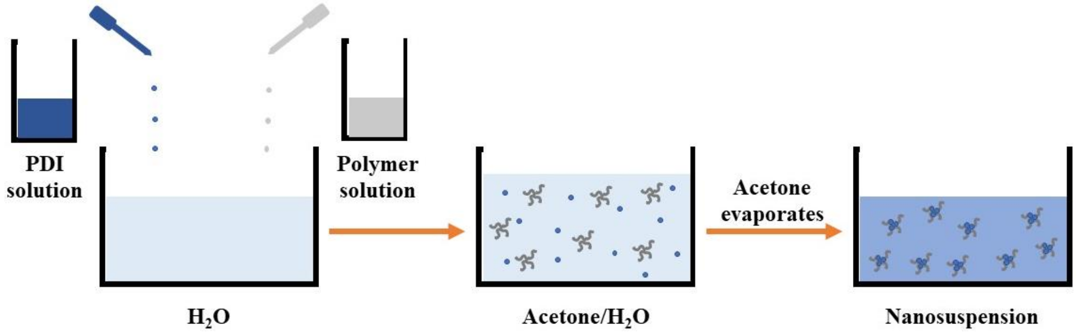

Figure 2.18: Schematic of nanoparticle formation *via* nanoprecipitation with SHBP stabiliser.

2.3.3.1 PDI-SHBP Nanoparticle Characterisation

The ratio of PDI to SHBP stabiliser was varied by keeping the amount of PDI constant and changing the amount of stabiliser in order to optimise stability; nanoparticles with PDI:stabiliser ratios of 1:1, 2:1 and 3:1 were prepared.

The PDI nanoparticles were analysed with using Dynamic Light Scattering (DLS) techniques to assess the particle size. The DLS results are represented as the number particle size distribution as this considers the spherical shape of the nanoparticles and Mie scattering. Analysis of a dilute suspension of nanoparticles with DLS resulted in similar particles sizes of ~150-170 nm, where the particle size distribution for the 1:1 ratio is shown in Figure 2.19. The DLS graphs for the other particles with 2:1 and 3:1 ratios were similar (Figures A3 and A4, Appendix).

The DLS data is summarised in Table 2.1. The polydispersity index was slightly larger with the highest amount of stabiliser (1:1 ratio) however the zeta potential was similar for all nanoparticles.

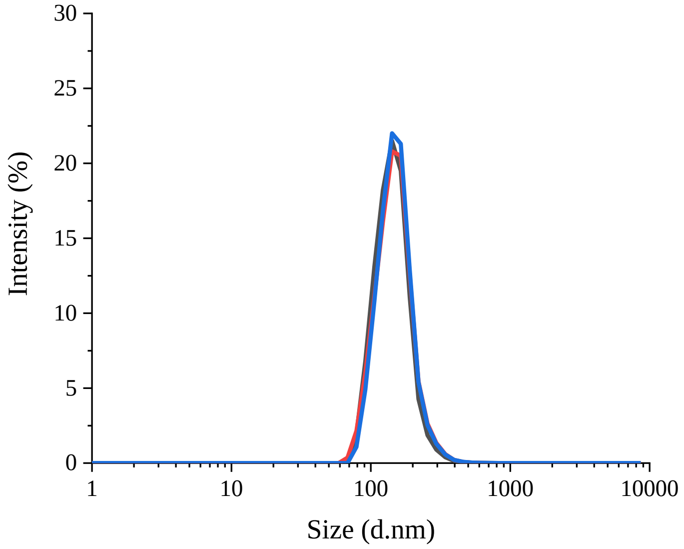

Figure 2.19: Number particle size distribution of PDI-SHBP nanoparticles (PDI:SHBP 1:1) measured using DLS. The different colours represent 3 measurement scans with DLS.

Table 2.1: Summary of DLS measurements of PDI nanoparticles prepared with SHBP stabiliser.

Ratio PDI:stabiliser	**Number Particle Size Distribution (nm)**	**Polydispersity index**	**Zeta potential (mV)**
1:1	147 ± 45	0.358	-7.0 ± 3.2
2:1	172 ± 45	0.258	-9.0 ± 3.6
3:1	168 ± 55	0.266	-8.2 ± 3.5

Analysis of the PDI nanoparticle suspensions with UV-vis spectroscopy resulted in similar profiles however the molar extinction coefficient (ε) decreased as the amount of stabiliser was reduced (Figure 2.20). PDI nanoparticles with PDI:SHBP ratio of 1:1, 2:1 and 3:1 had molar extinction coefficients of 7,906, 7,383 and 5,789 M^{-1} cm^{-1}, respectively. The peak positions were similar to the free dye at 440, 655 and 710 nm (Figure 2.16). Unexpectedly, the absorbance of the peaks at 665 and 710 nm are more similar in intensity, compared to the free dye where the peak at 700 nm is more pronounced.

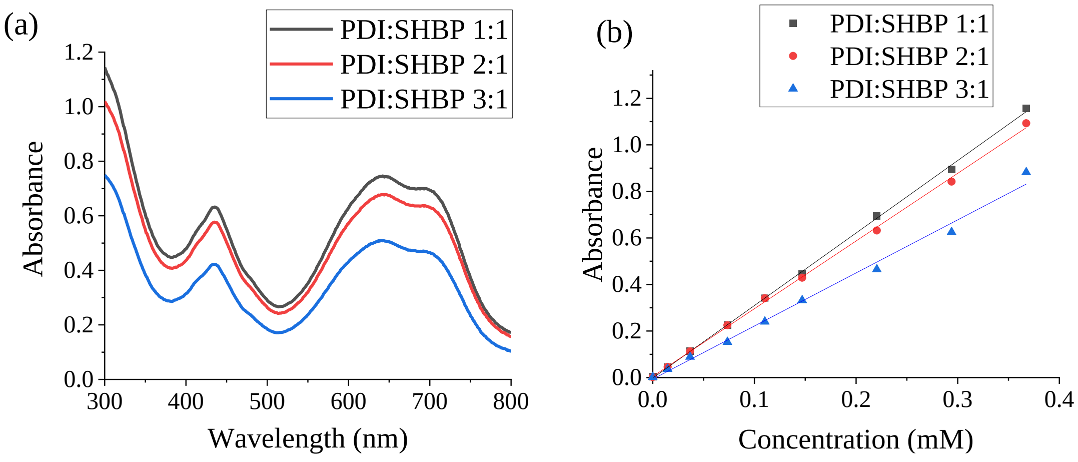

Figure 2.20: UV-vis spectroscopy of aqueous PDI-SHBP nanoparticle suspensions with various ratios of PDI to SHBP, showing the (a) UV-vis spectrum at a concentration of 0.15 mg/ml and (b) the calibration curve of absorbance at 700 nm for a range of nanoparticle concentrations.

SEM images showed small, spherical nanoparticles as well as some aggregates and rod-like structures, as shown in Figure 2.21. A similar result was observed with PDI:SHBP ratios of 2:1 and 3:1 (Figure A5, Appendix). As the nanoparticles had the required optical properties and stability, the few rod-like structures were not considered a problem.

Overall, the different sets of PDI nanoparticles prepared with SHBP stabiliser seem quite similar in terms of particle size and morphology; however, a higher molar extinction coefficient was observed with increased amounts of stabiliser. All three sets of PDI-SHBP nanoparticles were taken forward for evaluation in cell studies.

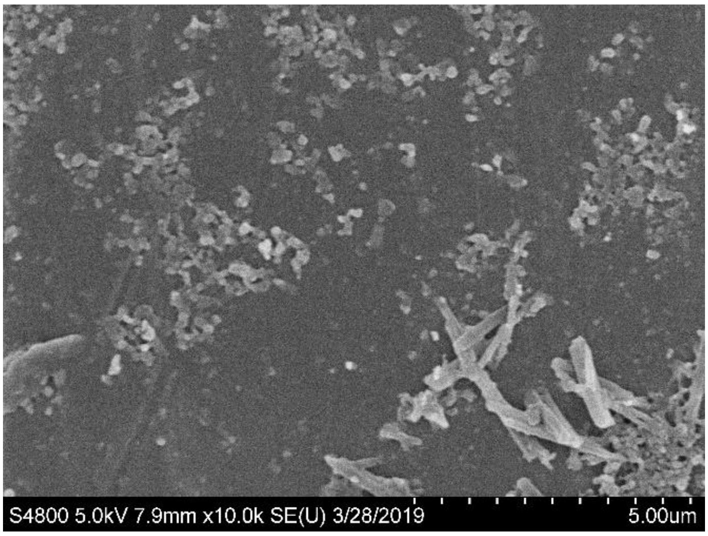

Figure 2.21: SEM images of PDI-SHBP nanoparticles (PDI:SHBP 1:1) prepared by nanoprecipitation method

2.3.4 *In vitro* Evaluation of PDI Nanoparticles with SHBP Stabiliser

Mesenchymal stromal cells (MSC) were labelled with PDI nanoparticles and tested *in vitro* to assess their biocompatibility and cellular uptake.

2.3.4.1 The Effect of PDI-SHBP Nanoparticles on Cell Viability

Firstly, the CellTiter® Glo assay was used to assess the viability of MSCs dosed with varying concentrations of PDI nanoparticles (0-40 μg/ml). Cells were seeded at a density of $2x10^4$ cells/well and incubated for 24hr. After this, the media was aspirated, and fresh media was added containing nanoparticle suspension. Cells were left for a further 24hr to allow uptake of nanoparticles.

Cell viability is measured as the amount of ATP produced from cells dosed with nanoparticles, compared to untreated cells. The amount of ATP produced in the untreated cells acts as the positive control and so ATP generation from treated cells is quoted as a percentage of the control, as shown in Figure 2.22.

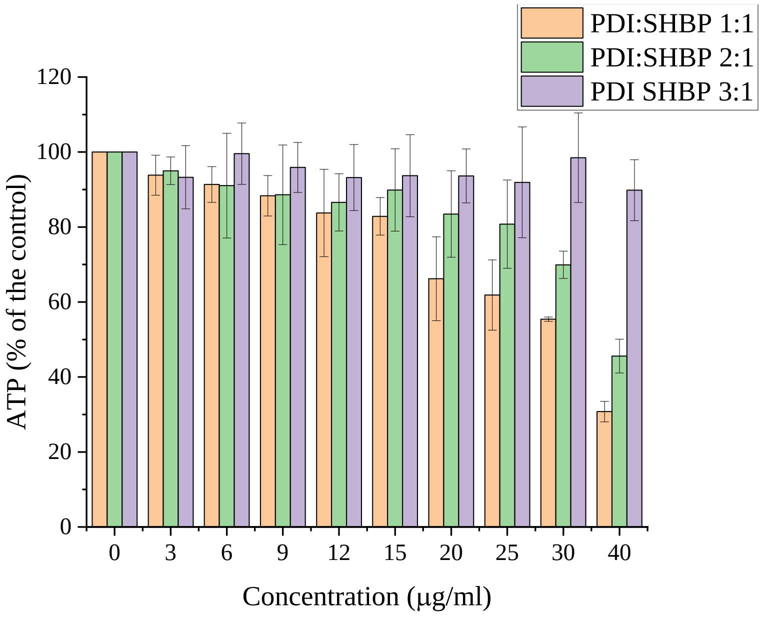

Figure 2.22: The effect of PDI-SHBP nanoparticles on ATP production in mesenchymal stromal cells. Cells were seeded at a density of 2x10^4 cells/well and nanoparticle dosing was for 24hr (n=3). Cell viability in dosed cells is measured as a percentage of untreated cells.

It was found that all types of PDI nanoparticles prepared with the SHBP stabiliser had a limited effect on cell viability up to a concentration of 15 µg/ml. However, at higher dosing concentrations, cell viability decreased the most when the highest amount of stabiliser was used (1:1). PDI nanoparticles with the lowest amount of stabiliser (3:1) were found to have a minimal effect on cell viability even at 40 µg/ml.

2.3.4.2 Assessing Cellular Uptake of PDI-SHBP Nanoparticles with Flow Cytometry

As it appeared that PDI nanoparticles were well-tolerated by MSCs, it was then essential to confirm that they had been efficiently taken up. Flow cytometry is a commonly used technique for analysing cell characteristics, in this case fluorescence intensity. Flow cytometry was carried out on live cell suspensions in PBS, after 24hr labelling with PDI nanoparticles of various concentrations (0-25 µg/ml).

Figure 2.23 shows the results for PDI nanoparticles prepared with a PDI:SHBP ratio of 1:1, however a similar trend was seen for the other ratios (Figure A6, Appendix). There was a relatively large shift from untreated cells to the lowest dosing concentration and fluorescence intensity increased with increasing concentration. For all dosing concentrations, the percentage of the cell population that was labelled was >92% (Figure A7, Appendix).

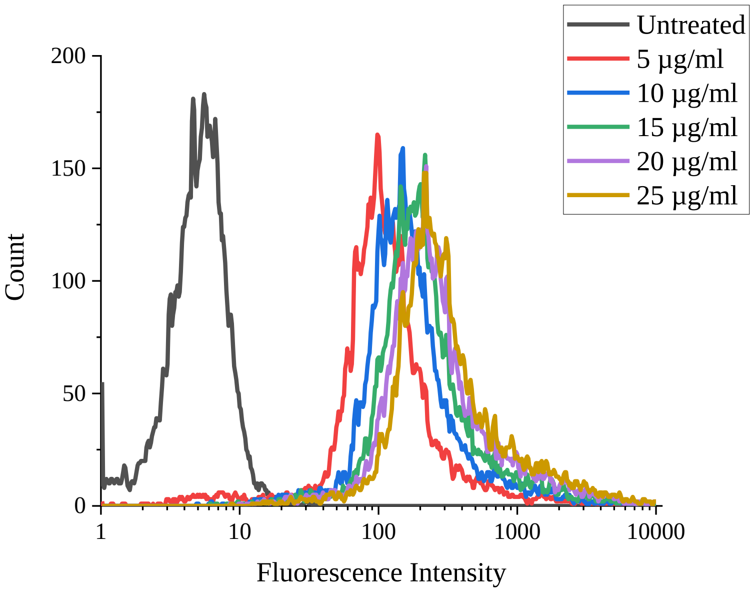

Figure 2.23: Live cell flow cytometry of MSCs in PBS labelled with PDI-SHBP nanoparticles (PDI:SHBP 1:1) where the percentage of cells positive was >92% for all concentrations. Fluorescence intensity was measured using FL3 filter (670 LP) and 10,000 events were counted.

When comparing the three types of nanoparticles in more detail, it appeared that uptake increased with increasing amounts of stabiliser; the highest uptake was seen with PDI:SHBP of 1:1 and the lowest uptake was with the 3:1 ratio (Figure 2.24). This was seen at all dosing concentrations; however, it is worth noting that the difference in fluorescence intensity is relatively small.

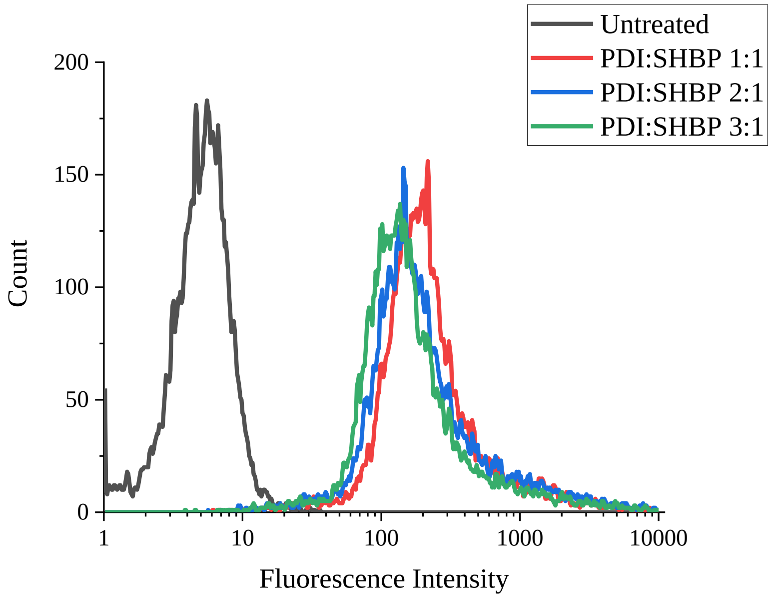

Figure 2.24: Live cell flow cytometry of MSCs in PBS labelled with PDI-SHBP nanoparticles (15 µg/ml). Fluorescence intensity was measured using FL3 filter (670 LP) and 10,000 events were counted.

2.3.4.3 Assessing Cellular Uptake of PDI-SHBP Nanoparticles with Confocal Fluorescence Microscopy

Confocal laser imaging was used to visually assess cell viability and uptake of PDI nanoparticles into MSCs. MSCs were labelled for 24hr with PDI nanoparticles prior to fixing with 4% PFA. Cells were then stained with DAPI and AlexaFluor® 488 phalloidin to show the nucleus and actin cytoskeleton, respectively. Multiple images were taken at different focal planes and combined to form z-stack images with a greater depth of field.

The images show that the PDI nanoparticles are within the cells, likely residing in endosomes and lysosomes (Figure 2.25). The z-stack imaging highlighted that particles were inside cells and not just associated with the cell surface. During imaging, some rod-like structures were also observed; however, these were seen when other ratios of stabilisers were used, as for SEM imaging (Figure 2.21). Smaller, spherical nanoparticles were much more abundant than rods. Confocal images for nanoparticles prepared with PAI:SHBP ratio of 2:1 and 3:1 can be found in Figure A8 in the Appendix.

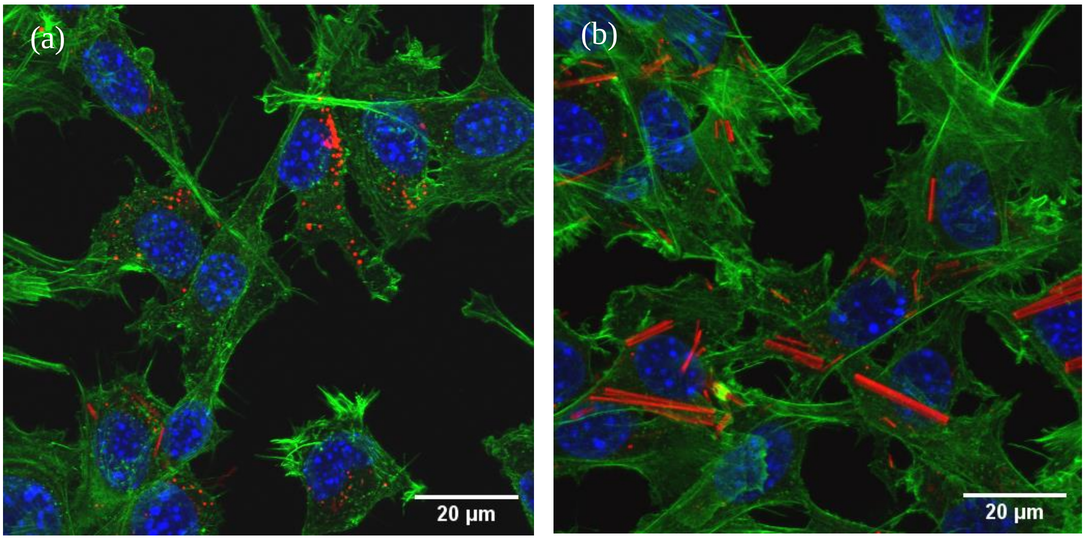

Figure 2.25: Confocal fluorescence image of MSCs, showing PDI-SHBP nanoparticles (PDI:SHBP 1:1, red) residing within cells (15 µg/ml). Cells were fixed and stained with DAPI (blue nuclei) and AlexaFluor ® 488 phallodin (green, actin cytoskeleton). The left image (a) is more representative of the whole view where spherical nanoparticles where abundant whereas the right image (b) shows rod-like structures.

Overall for PDI-SHBP nanoparticles, it was found that cell viability decreased with increasing amounts of stabiliser suggesting PDI-SHBP nanoparticles with a PDI:SHBP ratio of 3:1 were the least cytotoxic; however, >80% of cells were viable for all sets of nanoparticles at a labelling concentration of 15 µg/ml. Furthermore, cells labelled with PDI-SHBP nanoparticles with ratio of 1:1 showed greater increases in fluorescence intensity in flow cytometry experiments. This coupled with the high molar extinction coefficient observed in UV-vis spectroscopy pose the nanoparticles with PDI:SHBP ratio of 1:1 as a promising candidate for detecting cells with MSOT.

2.3.5 Preparation of PDI Nanoparticles *via* Nanoprecipitation with Poly(Vinyl Alcohol) Stabiliser

The PDI nanoparticles were also prepared with PVA stabiliser to see if the type of stabiliser had any effect on the properties of the probes. The nanoprecipitation method was slightly adapted with PVA due to its good solubility in water. The process was similar to that described in Figure 2.18 but PVA was first dissolved in water before adding the PDI solution (acetone) dropwise and again, leaving overnight for evaporation. The mass ratio of PDI:PVA was 1:40 as this had yielded a stable green-blue nanosuspension previously in our group.[278]

2.3.5.1 PDI-PVA Nanoparticle Characterisation

The nanoparticles were analysed with DLS and the number particle size distribution is shown in Figure 2.26. The particle size was 116 ± 36 nm and the polydispersity index was 0.195. The zeta potential was measured at -2.7 ± 2.7 mV. The UV-vis profile was identical to that of PDI nanoparticles prepared with the SHBP stabiliser however the molar extinction coefficient was slightly higher at 8240 M^{-1} cm^{-1} (Figure 2.27).

PDI-PVA nanoparticles were also imaged with SEM and both rod-like structures and small spherical nanoparticles could be visualised (Figure 2.28). Imaging of these nanoparticles, along with SHBP nanoparticles (1:1, 2:1 and 3:1 ratios), resulted in similar amounts of rod-like structures in the SEM images. This suggests that it is possibly dependent on the method parameters rather than the stabiliser.

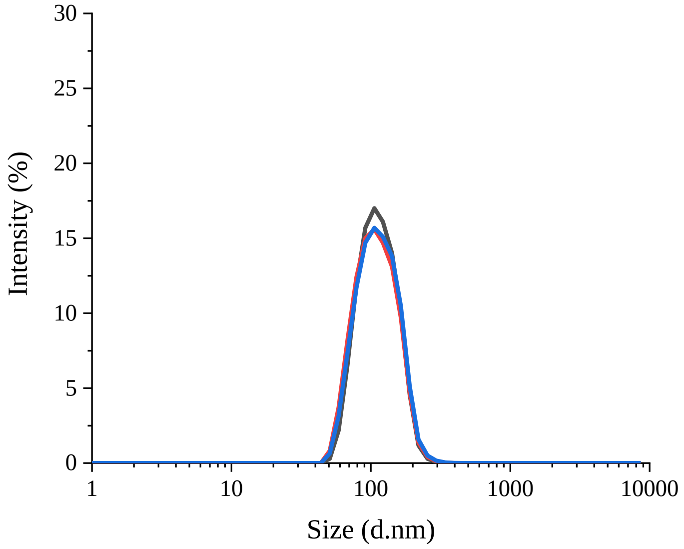

Figure 2.26: Number particle size distribution of PDI-PVA nanoparticles measured using DLS. The different colours represent 3 measurement scans with DLS.

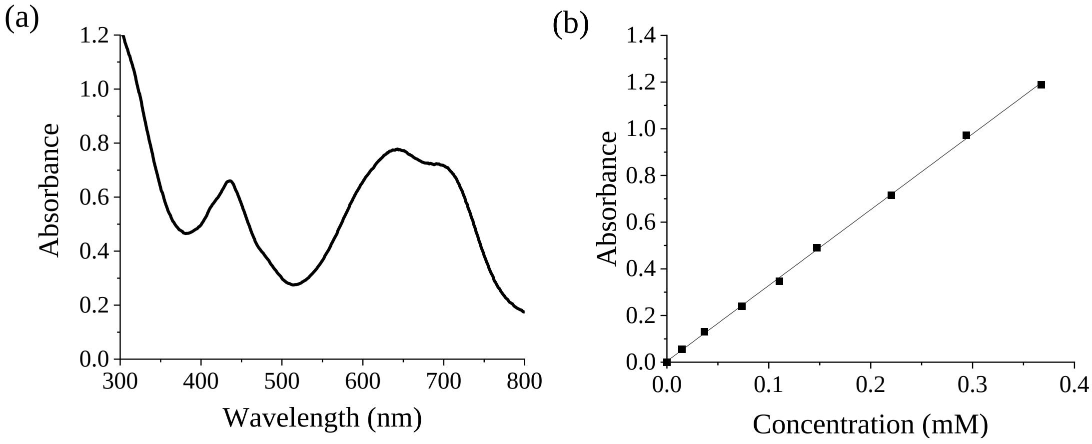

Figure 2.27: UV-vis spectroscopy of aqueous PDI-PVA nanoparticle suspensions, showing the (a) UV-vis spectrum at a concentration of 0.15 mg/ml and (b) the calibration curve of absorbance at 700 nm for a range of nanoparticle concentrations.

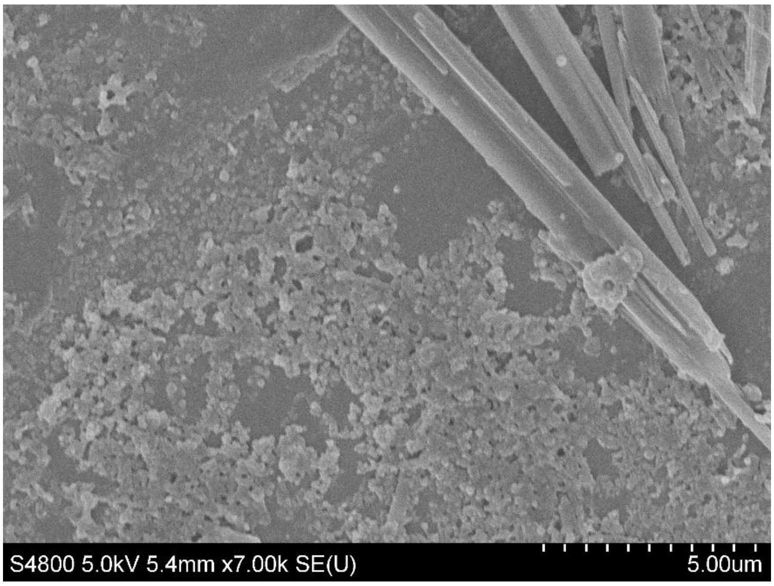

Figure 2.28: SEM image of PDI-PVA nanoparticles

2.3.6 *In vitro* Evaluation of PDI Nanoparticles with PVA Stabiliser

PDI-PVA nanoparticles were also assess for their biocompatibility and uptake into MSCs.

2.3.6.1 The Effect of PDI Nanoparticles on Cell Viability

The CellTiter-Glo® assay was once again used to assess the effect of the nanoparticles on cell viability. The same protocol was carried out as for the nanoparticles prepared with SHBP stabiliser, where MSCs were dosed (0-40 µg/ml) for 24hr ahead of the assay. The results showed that PDI-PVA nanoparticles had a limited effect on cell viability up to the highest concentration of 40 µg/ml, as shown in Figure 2.29.

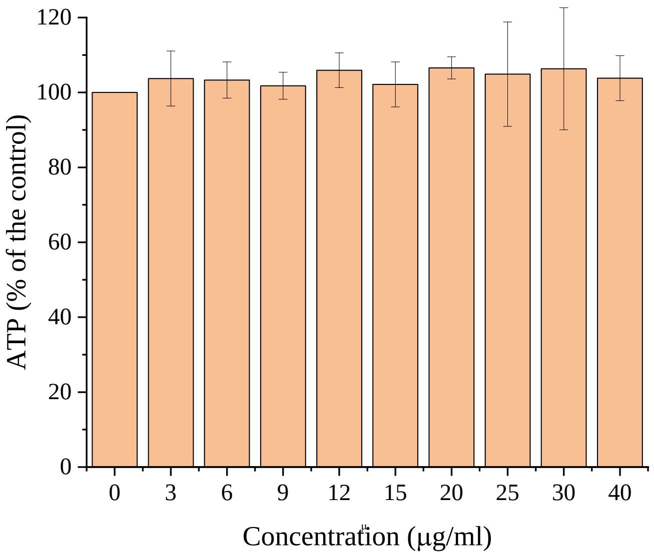

Figure 2.29: The effect of PDI-PVA nanoparticles on ATP production in MSCs. Cells were seeded at a density of $2x10^4$ cells/well and nanoparticle dosing was for 24hr (n=3). Cell viability in dosed cells is measured as a percentage of untreated cells.

2.3.6.2 Assessing Cellular Uptake of PDI-PVA Nanoparticles with Flow Cytometry

The cellular uptake of PDI-PVA nanoparticles was assessed using flow cytometry and confocal fluorescence microscopy. Similar to PDI-SHBP nanoparticles, there was a significant increase in fluorescence compared to untreated cells and fluorescence intensity increased with increasing concentration (Figure 2.30). The percentage of the cell population labelled was >80% for all concentrations (Figure A7, Appendix). The uptake and fluorescence intensity of PVA-stabilised nanoparticles was compared to SHBP-stabilised nanoparticles in Figure 2.31. This highlighted that SHBP-stabilised nanoparticles with a PDI:SHBP ratio of 1:1 had slightly higher fluorescence intensity.

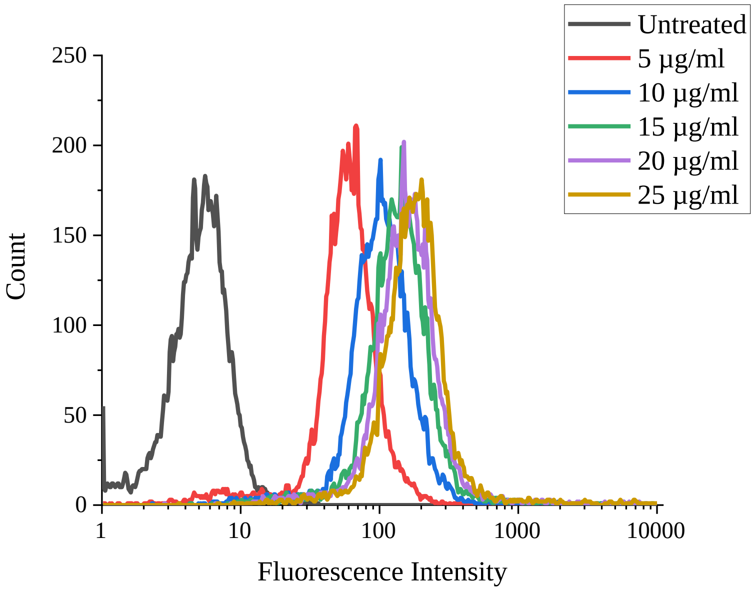

Figure 2.30: Live cell flow cytometry of MSCs in PBS labelled with PDI-PVA nanoparticles where the percentage of cells positive was >92% for all concentrations. Fluorescence intensity was measured using FL3 filter (670 LP) and 10,000 events were counted.

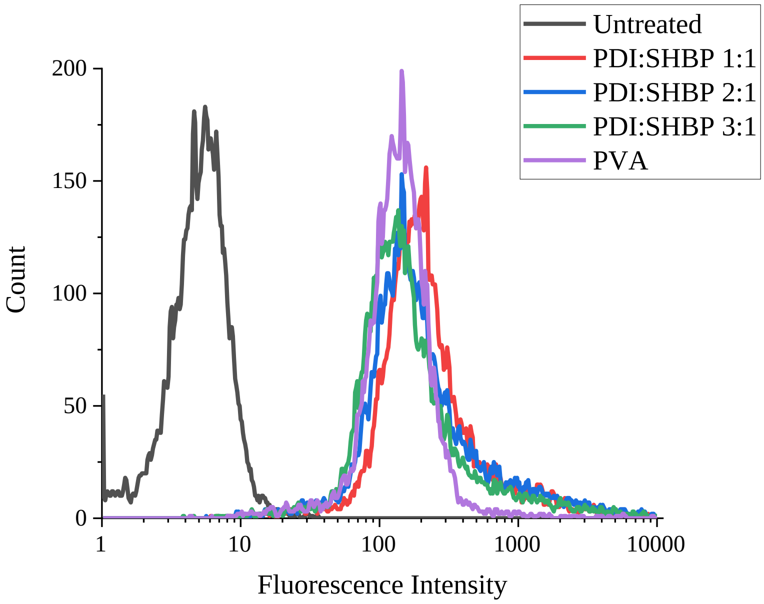

Figure 2.31: Live cell flow cytometry of MSCs in PBS labelled with PDI nanoparticles at a concentration of 15 µg/ml. Fluorescence intensity was measured using FL3 filter (670 LP) and 10,000 events were counted.

2.3.6.3 Assessing Uptake of PDI-PVA Nanoparticles with Confocal Fluorescence Microscopy

Confocal fluorescence microscopy was also carried out to visually assess the uptake of PDI-PVA nanoparticles into MSCs. Cells were fixed and stained 24hr post-labelling before imaging. PDI-PVA nanoparticles (red) can be visualised inside the MSCs, which is consistent with endosomal location (Figure 2.32). Some small rod-like structures can also be seen however the nanoparticles predominantly exist as small, spherical dots. Again, z-stack images were taken which highlighted that particles were inside cells and not just associated with the cell surface.

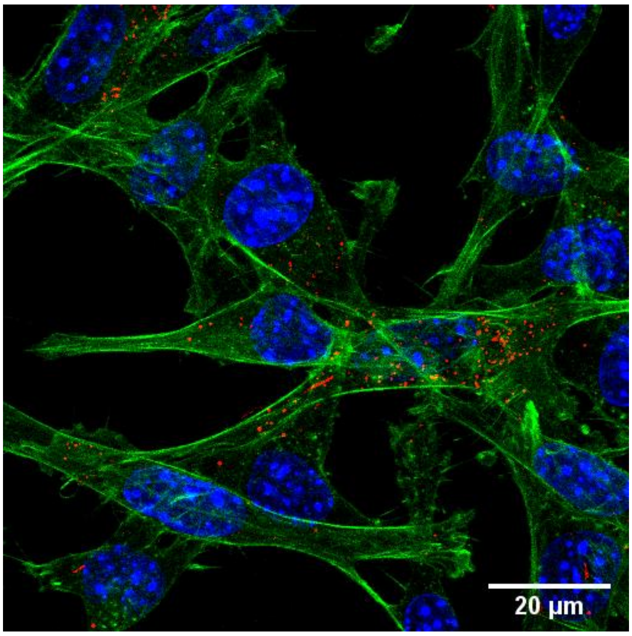

Figure 2.32: Confocal fluorescence microscope image of PDI-PVA nanoparticles (red) inside MSCs (15 µg/ml), where the cells were fixed 24hr post-labelling. The cytoskeleton (green) and nuclei (blue) have been stained with AlexaFluor 488® phallodin and DAPI, respectively. Z-stack images have been taken.

2.3.7 Imaging of PDI Nanoparticles with MSOT

In order to assess the photoacoustic signal, the PDI nanoparticles were imaged in agar phantoms with the MSOT. MSOT is a type of photoacoustic imaging where multiple wavelengths can be used to simultaneously excite a sample and the signal is detected by ultrasound. The nanoparticle solutions (0.25 mg/ml) were pipetted intro clear straws and sealed at each end. The straw was inserted into the agar phantom before placing into the MSOT bath for imaging. The sample was irradiated at 710 nm, which is consistent with the peak absorbance of the nanoparticles, and the images of the cross-section of the straw are shown in Figure 2.33. A strong MSOT signal was observed for both types of nanoparticles.

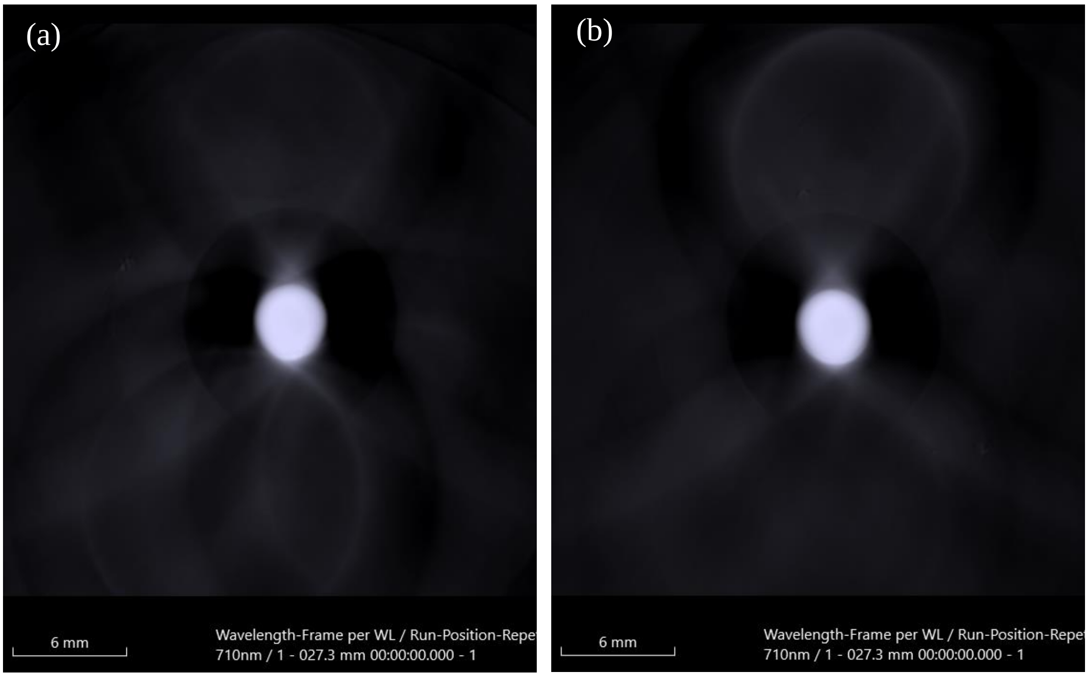

Figure 2.33: MSOT images at 710 nm of PDI nanoparticle solutions in phantoms. PDI nanoparticles stabilised with (a) SHBP (PDI:SHBP 1:1) and (b) PVA polymers are shown at a concentration of 0.25 mg/ml.

A graph of the MSOT mean pixel intensity across the wavelengths scanned is shown in Figure 2.34. The peak absorbance of the nanoparticles is shown where the MSOT signal is high at 710 nm compared to the PBS control were there was very little signal. The MSOT signal was similar for both types of nanoparticles.

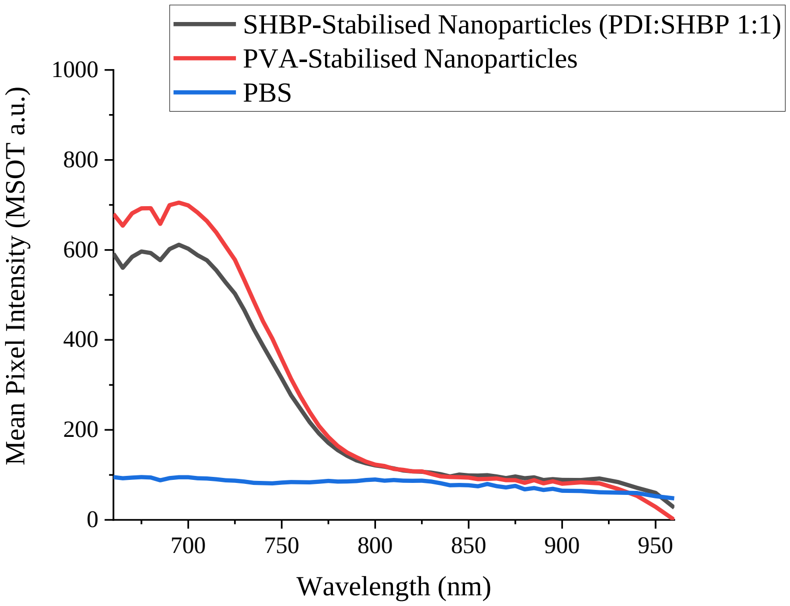

Figure 2.34: A graph of the MSOT mean pixel intensity at different wavelengths for PDI-SHBP (PDI:SHBP 1:1) and PDI-PVA nanoparticle solutions (0.25 mg/ml). PBS was also imaged as the control.

2.4 Discussion

The ability to monitor the fate and biodistribution of administered cells *in vivo* will aid the design of effective RMTs. A novel, non-invasive method involved the use of PAI techniques, such as MSOT, which offers many benefits including high spatial resolution, deep light penetration and spectral unmixing.[271, 279] PDI derivatives are ideal contrast agents for MSOT as they can be engineered to absorb in the NIR region, where tissue absorbance is low. In addition to this they have high photostability and are easily modified unlike other organic molecules, such as cyanine dyes.[245] The tuneability of optical properties is advantageous as two different PDI derivates could be prepared into nanoparticles for simultaneous cell and hydrogel tracking. PDI-based probes have been optimised herein for the non-invasive tracking of mesenchymal stromal cells with MSOT.

2.4.1 Synthesis of NIR-Absorbing PDI Derivative

A NIR-absorbing PDI derivative (*N,N'*-dicyclohexyl-1,7-di(pyrrolidinyl)perylene-3,4,9,10-tetracarboxy diimide) has been synthesized from commercially available PTCDA, following well-established protocols but on a larger scale.[236, 237] In the present study, the successful synthesis of each compound has been confirmed with ^{1}H NMR, FTIR and ultimately, UV-vis spectroscopy to show NIR absorbance. The process was repeated several times to obtain a high enough yield of the final NIR-absorbing PDI derivative for all experiments in this PhD project; the synthesis has previously been carried out in our group and has been shown to be successful.[278]

In the first part of the synthesis, commercially available starting material, PTCDA, was brominated at the bay area following the protocol developed by Sengupta *et al.*[237] This involved first opening the dianhydride to form a tetrabutylester derivative (compound 1a), before bay substitution (compound 1b) and then reforming the anhydride (compound 2). Although indirect, this method was chosen as it resulted in efficient disubstitution where other methods may require separation of the monosubstituted product.[235] Alternative methods in the literature have seen greater regioselectivity however harsher conditions are required and so the method utilised herein was chosen to minimise safety risks.

The first step was to prepare the perylene tetrabutylester (compound 1a), which resulted in a significant increase in solubility. Consequently, a nucleophilic aromatic substitution reaction was carried out to produce the 1,6- and 1,7-dibromoperylene tetrabutylesters (compound 1b), which could then be separated by double solvent recrystallisation. The 1,7-regioisomer crystallised first and the ^{1}H NMR suggested there were small traces of 1,6-regioisomer. The ratio of 1,7- to 1,6-regioisomer was 2:1 which is slightly different to the literature were multiple recrystallisation processes were carried out to attain higher purity.[237] This was not considered a priority in the present study as the peak absorption wavelength was the same for the two regioisomers.

The next step involved the reformation of the dianhydride to form brominated PTCDA (compound 2). The solubility severely decreased, owing to the loss of the tetrabutylester functionality, thus NMR was not possible, however the reaction was confirmed with FTIR. Furthermore, brominated PTCDA (compound 2) was red compared to the orange colour of compound 1b, which resulted in different UV-vis profiles further indicating the success of the reaction.

The brominated PTCDA derivative was then used to synthesize the NIR-absorbing PDI derivative, *N,N'*-dicyclohexyl-1,7-di(pyrrolidinyl)perylene-3,4,9,10-tetracarboxy diimide following a protocol by Sukul *et al*.[236] The first step was the formation of the diimide with cyclohexyl substituents (compound 3). Cyclohexylamine was used as a reagent as cyclohexyl groups are bulky enough to disrupt π-π stacking and the resultant derivative can be dissolved in common solvents, such as acetone and dichloromethane.[235]

The reaction likely proceeded *via* an S_N2 nucleophilic substitution of one carboxyl group to yield the amine and a carboxylic acid at one terminus, before a second nucleophilic attack to the neighbouring carboxyl group. The addition of the cyclohexyl substituent was clear with the presence of new peaks in both the ^{1}H NMR and the FTIR attributed to the aliphatic methylene groups of the cyclohexane ring. Additionally, the shift of the carboxyl peak to lower wavenumber is indicative of a change from dianhydride to diimide.

The next step in the synthesis involved the bay substitution of the bromine atoms for pyrrolidine groups. Pyrrolidine was chosen due to the electron donating character of the amine and the short C-N bond length compared to piperidine groups, resulting in significant red-shift to the NIR region.[240] This was realised in a peak shift from 525 nm (compound 3) to 700 nm (compound 4) in the UV-vis spectra (Figure 2.16) and a colour change from red to blue/green. NIR PDI had increased solubility in acetone and chlorinated solvents which was ideal for nanoparticle preparation.

2.4.2 Preparation of PDI Nanoparticles

PDI nanoparticles were prepared using nanoprecipitation; nanoprecipitation is a commonly used technique for the formulation of drug nanoparticles due to its simplicity and reproducibility.[280] The technique has previously been investigated in our group for encapsulation of hydrophobic drug molecules in order to increase bioavailability. Nanoprecipitation was the ideal technique for preparing PDI nanoparticles as NIR PDI (compound 4) is hydrophobic but has good solubility in acetone and so can be incorporated into the solvent phase.

Nanoparticles were prepared with either a novel hyperbranched block copolymer (SHBP), (DEAMA$_{50}$-*c*-DEGDMA$_{2}$)-*b*-(OEGMA$_{80}$), or PVA stabilisers. Acetone and water were used as the solvent and non-solvent phases, where PDI and SHBP could be dissolved in acetone however PVA had good water solubility. As acetone solutions are added to water, the solubility of PDI decreases causing supersaturation and consequently PDI molecules come together (nucleation). Polymer molecules associate with the interface and particles grow upon collision with neighbouring particles. As the acetone evaporates, nanoparticles are suspended in water. All sets of PDI nanoparticles were around 200 nm in size and had similar zeta potentials and UV-vis profiles, with a broad peak stretching into the NIR region and peak absorbance at 710 nm (Figure 2.20).

For PDI-SHBP nanoparticles, three ratios of PDI:SHBP stabiliser were tried: 1:1, 2:1 and 3:1 where the amount of stabiliser was varied but the PDI concentration was kept constant. All of the particles had a similar particle size although the polydispersity index of the nanoparticles with 1:1 ratio was slightly higher. It has been shown that more uniform particle size distributions can be achieved if the rate of solvent phase addition is slowed.[281] This was not the case in the present study but is a potential avenue for future applications where greater control may be required.

The optical properties of the nanoparticles were investigated with UV-vis spectroscopy. It was found that for PDI nanoparticles with SHBP stabiliser, the molar extinction coefficient increased with increasing concentration of stabiliser. Despite this, PVA-stabilised nanoparticles had the highest molar extinction coefficient of all

($8240 M^{-1} cm^{-1}$). The morphology of the particles was assessed with SEM where small, spherical nanoparticles were visualised and some rod-like structures.

2.4.2.1 In Vitro Assessment of PDI Nanoparticles

PDI nanoparticles were evaluated *in vitro* in MSCs to assess cytotoxicity and cellular uptake. In all cases, MSCs were seeded on day 1, labelled with nanoparticles on day 2 and the assay was carried out 24hr later on day 3. It was found that PDI nanoparticles had a limited cytotoxic effect on MSCs: all of the PDI nanoparticles were well-tolerated up to concentrations of 15 μg/ml. For SHBP-stabilised nanoparticle suspensions, cytotoxicity increased with increasing amounts of stabiliser. Both PDI-SHBP nanoparticles with ratio of 3:1 and PDI-PVA nanoparticles had >80% viability at 40 μg/ml.

Flow cytometry was then used to assess cellular uptake and it was found that MSCs effectively took up the SHBP- and PVA-stabilised nanoparticles. For all sets of nanoparticles, fluorescence intensity increased with increasing dosing concentrations. When comparing the uptake between the different sets of PDI nanoparticles in Figure 2.31, it was found that nanoparticles with PDI:SHBP ratio of 1:1 were more efficiently taken up by MSCs.

Confocal laser imaging allowed visualisation of the nanoparticles within the cells, by exploiting their fluorescence properties. The 640 nm laser was effective in exciting the nanoparticles due to the broadness of the far-red to NIR peak. Imaging agreed with the flow cytometry data and uptake of all PDI nanoparticles was observed, with nanoparticles present in a large proportion of the cells.

The nanoparticles predominantly appeared as bright, small spherical dots within the cells; however, a small number of large rod-like structures were observed in some cases (Figure 2.25). The confocal images were consistent with SEM imaging prior to cell work; i.e. the rod-like structures were seen for nanoparticles prepared with SHBP (all ratios) and PVA stabilisers. This suggests that the formation of rod-like structures is due to the nanoprecipitation technique and not the type of stabiliser. This was an unexpected result and has not been seen in previous work by our group or in the literature.[282, 283]

Rod formation could be investigated further by looking at each stage of the nanoprecipitation process in detail. In the present study, it appeared that rods were more reproducible and abundant for the 1:1 ratio of PDI to SHBP, however this was not quantified. This suggests that the rate of supersaturation may have an effect on rod formation. Hence further studies could be carried out to support this hypothesis, as well as looking at the rate of nucleation and particle growth stages. This was out of the scope of the present study as the nanoparticle morphology was predominantly spherical and the cellular uptake and NIR absorbance was optimal. Furthermore, the presence of the rods within the cells did not have any noticeable effect on cell viability.

2.4.2.2 Imaging PDI Nanoparticle Suspensions with MSOT

The photoacoustic signal of the nanoparticles was assessed by imaging the nanoparticle suspensions in phantoms with MSOT. Due to their higher uptake (as indicated by flow cytometry), SHBP-stabilised nanoparticles with a PDI:SHBP ratio of 1:1 were evaluated against PVA-stabilised nanoparticles. Both nanoparticle suspensions could be visualised when imaged at 710 nm and MSOT absorbance graphs were obtained which further highlighted the peak absorbance at 710 nm.

2.5 Conclusion

An NIR-absorbing PDI derivative has been successfully synthesized and fully characterised with ^{1}H NMR, FTIR and UV-vis spectroscopy. PDI nanoparticles have consequently been prepared by nanoprecipitation with our novel SHBP stabiliser and PVA stabiliser. These nanoparticles have limited cytotoxicity, good cellular uptake and high NIR signal in MSCs and can hence be used as probes for cell tracking with MSOT.

PDI nanoparticles with SHBP stabiliser (PDI:SHBP 1:1) showed more efficient uptake than with the PVA-stabilised nanoparticles. This is consistent with previous work in our group where PDI-SHBP nanoparticles enabled the *in vivo* tracking of MSCs in a rodent model with MSOT.[274, 278] In the present study, PVA-stabilised nanoparticles exhibited low cytotoxicity and high NIR absorbance. Furthermore, PVA has the added benefit of being commercially available and relatively low-cost. Both PVA- and SHBP-stabilised (PDI:SHBP 1:1) are viable candidates for *in vivo* cell tracking going forward.

When comparing PDI nanoparticles to other PA probes in the literature, such as gold nanoparticles, the ease and simplicity of the nanoprecipitation method is a key advantage for clinical translation, particularly as the process does not require heat or harmful solvents. Moreover, the PDI synthesis is straightforward and well-established enabling a range of PA probes to made with different spectral absorbance wavelengths that have excellent photostability compared to ICG. The limited toxicity and low cost of the materials are further benefits over other PA probes in the literature.[245]

The high MSOT signal of both PVA- and SHBP-stabilised nanoparticles has been demonstrated for cell tracking however it is also ideal for labelling hydrogels which would allow *in vivo* tracking of hydrogel integrity; hence, this is the focus of chapter 3 of this thesis.

Chapter 3: Labelling Cell-Encapsulating Hydrogels with Perylene Diimide Nanoparticles

3.1 Introduction

When developing regenerative medicine therapies (RMTs), it is important to consider the possible problems associated with the cell delivery process as the route of administration can affect the viability, retention, integration and functionality of cells.[284] The most common administration route is injection (e.g., intravenous, intramuscular, intracardiac) and thus the mechanical stress from the needle can affect cell viability.[285-287] Furthermore, once the cells have been administered, there are problems such as uneven settling and clumping and subsequent cell death may lead to macrophage infiltration.[32] These problems could contribute to a reduction in efficacy for RMTs and hence encapsulating cells in a protective polymer matrix offers a novel solution to this problem.

Hydrogels are defined as 3-dimensional (3D) crosslinked networks of hydrophilic polymers, where the liquid component of the gel is water. Biocompatible hydrogels have been developed with natural or synthetic polymers for a variety of biomedical applications, including drug and cell delivery, and tissue engineering.[288-290] Encapsulation of cells in biocompatible hydrogels can increase cell survival whilst encouraging 3D cell growth.[291]

3.1.1 Gel Materials

Hydrogels can be categorised into physical or chemical gels. Physical gels, also known as reversible, are networks of polymers held together by secondary interactions, such as hydrogen bonds, ionic or hydrophobic forces, whereas chemical gels (irreversible) involve the formation of covalent bonds.[290] Methods of covalent crosslinking include radical polymerisation, chemical reactions of complementary groups (e.g. addition and condensation reactions) and enzymatically catalysed gelation.[292-294] Alternately, physical gels can be formed by the addition of ions, changes in pH and temperature as well as self-assembly of amphiphilic block and graft copolymers.[295-297]

Hydrogels can be synthesized from natural or synthetic polymers. The most commonly utilised natural polymers include alginate and collagen however, there have been significant advances in synthetic hydrogels to enable greater control over stability, strength and functionality.[26] In regenerative medicine, a key consideration is the design of biocompatible hydrogels that mimic the extracellular matrix (ECM).[25]

3.1.1.1 Synthetic Hydrogels

Hydrogels prepared from synthetic polymers can be chemically and mechanically stronger than natural hydrogels which can improve durability by slowing degradation. Common materials include poly(ethylene glycol) (PEG), poly(lactic acid) (PLA), polyacrylamide (PAAm) and polyvinyl alcohol (PVA), among others.[298-300]

PEG is utilised in a variety of biomedical applications due to its high biocompatibility and hence it is approved by the Food and Drug Administration (FDA).[300] Furthermore, advances in PEG-hydrogels have been driven by the versatility of PEG chemistry; copolymerisation with other macromolecules can introduce biological moieties into the hydrogel structure to promote cell survival or function. An example of this is where PEG hydrogels containing the integrin binding peptide Arg-Gly-Asp (RGD) were shown to increase osteoblast viability.[301, 302]

Hydrogels can also be prepared with a combination of both natural and synthetic polymers to tune the gel properties.[303-305] For example, the addition of synthetic polymer (PAAm) to methacrylated gelatin produced a superior hybrid hydrogel with improved performance in terms of strength, elasticity and degradation rate, thus expanding the applications of gelatin-based hydrogels in soft tissue engineering.[306]

3.1.1.2 Natural Hydrogels

For biomedical applications, natural polymers have been deemed more suitable due to them being biocompatible and biodegradable, as well as containing biologically recognisable moieties.[307] Moreover, hydrogels prepared from natural polymers are mostly prepared using physical crosslinking methods, avoiding the need for toxic crosslinking agents.[27] Table 3.1 summarises some of the most common natural materials used to prepared hydrogels.

Table 3.1: Summary of common natural polymers used for hydrogels, adapted from reference.[300]

Name	**Source**	**Type**	**Gelation process**
Alginate	Seaweed	Polysaccharide	Ionotropic
Chitosan	Crustaceans	Polysaccharide	Ionotropic
Hyaluronic acid	ECM	Polysaccharide	Thermal/photo
Collagen	ECM	Protein	Thermal/pH
Gelatin	ECM/ collagen	Protein	Thermal

Alginate is one of the most common natural hydrogel materials widely utilised in biomedical applications including wound healing, drug delivery and tissue engineering. Alginate is derived from seaweed and is a polysaccharide which can vary in composition and sequence.[308] Alginate hydrogels are commonly prepared through the addition of divalent ionic crosslinking agents, such as calcium ions (Ca^{2+}).[309, 310] The widespread use of alginate hydrogels for cell encapsulation can be attributed to the formulation of such gels under physiological conditions having a limited effect on cell viability or function, as well as facile cell retrieval and a gel pore network that enables efficient nutrient and waste diffusion.[21] Furthermore, the ionotropic crosslinking methods renders alginate hydrogels injectable, which offers a further advantage over other hydrogel materials.[311]

Chitosan is a polysaccharide derived from chitin, a component of the exoskeleton of crustaceans. Similar to alginate, chitosan has gained traction in the biomedical field due to its biocompatibility and biodegradability, as well as high abundance and low cost.[312, 313] Furthermore, chitosan has bioadhesive properties which are beneficial for 3D cell growth. Chitosan can be covalently or ionotropically crosslinked, where the latter is favoured to avoid toxicity.[314]

Collagen hydrogels have also been widely explored for biomedical engineering, particularly as collagen is the main component of ECM in mammalian tissues.[300, 315] Furthermore, bioadhesion is an important consideration for cell-based hydrogels so that cells can adhere to the hydrogel structure enabling 3D cell growth.[316] Chitosan and collagen are two examples of natural polymers that inherently exhibit bioadhesion however, alginate hydrogels have been modified with the RGD ligand to increase cell adhesion properties and mimic the ECM.[309, 317]

3.1.2 Use of Gels in Regenerative Medicine

As previously mentioned, biocompatibility is a necessary property for hydrogels used in regenerative medicine. Moreover, the conditions of the gelation process are also an important consideration when designing cell-based hydrogels. Many of the chemical hydrogel preparation methods include organic solvents or toxic crosslinkers and hence, physical gels can provide a safer option and provide opportunity for injectable *in situ* forming hydrogels.[295, 296] For this, an aqueous mixture of gel precursor is administered *via* syringe and gelation occurs inside the body so hence the gelation process must occur under physiological conditions. Other advantages of injectable hydrogels is that administration is minimally invasive and the gels are mouldable, i.e. the gel construct can adapt to the space.[318]

3.1.2.1 Tissue Engineering

The field of tissue engineering emerged as a result of the high demand for organ transplants and not enough donors.[319] Tissue and cell-based constructs have been developed for implantation, where considerations must be made to ensure the body accepts the engineered tissue. Traditionally, the goal was to form functional tissue from these constructs however tissue engineering aligns closely with the field of regenerative medicine, where cells and biological moieties are included to promote repair through the body’s own regeneration mechanisms.[320] Furthermore, a combination of both these approaches could lead to more efficacious treatments and limited rejection by the body.

Hydrogels are ideal candidates for scaffold material as they can be carefully designed in terms of degradation rate.[321] In bone tissue engineering, scaffolds are designed as a template to promote bone regeneration as persistence of the graft material can have poor clinical outcomes and early resorption of the scaffold could destabilise initial bone formation.[322] When designing hydrogels, combining the mechanical tailoring properties of synthetic polymers with biomimetic natural polymers will offer a novel solution in the field of tissue engineering.[323] An example of this includes gelatin methacryloyl (GelMA) where hybrid hydrogel systems can include nanoparticles such as carbon nanotubes (CNTs) to improve mechanical strength without affecting porosity for 3D cell growth.[324, 325]

3.1.2.2 Cell Encapsulation

Hydrogels can also be used to deliver RMTs and many of the same concepts overlap with tissue engineering constructs, i.e. improving cell retention and survival.[326] Encapsulating cells in a hydrogel enables protection from the host's immune system. Similarly to tissue engineering constructs, hydrogels must be biocompatible, mechanically stable and have a porosity which allows for diffusion of nutrients.[23] An example of this is with the encapsulation of pancreatic islet cells to treat type 1 diabetes using alginate-based hydrogels.[327, 328] The success of islet transplantation has been hindered by the need for immunosuppressive regimens however it is thought that encapsulation offers a novel strategy to protect cells from immune system components whilst allowing insulin secretion.[329]

The encapsulation of neuronal cells in collagen hydrogels has been extensively explored for spinal cord injury (SCI) and injuries to the central nervous system (CNS), due to its similarity to the ECM.[41, 330] Furthermore, collagen gels are most commonly prepared by physical crosslinking where gelation can occur from changes in temperature or pH. This is particularly ideal for SCI or injuries to the CNS as hydrogels can be injected and formed *in situ*, offering an alternative to invasive surgeries. Furthermore, hydrogels can prevent cell migration to other parts of the CNS.[331]

3.1.3 Fate of Gels *In Vivo*

Whilst significant advances have been made to label cells and monitor release from hydrogels, it would also be useful to label the hydrogel. An example of the former is where cells have been labelled with iron oxide nanoparticles and encapsulated in collagen matrices; the nanoparticles allowed for the monitor of cell release using magnetic resonance imaging (MRI).[32, 332] Indeed, many of the probes discussed in the previous chapters of this thesis could be applied to tracking the release of cells from within a hydrogel.

Monitoring the fate of hydrogels *in vivo* would aid the design of encapsulated RMTs, as well as having significant use in the field of tissue engineering. Furthermore, monitoring scaffold degradation *in vivo* with bioimaging techniques would enable non-invasive longitudinal tracking in rodent models.[49, 333] Many of the biomaterials employed as hydrogel constructs mimic tissue and so novel probes can be used to label the hydrogels and provide contrast for various imaging modalities.

Fluorescence imaging and MRI have been explored for hydrogel tracking.[77, 123, 334] An example of this is where SPIONs were used to label cellulose/silk fibroin hydrogels.[84] Nuclear imaging has also been used where the radiometal ^{111}In acted as a crosslinker for alginate hydrogels, whilst also providing contrast for *in vivo* nuclear imaging.[51] This enabled the tracking of hydrogel for a multitude of applications including drug delivery, stem cell transplantation and cardiac tissue engineering.

To our knowledge, there are only a few examples in the literature of hydrogel tracking with photoacoustic imaging (PAI). One example was were gold nanoparticles were incorporated into an RGD-modified polypeptide hydrogel for targeted PAI.[335] Another example was CNTs were included in poly(lactide-co-glycolide) PLGA scaffolds to improve the mechanical properties and provide contrast for photoacoustic (PA) microscopy of constructs in phantoms.[50] Near- infrared (NIR) responsive hydrogels have also been developed for photothermal therapy (PTT) by formulating alginate gels with lanthanide-gold hybrid nanoparticles.[336]

Despite only a few examples, using PAI to track hydrogels has numerous advantages, including high spatial resolution and deep-tissue penetration.[337] Furthermore, PA contrast agents absorb in the near-infrared (NIR) region, where tissue absorption is low and hence the hydrogels can be effectively visualised against the background. Therefore, more research into hydrogel tracking with PAI is required.

We have demonstrated that PDI nanoparticles can be used for tracking of mesenchymal stromal cells (MSC) *in vivo* with multispectral optoacoustic tomography (MSOT, Chapter 2). The versatility of PDI chemistry allows tuning of the wavelength of absorbance of PDI derivatives. Hence, the nanoparticle platform developed in Chapter 2 could be utilised to prepared two sets of nanoparticles, with different PDI derivatives which can be spectrally unmixed. The different sets of PDI nanoparticles could be used to label cells and encapsulating hydrogels separately for simultaneous tracking with MSOT.

3.1.4 Aims

The purpose of the present study is to investigate the use of perylene diimide nanoparticles in labelling collagen hydrogels. Collagen was chosen as the material for the hydrogel constructs due to its biocompatibility and bioadhesive properties to nurture mesenchymal stromal cell growth, and also its high abundance and low cost. The aims of this study are as follows:

1. To encapsulate mesenchymal stromal cells in collagen hydrogels labelled with perylene diimide nanoparticles.
2. To assess the effect of collagen encapsulation on mesenchymal stromal cell viability and whether the inclusion of perylene diimide nanoparticles has an effect on this.

3. To image the gels *in vitro* with multispectral optoacoustic tomography.
4. To determine whether cells or perylene diimide nanoparticles are migrating out of the gels.

3.2 Experimental

3.2.1 Materials

Collagen I, rat tail was purchased from Gibco. The synthesis of NIR-absorbing PDI and preparation of PDI nanoparticles is detailed in Chapter 2 of this thesis.

3.2.2 Cell Culture

The murine mesenchymal stromal cell line D1 (ATCC) was used for all *in vitro* cell studies. All MSCs used had previously been modified by Dr Arthur Taylor (Murray group) to express firefly luciferase and ZsGreen, under control of the constitutive promoter, EF1α.[276, 277] MSCs were cultured in 6 cm or 10 cm tissue culture dishes (Greiner CELLSTAR®) in high glucose Dulbecco's Modified Eagle Medium (DMEM, Sigma Aldrich) containing 10% fetal bovine serum (FBS, Sigma Aldrich), 1% non-essential amino acids (Sigma Aldrich) and 2 mM L-glutamine (Gibco). Cells were incubated at 37°C and 5% v/v CO_2 and passaged with 1% trypsin-EDTA (Sigma Aldrich) when they reached 90% confluence.

3.2.3 Preparation of Collagen Gels

MSCs were encapsulated during the formation of collagen gels. The preparation of collagen gels (100 µl) was carried out following the manufacturer's guidelines with a collagen concentration of 2 mg/ml. All reagents were kept on ice, apart from cell culture medium which was warmed to 37°C. In a vial with the desired number of cells ($2x10^5$), nanoparticle suspension (original concentration 0.25 mg/ml) and media were added to prepare gels with PDI concentrations of 12.5-50 µg/ml and so that the total volume of nanoparticle suspension and media added was 21.6 µl. After this, 10x PBS (10 µl) and 1N NaOH solution (1.6 µl) were added. 66.7 µl of collagen was added and the mixture was quickly triturated and transferred to a 96-well plate. After all gels had been prepared, the plate was incubated for 30 minutes (37 °C, 5% CO_2) to allow gelation. 100 µl of cell culture media was added to each well and the gels were left overnight in the incubator.

3.2.4 Bioluminescence and Fluorescence Imaging

Fluorescence and bioluminescence images were acquired using an IVIS Spectrum In Vivo Imaging System (Perkin Elmer) and analysed with Living Image software. Gels were removed from their original wells and the bioluminescent/fluorescent signal of the gel was compared to wells that the gels had previously inhabited.

3.2.4.1 Bioluminescence imaging

Bioluminescence imaging was used to monitor cell migration and assess cell survival in the gels. The MSCs expressed firefly luciferase and D-luciferin (5 mM) was added prior to imaging. Automatic exposure time was used, F/stop was 1 and bioluminescent signal was measured in radiance ($p/s/cm^2/sr$).

3.2.4.2 Fluorescence Imaging

The fluorescence was measured with excitation and emission wavelengths of 710 nm and 750 nm, respectively and an exposure time of 45s. The fluorescent signal was measured in radiant efficiency ($p\ s^{-1}\ cm^{-2}\ sr$) / ($\mu W\ cm^{-2}$).

3.2.5 Multispectral Optoacoustic Tomography

Multispectral optoacoustic tomography (MSOT) was carried out using an inVision 256TF system (iThera Medical) to investigate the limit of detection of PDI nanoparticles in collagen gels. Prior to imaging, gels were first fixed with 4% paraformaldehyde (PFA).

3.2.5.1 Preparation of Phantoms

Agar phantoms were prepared for *in vitro* imaging with MSOT. 20 ml syringes were used as moulds by removing the end and pulling the plunger out. With the handle of the plunger taped to a surface, a straw (ends sealed) was suspended in the middle of the syringe and secured with tape. Next, intralipid (1.03 ml, Sigma Aldrich) was heated in a water bath whilst agar (0.75 g, Sigma Aldrich) was added to 50 ml of water and heated in a microwave. The solution was shaken and intralipid was added. The agar mixture was then poured into the syringe moulds and left to set for 30 minutes. Once set, the straws were removed and phantoms were stored in a small amount of water in the fridge to be used the following day.

3.2.5.2 Imaging

The fixed gels were put in clear plastic straws, filled with PBS and sealed at either end. The straws were then inserted into agar phantoms, covered in ultrasound gel and placed in the water bath (25°C) of the inVision System (iThera). Several slices were imaged across the wavelength range of 660-1000 nm in 5 nm intervals in order to clearest images of the gels possible (1 mm step). The following reconstruction parameters were utilised: backprojection 25mm(res:75μm), 50 kHz-6.5 MHz-IR and images were analysed using viewMSOT software (iThera),

3.3 Results

MSCs were encapsulated in collagen gels labelled with NIR-absorbing PDI nanoparticles. The purpose of the collagen gels is to provide a protective matrix in order to increase cell survival when administering cells *in vivo*. PDI nanoparticles were used to label the collagen matrix so that the hydrogel integrity can be tracked *in vivo* using PAI.

3.3.1 Preparation of Collagen Gels

The gels were prepared with a collagen concentration of 2 mg/ml; this was chosen so that the gels would be rigid enough to manipulate but not too high as this could affect cell viability. It was observed that including MSCs in the gel causes gel contraction, a phenomenon that is widely documented in the literature.[42, 338, 339] In the present study, $2x10^5$ MSCs were seeded in each collagen gel.

The gels were labelled with PDI nanoparticles; the PDI synthesis, nanoparticle preparation and characterisation are detailed in Chapter 2. Briefly, NIR-absorbing PDI (*N,N'*-dicyclohexyl-1,7-di(pyrrolidinyl)perylene-3,4,9,10-tetracarboxy diimide) was used to prepared polymer-stabilised nanoparticles *via* nanoprecipitation. Nanoparticles were stabilised with either our novel star hyperbranched block copolymer (SHBP) or PVA. The structures of the PDI and the polymer stabilisers are shown in Figure 3.1.

MSCs and nanoparticles were included with the starting materials for gel formation so that they could be effectively encapsulated within the collagen matrix. The two types of nanoparticle (SHBP- or PVA-stabilised) were compared at a range of concentrations (12.5-50 µg/ml) to optimise the gels in terms of PA signal and cell viability. All other parameters were kept consistent i.e. cell number, collagen concentration, gel size and incubation times. The concentration of 10x PBS and 1N NaOH was kept consistent and the amount of media varied depending on the nanoparticle concentration so that the total volume of nanoparticle suspension and media added up to 21.6 µl.

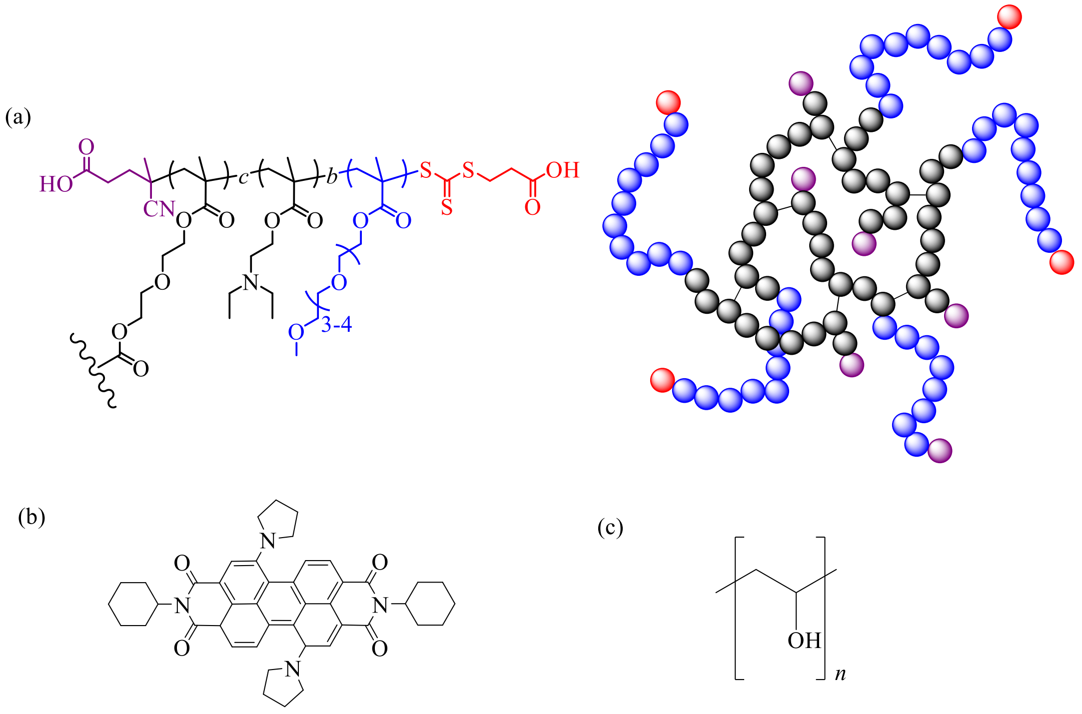

Figure 3.1: Structures of (a) SHBP stabiliser (DEAMA$_{50}$-*c*-DEGDMA$_2$)-*b*-(OEGMA$_{80}$), (b) NIR-absorbing PDI (*N,N'*-Dicyclohexyl-1,7-di(pyrrolidinyl)perylene-3,4,9,10-tetracarboxy diimide and (c) poly(vinyl alcohol) stabiliser.

The gels formed during the 30-minute incubation period and 100 µl of media was added to the top of the gels, before leaving overnight. After 24hr, the gels that contained MSCs had contracted, detached from the sides of the well and were floating in the media. These gels could easily be removed from the well using a small spatula. Gels which did not contain MSCs remained the same size as before the 24hr period and were less rigid; these control gels had to be carefully manipulated when removed so as to not break the gel. Gels were either moved to a new well and replenished with fresh media or fixed with 4% PFA and stored in PBS.

Gels labelled with PDI nanoparticles appeared blue in colour, whereas unlabelled gels were white. Due to the opaqueness of the gels, the nanoparticles and cells could not be visualised using a microscope without sectioning. Furthermore, the absorbance properties could not be evaluated with UV-vis spectroscopy due to light scattering.

3.3.2 Investigating Cell Survival and Migration

MSCs had been engineered to express luciferase therefore bioluminescence imaging could be used to investigate cell survival. Gels were prepared with $2x10^5$ MSCs and imaging was carried out 24hr later. Prior to imaging, the gels were moved to a new well so that the bioluminescent signal of this well could be compared with the signal of the gel; this gave an indication of whether cells remained inside the gel or migrated out and adhered to the surface of the well. PBS was added to the new well and luciferin (5 mM) was added to this and to the media in the previous well ahead of imaging. The measure of photon output is displayed as radiance.

In Figure 3.2, gels had been prepared in well 1 and moved to well 2 in a 96-well plate after 24hr. The lack of bioluminescent signal in well 1 suggested that cells did not migrate out of the gel however the gels can be clearly visualised in well 2 demonstrating that the MSCs are viable after 24hr in the gel. The outline of the signal does not include the whole well which is due to gel contraction. There is no signal in either well for the SHBP and PVA control gels where no cells were included however a signal can be seen for the collagen control with MSCs; this confirms that the signal is due to the MSCs and not the nanoparticles.

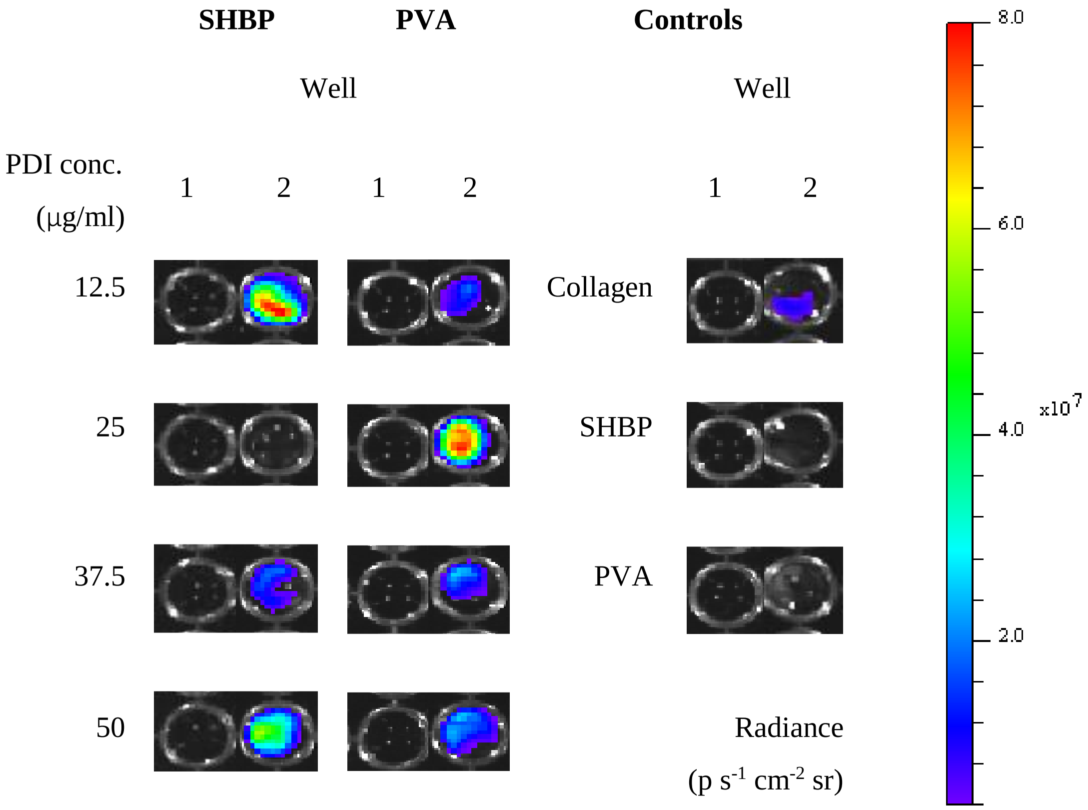

Figure 3.2: Bioluminescence imaging of gels which had been prepared in well 1 and moved to well 2 after 24hr. Gels labelled with SHBP- and PVA-stabilised PDI nanoparticles (0-50 µg/ml) were imaged along with control gels, including an unlabelled MSC collagen gel and labelled gels (25 µg/ml) without cells. All gels contained $2x10^5$ MSCs apart from the SHBP and PVA control gels. Luciferin was added to the wells at a concentration of 5 mM ahead of imaging.

There was no clear trend between signal strength and nanoparticle concentration. One possible reason for this could have been that the stated dosing concentration was inaccurate due to leaching and hence this was investigated further with fluorescence imaging. Furthermore, the lack of correlation can be attributed to other variables which may affect cell survival such as timings in the gel preparation process and the moving of the gels. Therefore, the lack of signal for the gel labelled with SHBP-stabilised nanoparticles at 25 µg/ml in Figure 3.2 can be considered an anomaly.

In a separate experiment, gels were prepared, and bioluminescence imaging was carried out after 1 week to assess cell survival over a longer timescale. Gels were prepared as in the previous experiment and moved to a new position in the 96-well plate every 1-3 days. After 1 week, the gels were moved for the final time and luciferin was added to the gel in PBS and to the leftover media in all the previous wells.

Figure 3.3 shows that most of the gels have a bioluminescent signal after 1 week which suggests that MSCs were still viable. Moreover, the lack of signal in wells that had previously contained the gels suggest that cells do no migrate out. A signal was observed in all of the gels labelled with SHBP-stabilised nanoparticles however gels labelled at higher concentrations of PVA-stabilised nanoparticles (37.5 and 50 μg/ml) did not have a bioluminescent signal in this case, suggesting that the cells may not tolerate the higher concentrations of PVA-stabilised nanoparticles. There is no signal for SHBP and PVA control gels however the collagen control can be visualised as it contained MSCs.

The total flux of the gels could be quantified and is shown in Figure 3.4. For the unlabelled control gel which contained MSCs, the total flux was higher at 1 week than 1 day suggesting cells were proliferating. For gels labelled with PDI-SHBP nanoparticles, this was the case for the majority of the gels; however, for gels labelled with PDI-PVA the signal was low or decreased at 1 week for gels labelled at 25, 37.5 and 50 μg/ml. The quantified flux is averaged over three separate experiments suggesting that overall PDI-PVA nanoparticles have a greater cytotoxic effect when incorporated in gels alongside MSCs.

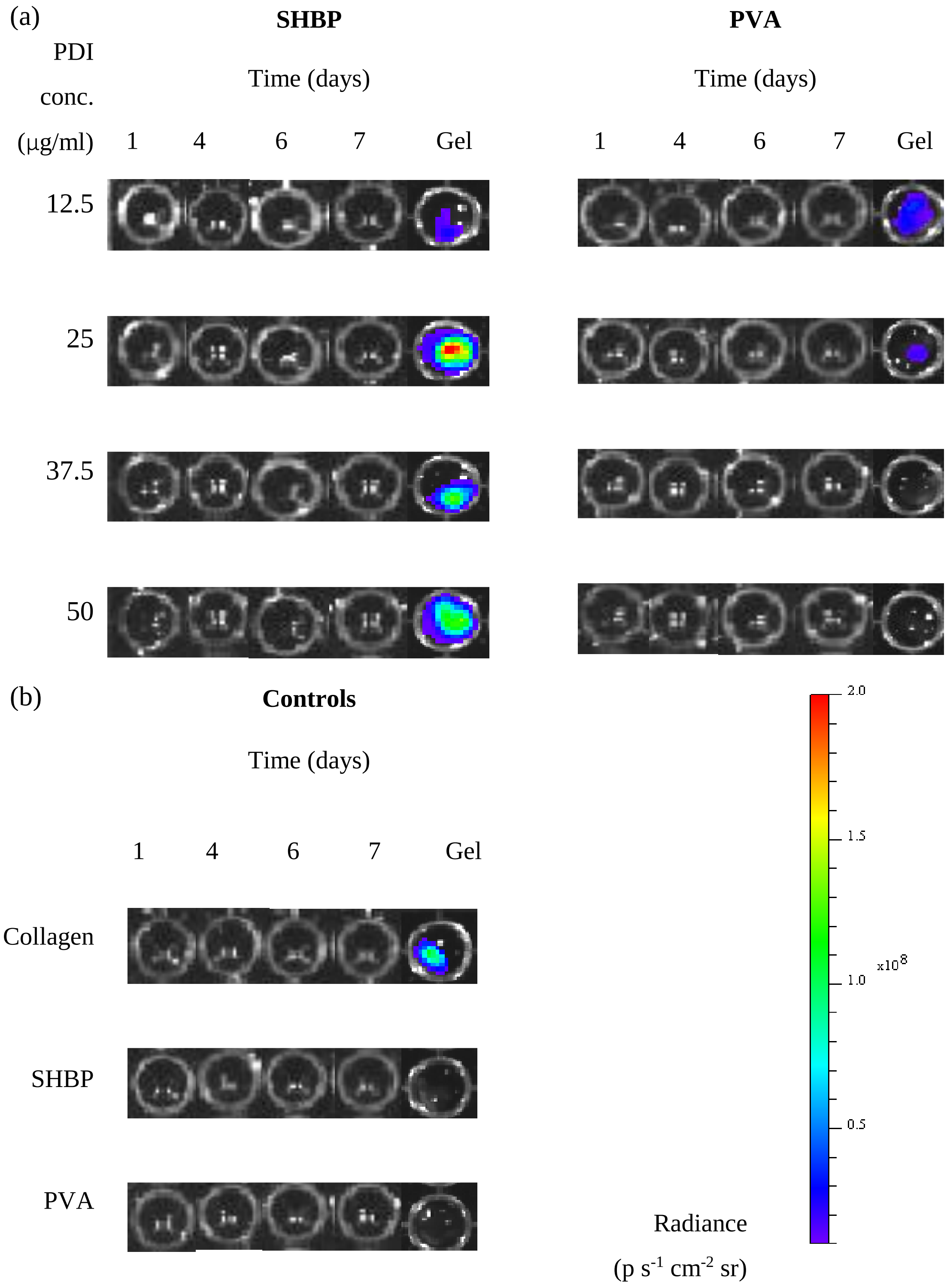

Figure 3.3: Bioluminescence imaging of gels which had been prepared on day 0 and moved to a new well every 1-3 days. Gels labelled with (a) SHBP- and PVA-stabilised PDI nanoparticles (0-50 µg/ml) were imaged on day 7 along with (b) control gels including an unlabelled MSC collagen gel and labelled gels (25 µg/ml) without cells.

All gels contained 2x10^5 MSCs apart from the SHBP and PVA control gels. Luciferin was added to the wells at a concentration of 5 mM ahead of imaging.

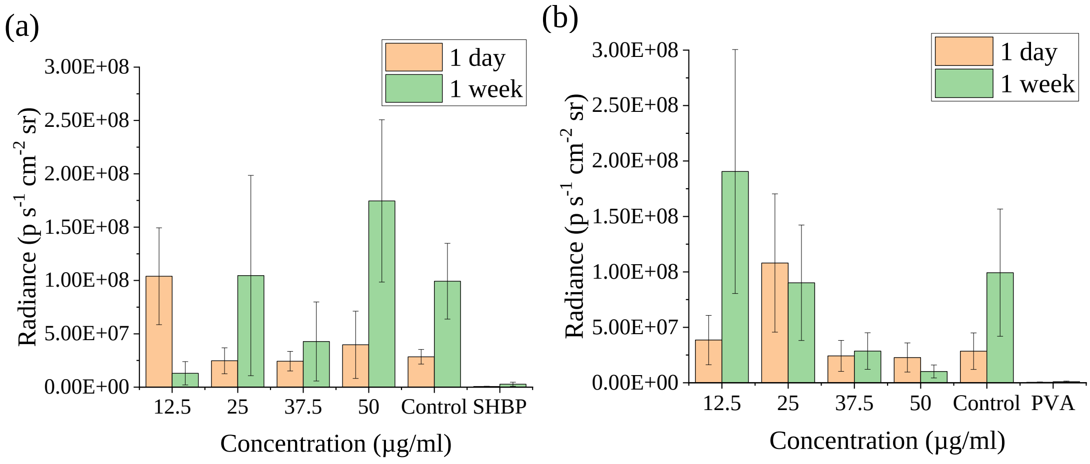

Figure 3.4: Bioluminescence imaging of gels at 1-day and 1-week post-synthesis. The total flux of the gels was quantified and is displayed as radiance for gels labelled with (a) PDI-SHBP and (b) PDI-PVA nanoparticles. The results are an average of three experiments and the error bars are the standard error of the mean.

3.3.3 MSOT Signal Detection

In vitro MSOT studies were carried out using agar phantoms. The MSOT irradiates the sample at multiple wavelengths and the signal is detected by ultrasound; the intensity of the acoustic waves undergoes tomographic reconstruction to form images of the gels. Gels were pushed into clear plastic straws and PBS was added to avoid air bubbles which can cause artefacts. The ends of the straw were sealed and the straw was inserted into a phantom for imaging. The gels were imaged from 650-1100 nm and images at 710 nm are shown, as it was found in Chapter 2 (Figure 2.20) that this coincided with the peak absorption of PDI nanoparticles. Gels were imaged at 1-day and 1-week post-synthesis to assess the changes in MSOT signal over time.

Figure 3.5 shows MSOT imaging of the control gels in phantoms which had been imaged after 1 day. Images are shown at 710 nm, as well as a graph displaying the mean pixel intensity of each of the gels over the range of wavelengths scanned.

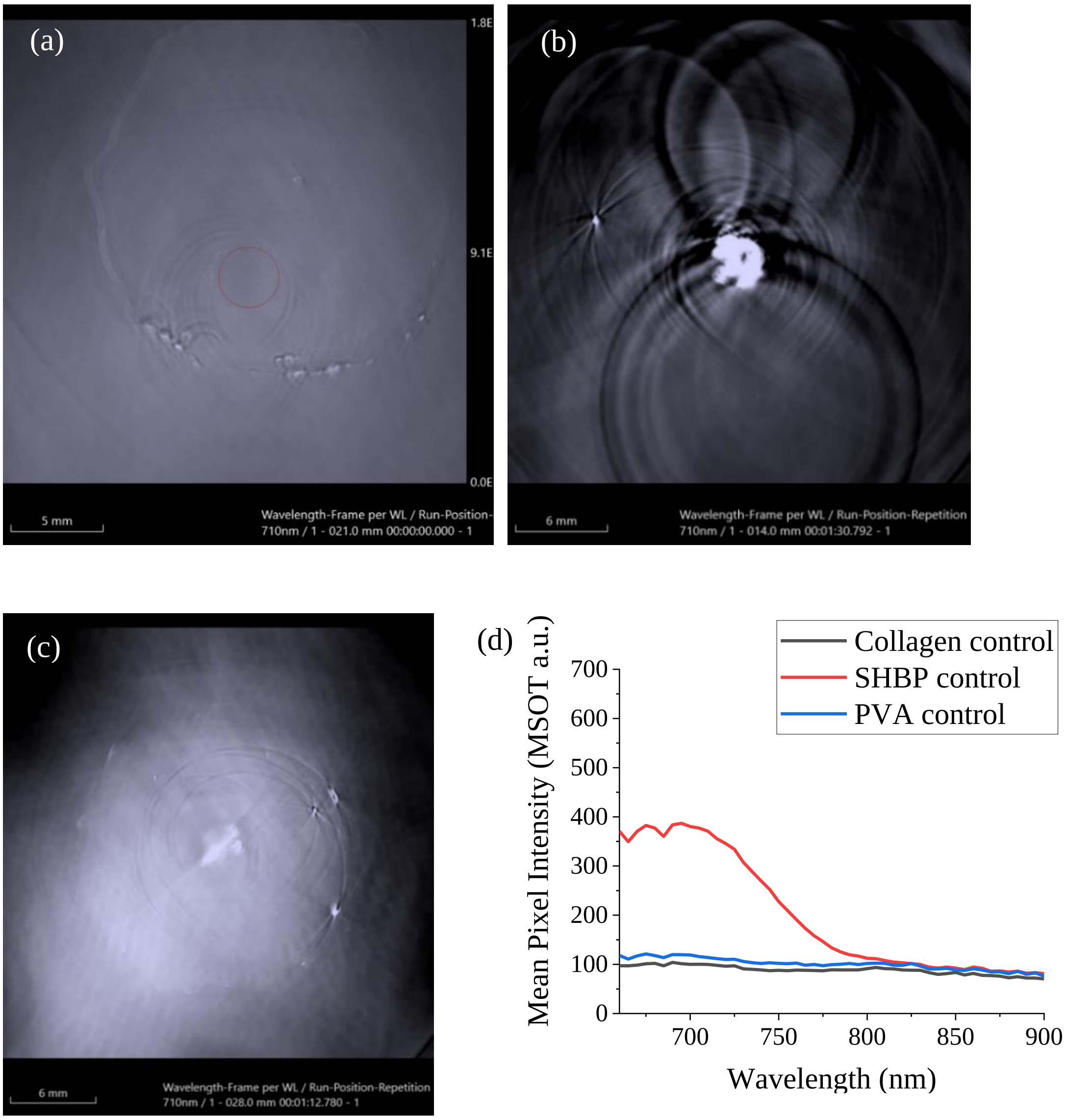

Figure 3.5: MSOT images at 710 nm of (a) unlabelled collagen gel and gels labelled with (b) SHBP-stabilised and (c) PVA-stabilised PDI nanoparticles (25 µg/ml) 1-day after gel preparation. A graph (d) showing MSOT mean pixel intensity of the gels vs. wavelength is also displayed. Imaging was carried out on fixed gels, 24hr post-synthesis.

The unlabelled collagen control gel (Figure 3.5a) could not be visualised at 710 nm however for the nanoparticle control gels, the shape of the gels can be seen in the images (Figure 3.5b and 3.5c). The mean pixel intensity (related to absorbance) of the gel labelled with SHBP-stabilised nanoparticles is significantly higher than the collagen control and the gel labelled with PVA-stabilised nanoparticles (Figure 3.5d).

MSCs were incorporated during gel preparation at a seeding density of $2x10^5$ cells/gel and fixed 24hr after gel preparation for imaging with MSOT. Figure 3.6 shows the results for two sets of gels labelled with SHBP- or PVA-stabilised PDI nanoparticles at a range of concentrations (0-50 µg/ml). Images of the gels at 710 nm are shown for the gels labelled at a concentration of 25 µg/ml and images of all other concentrations can be found in the Appendix (Figures A9 and A10).

When comparing the different concentrations for gels labelled with SHBP-stabilised nanoparticles, the highest concentration of 50 µg/ml gives the greatest signal however at all other concentrations tested the MSOT signal was relatively weak and signal intensity did not correlate with increasing concentration (Figure 3.6). A similar trend was seen for gels labelled with PVA-stabilised nanoparticles although here the MSOT signal was generally lower than for the gels labelled with SHBP-stabilised nanoparticles; this agrees with the control gels discussed in Figure 3.5. It is also worth noting that the signal intensity is much lower than for the nanoparticle solutions of equivalent concentrations (Figure 2.34, Chapter 2). This observation and the lack of correlation of signal with concentration was investigated further by fluorescence imaging to check for nanoparticle leaching.

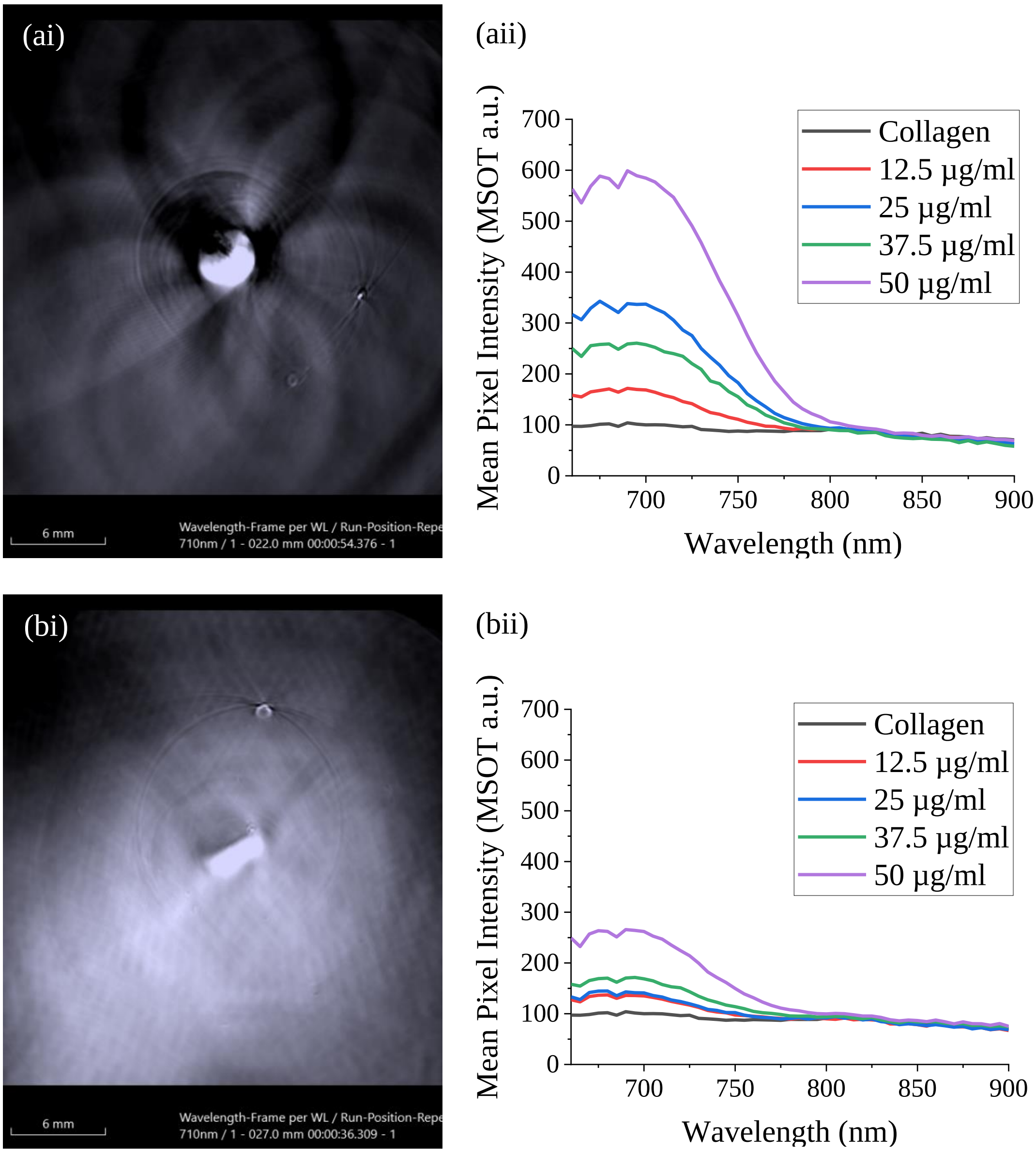

Figure 3.6: MSOT of gels prepared with 2x10^5 cells and imaged 1-day post-synthesis. Images of gels labelled with (ai) SHBP and (bi) PVA nanoparticles (25 µg/ml) are displayed, as well as graphs of MSOT mean pixel intensity vs. wavelength at different concentrations for (aii) SHBP and (bii) PVA labelled gels.

The controls gels (cell only and nanoparticle only) were remade and kept in an incubator for 1 week with a media change every 2-3 days. After this time, gels were imaged with MSOT. Figure 3.7 highlights the reduction in MSOT signal of gels labelled with SHBP-stabilised nanoparticles over the 1-week timescale.

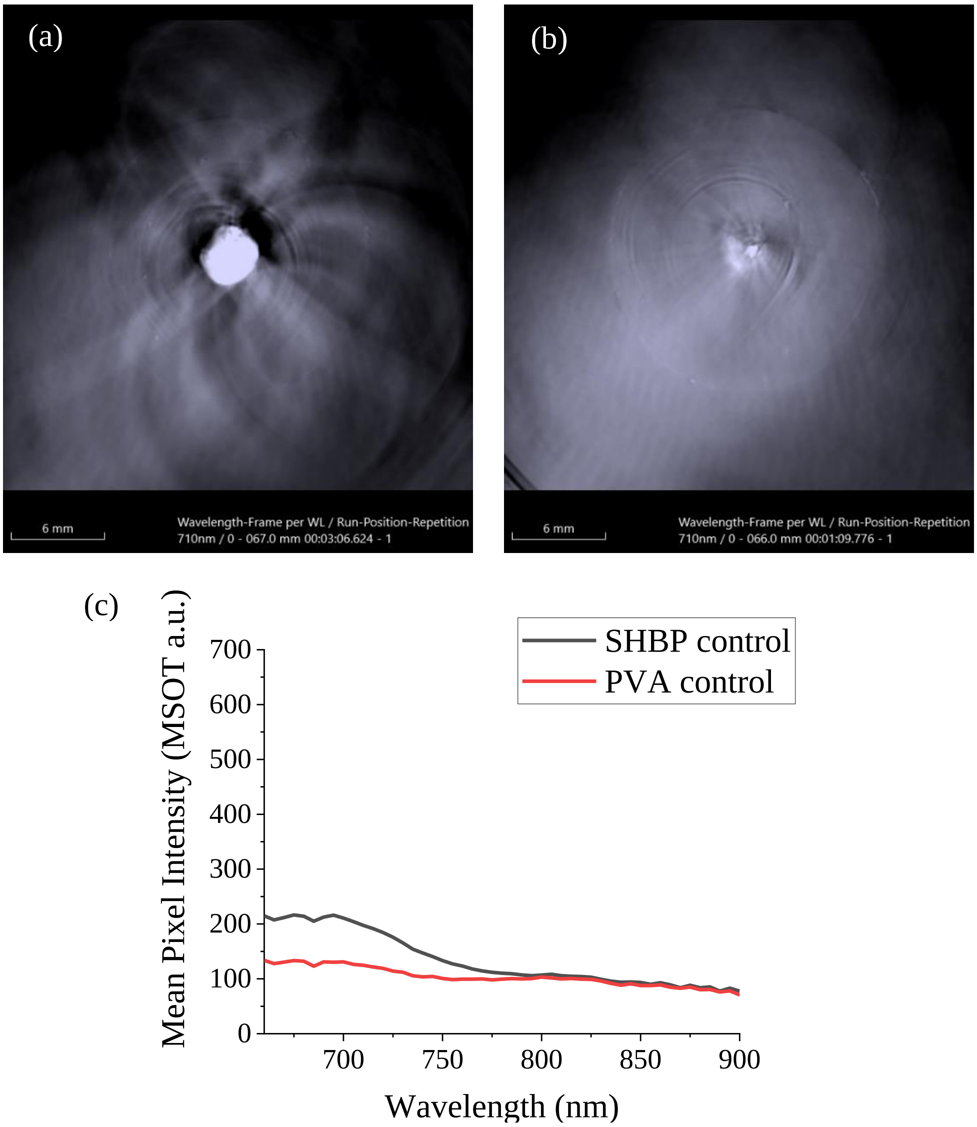

Figure 3.7: MSOT images at 710 nm of control gels labelled with (a) SHBP-stabilised and (b) PVA-stabilised PDI nanoparticles (25 µg/ml) 1-week after gel preparation. A graph (c) of MSOT mean pixel intensity of the gels vs. wavelength is also displayed. Imaging was carried out on fixed gels, 1-week post-synthesis.

The same set of gels were prepared with 2x10^5 MSCs seeding density. In a same experiment as the control, gels were kept in an incubator for 1 week and the media was changed every 2-3 days. The data is shown in Figure 3.8, where images at 710 nm is shown for gels labelled at nanoparticle concentrations of 25 µg/ml and the images with other concentrations can be found in the Appendix (Figure A11 and A12). When comparing MSOT at 1-week and 1-day timepoints, it has been observed that signal intensity decreases with time; this suggests that nanoparticles may be leaching out of the gels over time. For gels labelled with PVA-stabilised nanoparticles, there is very little signal compared to the collagen control after 1 week however gels with SHBP-stabilised nanoparticles have retained some signal (Figure 3.8).

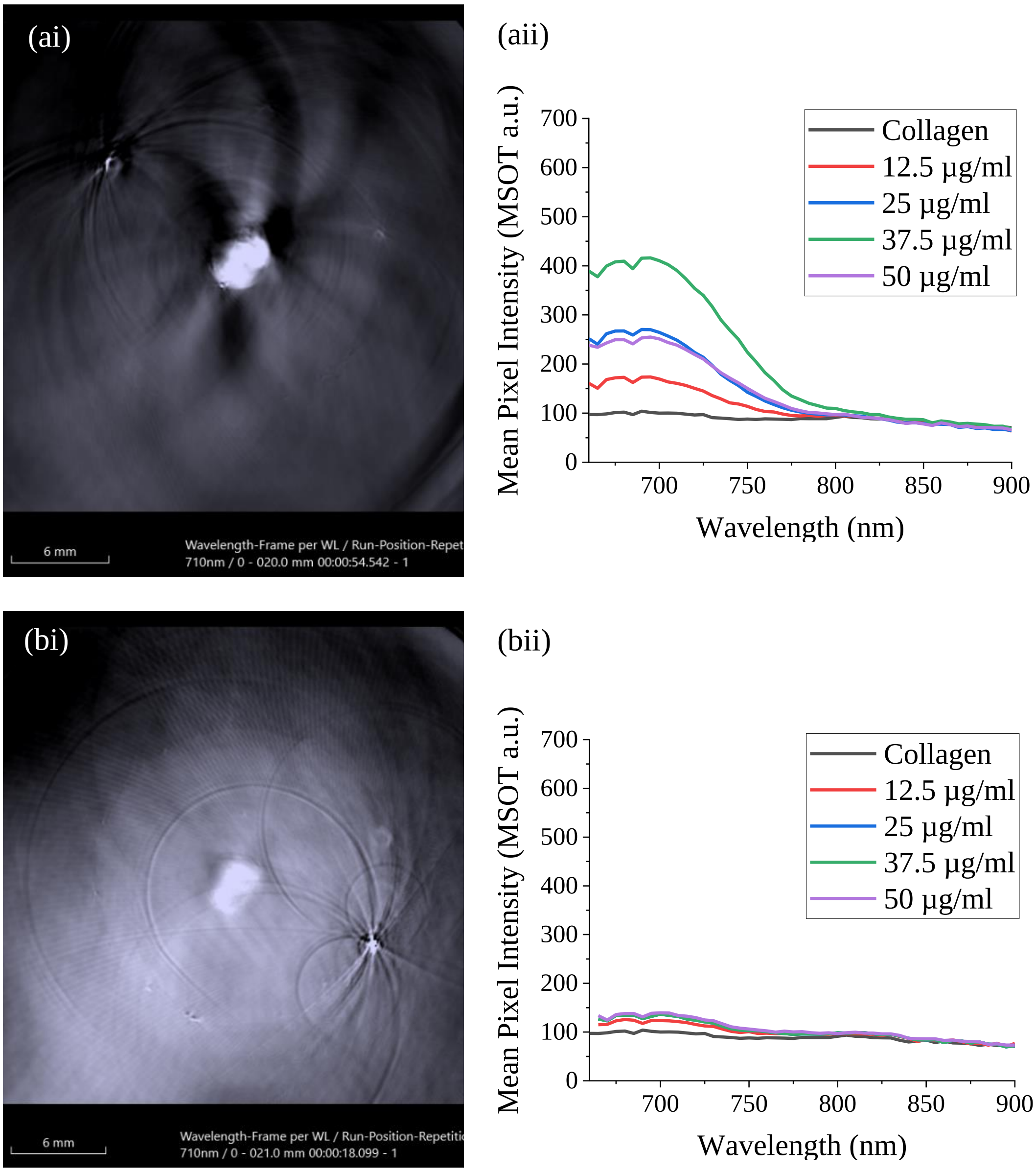

Figure 3.8: MSOT of gels prepared with 2x10^5 cells and fixed 1-week post-synthesis. Images of gels labelled with (ai) SHBP and (bi) PVA nanoparticles (25 μg/ml) are

displayed, as well as graphs of MSOT mean pixel intensity vs. wavelength at different concentrations for (aii) SHBP and (bii) PVA labelled gels

These findings were reproducible and repeats of the MSOT experiments are displayed in the Appendix (Figures A13 and A14). Again, there seemed to be no correlation between signal intensity and labelling concentration as it is likely that the concentrations stated are inaccurate due to nanoparticle leaching.

3.3.4 Investigating Nanoparticle Leaching

The PDI nanoparticles exhibit fluorescence at ~740 nm and so can be detected by fluorescence imaging. In the same experiment as with bioluminescence imaging, gels were prepared and after 24hr, gels were moved to a new well prior to imaging. The fluorescent signal output is displayed as radiant efficiency.

Fluorescent signal was observed in all wells apart from the unlabelled collagen control gel, as shown in Figure 3.9, which indicated that any signal was due to the presence of nanoparticles. The total flux in each well was also quantified and can be found in Figure A15 in the Appendix. The fluorescence signal in well 1 suggested that some nanoparticles were not included in the gel or had leached out during the 24hr period. The signal in well 2 is from the gel which suggested that there were still enough nanoparticles left in the gel to give a fluorescent signal.

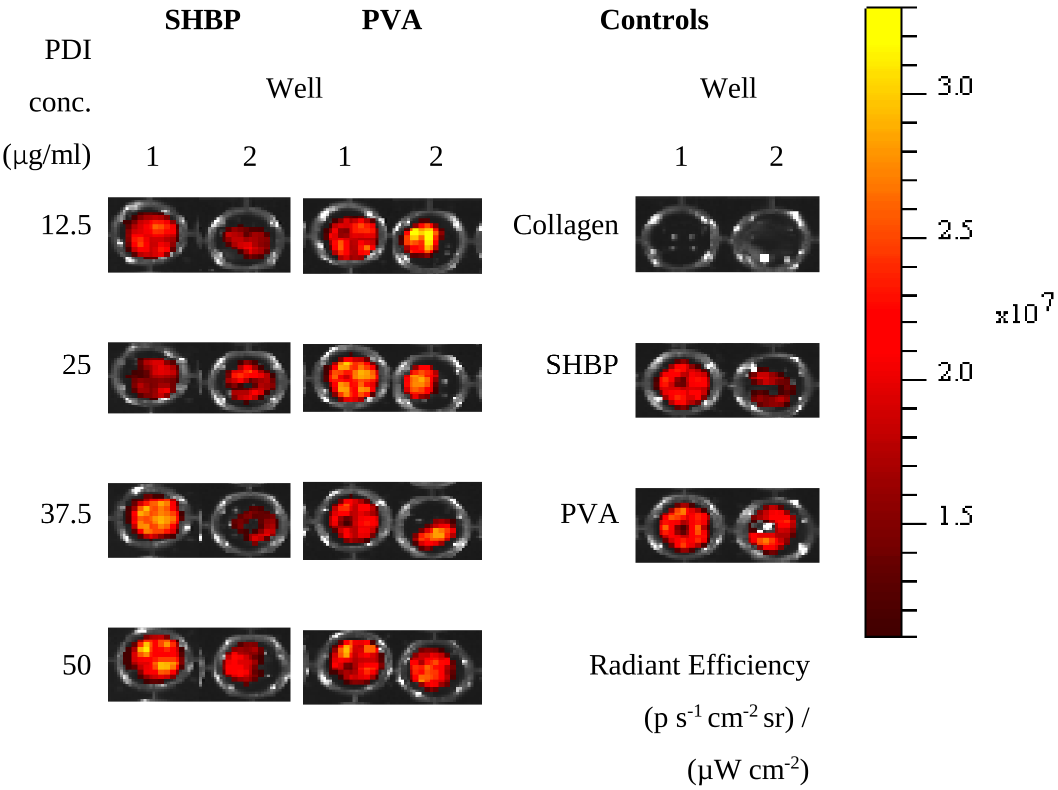

Figure 3.9: Fluorescence imaging of gels which had been prepared in well 1 and moved to well 2 after 24hr. Gels labelled with SHBP- and PVA-stabilised PDI nanoparticles (0-50 µg/ml) were imaged along with control gels including an unlabelled MSC collagen gel and labelled gels (25 µg/ml) without cells. All gels contained 2×10^5 MSCs apart from the SHBP and PVA control gels. Fluorescence imaging was carried out with excitation and emission filters of 710 nm and 750 nm, respectively.

It was possible that the nanoparticles were not included in the gel in the first place and had settled out into the original well during the gelation process. Therefore, an experiment was carried out where gels were prepared, moved to a new well every 1-3 days and covered with media before fluorescence imaging after 1 week. Any fluorescence signal from the now empty wells can be associated with nanoparticles that had migrated out of the gels and settled onto the well surface. Comparing the fluorescence signal from the gel and the previous wells enables an indication of the extent of nanoparticle leaching.

Figure 3.10 summarises the fluorescence imaging of the control gels, including collagen (with cells) as well as gels labelled with SHBP- and PVA-stabilised nanoparticles (without cells). The collagen control gel cannot be seen on the fluorescence image however the labelled gels can be visualised. Furthermore, the total flux of each well was quantified (Figure 3.10b) and is higher for the labelled gels whilst the collagen control does carry some value which can be attributed to background signal. These results confirm that the fluorescence signal comes from the nanoparticles. For the labelled gels, the fluorescence signal of the wells and gels are quite similar suggesting there are some nanoparticles remaining in the gels and also some residual nanoparticles that leached from the gel and settled on to the well surface.

Figures 3.11 and 3.12 show the results for MSC gels labelled with SHBP- and PVA-stabilised nanoparticles, respectively. The results show a similar trend to the nanoparticle control gels; fluorescence signal can be seen in the gels and in the wells. The total flux in each well was quantified and it was found that increasing the dosing concentration did not result in an increase in fluorescence intensity in the gels due to varied amounts of leaching from each gel (Figure 3.11b and 3.12b). There is still a fluorescent signal in the gel which is consistent with MSOT suggesting the gels could still be detected after 1 week.

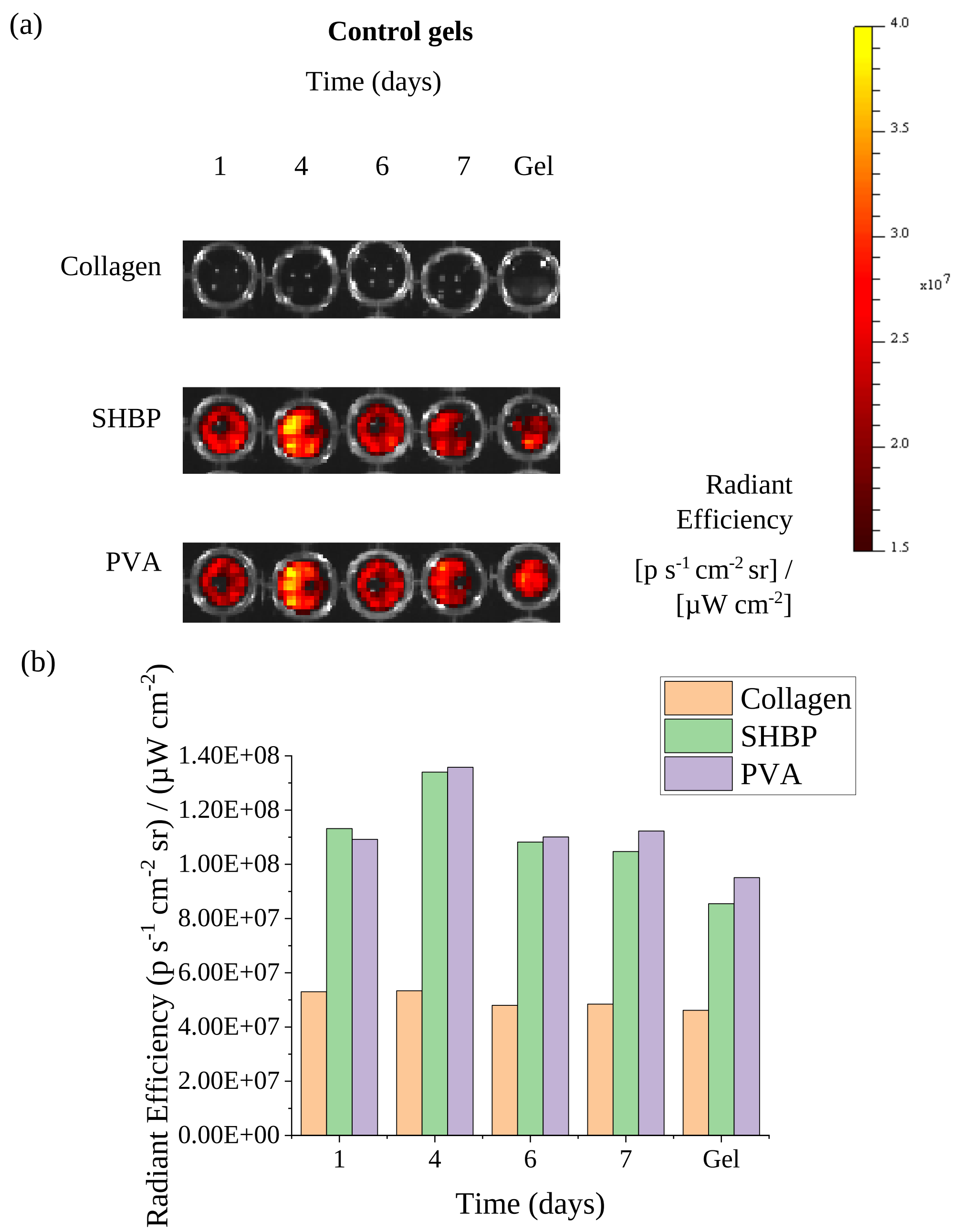

Figure 3.10: Fluorescence imaging of gels which had been prepared in well 1 and moved to new wells every 1-3 days, highlighted in (a) fluorescence images and (b) a graph to show radiance efficiency measurement of each well. Control gels were imaged, including an MSC collagen gel (2x10^5 cells) and gels labelled with SHBP- and PVA-stabilised PDI nanoparticles (25 µg/ml) which did not contain MSCs. Fluorescence imaging was carried out with excitation and emission filters of 710 nm and 750 nm, respectively.

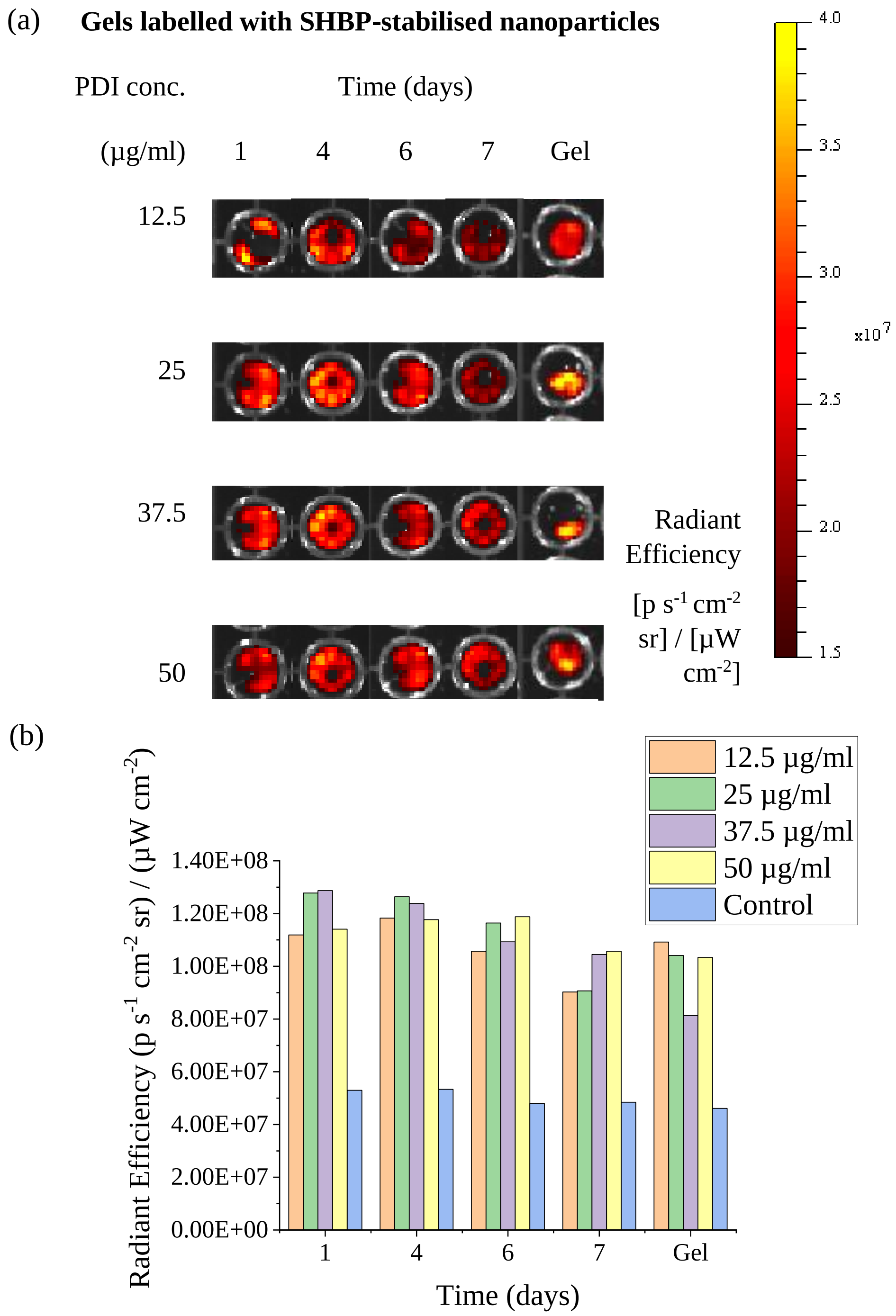

Figure 3.11: Fluorescence imaging of gels which had been prepared in well 1 and moved to new wells every 1-3 days, highlighted in (a) fluorescence images and (b) a graph to show radiance efficiency measurement of each well. Gels labelled with SHBP-stabilised PDI nanoparticles (0-50 µg/ml) were imaged, and all gels contained 2x10^5 MSCs. Fluorescence imaging was carried out with excitation and emission filters of 710 nm and 750 nm, respectively.

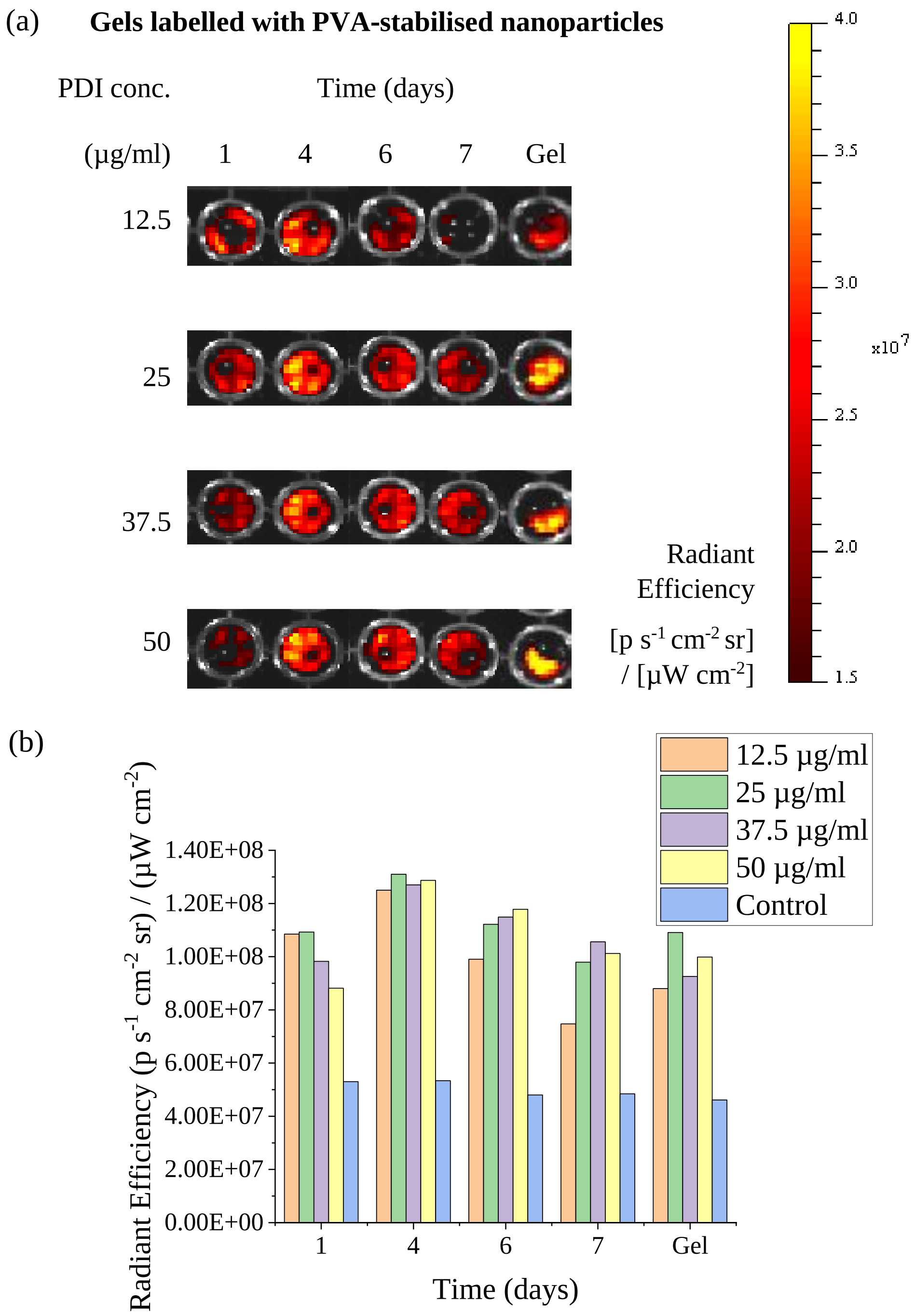

Figure 3.12: Fluorescence imaging of gels which had been prepared in well 1 and moved to new wells every 1-3 days, highlighted in (a) fluorescence images and (b) a graph to show radiance efficiency measurement of each well (right). Gels labelled with PVA-stabilised PDI nanoparticles (0-50 µg/ml) were imaged, and all gels contained 2x10^5 MSCs. Fluorescence imaging was carried out with excitation and emission filters of 710 nm and 750 nm, respectively.

3.4 Discussion

Collagen gels have been prepared as a protective matrix for the delivery of MSCs. Collagen was chosen as the construct material as it mimics the ECM and has bioadhesive properties, making it an ideal candidate for cell delivery applications in treating SCI.[32, 316, 331] The collagen gels have been labelled with NIR-absorbing PDI nanoparticles for tracking hydrogel integrity *in vivo* with MSOT. The aims of the present study were to optimise the labelled gels *in vitro* in terms of cell viability and PA signal.

The synthesis and characterisation of PDI nanoparticles is detailed in chapter 2. Briefly, PDI nanoparticles were prepared using a nanoprecipitation method with a polymer stabiliser. PVA and our novel SHBP stabiliser were used to prepare nanoparticles for labelling of separate gels to compare labelling efficiency and the effect on cell viability. A range of nanoparticle concentrations (12.5-50 µg/ml) were investigated to determine the optimum for achieving PA signal without affecting cell viability.

The collagen gels were prepared following the manufacturer's guidelines and gelation was initiated by both temperature and pH. The gel components were kept on ice prior to preparation as the collagen gelation is temperature-sensitive.[340] The gelation process also includes the addition of sodium hydroxide so that hydrogen bonds can form to strengthen the gel. The PDI nanoparticles and MSCs were included in the gel premix, along with the sodium hydroxide and 10% PBS, so that they could be encapsulated in the matrix during gelation. Gelation occurred during the 30-minute incubation period after gel preparation.

Gels containing MSCs contracted during the 24hr period which is a phenomenon widely observed in the literature.[42, 338, 339] The contraction results in a more rigid gel that can be more easily manipulated, whereas the control gels that did not contain MSCs were much more fragile and difficult to manipulate. A seeding density of 2×10^5 was selected to enable cells to be easily visualised with bioluminescence imaging and to provide some rigidity so as to facilitate manipulation of the gel. Higher seeding densities were avoided because excessive contraction of the gel would result in an increase in the local concentration of PDI nanoparticles around the cells, which could potentially reduce cell viability. The PDI nanoparticles did not have an effect on gel contraction but did give the gels a blue tinge.

3.4.1 Cell Survival and Migration

The fate of cells in the collagen gel was monitored using bioluminescence imaging as the MSCs had been engineered to express firefly luciferase. Luciferin was added to media/PBS surrounding the gel and a bioluminescent signal was detected suggesting luciferin could diffuse into the gels to reach the MSCs. Experiments had to be carried out in duplicate to compare cell viability after 1 day and 1 week as it was not possible to image with the IVIS under sterile conditions.

It was found that cells survived in all of the gels after 1 day as a bioluminescent signal could be detected. Conversely, there was no bioluminescent signal for any of the labelled control gels which did not contain MSCs. After 1 week, the cells were viable in the majority of gels. The bioluminescent signal of the gels could be quantified as total flux and it was found that the average flux increased for the unlabelled control gel at 1-week compared to 1-day, suggesting MSCs were proliferating. Furthermore, the total flux generally increased for the gels labelled with SHBP-stabilised nanoparticles. For the gels labelled with PVA-stabilised nanoparticles, the total flux was generally low for gels labelled at 37.5 and 50 μg/ml and decreased from 1-day to 1-week when labelled at 25 μg/ml. This suggested that the PDI-PVA nanoparticles had a cytotoxic effect which contradicts data in chapter 2 where PVA-stabilised nanoparticles were well-tolerated up to 40 μg/ml; however, mechanical forces in the gel will also have an effect.

When comparing different concentrations of the same type of nanoparticle, the strength of the bioluminescent signal was variable. This could be caused by the lack of precision in the number of cells that are incorporated in the gel when making batches of multiple gels or problems associated with luciferin diffusing through the gel and reaching all the cells. Furthermore, the nanoparticle concentrations were not accurate due to nanoparticle leaching. Despite this, over repeats of the experiments, the cytotoxic effect of gels labelled with PDI-PVA nanoparticles was evident.

It was found that MSCs did not migrate from within the collagen gel into the wells in the timescales used for this study. After 1 week, there was a strong bioluminescent signal for most of the gels however there was no signal in any of the wells that the gels had previously inhabited. This is consistent with the bioadhesive properties associated with collagen.

3.4.2 Tracking Gels with MSOT

The labelled gels were evaluated *in vitro* with MSOT using agar phantoms. Gels were prepared in duplicate and fixed at 1-day and 1-week timepoints for imaging with MSOT. All the gels could be effectively visualised with MSOT compared to the collagen control. The peak absorbance of the PDI nanoparticles is ~710 nm and all labelled gels had significantly higher MSOT mean pixel intensity at this wavelength compared to the unlabelled control. This suggested the incorporation of the nanoparticles enabled detection of the gel with MSOT.

The signal of gels labelled with SHBP-stabilised nanoparticles was generally much higher than with the PVA-stabilised nanoparticles. This is inconsistent with MSOT measurements of the nanoparticle solutions (Chapter 2) where similar MSOT absorbance was observed. Clearly, the gel structure will have an effect on this as only one slice of the gel is imaged and it is unclear if the nanoparticles are homogenous throughout the gel. Moreover, the leaching of the nanoparticles will have an effect on MSOT intensity.

There was a reduction in MSOT signal intensity for both sets of gels from 1-day to 1-week, where gels labelled with PVA-stabilised nanoparticles returned to baseline after 1 week. The gels labelled with SHBP-stabilised nanoparticles did lose some signal however all gels remained above the signal of the unlabelled collagen control. This observation and the fact that there was no correlation between labelling concentration and signal intensity suggests that nanoparticles were likely leaching from the gels.

3.4.3 Nanoparticle Leaching

Following the MSOT data, fluorescence imaging was used to determine whether nanoparticles were leaching from the gels. In the same experiment as for bioluminescence imaging, fluorescence was measured using the IVIS at 1-day and 1-week time points. For the 24hr experiment, the fluorescent signal of the gel was compared to the well that had previously held the gel. Both the well and the gel had a fluorescent signal however it was unclear whether nanoparticles had leached out or had not been incorporated in the gel in the first place, i.e. the PDI nanoparticles could have come out of the gel premix as the gel was forming.

Following this, gels were prepared and moved to new gels every 1-3 days and fluorescent imaging was carried out after a week. There was a fluorescent signal coming from all the wells that had previously held a gel that had been labelled with PDI nanoparticles and limited fluorescent signal for the collagen control. This suggested that nanoparticles leached out of the gels and settled onto the surface of the well. Despite this, there was still a fluorescent signal from the gel after 1 week which meant that some nanoparticles had remained in the gel. This is consistent with MSOT data where gels labelled with SHBP-stabilised nanoparticles could still be visualised after a week. There was a fluorescent signal from the gels labelled with PVA-stabilised nanoparticles after a week where no signal had been observed at this timepoint with MSOT. This could be due to differences in the sensitivity of the techniques in *in vitro* models, i.e. bioluminescence imaging is of the gel in a plate whereas MSOT is carried out in agar phantom. For animal experiments, imaging is at a greater depth and so MSOT is more sensitive.

The nanoparticle leaching explains why the nanoparticle labelling concentration did not correlate MSOT signal intensity. It is unknown how many PDI nanoparticles leached at each stage so the effect of concentration on MSOT signal intensity could not be determined. The fluorescence imaging shows that nanoparticles leached out over time and so it is likely that the dosing concentrations are inaccurate however the extent of leaching has been difficult to quantify using this technique. A similar phenomenon was observed in the literature for hydrogels that were labelled with SPIONs;[84] the MRI signal decreased over time suggesting the leaching of SPIONs. In the present application, future experiments could look to explore the extent of leaching further by dialysing the gels and taking UV-vis absorbance measurements of the surrounding medium.

Ultimately, work would be needed to prevent nanoparticle leaching; this could be explored through altering the surface properties of the PDI nanoparticles to increase the interaction with the collagen. This could be achieved by increasing the electrostatic interaction between nanoparticles and hydrogels or by direct conjugation of the nanoparticles to the polymer. An example of this is where gold nanoparticles was conjugated to a synthetic polymer hydrogel *via* carbodiimide coupling.[341] Another possible route is to increase the concentration of collagen which would decreased the gel pore size.[342, 343]

3.5 Conclusion

Preliminary studies herein suggest that PDI nanoparticles prepared with SHBP stabiliser can be used to label collagen gels for imaging with MSOT. The PDI nanoparticles could be used in a proof of principle experiment to assess whether it is possible to image the gels *in vivo* over the short-term. This would give insight into whether the gel fragments shortly after implantation. Furthermore, there is sufficient MSOT signal enabling gel fragmentation to be assessed for up to 1 week.

The major drawback of the constructs is that nanoparticles appear to leach from the gels over time. This suggests that they would not be useful for monitoring the extent of gel degradation over time as it would be difficult to decipher whether a reduction in MSOT signal would be due to leaching or degradation. Future experiments should look to investigate nanoparticle leaching further and over longer timescales to find the point at which the gels can be no longer detected with MSOT. Ultimately, this problem will need to be tackled by focussing on the probe design to increase the interaction between the nanoparticles and the collagen matrix to prevent leaching.

Chapter 4: Nanodiamonds as Fluorescent Probes for Cell Tracking

4.1 Introduction

Nanodiamonds (NDs) first emerged in the 1960s in the USSR, but have only attracted attention in the last few decades with the rise of other novel carbon-based materials.[344] The rigid diamond structure is made up of a dense network of sp^3 hybridised carbon atoms, each with tetrahedral symmetry. Each carbon atom forms four bonds to neighbouring carbon atoms resulting in a lack of free valence electrons which contributes to the high inertness. However, as for other nanoscale materials, the properties of NDs are predominantly as a result of the surface chemistry.[137] For NDs, the high surface area gives rise to properties that are different to the bulk material as surface carbon atoms cannot make four bonds and hence terminal groups, such as hydrogen and hydroxyl groups, are included to reduce unfavourable dangling bonds.

Both the intrinsic structure (sp^3 carbon network) and the surface chemistry of NDs can be exploited to alter material properties such as stability as well as optical and electronic properties. The tunability aspect, combined with their high biocompatibility and inexpensive large-scale synthesis, has meant that NDs are being explored for many potential biomedical applications.[345-347]

4.1.1 The Rise of Carbon-based Materials

Graphene, multi-walled carbon nanotubes (MWCNT) and fullerenes are among the most common carbon-based nanomaterials being exploited for their unique physicochemical properties.[132, 348] Graphene is defined as a single monolayer of carbon atoms arranged in hexagonal lattice, or honeycomb structure, which was first isolated from graphite (>10 layers of graphene) in 2004 at the University of Manchester.[349] The novel electronic properties of graphene can be attributed to its unique 2D structure, where changing the amount of graphene layers allows the electronic properties to be manipulated.[350] Other advantages, such as ease of surface functionalisation and processing in aqueous medium, have encouraged investigation into the possible biomedical applications of graphene.[129, 351, 352]

MWCNTs are structures made up of multiple graphene layers rolled up, which can be easily functionalised to alter solubility and electronic properties.[353] The direction of the graphene plane and the diameter of the nanotube can also be controlled to alter electronic properties.[354] MWCNTs have been extensively explored for *in vitro* and *in vivo* imaging owing to their intense and tuneable optical properties, including photoluminescence and NIR absorbance.[131, 210] It has been found that the success of MWCNTs *in vivo* is attributed to effective surface functionalisation with biocompatible coatings.[130, 131]

Fullerenes are caged structures made up of 60 carbon atoms, resembling a sheet of graphene rolled up to form a hollow sphere. The uses of fullerenes have been severely hampered by their lack of solubility in aqueous medium; however, functionalised fullerenes, such as fullerenol, have gained significant interest in the biomedical field.[132, 355, 356]

Carbon dots, sometimes referred to as carbon quantum dots, are a relatively new class of carbon-based materials that have nanoparticle morphology with a particle size range of 2-10 nm. They can be prepared from top-down methods, from graphene, MWCNTs or NDs, or bottom-up approaches from carbon-based precursors.[357] Carbon dots exhibit high fluorescence and are hence being explored in cellular imaging and photovoltaic applications.[358]

Studies have shown that NDs are more biocompatible than other carbon-based materials.[132, 135, 346] This is particularly notable as NDs also share many of the advantages of graphene, MWCNTs, fullerenes and carbon dots, such as the unique optical properties, ease of surface modification and large surface area. Furthermore, uniquely among the other carbon-based materials, NDs show no evidence of photobleaching making them highly attractive for imaging applications.[359]

4.1.2 Synthesis of Nanodiamonds

Diamond can be prepared by chemical vapour deposition (CVD), high-pressure high-temperature (HPHT) and detonation methods.[137] CVD, as the name suggests, involves the deposition of chemical vapours onto a substrate, resulting in the formation of diamond films. Nanocrystalline and ultrananocrystalline films, can be prepared with grain sizes of 5-100 and 3-5 nm, respectively; grain size is dependent on various parameters, such as composition of the growth precursors, temperature, pressure and voltage. CVD is commonly used to prepare diamond films for sensing and coating applications.[360]

NDs are more commonly prepared by HPHT or detonation of carbon explosives.[361] HPHT conditions are required to form NDs from graphite, in order to overcome the high energy barrier.[136] The process generally involves irradiation and annealing, as well as milling techniques to achieve smaller particle sizes. The high energy process results in defects within the diamond structure where carbon atoms are knocked out resulting in vacancies. When these vacancies are near to nitrogen centres, produced by including nitrogen compounds in the starting material, nitrogen-vacancy (NV) defects are formed.[137, 362] This results in unique absorbance/fluorescence properties which can be exploited for bioimaging.

4.1.2.1 Detonation NDs

It is difficult to achieve the small particle sizes required for biomedical applications using the HPHT process and hence the discovery of detonation NDs was paramount.[344] Carbon explosives are detonated by the generation of a shock wave which causes high enough temperatures and pressures to initiate explosion; this results in conditions of 3000–4000°C and 20–30 GPa within the chamber.[137] After this, the NDs are rapidly cooled, by inert cooling gas or water, in order to minimise phase transformations to graphitic forms. It is then essential to remove impurities, such as sp^2 carbon, metals, oxides and carbides from the chamber or starting mixture.[363]

Purification usually involves treating NDs with dilute nitric acid or hydrochloric acid at high temperature and pressure in order to remove impurities.[137, 364, 365] The non-diamond sp^2 carbon can also be oxidised with powerful liquid oxidisers, such as sodium peroxide.[136] The purification process is usually the most expensive part of the ND synthesis and there is also a high environmental cost. Gas phase treatment is an alternative and more eco-friendly method where NDs are reacted with ozone to convert the sp^2 carbon to CO and CO_2, thus avoiding corrosive liquid oxidisers.[366, 367] The nature of the oxidative purification process results in oxygen containing functionalities, such as hydroxyl, carboxyl and anhydride groups, to present on the surface, terminating the dangling bonds.[136, 363, 368]

4.1.2.2 Modified Nanodiamonds

Nitrogen Vacancy (NV) Defects

If a nitrogen atom is near to a vacancy within the ND structure, this is known as NV centre or defect. Some NV defects are inherent of the high energy process utilised to synthesize NDs however they can also be intentionally introduced to produce fluorescent NDs. NV defects are caused by irradiating the NDs with high energy particles, such as electrons, protons or helium ions, followed by thermal annealing under vacuum.[369, 370]

Most examples of NDs with NV defects are synthesized by HPHT though it is also possible to incorporate nitrogen in the detonation process. NV defects have been found in detonation NDs after electron irradiation and annealing, however intense and stable emission is only seen in the larger NDs (>30 nm).[371] Detonation NDs have many structural defects, both intrinsic and surface associated, which may result in fewer NV centres. It has been confirmed that NV defects can exist in smaller detonation NDs; however, there are only a relatively small amount due to the particle size and hence there is limited detectable fluorescence.[372]

There are two types of NV defects which have different fluorescence properties: the neutral NV^0 and negative NV^-.[138] The NV^- defect tends to be the more dominant product of the irradiation process which results in excitation and emission wavelengths of ~560 nm and 700 nm, respectively and a quantum efficiency of ~1.[373, 374] These wavelengths are particularly useful for imaging as there is limited cell autofluorescence in the far-red-NIR region.

Surface Modification

Detonation NDs can be up to 100 nm in size, however they are typically 5 nm and hence very prone to aggregation.[375] Various milling processes with ceramic beads can be used to de-aggregate the NDs, however this can result in impurities from the beads (ZrO_2 or SiO_2) and the likelihood of reaggregation is high.[376] Water-soluble salt- and sugar-assisted milling have also been explored to reduce contamination.[377]

Surface functionalisation provides a route to reducing ND reaggregation, where a simple route is from carboxylated NDs produced during the detonation process, as depicted in Figure 4.1.[136] NDs with carboxyl groups on the surface can be isolated by ozone treatment, followed by hydrochloric acid to hydrolyse anhydride functional groups and remove metal impurities. A wide selection of gas treatments and wet chemistry routes have been investigated to react with the carboxyl groups, providing routes to attachment of proteins, polymers and various other coatings.

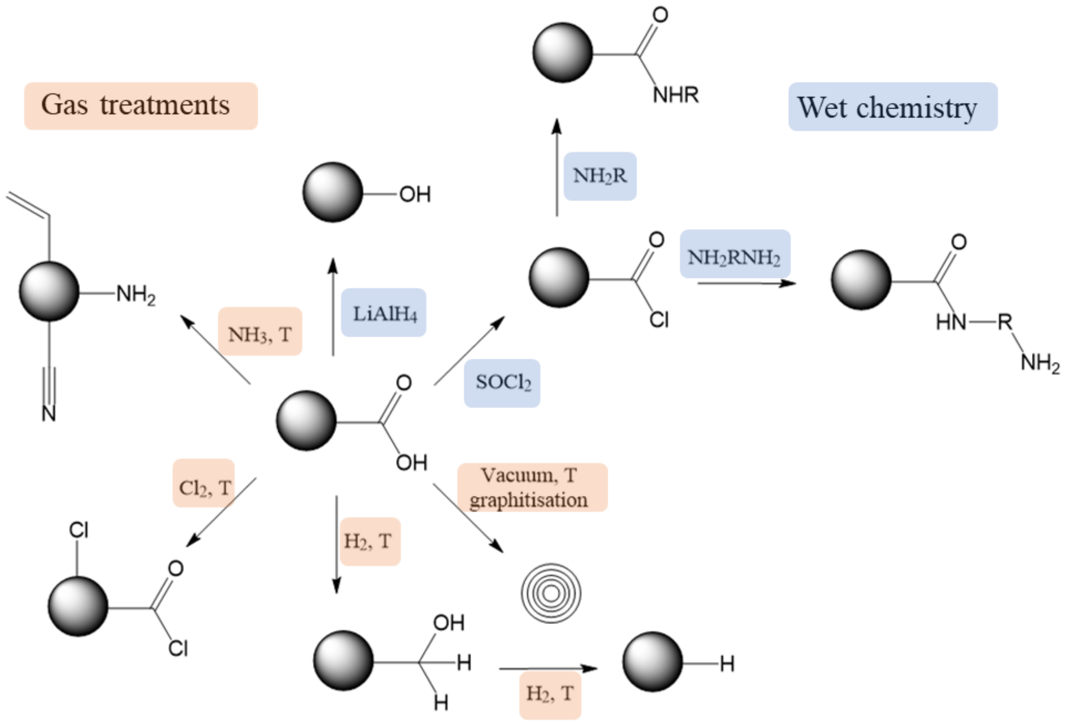

Figure 4.1: A simplified schematic to show examples of the surface modification of NDs, starting from a purified sample of NDs with carboxyl groups on the surface. Gas treatments are shown in orange and wet chemistry routes are in blue. Adapted from reference.[136]

It has been found that grafting poly(ethylene glycol) (PEG) to the surface of NDs can increase dispersibility in aqueous medium.[378] Similarly, functionalising NDs with lysine improved stability and dispersibility in water for applications as genetic carriers.[379] Various surfactants have also been investigated for improving the dispersion of NDs, where zwitterionic lecithin resulted in optimal cellular uptake.[380]

4.1.2 Biomedical Applications of Nanodiamonds

4.1.3.1 Drug Delivery

Extensive research into surface functionalisation of NDs has paved the way for an increase in biomedical applications, particularly drug delivery. For example, carboxyl groups on the surface of NDs were converted to acyl chloride, followed by the addition of PEG and subsequent physisorption of doxorubicin (DOX), a common chemotherapeutic drug.[381] Cellular uptake of ND-PEG-DOX was increased 2-fold compared to free DOX and the incorporation of PEG reduced aggregation resulting in increased stability. ND carriers have also been shown to overcome efflux mechanisms, thus increasing drug retention and efficacy.[140, 382, 383] This suggests that ND carriers could be used to treat chemoresistant tumours.

NDs can also be used to improve the solubility and dispersibility of hydrophobic drugs.[137, 139] Administration of such drugs has been limited due to the use of harmful solvents, resulting in non-clinically relevant formulations. Therefore, novel ND drug carriers offer the potential to enable clinical translation of many drug candidates which had previously been hindered.

4.1.3.2 Bioimaging Probes

One of the most commonly explored fluorescent probes is quantum dots; however, there have been major problems with cytotoxicity and hence there is a need to develop coatings in order to circumvent this.[373] Hence, the high biocompatibility of NDs combined with the fluorescence properties of the NV^- defect are particularly attractive in bioimaging. NDs have been shown to have long fluorescence lifetime, high quantum yield and low photobleaching.[136, 138, 373] It should be noted that most examples of NDs with NV defects are generally prepared by HPHT and there is little data for fluorescence of detonation NDs thus far.[136]

NDs with NV^-defect were used to investigate sentinel lymph node mapping in a mouse model and fluorescent signal could still be detected 37 days post-injection (subcutaneous or intraperitoneal).[142] This highlights the potential for long term imaging capabilities. Milled NDs, with mean particle size of 46 nm, have also shown good uptake into HeLa cells where the uptake mechanism was most likely *via* clathrin-mediated endocytosis.[384] In this study, it was found that NDs predominantly resided in endocytic vesicles; however, smaller NDs appeared to be free in the cytoplasm. This suggested that NDs can be used for cell labelling of mammalian cells and smaller NDs have high potential for biomolecule delivery.

The widespread use of NDs with NV defects as imaging probes is inhibited due to the high cost associated with production and hence, the surface modification with fluorophores offers an alternative route.[141] As for other nanoparticles, molecules can be added to the surface either covalently or non-covalently, i.e. physical adsorption.[385, 386] Cytochrome C (λ_{max} = 409 nm) was immobilised on the surface of 5 nm NDs firstly by physical adsorption, likely *via* electrostatic attraction between carboxyl groups on the ND surface and amino groups within the protein structure.[387] The resultant probe showed weak absorption at 409 nm which suggested that this approach was not successful and thus an alternative covalent method was developed to increase the density and strength of attachment. Poly-L-lysine was selected to aminate the surface of NDs for subsequent attachment of Cytochrome C, where strong absorption at 409 nm was demonstrated indicating more successful surface modification.

Hydrophobic blue fluorescent NDs have been prepared by the functionalisation of 5 nm NDs with octadecylamine (ODA).[141] The facile synthesis involved the formation of acid chloride groups on the ND surface followed by stirring at 90-100 °C for 96hr. The resultant ODA-NDs had peak excitation and emission wavelengths of 410 and 450 nm, respectively, which was not observed for the NDs or ODA separately. This phenomenon has not yet been explored; however, it is hypothesized that the optical properties are due to the thermal degradation of the ODA chains and formation of aromatic structures.

Despite the advances in NDs, fluorescence imaging for *in vivo* cell tracking is severely hampered by the limited penetration depth.[44] Hence, other imaging modalities, such as photoacoustic imaging (PAI) are more useful for cell tracking in rodent models. In many cases, *in vivo* imaging is corroborated by *ex vivo* histological analysis although sometimes this is difficult after long timescales due to signal dilution, i.e. signal is diluted 50% with each cell division. Fluorescent NDs are an excellent candidate for labelled cells for *ex vivo* studies as they have extremely high biocompatibility so high dosing concentrations are well-tolerated. NDs. Furthermore, NDs are eventually cleared by excretion into the urinary tract.[142]

4.1.3.3 Multimodal NDs

Multimodal ND carriers are NDs capable of multiple functions i.e. therapy, diagnostics and targeting. An example of this is multimodal NDs which been prepared by covalently attaching paclitaxel (PTX) to the ND surface *via* fluorescently labelled oligonucleotide strands, as well as anti-epidermal growth factor receptor monoclonal antibodies (anti-EGFR mAb).[388] The combination of PTX and mAb resulted in enhanced therapeutic efficacy and target specificity, where cellular uptake could be confirmed with fluorescence microscopy due to the labelled oligonucleotide strands.

This further highlights the broad range of molecules which can be loaded onto the ND surface and the ability to tailor the ND carrier for a desired application. In addition to this, introducing a NV defect into the ND structure means that in some cases a fluorophore would not need to be attached, thus contributing to the impressive multimodal capabilities of NDs.[389] This suggests that NDs could be used for simultaneous therapeutic and diagnostic applications (theranostics).[390]

4.1.3 Perylene Diimide and NDs

As previously mentioned, there is a high cost associated with using NDs with NV defect and hence attaching fluorescent dyes to the surface of NDs is another option. Perylene diimide (PDI) derivatives have been discussed in detail in Chapter 2 for their potential use in probes for multispectral optoacoustic tomography (MSOT). PDI derivatives also have strong fluorescence which can be utilised herein for preparing fluorescent NDs. The advantage of combining PDI with NDs is to hone the high biocompatibility of NDs which could enable high labelling concentrations for detecting cells in *ex vivo* fluorescence imaging.[142] Furthermore, a NIR-absorbing PDI derivative could be attached to NDs for *in vivo* cell tracking with MSOT and subsequent *ex vivo* fluorescence imaging.

4.1.4 Aims

The present study will investigate the potential of various types of nanodiamonds as probes for cell tracking with fluorescent imaging techniques. The aims are as follows:

1. To attach a perylene diimide derivative to the surface of detonation and high-pressure high-temperature nanodiamonds and assess these probes in terms of optical properties and stability.

2. To label mesenchymal stromal cells with perylene diimide-nanodiamonds and nanodiamonds with a nitrogen vacancy defect.
3. To assess and compare the effects of perylene diimide-nanodiamonds and nanodiamonds with a nitrogen vacancy defect on mesenchymal stromal cell viability.
4. To confirm the uptake and fluorescent signal of the perylene diimide-nanodiamonds and nanodiamonds with a nitrogen vacancy in MSCs.

4.2 Experimental

4.2.1 Materials

All reagents were used as received from the manufacturer. Sodium hydroxide (≥97%), *N*-(3-dimethylaminopropyl)-*N′*-ethylcarbodiimide hydrochloride (EDC) and *N*-hydroxysulfosuccinimide sodium salt (sulfo-NHS) were purchased from Sigma Aldrich. Detonation NDs (5-10 nm), HPHT NDs (50 nm) and NV NDs (40 nm and 90 nm) were provided by Element Six Ltd. *N,N'*-di(3,5-dicarboxylphenyl)perylene-3,4,9,10-tetracarboxylic diimide (red PDI derivative) was synthesized by Dr Xia Liu.[391]

4.2.2 Characterisation Methods

A Malvern Zetasizer Nano and associated Zetasizer software were used to determine the hydrodynamic diameter, polydispersity index and zeta potential of particles in water *via* dynamic light scattering (DLS). Samples were diluted with water (0.1 mg/ml) and sonicated for 10 minutes prior to DLS analysis. Images of particles were acquired with a Hitachi S4800 Scanning Electron Microscope (5 kV). Liquid samples were prepared by adding a drop of nanosuspension onto an SEM stub and leaving for the liquid to evaporate. Solid samples were adhered to the stub using conductive double-sided carbon tape. Spectroscopic data was obtained using a Vertex 70 Fourier Transform Infrared (FTIR) Spectrometer (Bruker); samples were dried ahead of the experiment. Optical properties were investigated using a μ-Quant Microplate Reader (BioTek) and a Fluorescence Lifetime Spectrometer (FLS) 1000 (Edinburgh Instruments). Samples were prepared at a concentration of 0.1 mg/ml and analysed using a front-face sample holder, 590 nm emission filter and excitation/emission bandwidths of 0.8-3 nm. Excitation wavelengths of 500 or 560 nm were used and emission was measured in the range of 550-800 nm with a 1 nm step and 0.2 s dwell time.

4.2.3 Surface Modification of HPHT NDs

Carboxylic acid functional groups were introduced by oxidation of the surface of HPHT NDs using a well-established protocol in the literature.[392] Briefly, 50 nm NDs (2 g) were dispersed in 80 ml acid solution (3:1 69% H_2SO_4/37% HNO_3) and heated to reflux for 24hr. Once cooled, the mixture was slowly added to distilled water and centrifuged (4000 rpm). Particles were washed three times by centrifugation and consequently dried under vacuum for 24hr.

4.2.4 Conjugation of PDI to detonation and HPHT NDs

Optimisation of NDs as probes was carried out using a red PDI previously prepared in abundance in our group.[391] The method of PDI conjugation was adapted from similar procedures in the literature.[393-395] PDI (7 mg, 0.01 mmol) was dissolved in 10 ml of basic water (0.06 mM NaOH). EDC (26.7 mg, 0.1 mmol) and sulfo-NHS (30.2 mg, 0.1 mmol) were added to 2 ml of the PDI solution (0.002 mmol). This was stirred at room temperature for 30 minutes before the addition of either detonation or HPHT NDs (2 ml, 0.7 wt%). This was stirred overnight and consequently washed by centrifugation in water.

4.2.5 Cell Culture

The murine mesenchymal stromal cell line D1 (ATCC) was used for all *in vitro* cell studies. MSCs had previously been modified by Dr Arthur Taylor (Murray group) to express firefly luciferase under the control of the constitutive promoter, EF1α.[276, 277] MSCs were cultured in 6 cm or 10 cm tissue culture dishes (Greiner CELLSTAR®) in high glucose Dulbecco's Modified Eagle Medium (DMEM, Sigma Aldrich) containing 10% fetal bovine serum (FBS, Sigma Aldrich), 1% non-essential amino acids (Sigma Aldrich) and 2 mM L-glutamine (Gibco). Cells were incubated at 37°C and 5% v/v CO_2 and passaged with 1% trypsin/EDTA (Sigma Aldrich) when they reached 90% confluence.

4.2.6 *In Vitro* Cell Studies

4.2.6.1 Cell Viability

CellTiter-Glo® Luminescent Cell Viability Assay (Promega) was used according to the manufacturer's guidelines. MSCs were seeded in triplicate at a density of $2x10^4$ cells/well in a 96-well plate and left to attach and grow for 24hr. After this, the medium was replaced with 200 µl fresh medium containing various concentrations of NDs (0-400 µg/ml). Cells were incubated for a further 24hr before carrying out the assay. The principle is based on cellular ATP released from lysed cells which react with luciferin/luciferase, leading to light emission at 562 nm. Cell viability was measured as the amount of ATP released from treated cells as a percentage of the ATP released from the control. Luminescence measurements were taken with a µ–Quant Microplate reader (BioTek).

4.2.6.2 Flow Cytometry

Flow cytometry was used to assess the cellular uptake and fluorescence properties of the NDs. MSCs were seeded at a density of $2x10^5$ cells/well (24-well plate) and incubated for 24hr. After this, the medium was aspirated and replaced with fresh medium containing nanoparticles of varying concentrations (0-100 µg/ml). After a further 24hr, cells were resuspended in PBS (1x) and kept on ice ahead of analysis. Flow cytometry was carried out using a BD FACSCalibur™ (BD Biosciences) with a 488 nm laser wavelength and a long pass FL3 filter (670 nm). When appropriate, threshold values for side scatter (SSC), front scatter (FSC) and FL3 were altered relative to the control to exclude unwanted events. 10,000 events were counted and the data was analysed with Flowing Software 2.5.1 (Turku Bioscience Centre).

4.2.6.3 Confocal Fluorescence Microscopy

Confocal fluorescence microscopy was employed to visualise and determine the location of NDs in MSCs. MSCs were seeded in 8-well chamber slides (Ibidi µ-Slide 8-well) at a density of $2x10^4$ cells/well. After 24hr labelling with nanoparticles (50 or 100 µg/ml), samples were fixed with 4% PFA (Sigma Aldrich). Cells were permeabilised with Triton-X (0.1 %v/v) and stained with 4′,6-diamidino-2-phenylindole (DAPI, 1:1000, Thermo Fisher) and Alexa Fluor™ 488 phalloidin (1:50, Invitrogen). Images were acquired with a Zeiss LSM 800 Airyscan confocal using 405 nm, 488 nm and 640 nm diode lasers and 63x oil objective. Z-stack images were obtained using a step size of 0.34 µm and the master gain of the PMT was set to 700 mV unless it was necessary to increase the brightness to visualise certain particles. Images were analysed in ImageJ (FIJI).

4.3 Results

NDs were provided by Element 6 Ltd., prepared by either detonation of carbon explosives or milling of diamond powders to give aqueous suspensions with particle sizes ranging from 5-100 nm. The NDs investigated in this study are detonation NDs (5-10 nm), milled HPHT NDs (50 nm), and NV NDs prepared by detonation followed by HPHT treatment (40 and 90 nm).

4.3.1 Perylene Diimide Conjugation to Detonation NDs

Perylene diimide (PDI) was conjugated to the surface of detonation NDs *via* carbodiimide coupling to amino groups on the ND surface. The PDI-NDs were fully characterised and *in vitro* cell studies were carried out to determine their cytotoxicity, cellular uptake and fluorescence properties.

4.3.1.1 Characterisation of Detonation NDs

NDs with approximate particle sizes of 5-10 nm were used which had amino groups on the surface for conjugation to PDI *via* carbodiimide coupling. The particle size was confirmed to be 5-10 nm with Transmission Electron Microscopy (TEM), as shown in Figure 4.2.

Dynamic Light Scattering (DLS) measurements were also carried out to determine the hydrodynamic diameter of the NDs. The DLS results are represented as the number particle size distribution as this considers the spherical shape of the nanoparticles and Mie scattering. The particle size of the detonation NDs was measured at 1625 ± 330 nm (Figure 4.3) with a polydispersity index of 0.152; this suggested the detonation NDs were prone to aggregation.

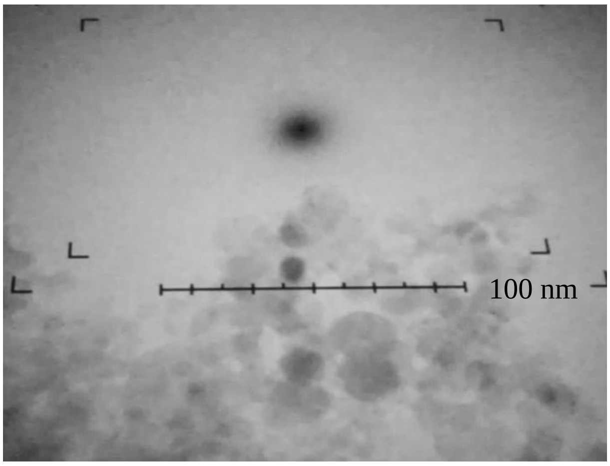

Figure 4.2: TEM image of detonation NDs with particle sizes of 5-10 nm. Images were taken by Dr Hripsime Gasparyan.

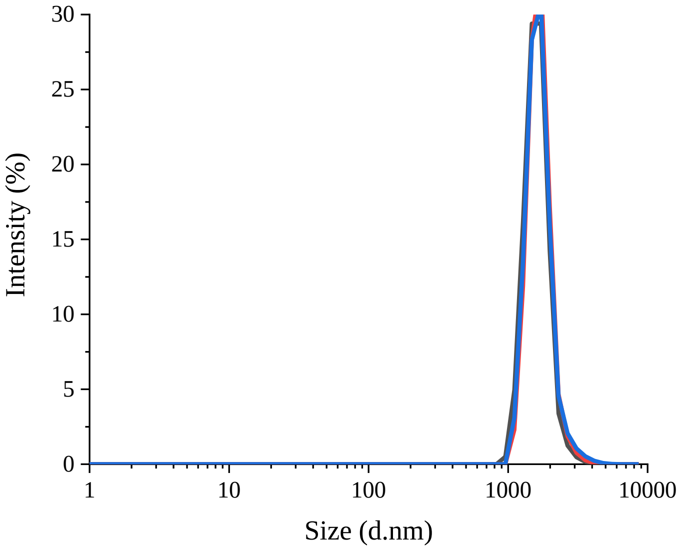

Figure 4.3: Number particle size distribution of detonation NDs in water (0.1 mg/ml). The different colours represent 3 measurement scans with DLS.

The presence of amino groups on the surface of the NDs was confirmed by measuring the zeta potential as in aqueous medium amino groups are protonated and hence result in positive surface charge. The zeta potential of the aminated NDs was +23.6 ± 9.82 mV compared to -33.4 ± 6.35 mV for non-aminated NDs (likely hydrogen or hydroxyl terminating groups from synthesis). This was also confirmed by Fourier-Transform

Infrared (FTIR) spectroscopy, shown in Figure 4.4; The broad stretch at 3300-3500 cm^{-1} is associated with free amine groups on ND surface and the stretch at 1630 cm^{-1} is also indicative of N-H bonding.

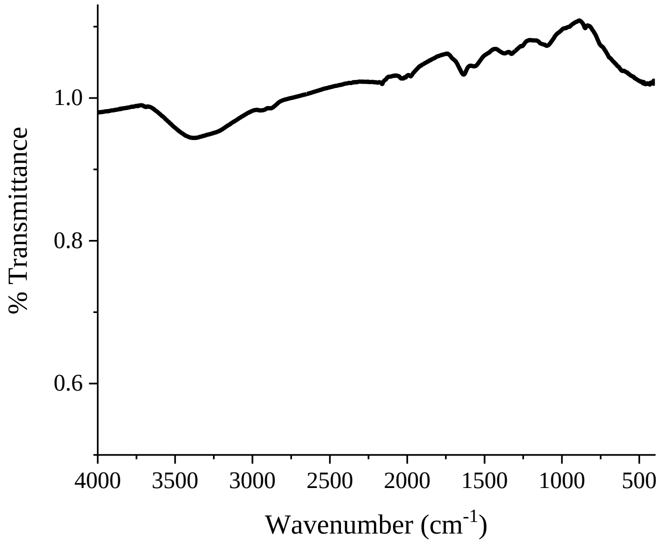

Figure 4.4: FTIR of detonation NDs (dried) with amino group surface functionality (particle sizes 5-10 nm).

4.3.1.2 PDI Conjugation

The PDI derivative used in these fluorescent probes, shown in Figure 4.5, was previously synthesized by our group for optimisation of PDI-based probes.[391] The carboxylic acid groups allow for conjugation to amino groups on the surface of detonation NDs.

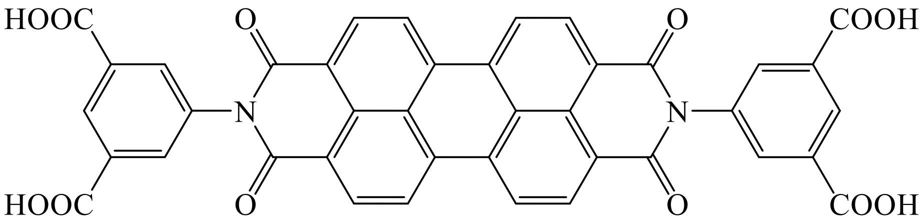

Figure 4.5: Chemical structure of PDI derivative containing carboxylic acid functionality for coupling to NDs.

The PDI derivative used has poor solubility in common solvents, including water, and hence basic water was used for the reaction. PDI was first dissolved in basic water (0.06 mM NaOH) and 1-ethyl-3-(3-dimethylaminopropyl)carbodiimide hydrochloride (EDC) and *N*-hydroxysulfosuccinimide sodium salt (sulfo-NHS) were added. After 30 minutes, NDs were added. The reaction was stirred at room temperature overnight. PDI-NDs were then washed by centrifugation and resuspended in neutral water to yield a cloudy pink suspension. UV-visible (UV-vis) spectroscopy was carried out with the supernatant phase of the centrifuged sample which showed no absorption in the visible spectrum. This suggested that the PDI was attached to the NDs, rather than dissolved in the basic water, as it had been at the start of the reaction.

The zeta potential of PDI-NDs significantly decreased to -19.2 ± 4.87 mV suggesting a decrease in vacant amino groups on the ND surface thus suggesting the attachment of PDI was successful. The reaction was also confirmed using FTIR spectroscopy where new stretches are seen around 1580 and 1350 cm^{-1} for PDI-NDs which are not seen for the unmodified NDs (Figure 4.6). The stretch at 1580 cm^{-1} can be attributed to the presence of aromatic C=C and the stretch at 1350 cm^{-1} is related to the C=O of free carboxylic acid groups, thus suggesting the presence of the PDI derivative.[396] Furthermore, the stretch at 1650 cm^{-1} is characteristic of C=O amide bond.[136] The broad stretch at 3300-3500 cm^{-1} is associated with free amine groups on the ND surface; this can be seen in the unmodified NDs and the PDI-NDs, suggesting that not all the amine groups had reacted.

The suspensions were prone to aggregation, partly due to the high concentration of the suspension (1 mg/ml) and hence dilutions were used for all characterisation and cell experiments. A concentration of 0.1 mg/ml was used for DLS following guidance from the manufacturer and the concentration for cell experiments was determined by assessing cytotoxicity. Ahead of DLS analysis, all samples were diluted and sonicated for 10 minutes using an ultrasonic bath. The particle size of PDI-NDs was similar to the unmodified NDs at 1771 ± 213 nm and the polydispersity index was 0.363 (Figure 4.7).

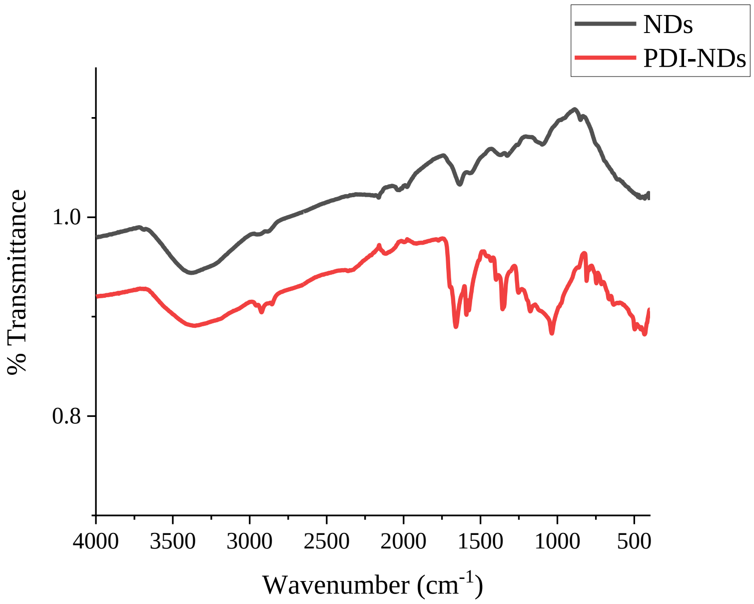

Figure 4.6: FTIR spectra of detonation NDs and PDI-NDs (dried).

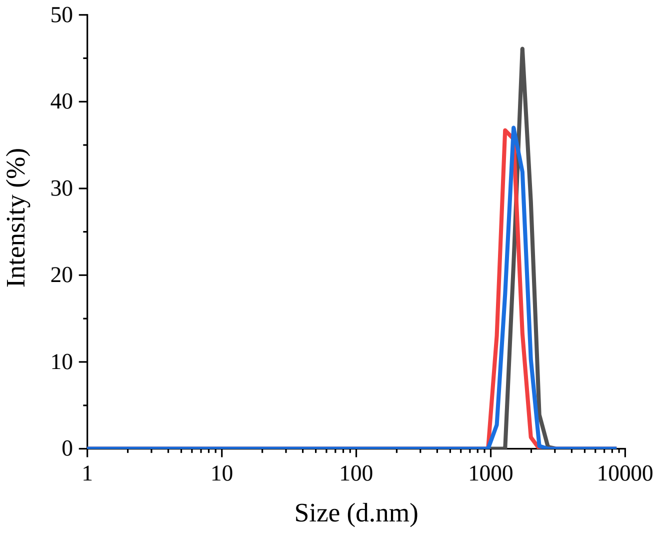

Figure 4.7: Number particle size distribution of detonation PDI-NDs (0.1 mg/ml). The different colours represent 3 measurement scans with DLS.

4.3.1.3 Optical Properties of PDI-NDs

The optical properties of the PDI-NDs were assessed using UV-vis spectroscopy and fluorescence spectrometry. The UV-vis spectrum of the PDI derivative showed peaks at 440, 470 and 510 nm, as shown in Figure 4.8. When the PDI-NDs were analysed, there was extremely high background signal due to the inherent light scattering properties of the NDs; this is consistent with results found in the literature.[387] The peak was also significantly lower; however. this is likely due to the amount of PDI in PDI-NDs compared to equivalent mass concentration of pure PDI and thus peak intensity is not considered important in this case. Higher concentrations of PDI-NDs could increase peak intensity but at the expense of increased light scattering.

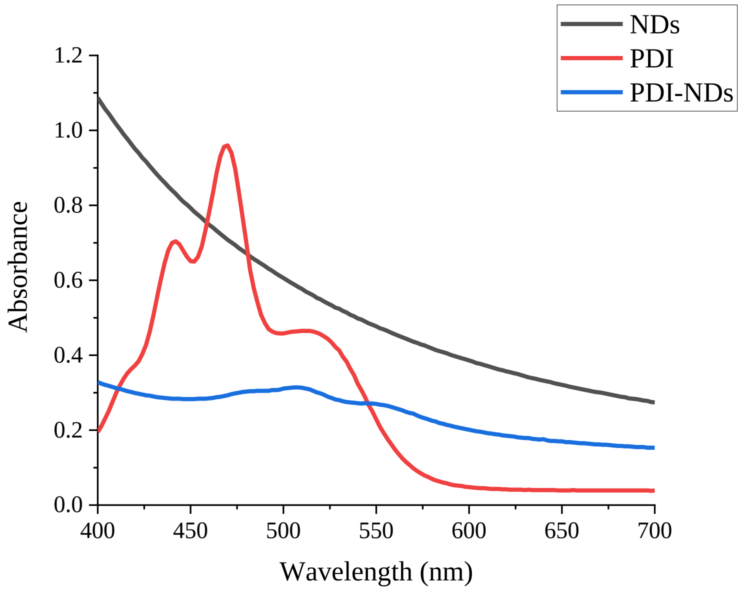

Figure 4.8: UV-vis spectra of PDI (0.1 mg/ml, 0.06 mM NaOH) and detonation PDI-NDs and NDs (0.1 mg/ml, neutral water).

The fluorescence properties of the PDI-NDs were assessed and compared with that of the free PDI dye and a sample of just NDs. Figure 4.9a show the emission spectra for pure PDI which demonstrates high emission intensity at 600 nm which is consistent with the literature.[258] When NDs and PDI-NDs were analysed at the same excitation wavelength, a 590 nm emission filter was needed to counteract the light scattering effects (Figure 4.9b). Emission spectra of NDs showed very low fluorescence, mostly associated with background signal and effects from the emission filter; however, for PDI-NDs the characteristic peak for PDI emission was observed at 600 nm.

(b)

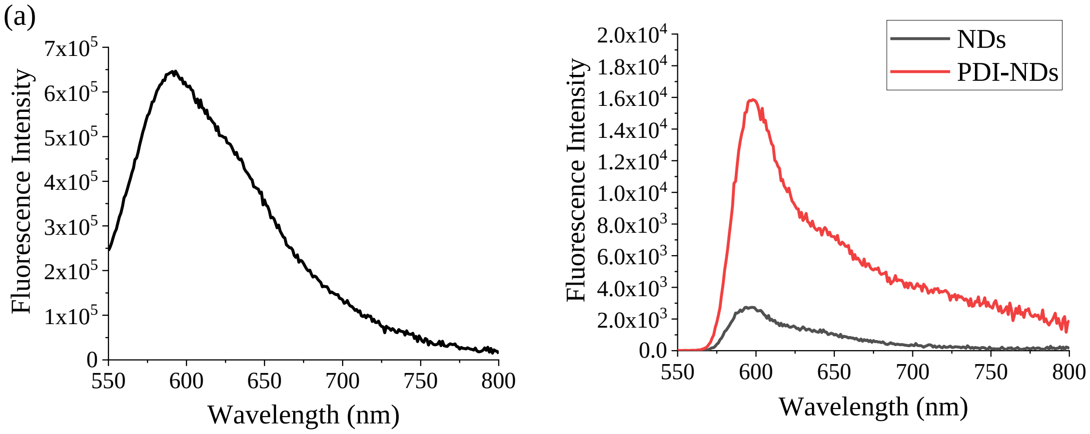

Figure 4.9: Emission spectra (λ_{ex} = 500 nm) for (a) pure PDI (0.06 mM NaOH solution) and (b) PDI-NDs and NDs (0.1 mg/ml, water). For PDI-NDs and NDs, an emission filter was used to block emission below 590 nm to counteract the effect of light scattering.

4.3.2 *In vitro* Evaluation of Detonation PDI-NDs as Fluorescent Probes

4.3.2.1 The Effect of Detonation PDI-NDs on Cell Viability

It was first essential to confirm the high biocompatibility reported for detonation NDs and whether PDI conjugation affected this. MSCs were seeded at a density of $2x10^4$ cells/well in a 96-well plate and left to grow and adhere for 24 hours. After this, the media was aspirated and replaced with fresh media containing various concentrations of unmodified detonation NDs and PDI-NDs. MSCs were then incubated for a further 24 hours before carrying out the CellTiter-Glo® luminescent cell viability assay; The assay principle involves cellular ATP released from lysed cells which react with luciferin/luciferase, leading to light emission at 562 nm. Cell viability was measured as the amount of ATP released from treated cells as a percentage of the ATP released from the control, as shown in Figure 4.10.

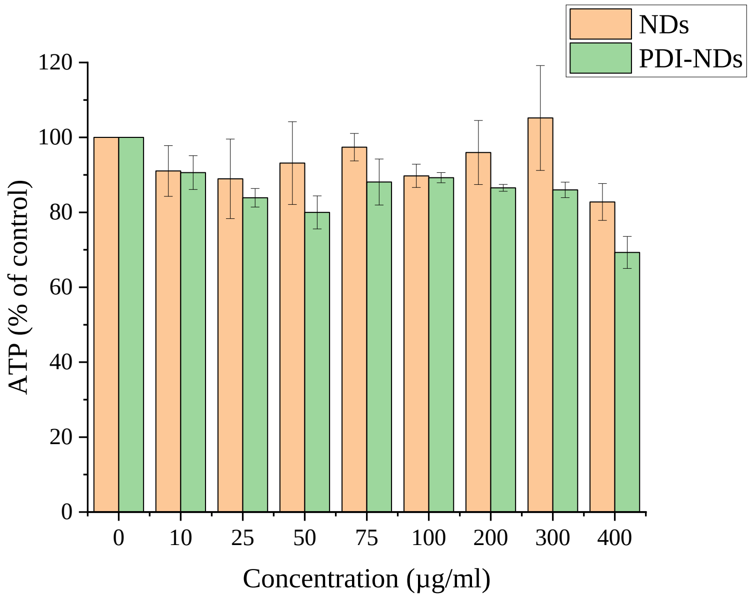

Figure 4.10: The effect of unmodified detonation NDs and PDI-NDs on ATP production in MSCs. Cells were seeded at a density of 2×10^4 cells/well (96-well plate) and incubated for 24 hours before dosing with NDs for a further 24 hours. The error bars represent standard deviation of biological repeats (n=3).

Both unmodified NDs and PDI-NDs have limited effect on the viability of MSCs up to concentrations of 300 µg/ml. The cell viability was slightly lower for PDI-ND; however, cell viability remained above 80% up to 300 µg/ml.

4.3.2.2 Assessing Cellular Uptake of Detonation PDI-NDs with Flow Cytometry

It was possible that the low cytotoxicity could be due to limited cellular uptake, particularly due to the large particle aggregates. Therefore, uptake was assessed by flow cytometry and confocal fluorescence microscopy. For flow cytometry, MSCs were seeded at a density of 2×10^5 cells/well and incubated for 24 hours ahead of dosing. The media was aspirated and replaced with fresh media containing NDs at concentrations of 25, 50 or 100 µg/ml; unmodified NDs as well as PDI-NDs were included. Flow cytometry was then carried out on live cell suspensions in PBS (10,000 cells were counted for each sample), as shown in Figure 4.11.

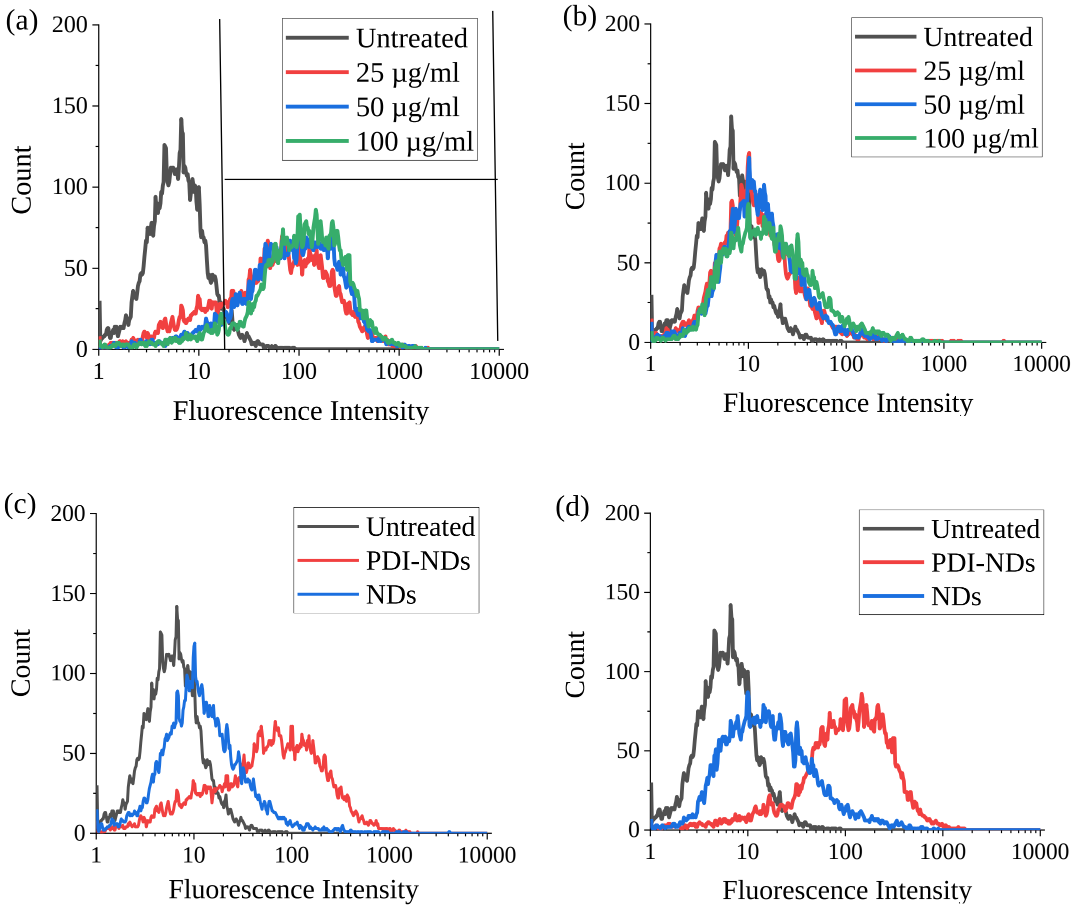

Figure 4.11: Live cell flow cytometry of MSCs in PBS labelled with various concentrations of detonation (a) PDI-NDs and (b) unmodified detonation NDs for 24 hours. The fluorescence intensity of MSCs labelled with both PDI-NDs and unmodified detonation NDs at concentrations of (c) 25 µg/ml and (d) 100 µg/ml is also shown. Fluorescence intensity was measured using FL3 filter (670 nm LP), where 10,000 events were counted, and the fluorescence gating used for all experiments is displayed in (a).

The results show an increase in fluorescence intensity for cells labelled with PDI-NDs compared to the untreated cells and this intensity increased slightly as the concentration of PDI-NDs increased (Figure 4.11a). The small increases in intensity could be due to more cells being labelled though the width of the peaks remained constant suggesting the concentration did not affect the amount of PDI-NDs taken up per cell. The change in fluorescence intensity when labelling cells with unmodified NDs was only small in comparison to untreated cells (Figure 4.11b). When comparing cells labelled with PDI-NDs and NDs, the fluorescence intensity is higher for PDI-NDs (Figures 4.11c-d)

The flow cytometry data was also represented as dot plots, shown in Figure 4.12, showing the change in the side and forward scatter of cells for unlabelled and labelled MSCs. The forward scatter indicates the size of the cell and side scatter is related to the cell complexity or granularity.[397] There is an increase in the side scatter for MSCs labelled with both PDI-NDs and unmodified NDs which suggests a change in cell granularity; this confirms that the change in fluorescence intensity is due to particle uptake.

The percentage of cells labelled cells was determined using Flowing software and the gate shown in Figure 4.11a. Any events found within this gate were counted as cells labelled with nanoparticles. When examining the percentage of cells which had been labelled with each type of particle (Figure 4.12d), >70% of the cells have taken up PDI-NDs compared to <30% with unmodified NDs at all concentrations. However, as the changes in side scatter suggest similar cell granularity for both types of particle, the differences in percentage of cells positive may be associated with the higher fluorescence of PDI-NDs compared to unmodified NDs.

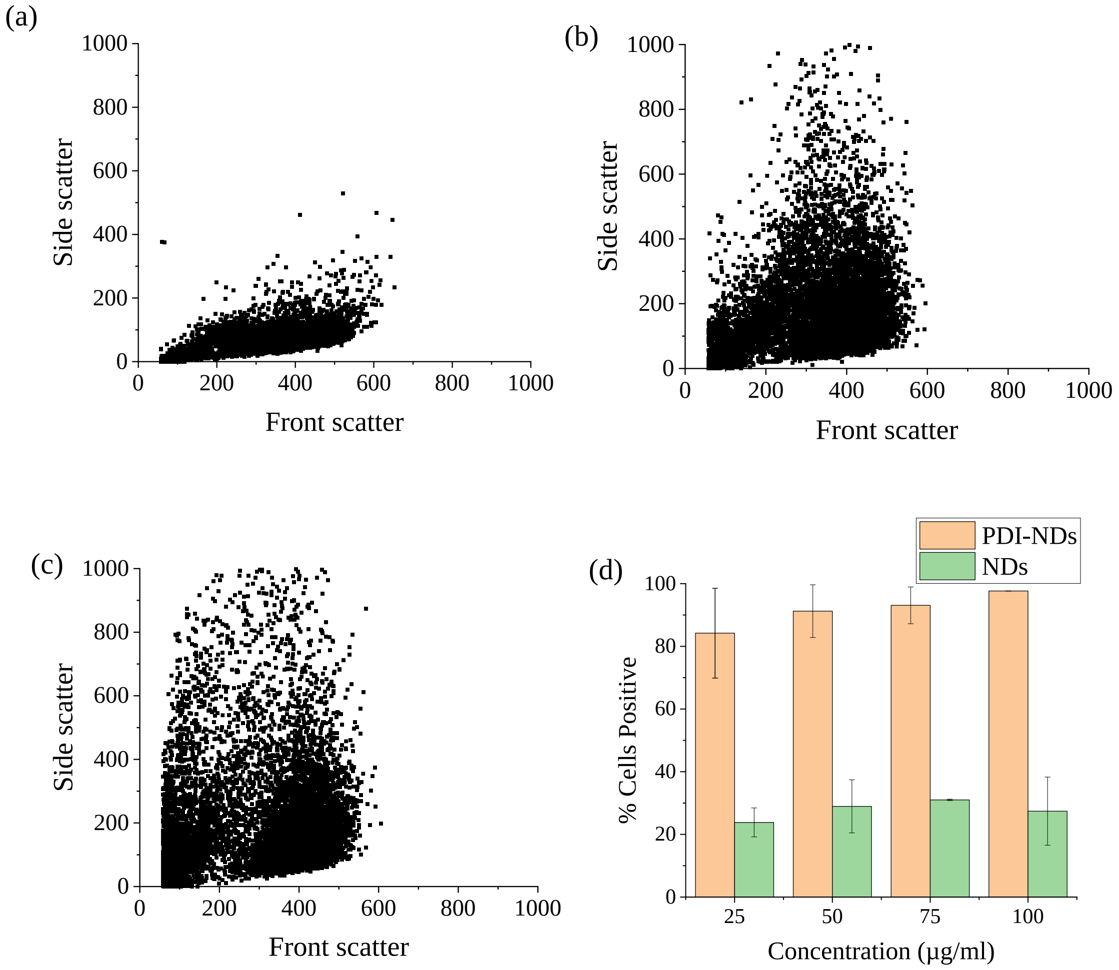

Figure 4.12: Flow cytometry dot plots showing changes in front and side scatter for (a) untreated MSCs and MSCs labelled with detonation (b) PDI-NDs and (c) unmodified detonation NDs at a concentration of 25 μg/ml. The bar chart (d) shows the percentage of cells positive with PDI-NDs and unmodified detonation NDs at various concentrations using gate shown previously in Figure 4.11a (n=2 and the error bars represent the range). Fluorescence intensity was measured using FL3 filter (670 nm LP), where 10,000 events were counted.

4.3.2.3 Assessing Cellular Uptake of Detonation PDI-NDs with Confocal Fluorescence Microscopy

Flow cytometry provided information on the proportion of fluorescent cells and degree of intensity per cell. However, confocal fluorescence microscopy was required to further assess the uptake of PDI-NDs into MSCs, as it was possible that particles could be associated with the surface rather than inside the cells. With confocal fluorescence microscopy, various planes can be imaged through the cell to confirm the internalisation and distribution of particles.

Confocal fluorescence microscopy was carried out on fixed samples after 24hr dosing. Cells were stained with DAPI and AlexaFluor® 488 phalloidin to show the nucleus (blue) and actin cytoskeleton (green), respectively. Multiple images were taken at different focal planes and combined to form z-stack images with a greater depth of field. This highlighted that particles were inside cells and not just associated with the cell surface.

Unmodified NDs could not be detected with the microscope however PDI-NDs could be visualised (red), as shown in Figure 4.13. The pattern of labelling within the cells is consistent with an endosomal location[398, 399] and it appears that the majority of cells were labelled, which agrees with the flow cytometry data where >70% of cells had taken up the particles.

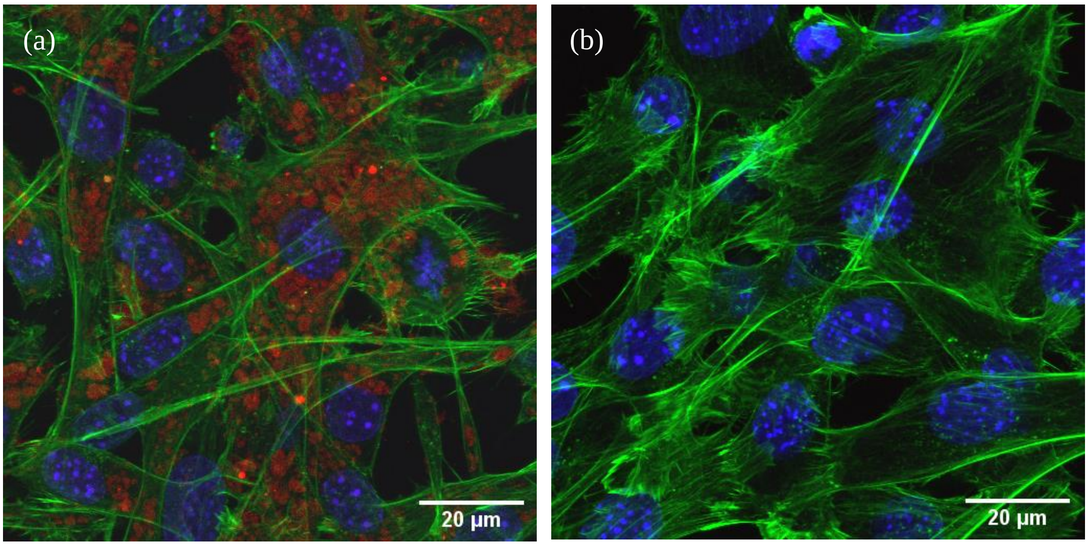

Figure 4.13: Confocal fluorescence microscope image of MSCs labelled with detonation (a) PDI-NDs and (b) unmodified detonation NDs (right). Cells were dosed at a concentration of 50 µg/ml for 24 hours and then were fixed and stained with DAPI (blue nuclei) and AlexaFluor ® 488 phalloidin (green, actin cytoskeleton). PDI-NDs can be seen in red within the MSCs. The master gain of the microscope was 800 V to increase the brightness and visualise the PDI-NDs.

The fluorescence of PDI-NDs did not appear bright, particularly when compared to the polymer-stabilised nanoparticles from chapter 2. The intensity of the 640 nm laser had to be increased in order for the PDI-NDs to be visualised, which was not the case for the polymer-stabilised nanoparticles. In addition to this, the PDI-ND aggregates can be seen clearly in Figure 4.13a.

4.3.3 PDI Conjugation to Larger NDs Prepared by HPHT

Due to the aggregation observed with detonation PDI-NDs, the PDI derivative (Figure 4.5) was also conjugated to the surface of HPHT NDs, which had been modified to have carboxylic acid surface functionality. Again, PDI-NDs were fully characterised and *in vitro* cell studies were carried out to determine their cytotoxicity, cellular uptake and fluorescence properties.

4.3.3.1 Characterisation of HPHT NDs

Due to the extreme aggregation of the detonation NDs, slightly larger NDs were investigated that had an estimated particle sizes of 50 nm. These NDs had been prepared by milling of ND powders and modified to contain carboxylic acid groups on the surface for conjugation to PDI. The carboxylation process was carried out using a well-known procedure which involved treatment of the NDs with concentrated H_2SO_4/HNO_3.[392]

The particle size was difficult to determine with SEM as the NDs were also prone to aggregation. An SEM image of COOH-NDs is shown in Figure 4.14 showing a large particle aggregate but individual NDs can be distinguished.

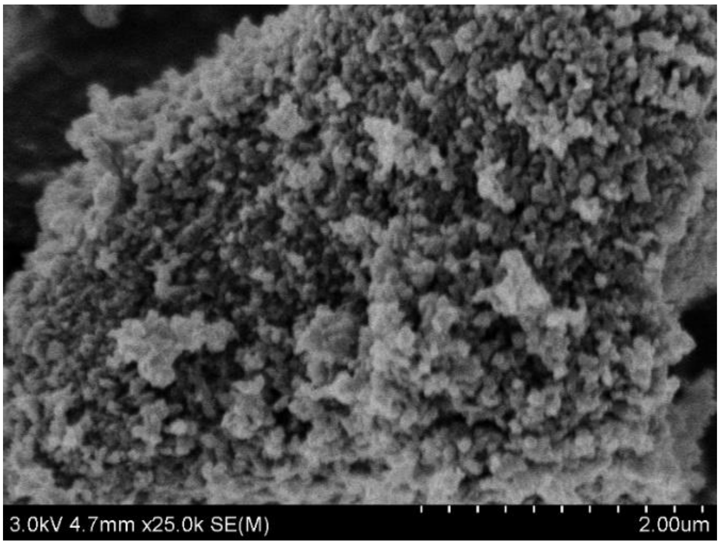

Figure 4.14: SEM image of NDs prepared by HPHT.

NDs were diluted and sonicated in an ultrasound bath ahead of DLS analysis. The measured hydrodynamic diameter of the particles was 67 ± 19 nm with a low particle size distribution of 0.065 (Figure 4.15). Hence, as there was limited aggregation in aqueous suspension, these NDs were taken forward for PDI conjugation and *in vitro* cell studies.

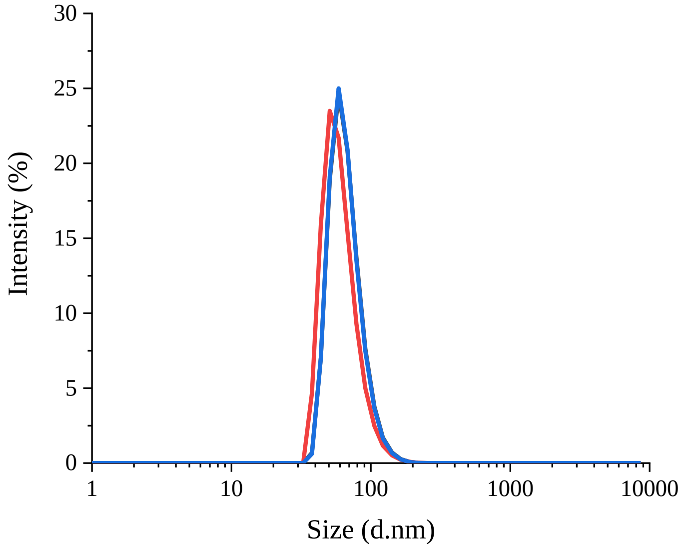

Figure 4.15: Number particle size distribution of HPHT NDs with carboxylic acid groups on the surface (0.1 mg/ml). The different colours represent 3 measurement scans with DLS.

The presence of carboxylic acid groups on the surface of the NDs was confirmed by measuring the zeta potential. COOH-NDs had a zeta potential of -57.6 ± 12.1 mV which is significantly more negative than NDs with hydrogen/hydroxyl terminating groups (-33.4 ± 6.35 mV). FTIR analysis showed broad stretches in the fingerprint region up to 1800 cm^{-1} (Figure 4.16). This is commonly seen and likely due to overlapping peaks relating to the various bonding stretches within the ND structure, e.g. C-C and those associated with NV defects.[136] Hence, the broad stretch from 1650-1850 cm^{-1} suggests that carboxylic acid groups are present on the surface.

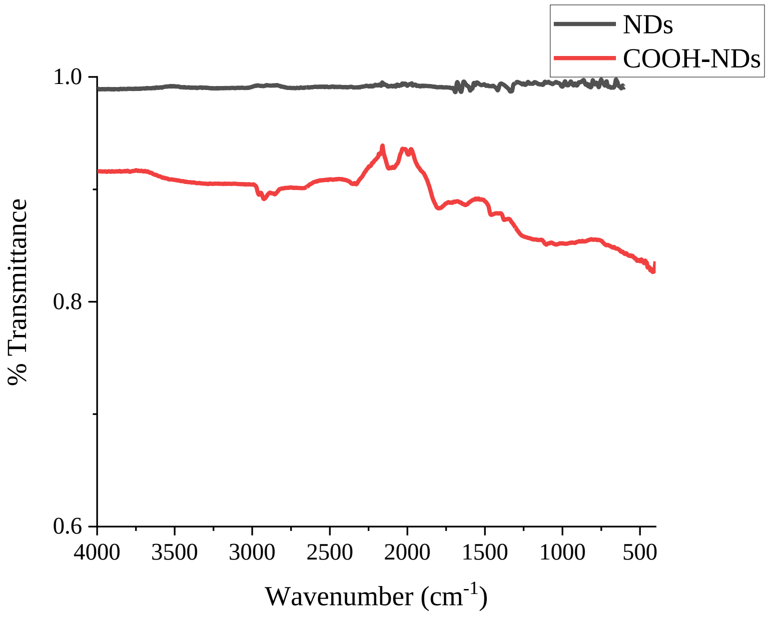

Figure 4.16: FTIR of HPHT NDs with carboxylic acid surface groups.

4.3.3.2 PDI Conjugation

PDI was attached to the surface of the COOH-NDs using the same protocol as for the detonation NDs with EDC/sulfo-NHS, only this time to form an anhydride bond rather than amide. The suspension of PDI-NDs was cloudy pink in colour compared to the grey colour of the NDs before PDI conjugation. Furthermore, after centrifugation, the supernatant was colourless suggesting PDI had been successfully attached.

The particle size distribution remained relatively consistent with the unreacted COOH-NDs at 85 ± 39 nm (Figure 4.17) and the polydispersity index was 0.136. The zeta potential was -54.3 ± 8.23 nm which was similar to without the PDI. For PDI-NDs prepared with detonation NDs with amine surface functionality, there was a decrease in zeta from +23.6 ± 9.82 mV to -19.2 ± 4.87 mV. However, in this case, as the COOH-NDs already had a negative zeta potential, it is not unusual that this did not change with the addition of PDI. The FTIR spectrum of the larger PDI-NDs (Figure 4.18) was similar to that of PDI-NDs prepared with detonation NDs; The stretch at 1580 cm^{-1} is consistent with C=C and the stretches at 1350 cm^{-1} and 1650 cm^{-1} can be associated with C=O of PDI. There is also broad absorption in the fingerprint region associated with various bonding stretches within the ND structure.

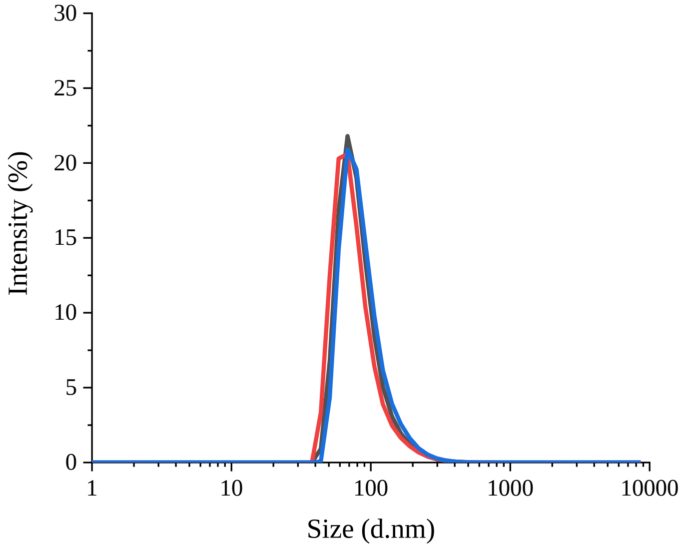

Figure 4.17: Number particle size distribution of HPHT PDI-NDs (0.1 mg/ml). The different colours represent 3 measurement scans with DLS.

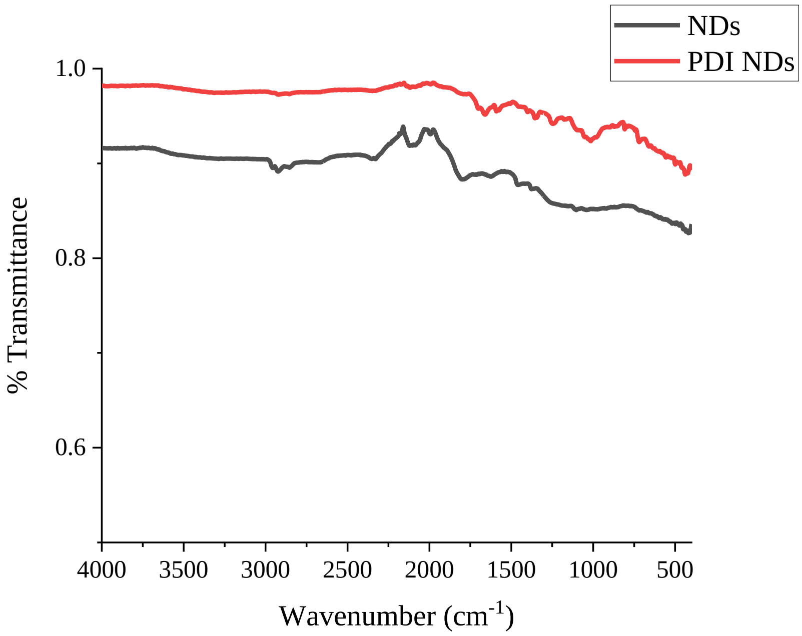

Figure 4.18: FTIR spectra of HPHT NDs and PDI-NDs.

4.3.3.3 Absorbance/Fluorescence Properties

The UV-vis absorbance profile of the larger HPHT PDI-NDs was similar to detonation PDI-NDs in that there was a large background signal due to the light scattering properties of the NDs. A slight peak can be seen around 460 nm which is similar to that of PDI alone, as shown in Figure 4.19.

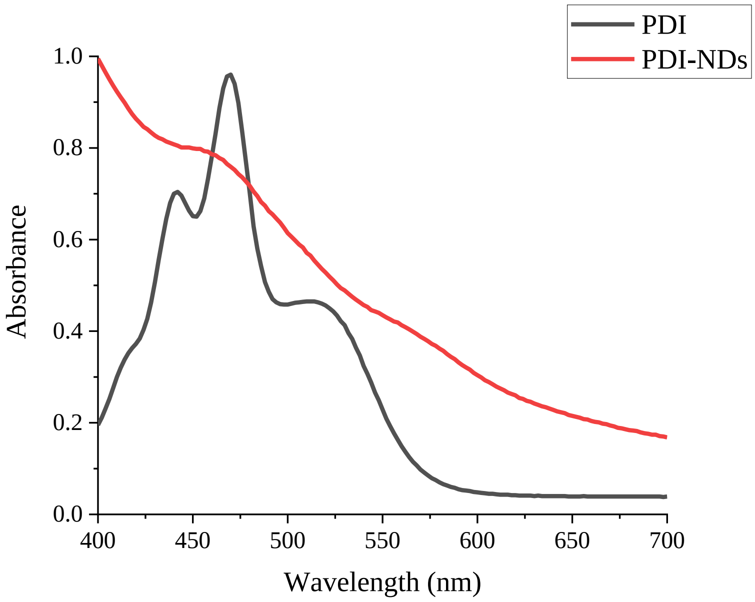

Figure 4.19: UV-vis spectra of HPHT PDI-NDs (0.1 mg/ml, water) and PDI (0.06 mM NaOH).

The fluorescence properties were also assessed using 590 nm emission filter to try and counteract the light scattering effects of the NDs. The characteristic emission peak for pure PDI is observed at 600 nm which is consistent with detonation PDI-NDs (Figure 4.20).

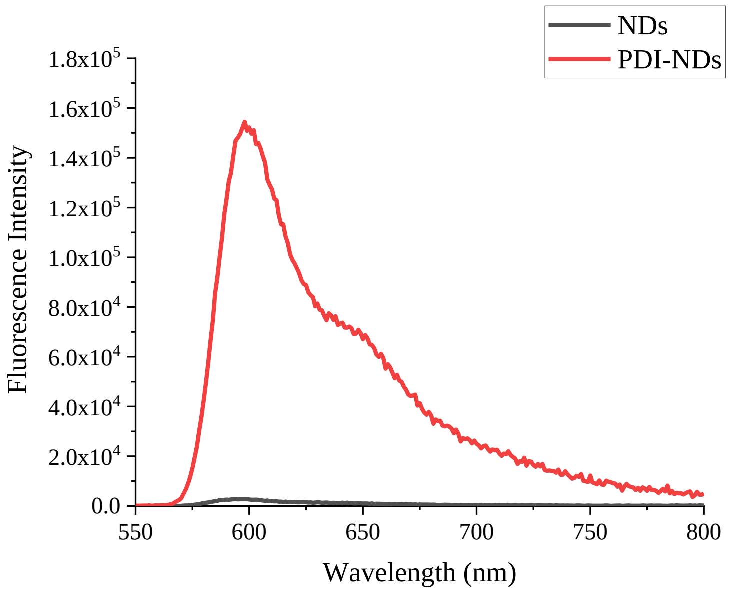

Figure 4.20: Emission spectra (λ_{ex} = 500 nm) of PDI-NDs and NDs (0.1 mg/ml water). An emission filter was used to block emission below 590 nm to counteract the effects of light scattering.

4.3.4 *In vitro* Evaluation of Larger HPHT PDI-NDs as Fluorescent Probes

4.3.4.1 The Effect of HPHT PDI-NDs on Cell Viability

The cytotoxicity of the PDI-NDs prepared from larger HPHT NDs was investigated. The same experimental protocol was used as for the detonation NDs: MSCs were seeded at a density of $2x10^4$ cells/well in a 96-well plate and left to grow and adhere for 24 hours. After this, the media was aspirated and replaced with fresh media containing various concentrations of unmodified HPHT NDs and PDI-NDs. MSCs were then incubated for a further 24 hours before carrying out the CellTiter-Glo® luminescent cell viability assay. Cell viability was measured as the amount of ATP released from treated cells as a percentage of the ATP released from the control.

Figure 4.21 shows that initially the HPHT PDI-NDs appeared to have a greater cytotoxic effect on MSCs compared to the detonation NDs. Even at a relatively low concentration of 25 µg/ml, the average cell viability decreases below 80% compared to detonation NDs where >80% viability was seen up to concentrations of 300 µg/ml (Figure 4.10). However, while viability decreased to ~75% at a concentration of 25 µg/ml, no further decrease in viability was observed as the concentration was increased to 400 µg/ml, with viability at all concentrations from 25-400 µg/ml remaining between 70-80%.

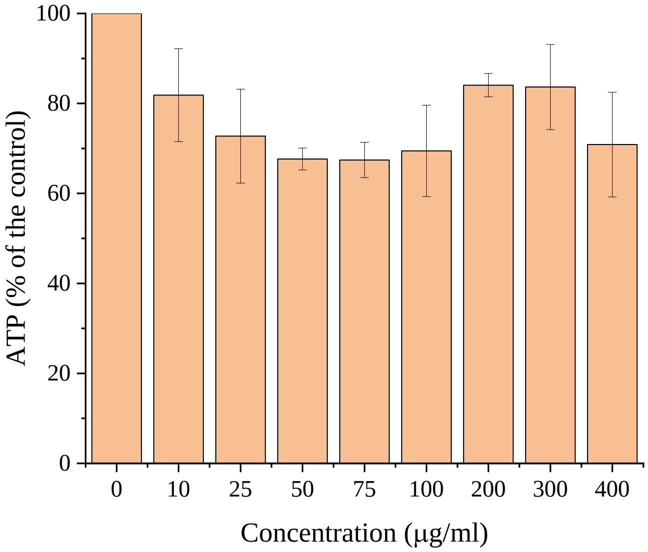

Figure 4.21: The effect of HPHT PDI-NDs on ATP production in MSCs. Cells were seeded at a density of 2x10^4 cells/well (96-well plate) and incubated for 24 hours before dosing with NDs for a further 24 hours. The error bars represent standard deviation of biological repeats (n=3).

4.3.4.2 Assessing Cellular Uptake of HPHT PDI-NDs with Flow Cytometry

Cellular uptake of HPHT PDI-NDs was assessed using flow cytometry and confocal fluorescence microscopy. Flow cytometry of cells labelled with HPHT PDI-NDs was carried out as for cells labelled with the detonation PDI-NDs. Briefly, MSCs were seeded at a density of $2x10^5$ cells/well and incubated for 24 hours ahead of dosing. The media was aspirated and replaced with fresh media containing HPHT PDI-NDs at concentrations of 25, 50 or 100 µg/ml. Flow cytometry was then carried out on live cell suspensions in PBS (10,000 cells were counted for each sample), as shown in Figure 4.22.

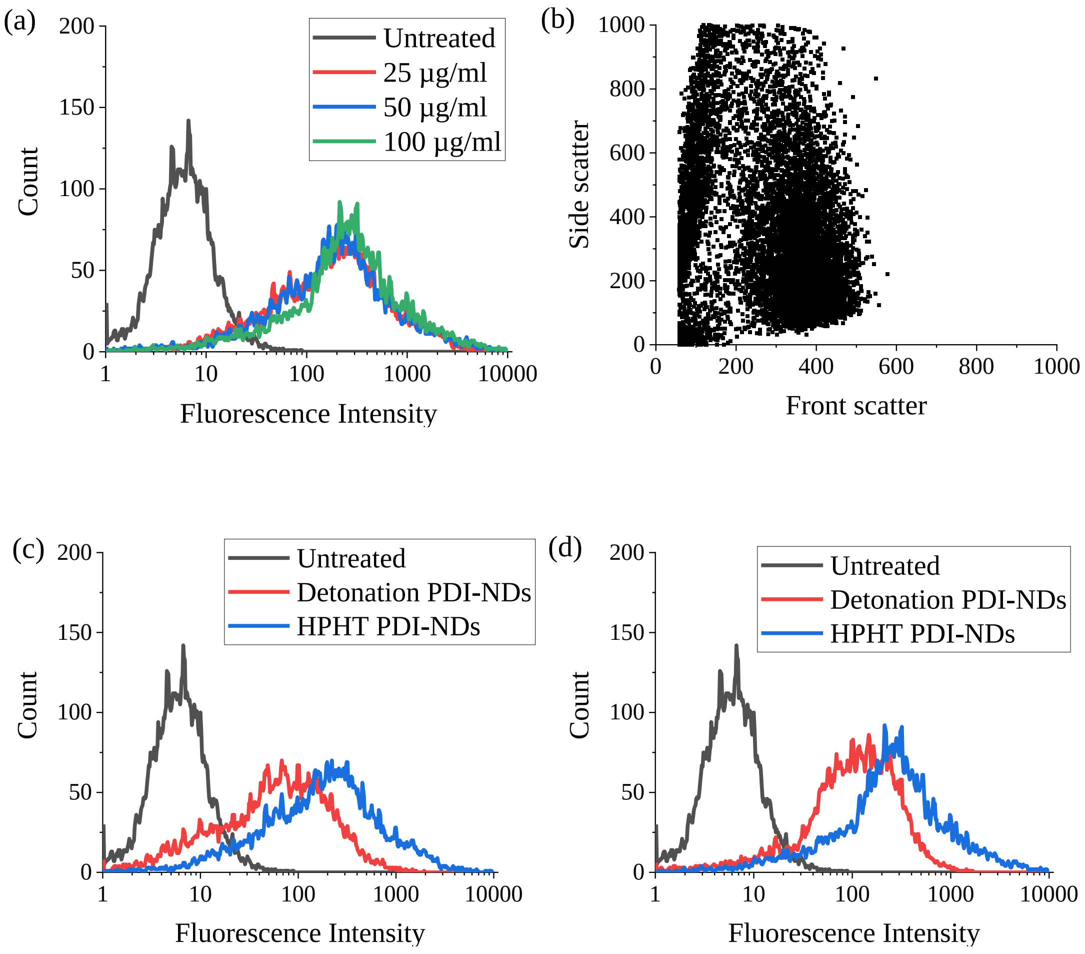

Figure 4.22: Live cell flow cytometry of MSCs in PBS labelled with HPHT PDI-NDs, where the (a) fluorescence intensity at various dosing concentrations and (b) dot plots of side scatter vs. front scatter (25 µg/ml) are displayed. The fluorescence intensity was compared to PDI-NDs prepared with detonation NDs at (c) 25 µg/ml and (d) 100

µg/ml. Fluorescence intensity was measured using FL3 filter (670 nm LP), where 10,000 events were counted.

There was an increase in fluorescence intensity for MSCs labelled with HPHT PDI-NDs compared to untreated cells suggesting that the fluorescent particles had been successfully taken up. This was also confirmed with an increase in side scatter suggesting a change in cell granularity compared to untreated cells (Figure 4.12a). The fluorescence intensity increased only slightly with increasing concentration of HPHT PDI-NDs and the peak width remained similar. Thus, it is unlikely that dosing at higher particle concentrations increased the number of particles taken up per cell. Furthermore, the percentage of the cell population that was labelled with >90% for all concentrations (Figure A16, Appendix).

The fluorescence intensity of both sets of PDI-NDs (detonation and HPHT) was compared and greater fluorescence was seen for those prepared with HPHT NDs (Figure 4.22c-d). This suggests that there is greater cellular uptake of these particles, possibly due to reduced aggregation.

4.3.4.3 Assessing Cellular Uptake of HPHT PDI-NDs with Confocal Fluorescence Microscopy

Similar to the detonation NDs, confocal fluorescence microscopy was again utilised to assess whether PDI-NDs were internalised or associated with the surface of MSCs. Imaging was carried out on fixed samples after 24hr dosing. Cells were stained with DAPI and AlexaFluor® 488 phalloidin to show the nucleus (blue) and actin cytoskeleton (green), respectively. Multiple images were taken at different focal planes and combined to form z-stack images with a greater depth of field. Figure 4.23 shows z-stack images which demonstrate that particles were inside cells and not just associated with the cell surface. The HPHT PDI-NDs (red) can be visualised within MSCs as aggregates, likely in endosomal locations. The degree of cell labelling appears to be similar to the detonation PDI-NDs, where the majority of cells were labelled.

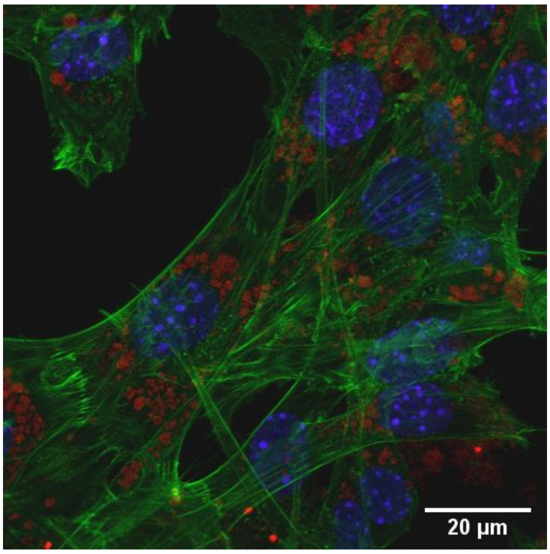

Figure 4.23: Confocal fluorescence microscope image of MSCs labelled with HPHT PDI-NDs (red). Cells were dosed at a concentration of 50 µg/ml for 24 hours and then were fixed and stained with DAPI (blue nuclei) and AlexaFluor ® 488 phalloidin (green, actin cytoskeleton). The master gain of the microscope was 800 V to increase the brightness and visualise the PDI-NDs.

4.3.5 NDs with Nitrogen-Vacancy Defects

Nitrogen-vacancy (NV) defects can be introduced into the ND structure by high energy irradiation. NV NDs were also investigated as fluorescent probes in the present study in order to compare their performance to PDI-NDs.

4.3.5.1 Characterisation of NV NDs

Two NV ND samples were evaluated which had estimated particle sizes of 40 nm (NV-40) and 90 nm (NV-90). Table 4.1 summarises the DLS measurements where the particle size was similar to the expected size (Figure 4.24) and a low polydispersity index was measured (~0.1) suggesting a narrow particle size distribution. Both NV NDs had a negative zeta potential but NV-40 was more negative. The negative zeta potential of the particles is expected due to hydrogen or hydroxyl terminating groups from the synthesis. The difference in zeta potential between the NV NDs can be explained by considering the particle sizes; zeta potential is calculated from electrophoretic mobility which is size-dependent.

Table 4.1: DLS analysis of NV NDs.

ND sample	Expected particle size (nm)	Number particle size distribution (nm)	Polydispersity index	Zeta potential (mV)
NV-40	40	39 ± 11	0.11	-46 ± 1
NV-90	90	63 ± 21	0.13	-35 ± 1

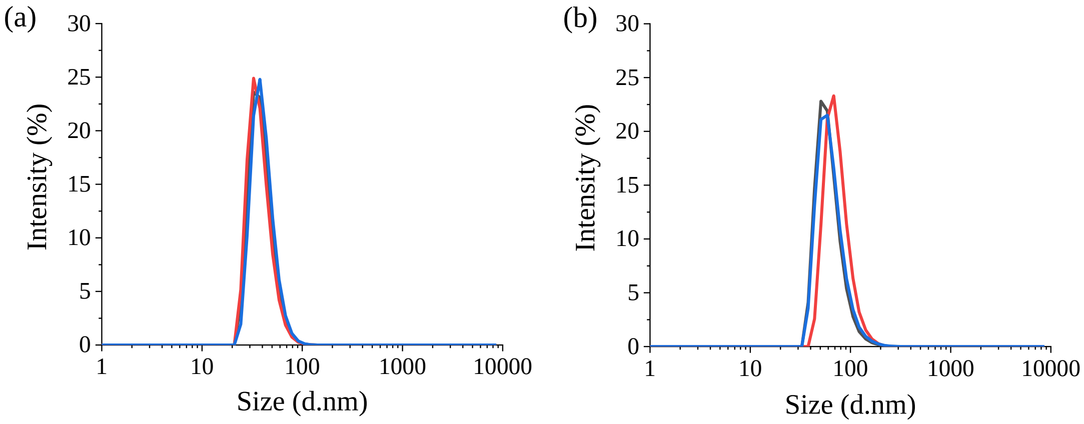

Figure 4.24: Number particle size distribution of (a) NV-40 and (b) NV-90 NDs (0.1 mg/ml). The different colours represent 3 measurement scans with DLS.

The absorption properties were investigated with UV-vis spectroscopy. However, as for detonation NDs, the light scattering effects of the NDs were apparent. Figure 4.25 shows the absorption profile of the NV NDs, where greater light scattering is seen for the larger NV-90 NDs.

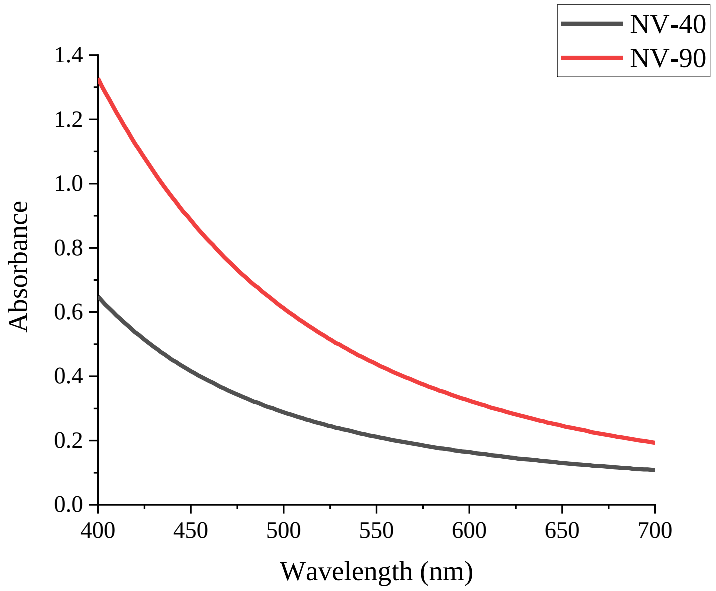

Figure 4.25: UV-vis spectra of NV NDs (water, 0.1 mg/ml).

The fluorescence properties of the NV NDs are shown in Figure 4.26. The light scattering properties of the NDs proved to be an issue again and so a filter was added to block emission below 590 nm. This enabled the detection of the peak associated with NV^- at ~700 nm, which was more pronounced for NV-90 NDs (Figure 4.26b); these results agree with similar experiments in the literature.[400] NDs without NV defect were also analysed using the same excitation wavelengths and only background signal was observed (Figure A17, Appendix).

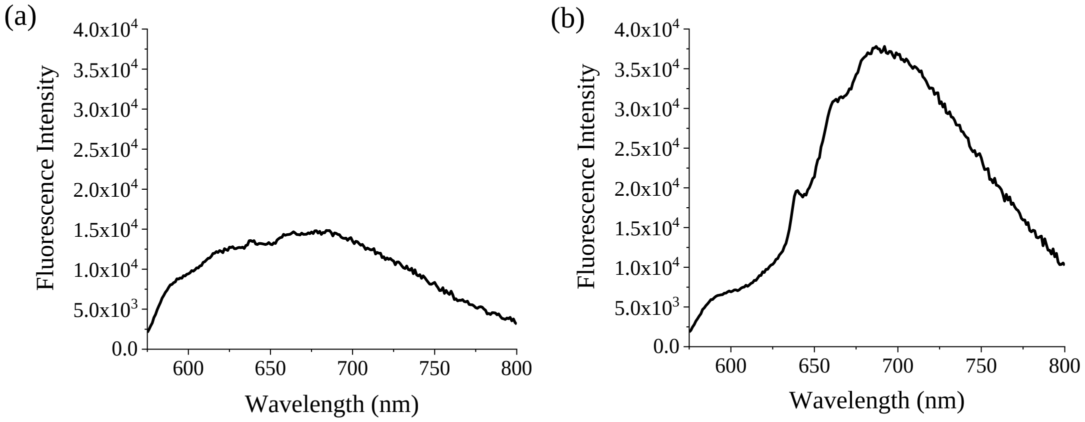

Figure 4.26: Emission spectra (λ_{ex} = 560 nm) for (a) NV-40 and (b) NV-90 NDs (0.1 mg/ml water). An emission filter was used to block emission below 590 nm to counteract the effects of light scattering.

4.3.6 *In vitro* Evaluation of NV ND as Fluorescent Probes

4.3.6.1 The Effect of NV NDs on Cell Viability

The CellTiter-Glo® assay was carried out to see whether NV NDs had an effect on the viability of MSCs. The protocol was carried out in the same way as for PDI-NDs. Previously, concentrations of up to 300 µg/ml were well-tolerated by MSCs for detonation and HPHT PDI-NDs. For the NV NDs, cell viability decreased with increasing concentration and NV-40 NDs appeared to have a greater cytotoxic effect than NV-90 NDs, as shown in Figure 4.27. The HPHT PDI-NDs had >80% viability at 200 µg/ml which is in line with the NV-90 which have a similar particle size. Cell viability remained >70% for both sets of NV NDs at all dosing concentrations.

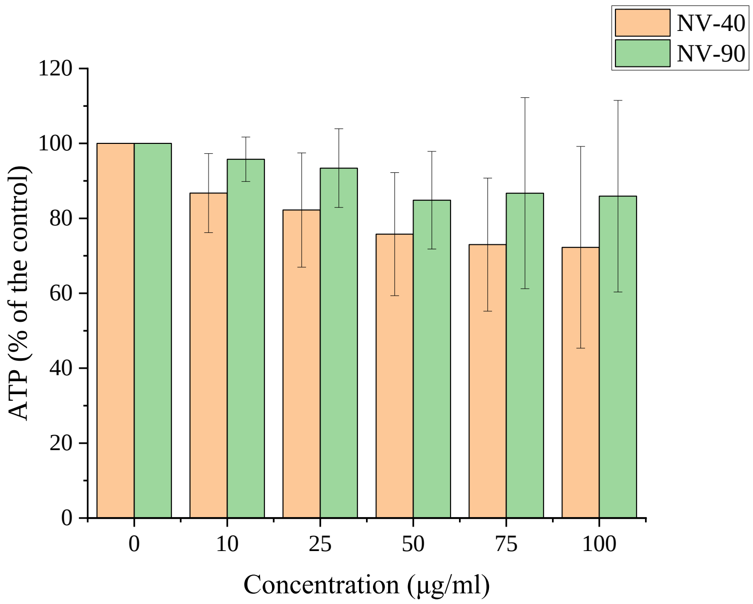

Figure 4.27: The effect of NV NDs on ATP production in MSCs. Cells were seeded at a density of 2×10^5 cells/well for 24 hours, NDs were then incubated with MSCs for a further 24 hours ahead of measuring ATP. The error bars represent the range (n=2).

In order to ascertain whether the greater cytotoxic effect of NV-40 NDs was due to particle size or number, the assay was repeated and cells were dosed by number of NV NDs rather than mass concentrations. The number of NDs was calculated using the average density of commercial NDs (3.5 g cm^{-1}),[401, 402] where 1.8×10^{10} particles correlates to approximately 10.7 µg/ml. Figure 4.28 highlights that NV NDs had a similar effect on cell viability when similar particle numbers were used, hence suggesting that the increased cytotoxicity of NV-40 NDs observed previously was due to the cells being exposed to a greater number of particles. Therefore, it is likely that more particles were taken up by the MSCs to cause the reduced viability.

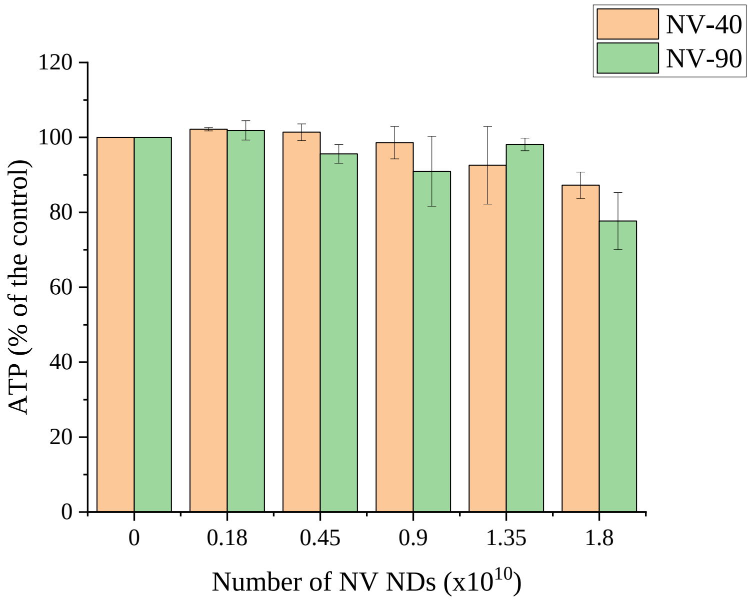

Figure 4.28: The effect of NV NDs on ATP production in MSCs. Cells were seeded at a density of 2×10^4 cells/well for 24 hours, NDs were then incubated with MSCs for a further 24 hours ahead of measuring ATP. The error bars represent the range (n=2).

4.3.6.2 Assessing Cellular Uptake of NV NDs with Flow Cytometry

Flow cytometry was used to assess the uptake of NV NDs into MSCs. As for PDI-NDs, MSCs were incubated with NV NDs for 24 hours ahead of flow cytometry on live cell suspensions in PBS. With both types of NV NDs there was an increase in fluorescence intensity with increasing ND concentrations; however, this was less pronounced with NV-40 NDs, as shown in Figure 4.29. More specifically, as the concentration was increased, the mean fluorescence intensity increases which suggests that the percentage of the population that is fluorescent has also increased.

The difference between NV-40 and NV-90 NDs was more obvious when comparing the percentage of cells positive with NDs in a bar chart (Figure 4.30). The percentage of labelled cells increased with increasing concentrations for both sets of ND; however, following labelling with NV-90 NDs, a greater proportion of the MSC population became fluorescent. Above 50 μg/ml, >80% of the cell population were labelled with NV-90 NDs.

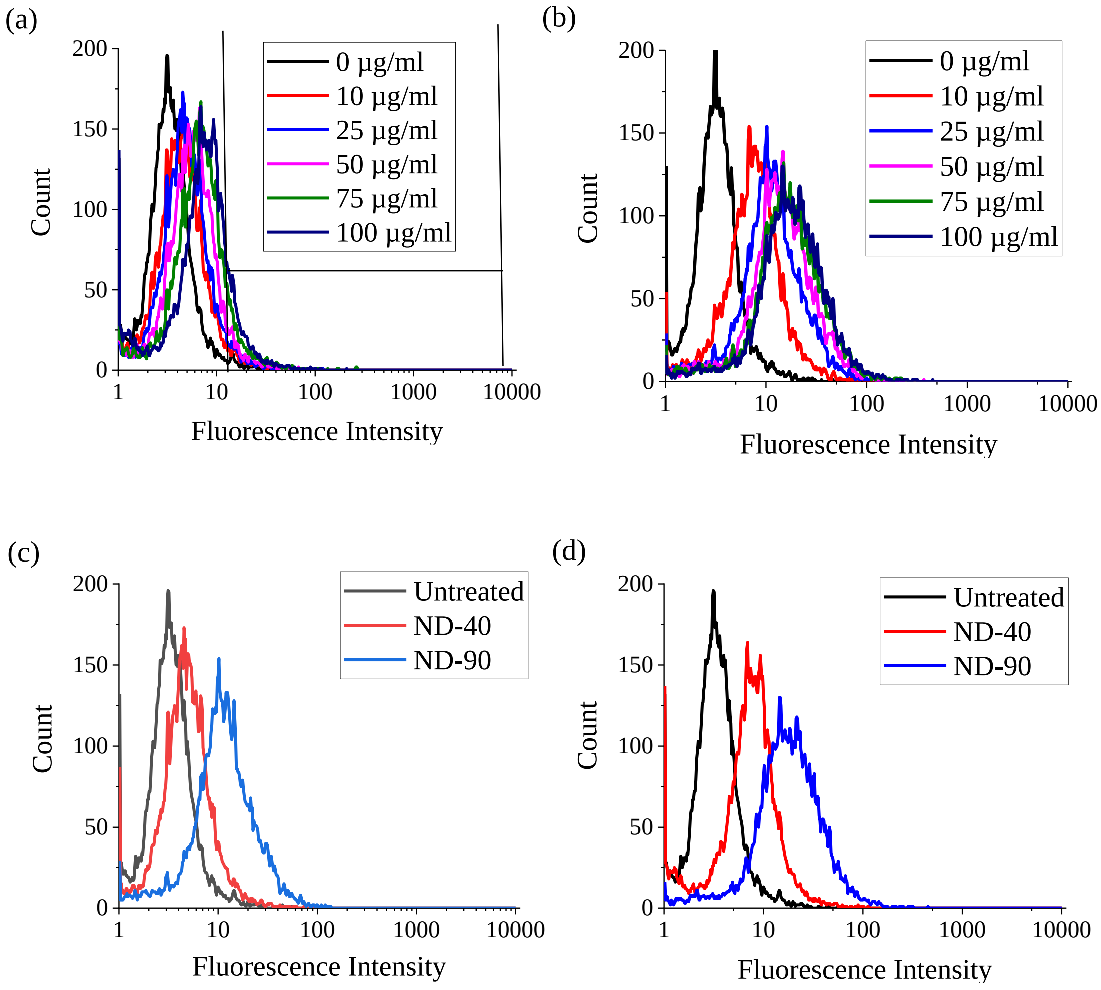

Figure 4.29: Live cell flow cytometry of MSCs in PBS labelled with various concentrations of (a) NV-40 and (b) NV-90 NDs for 24 hours. The fluorescence intensity of MSCs labelled with both NV NDs at concentrations of (c) 25 μg/ml and (d) 100 μg/ml is also shown. Fluorescence intensity was measured using FL3 filter (670 nm LP), where 10,000 events were counted, and the fluorescence gating used for all experiments is displayed in (a).

.

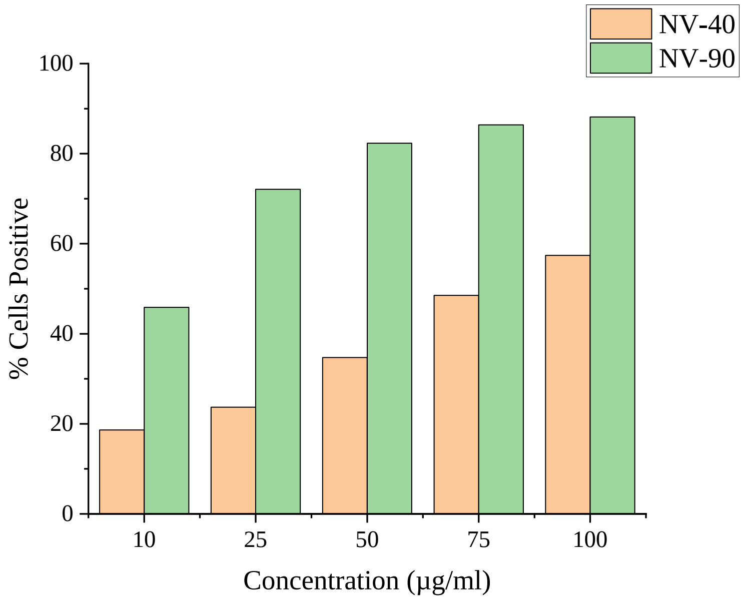

Figure 4.30: Comparison of the percentage of cells positive with various concentrations of NV-40 and NV-90 NDs using gate shown in Figure 26a. Fluorescence intensity was measured using FL3 filter (670 nm LP), where 10,000 events were counted.

Following the cytotoxicity results, which highlighted differences when MSCs were dosed based on mass concentration and estimated number of NDs, a flow cytometry experiment was carried out on MSCs which had been dosed with various estimated numbers of NV NDs. In this case, there was very little change in fluorescence intensity between untreated cells and those dosed with various numbers of NV-40 NDs, as shown in Figure 4.31. The difference to the mass-based dosing is likely because $1.8x10^{10}$ particles correlates to approximately 10.7 µg/ml. However, for NV-90 NDs, fluorescence intensity increased with increasing number of NDs.

When comparing the percentage of cells positive, uptake of NV-90 NDs increased with increasing number of NDs (Figure 4.32). At the highest number ($1.8x10^{10}$), >40% of cells had taken up NV-90, which is consistent with the equivalent mass-based dosing concentration of ~10 µg/ml. The flow cytometry data suggests that NV-90 NDs have more intense fluorescence than NV-40 NDs. Higher numbers of NV-40 NDs were required to see increases in fluorescence intensity and even then, it was not as high as NV-90 NDs.

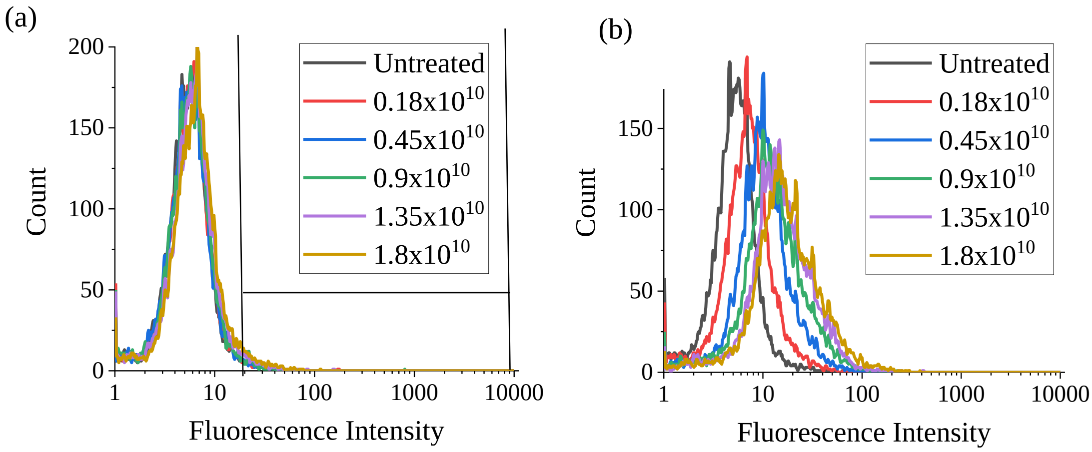

Figure 4.31: Live cell flow cytometry of MSCs in PBS labelled with various numbers of (a) NV-40 and (b) NV-90 NDs for 24 hours. Fluorescence intensity was measured using FL3 filter (670 nm LP), where 10,000 events were counted, and the fluorescence gating used for all experiments is displayed in (a).

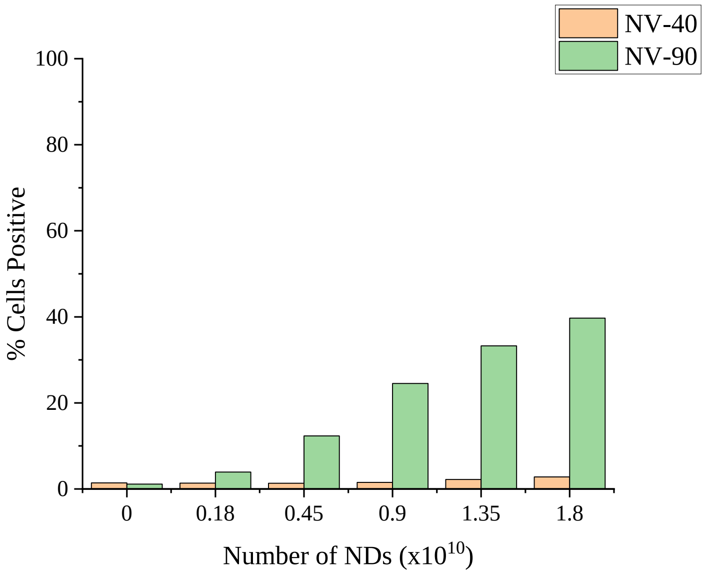

Figure 4.32: Comparison of the percentage of cells positive with various numbers of NV-40 and NV-90 NDs using gate shown in Figure 28. Fluorescence intensity was measured using FL3 filter (670 nm LP), where 10,000 events were counted.

4.3.6.3 Assessing Cellular Uptake of NV NDs with Confocal Fluorescence Microscopy

As for other flow cytometry experiments, 2×10^4 cells were seeded into chamber slides and left to grow and adhere for 24 hours ahead of dosing with NDs (100 µg/ml). Cells were subsequently fixed and stained with DAPI and AlexaFluor® 488 phalloidin to show the nucleus and actin cytoskeleton, respectively. ND-90 NDs were much more abundant and brighter compared to NV-40 NDs when imaged at the same laser intensity (Figure 4.33). This is particularly significant, as for the same mass concentration, there would be much more NV-40 NDs exposed to the cells compared with NV-90 NDs. Hence, the more effective visualisation of the NV-90 NDs is likely attributed to more intense fluorescence, which is consistent with the flow cytometry analysis (Figure 4.29).

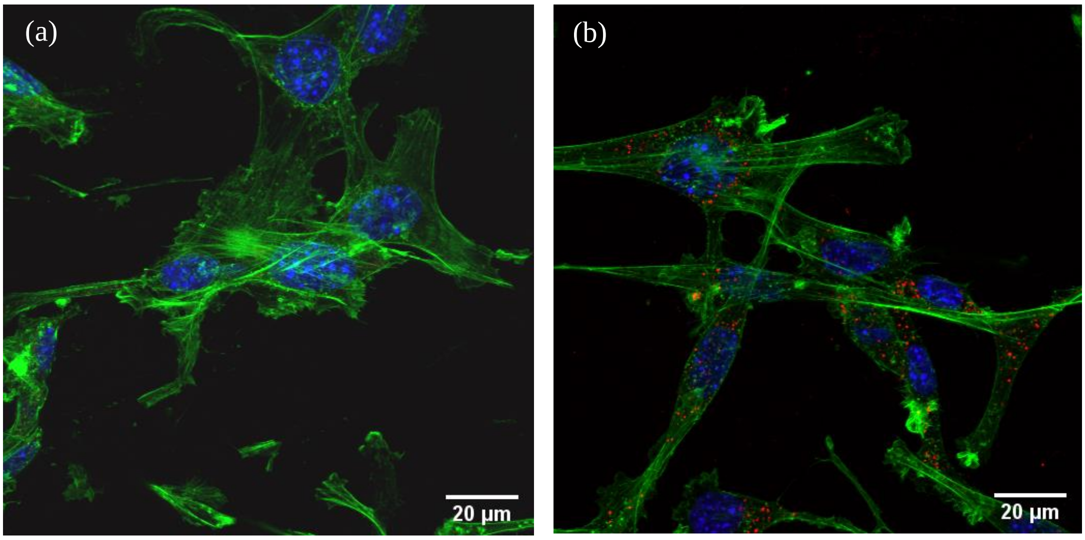

Figure 4.33: Confocal fluorescence microscope images of MSCs dosed with (a) NV-40 and (b) NV-90 NDs. MSCs were seeded in chamber slides (2×10^4 cells/well) and left to grow and adhere for 24 hours before dosing with 100 µg/ml ND for a further 24 hours. Cells were fixed with 4% PFA and stained with DAPI (blue) and AlexaFluor® 488 (green); NDs are seen in red.

When comparing NV NDs to PDI-NDs, a lower laser intensity was required to image NV NDs suggesting PDI-NDs have relatively weaker fluorescence. Furthermore, the staining pattern observed in Figure 4.33 shows NV NDs as small spherical particles rather than the aggregates observed for PDI-NDs (Figure 4.23).

4.4 Discussion

Two types of fluorescent ND were evaluated in this study: NDs functionalised with an organic fluorophore and NDs with NV defects. The NV NDs have been widely studied in the literature as fluorescent probes for various biomedical applications.[142, 384] One major disadvantage is the high cost associated with forming the NV centres and hence an alternative way to enhance the optical properties of NDs would be to harness the ease of surface modification of NDs. Three types of ND were provided by Element 6 Ltd. for this study: fluorescent NV NDs (40 nm and 90 nm) and non-fluorescent NDs prepared by either detonation (5-10 nm) or HPHT (50 nm).

The non-fluorescent NDs were first characterised with SEM and DLS to investigate particle size. Detonation NDs were found to be their expected particle size of 5-10 nm using TEM (Figure 4.2). However, when analysing the aqueous ND suspension with DLS, a particle size of just under 2000 nm and a high polydispersity index of 0.152 was measured. This suggests that that NDs exist mainly as aggregates in aqueous medium. Aggregation of detonation NDs is a problem widely observed in the literature and hence larger HPHT NDs were also investigated in this study.[375, 376]

The HPHT NDs used in this study were found to be ~70 nm with DLS and had a low polydispersity index of 0.065. The particle size was slightly larger than expected and can be explained by the knowledge that DLS measures hydrodynamic diameter; HPHT NDs had a negative zeta potential (-57.6 ± 12.1 mV) due to the carboxylic surface functionality which is likely to affect the hydration shell. SEM of HPHT NDs suggested these NDs were also prone to aggregation (Figure 4.14).

FTIR spectroscopy was used to confirm the presence of amino groups and carboxylic acid groups on the detonation and HPHT NDs, respectively (Figure 4.4 and 4.16).

Broad absorption was observed in the fingerprint region up to ~1800 cm^{-1} which is characteristic of NDs.[136] The absorption can be explained by overlapping stretches due to the many bonding stretches present in the NDs structure. The amino and carboxylic acid groups were utilised for carbodiimide coupling to the fluorescent dye, PDI.

4.4.1 PDI Conjugation to Detonation NDs

A fluorescent PDI derivative has absorbance in the visible region and was used in order to optimise the probe. The detonation NDs had been provided with amino groups on the surface for carbodiimide coupling to the free carboxylic acid groups in the PDI derivative. EDC and Sulfo-NHS were employed to improve the efficiency of the coupling reaction, particularly because of their good solubility in water which is ideal for the biomedical applications of the probes.[403, 404]

The coupling experiment was carried out in basic water (0.06 mM NaOH) due to the limited solubility of the PDI derivative in neutral water.[391] Although neutral pH is optimal for EDC, the basic pH was necessary for solubilising the PDI derivative. Sulfo-NHS was included to improve reaction efficiency by reducing the formation of the stable *N*-acylurea side product, as shown in Figure 4.34. Firstly, the PDI derivative containing the carboxylate functionality was mixed with EDC/sulfo-NHS to form the amine reactive sulfo-NHS ester which can then go on to react with the amino groups on the NDs surface. The reaction was carried out at room temperature and left overnight for amide formation. PDI-NDs were then washed with centrifugation to remove EDC/sulfo-NHS and resuspended in neutral water. The supernatant from centrifugation had no absorbance in the visible spectrum and hence suggested PDI was successfully attached, rather than still dissolved in the basic water. The resultant product was a cloudy, pink PDI-NDs suspension.

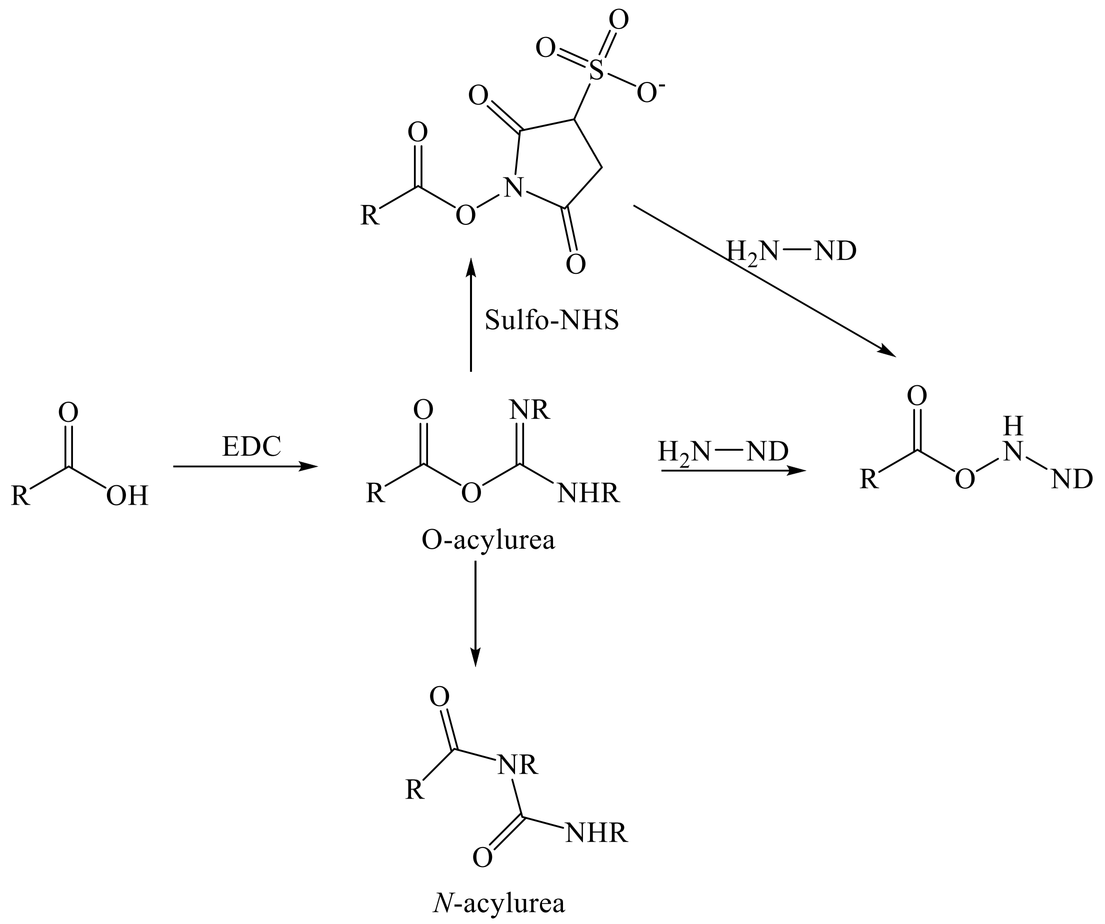

Figure 4.34: Schematic of the reaction of EDC to form an amide showing the production of unfavourable side product, *N*-acylurea, and alternative reaction pathway with sulfo-NHS.[393] The same reaction scheme occurs if another carboxylic acid is introduced instead of an amine; this time to form an anhydride

Focussing first on the detonation NDs, the attachment of PDI was confirmed with FTIR where stretches could be seen which corresponds to the carboxylic acid groups and aromatic structure of PDI (Figure 4.6), as well as a new peak associated with amide bond (1650 cm^{-1}). There was also stretches associated with free amine groups however the zeta potential significantly decreased from +23.6 ± 9.82 mV for the unmodified NDs to -19.2 ± 4.87 mV, indicating a reduction in the amount of free amino groups on the surface. The PDI-NDs still appeared to aggregate as the particle size remained ~2000 nm in DLS, as discussed in Figure 4.7.

UV-vis spectrometry and fluorescence analysis also suggested the presence of PDI, as small peaks could be seen which correspond to the wavelengths associated with PDI alone. It should be noted that the absorbance/fluorescence data is not ideal due to the high refractive index (RI) of NDs resulting in significant scattering.[137, 387] Peaks at 470 and 500 nm can be seen in the UV-vis spectrum (Figure 4.8) and an emission peak 600 nm were observed after excitation at 500 nm (Figure 4.9). These wavelengths are consistent with that of free PDI. Hence, despite the stability issues, the probes were taken forward for *in vitro* cell studies, as the optical properties appeared promising. Furthermore, the high biocompatibility reported in the literature suggested NDs will be well-tolerated by cells, despite the aggregation.[135]

The murine MSC cell line was used for *in vitro* studies, where cells were labelled by incubation with media containing particles for 24 hours. NDs and PDI-NDs had a limited cytotoxic effect in MSCs up to concentrations of 300 μg/ml. This is consistent with the literature where the high biocompatibility of NDs in various cell lines has been demonstrated.[135-137] The conjugation of PDI did not affect cell viability which suggests the centrifuge washes were effective in removing EDC/sulfo-NHS. The concentration of 300 μg/ml is particularly high, especially compared to polymer-stabilised PDI nanoparticles prepared in Chapter 2 where cell viability decreased below 80% at a labelling concentration of 20 μg/ml (Figure 2.22).

Flow cytometry and confocal fluorescence microscopy were then used to assess cellular uptake as it was possible that the low cytotoxic effect could be attributed to limited uptake, particularly as DLS suggested NDs existed predominantly as large aggregates. MSCs were labelled with NDs and PDI-NDs for 24 hours and flow cytometry was carried out on live cell suspensions in PBS. The MSCs labelled with PDI-NDs exhibited increased fluorescence at 670 nm compared to untreated MSCs

(Figure 4.11). Cells labelled with unmodified NDs showed a slight increase in fluorescence but it was not as noteworthy as with the PDI-NDs. Both PDI-NDs and unmodified NDs showed very little change in fluorescence intensity with increasing dosing concentrations and the width of the peaks did not change; this suggests that increasing the dosing concentration did not affect the amount of NDs taken up per cell.

During the flow cytometry experiment, there was a change in the laser side scatter between the untreated cells and both PDI-NDs and unmodified NDs (Figure 4.12). Side scatter is related to cell granularity, which is an indication of cellular uptake thus suggesting that the cells had taken up both unmodified NDs and PDI-NDs. It is also worth noting that the high RI of NDs may also affect laser scattering. The side scatter was similar for PDI-NDs and unmodified NDs which suggests that there was a similar amount of cellular uptake for both sets of particles. The difference in fluorescence intensity but similar side scatter suggests that PDI-NDs have greater fluorescence at 670 nm than unmodified NDs.

Confocal fluorescence microscopy was also carried out to visualise the PDI-NDs within the cells. PDI-NDs could be visualised in the majority of cells, which is consistent with the flow cytometry data where >80% of cells had taken up particles at 100 µg/ml however unmodified NDs were not visible. PDI-NDs could only be visualised within cells when the 640 nm laser intensity was increased. Hence, the fluorescence is relatively low compared to polymer-stabilised nanoparticles in Chapter 2. This could be partly due to a lower PDI concentration (MSCs were dosed based on the overall mass concentration of PDI-NDs) but also the light scattering effects of the ND aggregates may have an effect.

4.4.2 PDI Conjugation to HPHT NDs

Although the detonation NDs had low cytotoxicity, the aggregation was not ideal. Hence, larger NDs prepared by milling of larger HPHT diamond powders were investigated. Carboxylic acid groups were introduced to the NDs surface using an acid treatment which has been widely employed in the literature.[392, 405, 406] A negative zeta potential (-57.6 ± 12.1 mV) was measured for COOH-NDs which confirmed the presence of carboxylic acid groups which exist as COO^- groups in aqueous medium. This is significantly more negative than NDs with hydrogen/hydroxyl terminating groups which had a zeta potential of -33.4 ± 6.35 mV. FTIR also showed a broad stretch from 1650-1850 cm^{-1} which is indicative of carboxylic acid functionality, likely amongst other overlapping peaks due to the ND structure.[136]

PDI was then conjugated to the surface using the exact same method as for the detonation NDs only this time to form an anhydride, rather than an amide bond. The PDI-NDs were washed by centrifugation to remove EDC/sulfo-NHS and resuspended in neutral water to form a cloudy pink suspension. The basic water supernatant did not have absorption in the visible region suggesting PDI had attached to the NDs.

PDI conjugation was also confirmed with FTIR, where peaks at 1580, 1350 and 1650 cm^{-1} were observed which can be attributed to C=O and aromatic C=C bonds in the PDI (Figure 4.18). In this case, a peak associated with a new anhydride bond could not be located however FTIR broad absorption was seen from in the fingerprint region up to ~1700 cm^{-1}. This is a common occurrence for NDs due to overlapping peaks associated with the various bonding stretches within the ND structure.[136] The zeta potential was ~-57 mV for both the PDI-NDs and unmodified NDs. For the detonation NDs, a decrease in zeta potential had been observed which suggested a reduction in the amount of free amino groups. However, in this case, it is not unexpected that the zeta potential remained similar as the carboxylic acid groups in the unmodified NDs are likely to exist as COO^- in aqueous suspension. The particle size and polydispersity index of PDI-NDs remained relatively unchanged compared to the unmodified HPHT NDs.

Light scattering effects resulted in broad absorption in the UV-vis spectrum for HPHT PDI-NDs, similarly to detonation NDs. A shoulder in the absorption profile occurs around 470 nm, which is consistent with the peak absorption for PDI. There was also fluorescence at 600 nm in the emission spectrum of HPHT PDI-NDs which further proved that PDI conjugation was successful. Therefore, the particles were taken forward for *in vitro* cell studies.

MSCs were labelled with HPHT PDI-NDs for 24 hours, in the same way as for the detonation PDI-NDs. It initially appeared that HPHT PDI-NDs were slightly more cytotoxic than the detonation PDI-NDs as the average cell viability dipped below 80% at some of the lower concentrations, however the standard deviation was quite high. Cell viability did not decrease with increasing dosing concentrations and >80% viability was observed at 200 and 300 µg/ml.

Cellular uptake was assessed using flow cytometry and confocal fluorescence microscopy. The flow cytometry was carried out in the same way as with the detonation PDI-NDs. The fluorescence intensity at 670 nm increased compared to the untreated cells; however, increasing the dosing concentration only moved the peak slightly (Figure 4.22). Cellular uptake was also confirmed from seeing a change in cell granularity by measuring the side scatter compared to untreated MSCs. When comparing the detonation and HPHT NDs, it appeared that HPHT PDI-NDs had greater fluorescence intensity. This could be due to increased cellular uptake or brighter fluorescence, both of which may be attributed to less particle aggregation.

Confocal fluorescence microscopy enabled the visualisation of the HPHT PDI-NDs within MSCs. The degree of labelling seemed similar to that of detonation NDs (~80%); this may mean that the cellular uptake is similar but the fluorescence of HPHT PDI-NDs is stronger. As for the detonation PDI-NDs, the laser intensity has to be increased in order to visualise the HPHT PDI-NDs. This was not the case for the polymer-stabilised nanoparticles from Chapter 2 and so NV NDs were investigated to see if they had a stronger fluorescent signal for cell tracking.

4.4.3 NV NDs

Despite the higher cost, NDs with NV defect were evaluated for comparison with PDI-NDs. NV ND with expected particle sizes of 40 nm (NV-40) and 90 nm (NV-90) were obtained from Element 6 Ltd. The particle size was confirmed by DLS and the low polydispersity index (~0.1) for both samples indicated an even particle size distribution. The zeta potential of both NDs was negative; however, NV-40 was more negative which can be explained by the fact that the measurement is derived from electrophoretic mobility which is size-dependent. In addition to this, there has long since been an issue with standardising ND synthesis and so many of the properties of NV NDs vary. This is due to the large number of factors which influence the defects, such as particle size, the percentage of graphitic form of carbon, surface functionality, ND density and RI of the layers.[138] Hence, the difference in zeta potential could be related to the number of NV centres near the surface.

The absorption properties of the NV NDs were investigated with UV-vis spectroscopy (Figure 4.25). The light scattering properties were evident which is consistent with data reported in the literature and can be explained by the knowledge that NDs have high RI of 2.42.[137, 387]. For the PDI-NDs, the peak absorption of the PDI could be identified however there were no peaks in the NV NDs UV-vis spectra. NV NDs usually have absorbance at ~560 nm which corresponds to emission at ~700 nm, a characteristic of the major defect (NV^-) which can be seen in Figure 4.26.[373] Following this result, the optical properties were later assessed in cells to explore this further.

Similarly, NV NDs were evaluated in *in vitro* cell studies to assess cytotoxicity (ATP assay), labelling efficiency (flow cytometry) and intracellular localisation (confocal fluorescence microscopy). Both NV-40 and NV-90 NDs appeared to be slightly more cytotoxic than PDI-NDs; however, cell viability remained >70% at all concentrations (up to 100 µg/ml, shown in Figure 4.27). It was found that cell viability decreased with increasing concentrations and it appeared that NV-40 NDs were more cytotoxic. This was investigated further by dosing MSCs by ND number rather than mass concentration, which was estimated based on an approximate density of 3.5 g cm^{-3} for commercial NDs and assuming perfect spherical morphology.[401, 402] In this case, it was found that NV-40 and NV-90 NDs had a similar effect on cell viability suggesting that the amount of NDs, rather than the particle size, caused the cytotoxic effect. Much higher cell viability was seen in this experiment, compared with mass concentration dosing, as the numbers of NDs used did not reach the higher dosing concentrations previously ($1.8x10^{10}$ NDs = ~10 µg/ml).

Flow cytometry showed greater increases in fluorescence intensity and a higher percentage of fluorescent cells when MSCs were dosed with NV-90 NDs (Figure 4.29). At the highest concentration of 100 µg/ml, 88% and 57% of the cell population were labelled with NV-90 and NV-40 NDs, respectively. When comparing MSCs dosed with different numbers of NDs, rather that mass concentration, MSCs dosed with NV-40 NDs displayed negligible fluorescence. When cells were labelled with 1.8×10^{10} NV-90 NDs, >40% cell uptake was observed, which is consistent with equivalent mass-based dosing concentration of 10 µg/ml. The flow cytometry results from dosing by ND numbers suggested that NV-90 NDs had stronger fluorescence.

The NV NDs were subsequently visualised in MSCs using confocal fluorescence microscopy. NV-90 NDs could be seen in the majority of cells whereas NV-40 NDs were more difficult to see (Figure 4.33). There are two possible reasons for this difference: either fewer NV-40 NDs are taken up by cells or they emit lower levels of fluorescence. It is most likely the latter as for confocal imaging, MSCs were dosed at 100 µg/ml so there should be more NV-40 NDs than NV-90 NDs. In addition to this, cellular uptake has been observed for all NDs in this study and is widely reported in the literature. Therefore, it is likely that NV-40 NDs emit lower levels of fluorescence than NV-90 NDs. This statement agrees with the literature as larger NDs tend to have more NV defects.[372]

4.5 Conclusion

A selection of NDs have been evaluated as fluorescent probes: PDI-NDs (detonation and HPHT) and NV NDs (NV-40 and NV-90). NV-90 NDs have shown to be superior to the smaller NV-40 NDs in terms of fluorescence intensity, cellular uptake and cytotoxicity. Additionally, NV-90 performed better than non-irradiated NDs and PDI-NDs.

Non-irradiated NDs have weak fluorescence intensity due to the fewer number of NV centres. PDI-NDs, prepared by attaching PDI fluorophore to the surface of non-irradiated NDs, were prepared as it was thought it would provide a cheaper alternative to NV NDs. However, the processing of small NDs results in significant aggregation which could not be combatted by surface modification in the present study. Initially, it appeared that HPHT NDs would be less prone to aggregation than detonation NDs; however, NV-90 NDs still performed better in flow cytometry and aggregates of HPHT NDs could be seen in confocal images. Future work could involve functionalising the surface of NDs with stabilisers, such as PEG.[378]

The results herein suggest that NV NDs of 90 nm size can be used as effective fluorescent probes for the tracking of MSCs. Other common fluorescent probes, such as other carbon-based materials and quantum dots (QD), rely on surface coatings to reduce cytotoxicity. The high fluorescence of the 90 nm NV NDs, in combination with the capacity for high dosing due to the inherent biocompatibility, pose 90 nm NV NDs as promising candidates for many biomedical applications; particularly for determining the fate and biodistribution of administered cells using fluorescent imaging techniques. Furthermore, these particles could be used for tracking cells in organoids *in vitro* and detecting administered cells *ex vivo* using fluorescence microscopy.

Despite this, there are still further challenges which will need to be met in order to see clinical translation of ND probes. Even though ND-90 had the best performance, this study has highlighted the difficulties in working with NDs, specifically when characterising surface chemistry and preventing reaggregation. Furthermore, the scalability of ND synthesis and the irradiation process to achieve NV defects is not fully developed.[407]

Chapter 5: General Discussion and Perspectives

The aim of the present work was to investigate the use of perylene diimide (PDI) based nanoparticles in cell and hydrogel tracking. Regenerative medicine therapies (RMT) have great potential as treatments for a variety of diseases and injuries however clinical translation is hindered by lack of safety and efficacy data.[20, 44] Encapsulation of RMTs in protective hydrogels can increase cell survival by providing a scaffold for cell growth; this is particularly relevant in the treatment of spinal cord injury (SCI) where hydrogels can increase local retention and prevent cell sedimentation.[33, 34] Herein, PDI nanoparticles have been investigated for their ability to label mesenchymal stromal cells (MSC) and their encapsulating collagen hydrogels for cell and hydrogel tracking *in vivo* with multispectral optoacoustic tomography (MSOT). Furthermore, PDI has also been combined with nanodiamonds to assess their biocompatibility and performance as fluorescent probes.

PDI stands out as an excellent candidate for designing photoacoustic (PA) probes due to its high molar extinction coefficient meaning that it can be detected by both photoacoustic imaging (PAI) and fluorescence imaging. Furthermore, PDI exhibits extremely high photostability, setting it apart from other small molecule dyes such as cyanine dyes. In the present study, a near-infrared (NIR) absorbing PDI derivative was prepared following well-established procedures from commercially available perylene-3,4,9,10-tetracarboxylic dianhydride, (PTCDA). A brominated PTCDA derivative was first prepared using a protocol from Sengupta *et al*.[237] Following this, the diimide was formed and the bay bromine substituents were substituted for pyrrolidine groups as reported by Sukul *et al*.[236] This resulted in a red-shift to the NIR region with peak absorbance at 710 nm. The synthesis was carried out successfully on a larger scale to yield enough NIR PDI for all experiments; each step of the procedure was fully characterised with ^{1}H NMR, FTIR and UV-vis spectroscopy.

NIR PDI was then used to prepared nanoparticles for cell and hydrogel labelling. A nanoprecipitation method was employed as a simple route to prepare stable nanosuspensions. This method took advantage of the hydrophobicity of NIR PDI, dissolving first in acetone before adding to water in the presence of a stabiliser. Two polymer stabilisers were investigated: our novel star hyperbranched block copolymer (SHBP) and poly(vinyl alcohol) (PVA).[275] All nanoparticles prepared with SHBP stabiliser had a particle size of ~150-170 nm and PVA nanoparticles were sized slightly smaller at ~115 nm; both of which were suitable for cell labelling.

The NIR absorbance of the PDI nanoparticles was confirmed by UV-vis spectroscopy and MSOT of the nanoparticle solutions in phantoms. Absorbance at 710 nm was observed in both UV-vis spectroscopy and MSOT and the nanoparticle solutions could be effectively visualised with MSOT when irradiated at 710 nm. PDI nanoparticles were then used to label MSCs by incubating cells with the nanoparticles over a 24hr period. The CellTiter-Glo® assay was carried out and it was observed that PDI nanoparticles were well-tolerated by MSCs up to a concentration of 15 μg/ml for all batches; however, when the ratio of PDI:SHBP was varied, it was found that higher amounts of stabiliser resulted in a decrease in cell viability. PVA-stabilised nanoparticles had a limited cytotoxicity up to the highest dosing concentration (40 μg/ml).

The cellular uptake of PDI nanoparticles was assessed with flow cytometry and confocal fluorescence microscopy. All PDI nanoparticles were efficiently taken up by MSCs and the highest uptake was seen for PDI-SHBP nanoparticles with a PDI:SHBP ratio of 1:1. PDI nanoparticles could also be visualised inside MSCs using confocal fluorescence microscopy and the pattern of labelling was consistent with endosomal location. The PDI nanoparticles predominantly existed as small, spherical nanoparticles although some rod-like structures were observed in both confocal fluorescence microscopy and scanning electron microscopy (SEM). This effect was independent of the type or amount of stabiliser used and is more likely to be associated with experimental parameters in the nanoprecipitation method, for example, the rate of addition of PDI/stabiliser or the rate of solvent evaporation. Future work could investigate this further by gaining greater control over the rate of solvent addition (i.e. automation) however it was out of the scope of the present study. Furthermore, the rod-like structures were in the minority compared to those of spherical morphology and they did not appear to affect the viability of the cells.

The results in Chapter 2 have demonstrated a straightforward route for preparing NIR-absorbing PDI nanoparticles. These particles exhibit high absorbance at 710 nm and can be efficiently detected with MSOT. Moreover, the nanoparticles are efficiently taken up by MSCs with limited cytotoxic effect at a labelling concentration of 15 μg/ml. PDI nanoparticles with SHBP stabiliser (PDI: SHBP 1:1) stand out due to having the most efficient cellular uptake and these particles have also been explored in rodent models previously in our group.[274] In the present study, PVA-stabilised PDI nanoparticles were also identified as viable candidates for cell tracking as although cellular uptake was slightly lower, these particles had a limited cytotoxic effect up to a dosing concentration of 40 μg/ml. The tuneability and photostability of the PDI, coupled with the ease of nanoparticle preparation and limited toxicity are key advantages that PDI nanoparticles have over other probes on the market such as gold nanoparticles, QDs and cyanine dyes.[245]

The PDI nanoparticles (PDI:SHBP 1:1 and PVA) were also investigated for their ability to label encapsulating hydrogels (Chapter 3). Collagen constructs were prepared following a well-established procedure as collagen is a component of the extracellular matrix (ECM) and has previously been applied to SCI.[32] MSCs were included in the collagen premix to enable cell encapsulation during the gelation procedure. Collagen gelation was initiated by both pH and temperature; NaOH was added to the collagen (previously stored in acetic acid solution) and the gels were incubated at 37 °C (previously stored on ice). The incorporation of MSCs caused a contraction of the collagen gel which is a phenomenon widely observed in the literature.[42, 339] PDI nanoparticles were also included in the gel premix in order to label the gels.

The MSCs had been engineered to express luciferase and hence cell viability could be determined by measuring the bioluminescent signal after the addition of luciferase. A signal could be observed in all of the gels 1-week post-synthesis, although cell viability was generally lower in gels labelled PVA-stabilised nanoparticles. There was no bioluminescent signal from the control gels containing nanoparticles but no cells, thus confirming the signal was associated with cells and not nanoparticles. The total flux of each gel could be quantified which highlighted that overall, there was greater flux at 1 week for unlabelled gels and gels labelled with PDI-SHBP nanoparticles thus suggesting the cells were viable and proliferating. For gels labelled with PDI-PVA nanoparticles, signal was relatively low or decreased from 1 day to 1 week which suggested that these nanoparticles had a cytotoxic effect when incorporated into gels. The experiments also highlighted that cells remained inside the gels for 1 week and did not migrate out to the well.

The gels were then analysed with MSOT to check that the PDI nanoparticles could effectively provide contrast in the gels. It was found that SHBP-stabilised nanoparticles had greater MSOT signal in gels compared to PVA-stabilised nanoparticles. This result was unusual as MSOT of the nanoparticle suspensions produced similar MSOT signal. The difference could be due to the fact that the MSOT only images one slice of the gels and it is not known whether PDI nanoparticles are homogenous throughout the gel. Furthermore, for both sets of gels, the MSOT signal was lower at 1-week compared to 1-day. Both of these observations suggested nanoparticles were leaching from the gels and it was possible that the extent of leaching was more pronounced for PVA-stabilised nanoparticles. This may be associated with the knowledge that SHBP is a more complex, branched polymer with hydrophilic and hydrophobic regions and thus may have more of an interaction with the amphoteric collagen compared to the simpler linear PVA chains.[274, 275, 408, 409]

The leaching was investigated in an experiment where gels were prepared in 96-well plates and moved to a new well every few days and fluorescence imaging was carried out after 1 week. A fluorescent signal was observed for all gels that contained nanoparticles but only background signal was observed for the MSC control gel without nanoparticles; this confirmed that the nanoparticle fluorescent signal was being detected. Fluorescence was also observed in all the wells that had previously contained a labelled gel thus showing that the nanoparticles leach from the gels. When this was quantified as the total flux of each well, the amount of fluorescent signal in each well was similar and it was difficult to quantify the extent of leaching for each nanoparticle concentration. Future work should investigate this further by dialysing the gels and taking UV-vis spectroscopy measurements of the surrounding medium.

The SHBP-stabilised PDI nanoparticles could effectively label collagen hydrogels and be detected with MSOT and hence can be used to track gel fragmentation in the short term; however, the labelled constructs would need to be optimised for longer studies to monitor hydrogel degradation over time. Future work should look to optimise the constructs to limit nanoparticle leaching; studies in the literature have shown that increasing collagen concentration will decrease the pore size of the gel thus limiting space for diffusion of molecules.[342, 343] This will need to be carefully considered in order to avoid compromising cell viability in the gels. An alternative option would be to modify the PDI nanoparticles to increase the interaction with the collagen, for example by increasing electrostatic interactions or by covalent conjugation.[341, 408]

In a separate study (Chapter 4), a different red PDI derivative was attached to the surface of nanodiamonds (NDs). This red PDI derivative was used in order to optimise the probes with the idea that the protocols could be applied to NIR PDI in the future. Furthermore, the high fluorescence of the red PDI derivative combined with the high biocompatibility of NDs is ideal for tracking cells in organoids *in vitro* and detecting administered cells *ex vivo* using fluorescence microscopy. The performance of the PDI-NDs was compared to commercially available fluorescence NDs with nitrogen-vacancy (NV) defects. NV NDs have been explored for fluorescence imaging applications however a major drawback is the cost associated with the high energy processes required to produce the defects.[142]

PDI was conjugated to the surface of detonation NDs and milled high-pressure high-temperature (HPHT) NDs *via* carbodiimide coupling. This produced pink cloudy suspensions where changes in the FTIR spectra and measured zeta potential indicated PDI attachment. The optical properties of the NDs also confirmed PDI attachment as peaks associated with PDI could be identified; however, the light scattering effect of the NDs was apparent. When measuring the particle size distribution of the detonation NDs, particle sizes of ~2000 nm were measured suggesting severe aggregation, which is consistent with detonation NDs in the literature.[375, 376] Hence why HPHT NDs were also investigated which had a particle size of ~70 nm and NV NDs with particle sizes of 40 nm (NV-40) and 90 nm (NV-90) were also explored. Analysis of the fluorescence properties of NV NDs identified emission peaks associated with the NV^- defect.[400]

All of the NDs were assessed *in vitro* for labelling of MSCs. Extremely low cytotoxicity was observed for all PDI-NDs, where >80% of cells were viable at dosing concentrations of up to 300 µg/ml. When comparing to PDI nanoparticles from Chapter 2, where cell viability decreased >20 µg/ml, there is a huge difference and hence highlights the high biocompatibility of NDs.[135] For NV NDs, the highest labelling concentration was 100 µg/ml where the cell viability was >70% for all concentrations. It appeared that NV-40 NDs were more cytotoxic however further experiments of dosing by number rather than mass concentration suggested that this was due to a higher number of NDs and not a particle size effect.

The cellular uptake of the NDs was assessed with flow cytometry and confocal fluorescence microscopy. For PDI-NDs, increases in fluorescence intensity and side scatter of cells (related to cell granularity) suggested the particles had been taken up. There was a slight increase for unmodified NDs suggesting good cellular uptake however the low fluorescence here suggested the attachment of PDI increased fluorescence in cells labelled with PDI-NDs. The increase in fluorescence intensity was greater for HPHT PDI-NDs compared to detonation PDI-NDs which may be due to greater uptake or brighter fluorescence, both of which can be associated with less particle aggregation. For NV NDs, NV-90 NDs showed greater increases in fluorescence intensity and a higher percentage of cells fluorescent compared to NV-40 NDs, this is consistent with the literature where larger NDs have more NV defects.[372]

Confocal fluorescence microscopy was carried out on MSCs which had been labelled with NDs and subsequently fixed and stained. PDI-NDs could be visualised within MSCs however the excitation laser had to be increased which was not the case for NV NDs; this suggested the fluorescence of PDI-NDs was relatively weak. NV-90 NDs exhibited bright fluorescence in MSCs however NV-40 NDs were more difficult to visualise which can be attributed to their weaker fluorescence.

Overall, the findings of Chapter 4 suggest that NV-90 NDs can be used as effective fluorescent probes for labelling of MSCs as they have limited cytotoxicity, good cellular uptake and bright fluorescence. The study also highlighted the potential for the use of HPHT PDI-NDs however optimisation would be required to stabilise these NDs and increase PDI loading. Once optimised, NIR PDI could be attached to the surface using the same protocols and the probes could be utilised in cell tracking with MSOT. Moreover, the extremely high biocompatibility demonstrated herein suggest PDI-NDs could be used for labelling cells for *ex vivo* fluorescence microscopy; the use of high dosing concentrations could counteract problems associated with signal dilution upon cell division.[142] This poses NDs as a great alternative to common fluorescent probes, such as metal-based QDs, where surface coatings are required to prevent toxicity.[121] Furthermore, the extremely low toxicity of the NDs stands out from other carbon-based materials, such as graphene, MWCNTs, fullerene and carbon dots, making NDs ideal for the present application.[359]

5.1 Conclusion

In conclusion, PDI derivatives hold great promise for the design of novel probes for cell tracking with MSOT and fluorescence imaging. MSOT can be used for the tracking of administered cells and encapsulating hydrogels in rodent models where one of the key advantages is the ability to spectrally unmix the signals amongst multiple endogenous and exogenous absorbers. The versatility of PDI derivatives is therefore highly advantageous for MSOT, as a library of PDI derivatives with different absorption profiles have been synthesized. Two PDI nanoparticle systems have been investigated herein: PDI nanoparticles by nanoprecipitation (Chapter 2) and PDI-NDs (Chapter 4). The nanoprecipitation method stands out as a facile way to prepare PDI-based probes where different PDI derivatives could be used to prepare probes for simultaneous cell and hydrogel tracking with MSOT.

We have previously published a study for tracking of MSCs in rodent models with PDI nanoparticles (Chapter 2);[274] however, the hydrogel construct explored in Chapter 3 will need further optimisation to prevent nanoparticle leaching and enable longitudinal tracking of hydrogel integrity. Furthermore, the present work has shown that combining PDI with NDs (Chapter 4) will enable high dosing concentrations due to the biocompatibility of the NDs and hence future work should look into stabilising these particles against aggregation. NDs could be used as a versatile PDI-based probe for MSOT which could also be used for *ex vivo* fluorescence microscopy; moreover, the surface chemistry of NDs is widely explored to enable conjugation of other contrast agents, thus posing NDs as an interesting candidate for designing multimodal probes.[388, 389] Whilst PDI nanoparticles prepared by nanoprecipitation perform the best in the present study, particularly due to high MSOT signal and limited aggregation, further optimisation could also present PDI-NDs as viable candidates for cell tracking.

5.2 Future Work

At present, the labelled collagen gels are being tested *in vivo* in our group to investigate cell viability and MSOT signal in rodent models. Future work on this project should aim to investigate the stability and homogeneity of the nanoparticles in the gel, and look to prevent nanoparticle leaching by increasing the interaction of the PDI nanoparticles with the collagen matrix. This could include looking at altering the surface charge of the nanoparticles for increasing electrostatic attraction with the collagen, or alternatively increasing the collagen concentration could decrease the pore size hindering diffusion of the nanoparticles. Another route could look at covalently attaching the PDI nanoparticles to the collagen however all of these options will need to carefully consider the effect on cell viability.

Further work could also be carried out to optimise the PDI-NDs by increasing the surface loading of PDI and confirming that the PDI does not come off the surface of the NDs with time. It would also be beneficial to investigate other functional groups which could be introduced to the surface to prevent aggregation. Once the particles have been optimised in terms of signal and stability, a NIR-absorbing PDI derivative could be synthesized with appropriate functional groups for conjugation to the ND surface. These probes could then be investigated for use in *in vivo* PA imaging and *ex vivo* fluorescence microscopy in rodent models to obtain preclinical data, such as information about biodistribution and nanoparticle clearance.

On a final note, the design of novel probes for cell and hydrogel tracking will improve our understanding of the mechanisms and biodistribution of administered cell-based RMTs. In turn, having more safety and efficacy data will aid the design and support the clinical translation of RMTs. In order to obtain as much information as possible, a multi-pronged approach is needed. Hence, combing PA probes with cells expressing bioluminescent or fluorescent reporter genes would provide information from multiple imaging modalities. Moreover, the design of multimodal probes is also of great interest in the field of regenerative medicine.

Bibliography

1. A. S. Mao and D. J. Mooney, *Proc. Natl. Acad. Sci. U. S. A.*, 2015, **112**, 14452-14459.
2. A. Golchin and T. Z. Farahany, *Stem Cell Rev. Rep.*, 2019, **15**, 166-175.
3. R. S. Mahla, *Int. J. Cell Biol.*, 2016, **2016**, 6940283-6940283.
4. G. Kolios and Y. Moodley, *Respiration*, 2013, **85**, 3-10.
5. J. P. Vacanti, J.-B. Otte and J. A. Wertheim, in *Regenerative Medicine Applications in Organ Transplantation*, eds. G. Orlando, J. Lerut, S. Soker and R. J. Stratta, Academic Press, Boston, 2014, pp. 1-15.
6. A. S. Wayne, K. Baird and R. M. Egeler, *Pediat. Clin. N. Am.*, 2010, **57**, 1-25.
7. B. Wernly, M. Mirna, R. Rezar, C. Prodinger, C. Jung, B. K. Podesser, A. Kiss, U. C. Hoppe and M. Lichtenauer, *Int. J. Mol. Sci.*, 2019, **20**, 13.
8. P. A. Murray and A. S. Woolf, *Curr. Opin. Organ Transplant*, 2014, **19**, 140-144.
9. J. Marcheque, B. Bussolati, M. Csete and L. Perin, *Stem Cells Transl. Med.*, 2019, **8**, 82-92.
10. O. Lindvall, Z. Kokaia and A. Martinez-Serrano, *Nat. Med.*, 2004, **10**, S42-S50.
11. J. A. Thomson, J. Itskovitz-Eldor, S. S. Shapiro, M. A. Waknitz, J. J. Swiergiel, V. S. Marshall and J. M. Jones, *Science*, 1998, **282**, 1145.
12. G. R. Martin, *Proc. Natl. Acad. Sci. U. S. A.*, 1981, **78**, 7634-7638.
13. C. Brown, C. McKee, S. Bakshi, K. Walker, E. Hakman, S. Halassy, D. Svinarich, R. Dodds, C. K. Govind and G. R. Chaudhry, *J. Tissue Eng. Regen. Med.*, 2019, **13**, 1738-1755.

14. M. F. Pittenger, D. E. Discher, B. M. Péault, D. G. Phinney, J. M. Hare and A. I. Caplan, *NPJ Regen. Med.*, 2019, **4**, 22.

15. A. Andrzejewska, B. Lukomska and M. Janowski, *Stem Cells*, 2019, **37**, 855-864.

16. B. Lukomska, L. Stanaszek, E. Zuba-Surma, P. Legosz, S. Sarzynska and K. Drela, *Stem Cells Int.*, 2019, **2019**, 9628536.

17. M. Patrikoski, B. Mannerström and S. Miettinen, *Stem Cells Int.*, 2019, **2019**, 5858247.

18. J. Sharkey, L. Scarfe, I. Santeramo, M. Garcia-Finana, B. K. Park, H. Poptani, B. Wilm, A. Taylor and P. Murray, *Eur. J. Pharmacol.*, 2016, **790**, 74-82.

19. A. S. Lee, C. Tang, F. Cao, X. Xie, K. van der Bogt, A. Hwang, A. J. Connolly, R. C. Robbins and J. C. Wu, *Cell Cycle*, 2009, **8**, 2608-2612.

20. J. A. Heslop, T. G. Hammond, I. Santeramo, A. T. Piella, I. Hopp, J. Zhou, R. Baty, E. I. Graziano, B. P. Marco, A. Caron, P. Skold, P. W. Andrews, M. A. Baxter, D. C. Hay, J. Hamdam, M. E. Sharpe, S. Patel, D. R. Jones, J. Reinhardt, E. H. J. Danen, U. Ben-David, G. Stacey, P. Bjorquist, J. Piner, J. Mills, C. Rowe, G. Pellegrini, S. Sethu, D. J. Antoine, M. J. Cross, P. Murray, D. P. Williams, N. R. Kitteringham, C. E. P. Goldring and B. K. Park, *Stem Cells Transl. Med.*, 2015, **4**, 389-400.

21. J. C. Sun and H. P. Tan, *Materials*, 2013, **6**, 1285-1309.

22. J. A. Yang, J. Yeom, B. W. Hwang, A. S. Hoffman and S. K. Hahn, *Prog. Polym. Sci.*, 2014, **39**, 1973-1986.

23. A. Kang, J. Park, J. Ju, G. S. Jeong and S.-H. Lee, *Biomaterials*, 2014, **35**, 2651-2663.

24. P. de Vos, H. A. Lazarjani, D. Poncelet and M. M. Faas, *Adv. Drug Deliv. Rev.*, 2014, **67-68**, 15-34.

25. M. W. Tibbitt and K. S. Anseth, *Biotechnol. Bioeng.*, 2009, **103**, 655-663.

26. E. M. Ahmed, *J. Adv. Res.*, 2015, **6**, 105-121.

27. M. C. Catoira, L. Fusaro, D. Di Francesco, M. Ramella and F. Boccafoschi, *J. Mater. Sci.: Mater. Med.*, 2019, **30**, 115.

28. N. Granger, H. Blamires, R. J. M. Franklin and N. D. Jeffery, *Brain*, 2012, **135**, 3227-3237.

29. J. W. Hur, T.-H. Cho, D.-H. Park, J.-B. Lee, J.-Y. Park and Y.-G. Chung, *J. Spinal Cord Med.*, 2016, **39**, 655-664.

30. K. Yamazaki, M. Kawabori, T. Seki and K. Houkin, *Int. J. Mol. Sci.*, 2020, **21**, 3994.

31. P. Tabakow, G. Raisman, W. Fortuna, M. Czyz, J. Huber, D. Li, P. Szewczyk, S. Okurowski, R. Miedzybrodzki, B. Czapiga, B. Salomon, A. Halon, Y. Li, J. Lipiec, A. Kulczyk and W. Jarmundowicz, *Cell Transplant.*, 2014, **23**, 1631-1655.

32. J. A. Tickle, H. Poptani, A. Taylor and D. M. Chari, *Nanomedicine*, 2018, **13**, 1333-1348.

33. N. Ghane, M.-H. Beigi, S. Labbaf, M.-H. Nasr-Esfahani and A. Kiani, *J. Mater. Chem. B*, 2020, **8**, 10712-10738.

34. J. M. Oliveira, L. Carvalho, J. Silva-Correia, S. Vieira, M. Majchrzak, B. Lukomska, L. Stanaszek, P. Strymecka, I. Malysz-Cymborska, D. Golubczyk, L. Kalkowski, R. L. Reis, M. Janowski and P. Walczak, *NPJ Regen. Med.*, 2018, **3**, 8.

35. H. J. Lee, J. S. Ryu and P. J. S. Vig, *Therapeutic Delivery*, 2019, **10**, 251-263.

36. D. Macaya and M. Spector, *Biomed. Mater.*, 2012, **7**, 22.

37. R. C. Assunção-Silva, E. D. Gomes, N. Sousa, N. A. Silva and A. J. Salgado, *Stem Cells Int.*, 2015, **2015**, 948040.

38. A. Mosahebi, M. Wiberg and G. Terenghi, *Tissue Eng.*, 2003, **9**, 209-218.

39. L. N. Novikova, A. Mosahebi, M. Wiberg, G. Terenghi, J.-O. Kellerth and L. N. Novikov, *J. Biomed. Mater. Res.*, 2006, **77A**, 242-252.

40. C. J. Medberry, P. M. Crapo, B. F. Siu, C. A. Carruthers, M. T. Wolf, S. P. Nagarkar, V. Agrawal, K. E. Jones, J. Kelly, S. A. Johnson, S. S. Velankar, S. C. Watkins, M. Modo and S. F. Badylak, *Biomater.*, 2013, **34**, 1033-1040.

41. M. Antman-Passig, S. Levy, C. Gartenberg, H. Schori and O. Shefi, *Tissue Eng.*, 2017, **23**, 403-414.

42. H. A. Awad, D. L. Butler, M. T. Harris, R. E. Ibrahim, Y. Wu, R. G. Young, S. Kadiyala and G. P. Boivin, *J. Biomed. Mater. Res.*, 2000, **51**, 233-240.

43. C.-S. Lin, Z.-C. Xin, J. Dai and T. F. Lue, *Histol. Histopathol.*, 2013, **28**, 1109-1116.

44. L. Scarfe, N. Brillant, J. D. Kumar, N. Ali, A. Alrumayh, M. Amali, S. Barbellion, V. Jones, M. Niemeijer, S. Potdevin, G. Roussignol, A. Vaganov, I. Barbaric, M. Barrow, N. C. Burton, J. Connell, F. Dazzi, J. Edsbagge, N. S. French, J. Holder, C. Hutchinson, D. R. Jones, T. Kalber, C. Lovatt, M. F. Lythgoe, S. Patel, P. S. Patrick, J. Piner, J. Reinhardt, E. Ricci, J. Sidaway, G. N. Stacey, P. J. S. Lewis, G. Sullivan, A. Taylor, B. Wilm, H. Poptani, P. Murray, C. E. P. Goldring and B. K. Park, *NPJ Regen. Med.*, 2017, **2**, 13.

45. A. V. Naumova, M. Modo, A. Moore, C. E. Murry and J. A. Frank, *Nat. Biotechnol.*, 2014, **32**, 804-818.

46. H. J. Jeong, R. J. Yoo, J. K. Kim, M. H. Kim, S. H. Park, H. Kim, J. W. Lim, S. H. Do, K. C. Lee, Y. J. Lee and D. W. Kim, *Biomaterials*, 2019, **199**, 32-39.

47. M. L. James and S. S. Gambhir, *Physiol. Rev.*, 2012, **92**, 897-965.

48. J. Comenge, J. Sharkey, O. Fragueiro, B. Wilm, M. Brust, P. Murray, R. Levy and A. Plagge, *Elife*, 2018, **7**, 22.

49. D. Bermejo-Velasco, W. Q. Dou, A. Heerschap, D. Ossipov and J. Hilborn, *Carbohydr. Polym.*, 2018, **197**, 641-648.

50. X. Cai, B. S. Paratala, S. Hu, B. Sitharaman and L. V. Wang, *Tissue Eng., Methods*, 2012, **18**, 310-317.

51. P. S. Patrick, J. C. Bear, H. E. Fitzke, M. Zaw-Thin, I. P. Parkin, M. F. Lythgoe, T. L. Kalber and D. J. Stuckey, *Biomater.*, 2020, **243**, 119930.

52. C. M. Moran and A. J. W. Thomson, *Front. Phys.*, 2020, **8**, 124.

53. S. I. Ziegler, *Nucl. Phys.*, 2005, **752**, 679-687.

54. A. Rahmim and H. Zaidi, *Nucl. Med. Commun.*, 2008, **29**, 193-207.

55. O. Couturier, A. Luxen, J. F. Chatal, J. P. Vuillez, P. Rigo and R. Hustinx, *Eur. J. Nucl. Med. Mol. Imaging*, 2004, **31**, 1182-1206.

56. D. Delbeke, *J. Nucl. Med*, 1999, **40**, 591-603.

57. S. M. Okarvi, *Eur. J. Nucl. Med.*, 2001, **28**, 929-938.

58. T. J. Ferris, P. Charoenphun, L. K. Meszaros, G. E. D. Mullen, P. J. Blower and M. J. Went, *Dalton Trans.*, 2014, **43**, 14851-14857.

59. W. J. Kang, H. J. Kang, H. S. Kim, J. K. Chung, M. C. Lee and D. S. Lee, *J Nucl. Med.*, 2006, **47**, 1295-1301.

60. J. Terrovitis, R. Lautamäki, M. Bonios, J. Fox, J. M. Engles, J. Yu, M. K. Leppo, M. G. Pomper, R. L. Wahl, J. Seidel, B. M. Tsui, F. M. Bengel, M. R. Abraham and E. Marbán, *J. Am. Coll. Cardiol.*, 2009, **54**, 1619-1626.

61. S. L. Rice, C. A. Roney, P. Daumar and J. S. Lewis, *Semin. Nucl. Med.*, 2011, **41**, 265-282.

62. B. X. Yang, A. Brahmbhatt, E. N. Torres, B. Thielen, D. L. McCall, S. Engel, A. Bansal, M. K. Pandey, A. B. Dietz, E. B. Leof, T. R. DeGrado, D. Mukhopadhyay and S. Misra, *Radiology*, 2016, **279**, 513-522.

63. N. Sato, H. Wu, K. O. Asiedu, L. P. Szajek, G. L. Griffiths and P. L. Choyke, *Radiology*, 2015, **275**, 490-500.

64. W. Brenner, A. Aicher, T. Eckey, S. Massoudi, M. Zuhayra, U. Koehl, C. Heeschen, W. U. Kampen, A. M. Zeiher, S. Dimmeler and E. Henze, *J. Nucl. Med.*, 2004, **45**, 512-518.

65. W. K. Laskey, L. E. Feinendegen, R. D. Neumann and V. Dilsizian, *JACC Cardiovasc. Imaging*, 2010, **3**, 517-524.

66. R.-J. M. van Geuns, P. A. Wielopolski, H. G. de Bruin, B. J. Rensing, P. M. A. van Ooijen, M. Hulshoff, M. Oudkerk and P. J. de Feyter, *Prog. Cardiovasc. Dis.*, 1999, **42**, 149-156.

67. J. C. Gore, *J. Clin. Investig.*, 2003, **112**, 4-9.

68. H. B. Na and T. Hyeon, *J. Mater. Chem.*, 2009, **19**, 6267-6273.

69. E. T. Bullmore and O. Sporns, *Nature Rev. Neurosci.*, 2009, **10**, 186-198.

70. M. Markl, P. J. Kilner and T. Ebbers, *J. Cardiovasc. Magn. Reson.*, 2011, **13**, 22.

71. P. Caravan, J. J. Ellison, T. J. McMurry and R. B. Lauffer, *Chem. Rev.*, 1999, **99**, 2293-2352.

72. I. Solomon, *Phys. Rev.*, 1955, **99**, 559-565.

73. N. Bloembergen and L. O. Morgan, *J. Chem. Phys.*, 1961, **34**, 842-850.

74. T. J. Fraum, D. R. Ludwig, M. R. Bashir and K. J. Fowler, *J. Magn. Reson. Imaging*, 2017, **46**, 338-353.

75. J.-K. Hsiao, C.-P. Tsai, T.-H. Chung, Y. Hung, M. Yao, H.-M. Liu, C.-Y. Mou, C.-S. Yang, Y.-C. Chen and D.-M. Huang, *Small*, 2008, **4**, 1445-1452.

76. M. Modo, K. Mellodew, D. Cash, S. E. Fraser, T. J. Meade, J. Price and S. C. R. Williams, *NeuroImage*, 2004, **21**, 311-317.

77. J. Liu, K. Wang, J. Luan, Z. Wen, L. Wang, Z. Liu, G. Wu and R. Zhuo, *J. Mater. Chem. B*, 2016, **4**, 1343-1353.

78. C. Sun, J. S. H. Lee and M. Zhang, *Adv. Drug Deliv. Rev.*, 2008, **60**, 1252-1265.

79. A. K. Gupta and M. Gupta, *Biomaterials*, 2005, **26**, 3995-4021.

80. W. Wu, C. Z. Jiang and V. A. L. Roy, *Nanoscale*, 2016, **8**, 19421-19474.

81. M. Barrow, A. Taylor, A. M. Fuentes-Caparrós, J. Sharkey, L. M. Daniels, P. Mandal, B. K. Park, P. Murray, M. J. Rosseinsky and D. J. Adams, *Biomater. Sci.*, 2018, **6**, 101-106.

82. M. Barrow, A. Taylor, D. J. Nieves, L. K. Bogart, P. Mandal, C. M. Collins, L. R. Moore, J. J. Chalmers, R. Levy, S. R. Williams, P. Murray, M. J. Rosseinsky and D. J. Adams, *Biomater. Sci.*, 2015, **3**, 608-616.

83. J. Sharkey, P. J. Starkey Lewis, M. Barrow, S. M. Alwahsh, J. Noble, E. Livingstone, R. J. Lennen, M. A. Jansen, J. G. Carrion, N. Liptrott, S. Forbes, D. J. Adams, A. E. Chadwick, S. J. Forbes, P. Murray, M. J. Rosseinsky, C. E. Goldring and B. K. Park, *Cytotherapy*, 2017, **19**, 555-569.

84. Z. L. Chen, C. G. Yan, S. N. Yan, Q. Liu, M. R. Hou, Y. K. Xu and R. Guo, *Theranostics*, 2018, **8**, 1146-1158.

85. P. Bachert, *Prog. Nucl. Magn. Reson. Spectrosc.*, 1998, **33**, 1-56.

86. F. Chapelin, C. M. Capitini and E. T. Ahrens, *J. Immunother. Cancer*, 2018, **6**, 105.

87. M. Srinivas, A. Heerschap, E. T. Ahrens, C. G. Figdor and I. J. M. d. Vries, *Trends Biotechnol.*, 2010, **28**, 363-370.

88. G. P. Biro, P. Blais and A. L. Rosen, *Crit. Rev. Oncol. Hematol.*, 1987, **6**, 311-374.

89. J. Jägers, A. Wrobeln and K. B. Ferenz, *Pflügers Archiv*, 2021, **473**, 139-150.

90. C. Fink, M. Smith, J. M. Gaudet, A. Makela, P. J. Foster and G. A. Dekaban, *Mol. Imaging Biol.*, 2020, **22**, 549-561.

91. D. Bartusik and D. Aebisher, *Biomed. Pharmacother.*, 2014, **68**, 813-817.

92. J. M. Janjic and E. T. Ahrens, *WIREs Nanomed. Nanobiotechnol.*, 2009, **1**, 492-501.

93. M. Srinivas, J. Tel, G. Schreibelt, F. Bonetto, L.-J. Cruz, H. Amiri, A. Heerschap, C. G. Figdor and I. J. M. de Vries, *Nanomedicine*, 2015, **10**, 2339-2348.

94. A. H. J. Staal, K. Becker, O. Tagit, N. Koen van Riessen, O. Koshkina, A. Veltien, P. Bouvain, K. R. G. Cortenbach, T. Scheenen, U. Flögel, S. Temme and M. Srinivas, *Biomaterials*, 2020, **261**, 120307.

95. E. Swider, K. Daoudi, A. H. J. Staal, O. Koshkina, N. K. van Riessen, E. van Dinther, I. J. M. de Vries, C. L. de Korte and M. Srinivas, *Nanotheranostics*, 2018, **2**, 258-268.

96. L. Zerrillo, K. B. S. S. Gupta, F. A. W. M. Lefeber, C. G. Da Silva, F. Galli, A. Chan, A. Veltien, W. Dou, R. Censi, P. Di Martino, M. Srinivas and L. Cruz, *Pharmaceutics*, 2021, **13**, 235.

97. A. Sato, B. Klaunberg and R. Tolwani, *Comp. Med.*, 2004, **54**, 631-634.

98. H. Fraga, *Photochem. Photobiol. Sci.*, 2008, **7**, 146-158.

99. R. T. Sadikot and T. S. Blackwell, *Proc. Am. Thorac. Soc.*, 2005, **2**, 537-540.

100. M. Rudin and R. Weissleder, *Nat. Rev. Drug Discov.*, 2003, **2**, 123.

101. J. E. Kim, S. Kalimuthu and B.-C. Ahn, *Nucl. Med. Mol. Imaging*, 2015, **49**, 3-10.

102. C. H. Contag and M. H. Bachmann, *Annu. Rev. Biomed. Eng.*, 2002, **4**, 235-260.

103. D. K. Welsh and S. A. Kay, *Curr. Opin. Biotechnol.*, 2005, **16**, 73-78.

104. S. Mohsin, M. Khan, H. Toko, B. Bailey, C. T. Cottage, K. Wallach, D. Nag, A. Lee, S. Siddiqi, F. Lan, K. M. Fischer, N. Gude, P. Quijada, D. Avitabile, S. Truffa, B. Collins, W. Dembitsky, J. C. Wu and M. A. Sussman, *J. Am. Coll. Cardiol.*, 2012, **60**, 1278-1287.

105. F. Cao, S. Lin, X. Xie, P. Ray, M. Patel, X. Zhang, M. Drukker, S. J. Dylla, A. J. Connolly, X. Chen, I. L. Weissman, S. S. Gambhir and J. C. Wu, *Circulation*, 2006, **113**, 1005-1014.

106. H. Wang, F. Cao, A. De, Y. Cao, C. Contag, S. S. Gambhir, J. C. Wu and X. Y. Chen, *Stem Cells*, 2009, **27**, 1548-1558.

107. F. Togel, Y. Yang, P. Zhang, Z. M. Hu and C. Westenfelder, *Am. J. Physiol. Renal Physiol.*, 2008, **295**, F315-F321.

108. J. W. Lichtman and J. A. Conchello, *Nat. Methods*, 2005, **2**, 910-919.

109. C. Wurth, M. Grabolle, J. Pauli, M. Spieles and U. Resch-Genger, *Nat. Protoc.*, 2013, **8**, 1535-1550.

110. T. G. Phan and A. Bullen, *Immunol. Cell Biol.*, 2010, **88**, 438-444.

111. J. Zhang, R. E. Campbell, A. Y. Ting and R. Y. Tsien, *Nat. Rev. Mol. Cell Biol.*, 2002, **3**, 906-918.

112. K. E. Luker, P. Pata, I. I. Shemiakina, A. Pereverzeva, A. C. Stacer, D. S. Shcherbo, V. Z. Pletnev, M. Skolnaja, K. A. Lukyanov, G. D. Luker, I. Pata and D. M. Chudakov, *Sci. Rep.*, 2015, **5**, 10332.

113. A. P. Alivisatos, *Science*, 1996, **271**, 933-937.

114. U. Resch-Genger, M. Grabolle, S. Cavaliere-Jaricot, R. Nitschke and T. Nann, *Nature Methods*, 2008, **5**, 763.

115. I. L. Medintz, H. T. Uyeda, E. R. Goldman and H. Mattoussi, *Nat. Mater.*, 2005, **4**, 435-446.

116. S. Kim, Y. T. Lim, E. G. Soltesz, A. M. De Grand, J. Lee, A. Nakayama, J. A. Parker, T. Mihaljevic, R. G. Laurence, D. M. Dor, L. H. Cohn, M. G. Bawendi and J. V. Frangioni, *Nat. Biotechnol.*, 2004, **22**, 93-97.

117. O. I. Mićić, J. Sprague, Z. Lu and A. J. Nozik, *Appl. Phys. Lett.*, 1996, **68**, 3150-3152.

118. W. W. Yu, L. H. Qu, W. Z. Guo and X. G. Peng, *Chem. Mater.*, 2003, **15**, 2854-2860.

119. Y.-P. Sun, B. Zhou, Y. Lin, W. Wang, K. A. S. Fernando, P. Pathak, M. J. Meziani, B. A. Harruff, X. Wang, H. Wang, P. G. Luo, H. Yang, M. E. Kose, B. Chen, L. M. Veca and S.-Y. Xie, *J. Am. Chem. Soc.*, 2006, **128**, 7756-7757.

120. M. V. Wolkin, J. Jorne, P. M. Fauchet, G. Allan and C. Delerue, *Phys. Rev. Lett.*, 1999, **82**, 197-200.

121. A. M. Derfus, W. C. W. Chan and S. N. Bhatia, *Nano Lett.*, 2004, **4**, 11-18.

122. B. Ballou, B. C. Lagerholm, L. A. Ernst, M. P. Bruchez and A. S. Waggoner, *Bioconjugate Chem.*, 2004, **15**, 79-86.

123. Y. Zhang, F. Rossi, S. Papa, M. B. Violatto, P. Bigini, M. Sorbona, F. Redaelli, P. Veglianese, J. Hilborn and D. A. Ossipov, *Acta Biomaterialia*, 2016, **30**, 188-198.

124. Z. H. Sheng, D. H. Hu, M. M. Xue, M. He, P. Gong and L. T. Cai, *Nano-Micro Letters*, 2013, **5**, 145-150.

125. M. Filippi, F. Garello, C. Pasquino, F. Arena, P. Giustetto, F. Antico and E. Terreno, *J. Biophotonics*, 2019, **12**, e201800035.

126. M. V. Marshall, J. C. Rasmussen, I. C. Tan, M. B. Aldrich, K. E. Adams, X. Wang, C. E. Fife, E. A. Maus, L. A. Smith and E. M. Sevick-Muraca, *Open Surgic. Oncol. J.*, 2010, **2**, 12-25.

127. L. Q. Fan, Y. P. Xu and H. Tian, *Tetrahedron Lett.*, 2005, **46**, 4443-4447.

128. C. Kohl, T. Weil, J. Q. Qu and K. Mullen, *Chem. Eur. J.l*, 2004, **10**, 5297-5310.

129. C. Chung, Y. K. Kim, D. Shin, S. R. Ryoo, B. H. Hong and D. H. Min, *Acc. Chem. Res.*, 2013, **46**, 2211-2224.

130. A. Bianco, K. Kostarelos, C. D. Partidos and M. Prato, *Chem. Commun.*, 2005, 571-577.

131. Z. Liu, S. Tabakman, K. Welsher and H. J. Dai, *Nano Res.*, 2009, **2**, 85-120.

132. S. Augustine, J. Singh, M. Srivastava, M. Sharma, A. Das and B. D. Malhotra, *Biomater. Sci.*, 2017, **5**, 901-952.

133. B. Unnikrishnan, R.-S. Wu, S.-C. Wei, C.-C. Huang and H.-T. Chang, *ACS Omega*, 2020, **5**, 11248-11261.

134. T. Malina, K. Poláková, J. Skopalík, V. Milotová, K. Holá, M. Havrdová, K. B. Tománková, V. Čmiel, L. Šefc and R. Zbořil, *Carbon*, 2019, **152**, 434-443.

135. X. Y. Zhang, W. B. Hu, J. Li, L. Tao and Y. Wei, *Toxicol. Res.*, 2012, **1**, 62-68.

136. V. N. Mochalin, O. Shenderova, D. Ho and Y. Gogotsi, *Nat. Nanotechnol.*, 2011, **7**, 11.

137. R. Kaur and I. Badea, *Int. J. Nanomed.*, 2013, **8**, 203-220.

138. C. Laube, T. Oeckinghaus, J. Lehnert, J. Griebel, W. Knolle, A. Denisenko, A. Kahnt, J. Meijer, J. Wrachtrup and B. Abel, *Nanoscale*, 2019, **11**, 1770-1783.

139. M. Chen, E. D. Pierstorff, R. Lam, S. Y. Li, H. Huang, E. Osawa and D. Ho, *ACS Nano*, 2009, **3**, 2016-2022.

140. E. K. Chow, X. Q. Zhang, M. Chen, R. Lam, E. Robinson, H. J. Huang, D. Schaffer, E. Osawa, A. Goga and D. Ho, *Sci. Transl. Med.*, 2011, **3**, 10.

141. V. N. Mochalin and Y. Gogotsi, *J. Am. Chem. Soc.*, 2009, **131**, 4594-4595.

142. V. Vaijayanthimala, P. Y. Cheng, S. H. Yeh, K. K. Liu, C. H. Hsiao, J. I. Chao and H. C. Chang, *Biomaterials*, 2012, **33**, 7794-7802.

143. J. Wang and J. V. Jokerst, *Stem Cells Int.*, 2016, **2016**, 9240652-9240652.

144. D. Cosgrove and C. Harvey, *Med. Biolog. Eng. Comput.*, 2009, **47**, 813-826.

145. E. Stride and N. Saffari, *Proc. Inst. Mech. Eng. Part H-J. Eng. Med.*, 2003, **217**, 429-447.

146. J. R. Lindner, *Nat. Rev. Drug Discov.*, 2004, **3**, 527-532.

147. K. Ferrara, R. Pollard and M. Borden, *Annu. Rev. Biomed. Eng.*, 2007, **9**, 415-447.

148. D. Omata, J. Unga, R. Suzuki and K. Maruyama, *Adv. Drug Deliv. Rev.*, 2020, **154-155**, 236-244.

149. C. Szíjjártó, S. Rossi, G. Waton and M. P. Krafft, *Langmuir*, 2012, **28**, 1182-1189.

150. S. Qin, C. F. Caskey and K. W. Ferrara, *Phys. Med. Biol.*, 2009, **54**, R27-R57.

151. W. Cui, S. Tavri, M. J. Benchimol, M. Itani, E. S. Olson, H. Zhang, M. Decyk, R. G. Ramirez, C. V. Barback, Y. Kono and R. F. Mattrey, *Biomaterials*, 2013, **34**, 4926-4935.

152. M. A. Kuliszewski, H. Fujii, C. Liao, A. H. Smith, A. Xie, J. R. Lindner and H. Leong-Poi, *Cardiovasc. Res.*, 2009, **83**, 653-662.

153. H. Leong-Poi, *Cardiovasc. Res.*, 2009, **84**, 190-200.

154. O. Koshkina, G. Lajoinie, F. Baldelli Bombelli, E. Swider, L. J. Cruz, P. B. White, R. Schweins, Y. Dolen, E. A. W. van Dinther, N. K. van Riessen, S. E. Rogers, R. Fokkink, I. K. Voets, E. R. H. van Eck, A. Heerschap, M. Versluis, C. L. de Korte, C. G. Figdor, I. J. M. de Vries and M. Srinivas, *Adv. Funct. Mater.*, 2019, **29**, 1806485.

155. J. Yao and L. V. Wang, *Contrast Media Mol. Imaging*, 2011, **6**, 332-345.

156. L. H. V. Wang and S. Hu, *Science*, 2012, **335**, 1458-1462.

157. V. Neuschmelting, N. C. Burton, H. Lockau, A. Urich, S. Harmsen, V. Ntziachristos and M. F. Kircher, *Photoacoustics*, 2016, **4**, 1-10.

158. M. Li, Y. Tang and J. Yao, *Photoacoustics*, 2018, **10**, 65-73.

159. Y. Y. Jiang and K. Y. Pu, *Small*, 2017, **13**, 19.

160. D. Razansky, M. Distel, C. Vinegoni, R. Ma, N. Perrimon, R. W. Koster and V. Ntziachristos, *Nat. Photonics*, 2009, **3**, 412-417.

161. A. Taruttis, S. Morscher, N. C. Burton, D. Razansky and V. Ntziachristos, *Plos One*, 2012, **7**, 6.

162. S. Lal, S. E. Clare and N. J. Halas, *Acc. Chem. Res.*, 2008, **41**, 1842-1851.

163. A. C. V. Doughty, A. R. Hoover, E. Layton, C. K. Murray, E. W. Howard and W. R. Chen, *Materials (Basel)*, 2019, **12**, 779.

164. G. S. Filonov, A. Krumholz, J. Xia, J. Yao, L. V. Wang and V. V. Verkhusha, *Angew. Chem. Int. Ed.*, 2012, **51**, 1448-1451.

165. J. Xia, J. Yao and L. V. Wang, *Electromagnetic waves (Camb..)*, 2014, **147**, 1-22.

166. A. Krumholz, D. M. Shcherbakova, J. Xia, L. H. V. Wang and V. V. Verkhusha, *Sci. Rep.*, 2014, **4**, 7.

167. G. S. Filonov, K. D. Piatkevich, L.-M. Ting, J. Zhang, K. Kim and V. V. Verkhusha, *Nat. Biotechnol.*, 2011, **29**, 757-761.

168. N. C. Deliolanis, A. Ale, S. Morscher, N. C. Burton, K. Schaefer, K. Radrich, D. Razansky and V. Ntziachristos, *Mol. Imaging Biol.*, 2014, **16**, 652-660.

169. A. Krumholz, S. J. VanVickle-Chavez, J. J. Yao, T. P. Fleming, W. E. Gillanders and L. H. V. Wang, *J. Biomed. Opt.*, 2011, **16**, 3.

170. J. Brunker, J. J. Yao, J. Laufer and S. E. Bohndiek, *J. Biomed. Optics*, 2017, **22**, 18.

171. C. B. Liu, X. J. Gong, R. Q. Lin, F. Liu, J. Q. Chen, Z. Y. Wang, L. Song and J. Chu, *Theranostics*, 2016, **6**, 2414-2430.

172. A. P. Jathoul, J. Laufer, O. Ogunlade, B. Treeby, B. Cox, E. Zhang, P. Johnson, A. R. Pizzey, B. Philip, T. Marafioti, M. F. Lythgoe, R. B. Pedley, M. A. Pule and P. Beard, *Nat. Photonics*, 2015, **9**, 239-246.

173. E. Hutter and J. H. Fendler, *Advanced Materials*, 2004, **16**, 1685-1706.

174. S. Mallidi, T. Larson, J. Tam, P. P. Joshi, A. Karpiouk, K. Sokolov and S. Emelianov, *Nano Lett.*, 2009, **9**, 2825-2831.

175. J. Homola, *Anal. Bioanal. Chem.*, 2003, **377**, 528-539.

176. E. Boisselier and D. Astruc, *Chem. Soc. Rev.*, 2009, **38**, 1759-1782.

177. X. Yang, E. W. Stein, S. Ashkenazi and L. V. Wang, *WIREs: Nanomed. Nanobiotechnol.*, 2009, **1**, 360-368.

178. M. A. Hahn, A. K. Singh, P. Sharma, S. C. Brown and B. M. Moudgil, *Anal. Bioanal. Chem.*, 2011, **399**, 3-27.

179. M. L. Brongersma, *Nat. Mater.*, 2003, **2**, 296-297.

180. C. Loo, A. Lowery, N. Halas, J. West and R. Drezek, *Nano Lett.*, 2005, **5**, 709-711.

181. S. J. Madsen, S.-K. Baek, A. R. Makkouk, T. Krasieva and H. Hirschberg, *Ann. Biomed. Eng.*, 2012, **40**, 507-515.

182. R. Bardhan, S. Lal, A. Joshi and N. J. Halas, *Acc. Chem. Res.*, 2011, **44**, 936-946.

183. C. Loo, L. Hirsch, M. H. Lee, E. Chang, J. West, N. J. Halas and R. Drezek, *Optics Lett.*, 2005, **30**, 1012-1014.

184. B. Nikoobakht and M. A. El-Sayed, *Chem. Mater.*, 2003, **15**, 1957-1962.

185. A. Agarwal, S. W. Huang, M. O'Donnell, K. C. Day, M. Day, N. Kotov and S. Ashkenazi, *J. Appl. Phys.*, 2007, **102**, 4.

186. K. S. Dhada, D. S. Hernandez and L. J. Suggs, *ACS Nano*, 2019, **13**, 7791-7799.

187. P. K. Jain and M. A. El-Sayed, *Chem. Phys. Lett.*, 2010, **487**, 153-164.

188. W. Q. Zhang, Y. L. Ji, X. C. Wu and H. Y. Xu, *ACS Appl. Mater. Interfaces*, 2013, **5**, 9856-9865.

189. J. Comenge, O. Fragueiro, J. Sharkey, A. Taylor, M. Held, N. C. Burton, B. K. Park, B. Wilm, P. Murray, M. Brust and R. Lévy, *ACS Nano*, 2016, **10**, 7106-7116.

190. J. V. Jokerst, M. Thangaraj, P. J. Kempen, R. Sinclair and S. S. Gambhir, *ACS Nano*, 2012, **6**, 5920-5930.

191. S. E. Skrabalak, J. Y. Chen, Y. G. Sun, X. M. Lu, L. Au, C. M. Cobley and Y. N. Xia, *Acc. Chem. Res.*, 2008, **41**, 1587-1595.

192. J. Chen, B. Wiley, Z. Y. Li, D. Campbell, F. Saeki, H. Cang, L. Au, J. Lee, X. Li and Y. Xia, *Adv. Mater.*, 2005, **17**, 2255-2261.

193. J. Y. Chen, D. L. Wang, J. F. Xi, L. Au, A. Siekkinen, A. Warsen, Z. Y. Li, H. Zhang, Y. N. Xia and X. D. Li, *Nano Lett.*, 2007, **7**, 1318-1322.

194. Y. N. Xia, W. Y. Li, C. M. Cobley, J. Y. Chen, X. H. Xia, Q. Zhang, M. X. Yang, E. C. Cho and P. K. Brown, *Acc. Chem. Res.*, 2011, **44**, 914-924.

195. M. S. Yavuz, Y. Y. Cheng, J. Y. Chen, C. M. Cobley, Q. Zhang, M. Rycenga, J. W. Xie, C. Kim, K. H. Song, A. G. Schwartz, L. H. V. Wang and Y. N. Xia, *Nat. Mater.*, 2009, **8**, 935-939.

196. X. M. Yang, S. E. Skrabalak, Z. Y. Li, Y. N. Xia and L. H. V. Wang, *Nano Lett.*, 2007, **7**, 3798-3802.

197. Y. S. Zhang, Y. Wang, L. D. Wang, Y. C. Wang, X. Cai, C. Zhang, L. H. V. Wang and Y. N. Xia, *Theranostics*, 2013, **3**, 532-543.

198. E. C. Dreaden, A. M. Alkilany, X. H. Huang, C. J. Murphy and M. A. El-Sayed, *Chem. Soc. Rev.*, 2012, **41**, 2740-2779.

199. P. Ghosh, G. Han, M. De, C. K. Kim and V. M. Rotello, *Adv. Drug Deliv. Rev.*, 2008, **60**, 1307-1315.

200. X. Liu, W.-C. Law, M. Jeon, X. Wang, M. Liu, C. Kim, P. N. Prasad and M. T. Swihart, *Adv. Healthc. Mater.*, 2013, **2**, 952-957.

201. G. Ku, M. Zhou, S. Song, Q. Huang, J. Hazle and C. Li, *ACS Nano*, 2012, **6**, 7489-7496.

202. E. V. Shashkov, M. Everts, E. I. Galanzha and V. P. Zharov, *Nano Lett.*, 2008, **8**, 3953-3958.

203. V. P. Zharov, J. W. Kim, D. T. Curiel and M. Everts, *Nanomed. Nanotechnol. Biol. Med.*, 2005, **1**, 326-345.

204. J. C. Ge, Q. Y. Jia, W. M. Liu, L. Guo, Q. Y. Liu, M. H. Lan, H. Y. Zhang, X. M. Meng and P. F. Wang, *Adv. Mater.*, 2015, **27**, 4169-4177.

205. K. Yang, L. Feng, X. Shi and Z. Liu, *Chem. Soc. Rev.*, 2013, **42**, 530-547.

206. J. T. Robinson, S. M. Tabakman, Y. Liang, H. Wang, H. Sanchez Casalongue, D. Vinh and H. Dai, *J. Am. Chem. Soc.*, 2011, **133**, 6825-6831.

207. Z. Sheng, L. Song, J. Zheng, D. Hu, M. He, M. Zheng, G. Gao, P. Gong, P. Zhang, Y. Ma and L. Cai, *Biomater.*, 2013, **34**, 5236-5243.

208. H. Moon, D. Kumar, H. Kim, C. Sim, J.-H. Chang, J.-M. Kim, H. Kim and D.-K. Lim, *ACS Nano*, 2015, **9**, 2711-2719.

209. Q. Fu, R. Zhu, J. Song, H. Yang and X. Chen, *Adv. Mater.*, 2019, **31**, 1805875.

210. A. De La Zerda, C. Zavaleta, S. Keren, S. Vaithilingam, S. Bodapati, Z. Liu, J. Levi, B. R. Smith, T.-J. Ma, O. Oralkan, Z. Cheng, X. Chen, H. Dai, B. T. Khuri-Yakub and S. S. Gambhir, *Nat. Nanotechnol.*, 2008, **3**, 557-562.

211. H. Gong, R. Peng and Z. Liu, *Adv. Drug Deliv. Rev.*, 2013, **65**, 1951-1963.

212. X. Liu, H. Tao, K. Yang, S. Zhang, S.-T. Lee and Z. Liu, *Biomater.*, 2011, **32**, 144-151.

213. J.-W. Kim, E. I. Galanzha, E. V. Shashkov, H.-M. Moon and V. P. Zharov, *Nat. Nanotechnol.*, 2009, **4**, 688.

214. S. Zanganeh, H. Li, P. D. Kumavor, U. Alqasemi, A. Aguirre, I. Mohammad, C. Stanford, M. B. Smith and Q. Zhu, *J. Biomed. Optics*, 2013, **18**, 96006.

215. Vlasov, II, A. S. Barnard, V. G. Ralchenko, O. I. Lebedev, M. V. Kanzyuba, A. V. Saveliev, V. I. Konov and E. Goovaerts, *Adv. Mater.*, 2009, **21**, 808.

216. K. Bray, L. Cheung, K. R. Hossain, I. Aharonovich, S. M. Valenzuela and O. Shimoni, *J. Mater. Chem. B*, 2018, **6**, 3078-3084.

217. S. Orlanducci, *Eur. J. Inorg. Chem.*, 2018, **2018**, 5138-5145.

218. D. Lee, E.-J. Park, S.-E. Lee, S. H. Jeong, J. Y. Lee and E. Kang, *ACS Sustain. Chem. Eng.*, 2017, **5**, 8284-8293.

219. K. Y. Pu, N. Chattopadhyay and J. H. Rao, *J. Control. Rel.*, 2016, **240**, 312-322.

220. B. R. Saunders and M. L. Turner, *Adv. Colloid Interface Sci.*, 2008, **138**, 1-23.

221. D. Tuncel and H. V. Demir, *Nanoscale*, 2010, **2**, 484-494.

222. J. Pecher and S. Mecking, *Chem. Rev.*, 2010, **110**, 6260-6279.

223. L. Feng, C. Zhu, H. Yuan, L. Liu, F. Lv and S. Wang, *Chem. Soc. Rev.*, 2013, **42**, 6620-6633.

224. Y. Lyu and K. Pu, *Adv. Sci.*, 2017, **4**, 1600481.

225. A. B. Sanghvi, K. P. H. Miller, A. M. Belcher and C. E. Schmidt, *Nat. Mater.*, 2005, **4**, 496-502.

226. Y. Liu, P. Bhattarai, Z. Dai and X. Chen, *Chem. Soc. Rev.*, 2019, **48**, 2053-2108.

227. F. M. Ye, C. F. Wu, Y. H. Jin, Y. H. Chan, X. J. Zhang and D. T. Chiu, *J. Am. Chem. Soc.*, 2011, **133**, 8146-8149.

228. K. Y. Pu, A. J. Shuhendler, J. V. Jokerst, J. G. Mei, S. S. Gambhir, Z. N. Bao and J. H. Rao, *Nat. Nanotechnol.*, 2014, **9**, 233-239.

229. C. Yin, G. Wen, C. Liu, B. Yang, S. Lin, J. Huang, P. Zhao, S. H. D. Wong, K. Zhang, X. Chen, G. Li, X. Jiang, J. Huang, K. Pu, L. Wang and L. Bian, *ACS Nano*, 2018, **12**, 12201-12211.

230. L. Scarfe, A. Rak-Raszewska, S. Geraci, D. Darssan, J. Sharkey, J. Huang, N. C. Burton, D. Mason, P. Ranjzad, S. Kenny, N. Gretz, R. Lévy, B. Kevin Park, M. García-Fiñana, A. S. Woolf, P. Murray and B. Wilm, *Sci. Rep.*, 2015, **5**, 13601.

231. J. Kang, D. Kim, J. Wang, Y. Han, J. M. Zuidema, A. Hariri, J.-H. Park, J. V. Jokerst and M. J. Sailor, *Adv. Mater.*, 2018, **30**, 1800512.

232. Z. Chaudhary, G. M. Khan, M. M. Abeer, N. Pujara, B. Wan-Chi Tse, M. A. McGuckin, A. Popat and T. Kumeria, *Biomater. Sci.*, 2019, **7**, 5002-5015.

233. G. Kim, S. W. Huang, K. C. Day, M. O'Donnell, R. R. Agayan, M. A. Day, R. Kopelman and S. Ashkenazi, *J. Biomed. Opt.*, 2007, **12**, 8.

234. J. J. Feng, W. Jiang and Z. H. Wang, *Chem.- Asian J.*, 2018, **13**, 20-30.

235. C. Huang, S. Barlow and S. R. Marder, *J. Org. Chem.*, 2011, **76**, 2386-2407.

236. P. K. Sukul, A. Datta and S. Malik, *Chem.- Eur. J.*, 2014, **20**, 3019-3022.

237. S. Sengupta, R. K. Dubey, R. W. M. Hoek, S. P. P. van Eeden, D. D. Gunbaş, F. C. Grozema, E. J. R. Sudhölter and W. F. Jager, *J. Org. Chem.*, 2014, **79**, 6655-6662.

238. P. S. Hariharan, J. Pitchaimani, V. Madhu and S. P. Anthony, *J. Fluoresc.*, 2016, **26**, 395-401.

239. T. Weil, T. Vosch, J. Hofkens, K. Peneva and K. Mullen, *Angew. Chem. Int. Ed.*, 2010, **49**, 9068-9093.

240. J. Feng, D. Wang, H. Wang, D. Zhang, L. Zhang and X. Li, *J. Phys. Org. Chem.*, 2011, **24**, 621-629.

241. Z. Tian, A. D. Shaller and A. D. Q. Li, *Chem. Commun.*, 2009, 180-182.

242. C. Fryer, Y. Yang, T. Wang, P. Murray and H. Zhang, in *Materials Science and Technology*, ed. P. H. R. W. Cahn, E. J. Kramer, 2020.

243. G. Kaptay, *Int. J. Pharm.*, 2012, **430**, 253-257.

244. R. Nagarajan, in *Nanoparticles: Synthesis, Stabilization, Passivation, and Functionalization*, American Chemical Society, 2008, vol. 996, ch. 1, pp. 2-14.

245. Q. Fan, K. Cheng, Z. Yang, R. Zhang, M. Yang, X. Hu, X. Ma, L. Bu, X. Lu, X. Xiong, W. Huang, H. Zhao and Z. Cheng, *Adv. Mater.*, 2015, **27**, 843-847.

246. C. Cui, Z. Yang, X. Hu, J. Wu, K. Shou, H. Ma, C. Jian, Y. Zhao, B. Qi, X. Hu, A. Yu and Q. Fan, *ACS Nano*, 2017, **11**, 3298-3310.

247. P. Sun, P. Yuan, G. Wang, W. Deng, S. Tian, C. Wang, X. Lu, W. Huang and Q. Fan, *Biomacromolecules*, 2017, **18**, 3375-3386.

248. Z. Yang, R. Tian, J. Wu, Q. Fan, B. C. Yung, G. Niu, O. Jacobson, Z. Wang, G. Liu, G. Yu, W. Huang, J. Song and X. Chen, *ACS Nano*, 2017, **11**, 4247-4255.

249. Z. Yang, Y. Dai, C. Yin, Q. Fan, W. Zhang, J. Song, G. Yu, W. Tang, W. Fan, B. C. Yung, J. Li, X. Li, X. Li, Y. Tang, W. Huang, J. Song and X. Chen, *Adv. Mater.*, 2018, **30**, 1707509.

250. K. Nakabayashi, D. Noda, Y. Watanabe and H. Mori, *Polymer*, 2015, **68**, 17-24.

251. X. W. Zhan, A. Facchetti, S. Barlow, T. J. Marks, M. A. Ratner, M. R. Wasielewski and S. R. Marder, *Adv. Mater.*, 2011, **23**, 268-284.

252. A. Herrmann and K. Mullen, *Chem. Lett.*, 2006, **35**, 978-985.

253. Y. Avlasevich, C. Li and K. Müllen, *J. Mater. Chem.*, 2010, **20**, 3814-3826.

254. M. Greene, in *High Performance Pigments*, ed. H. M. Smith, Wiley-VCH, Weinheim, Germany, 2003, pp. 249-261.

255. Y. Geerts, H. Quante, H. Platz, R. Mahrt, M. Hopmeier, A. Böhm and K. Müllen, *J. Mater. Chem.*, 1998, **8**, 2357-2369.

256. L. Chen, C. Li and K. Mullen, *J. Mater. Chem. C*, 2014, **2**, 1938-1956.

257. E. Kozma and M. Catellani, *Dyes Pigments*, 2013, **98**, 160-179.

258. P. K. Sukul, D. Asthana, P. Mukhopadhyay, D. Summa, L. Muccioli, C. Zannoni, D. Beljonne, A. E. Rowan and S. Malik, *Chem. Commun.*, 2011, **47**, 11858-11860.

259. F. Würthner, V. Stepanenko, Z. Chen, C. R. Saha-Möller, N. Kocher and D. Stalke, *J. Org. Chem.*, 2004, **69**, 7933-7939.

260. B. Baumgartner, A. Svirkova, J. Bintinger, C. Hametner, M. Marchetti-Deschmann and M. M. Unterlass, *Chem. Commun.*, 2017, **53**, 1229-1232.

261. H. Langhals, *Heterocycles*, 1995, **40**, 477-500.

262. S. Chen, P. Slattum, C. Wang and L. Zang, *Chem. Rev.*, 2015, **115**, 11967-11998.

263. P. Rajasingh, R. Cohen, E. Shirman, L. J. W. Shimon and B. Rybtchinski, *J. Org. Chem.*, 2007, **72**, 5973-5979.

264. K. S. Valluru and J. K. Willmann, *Ultrasonography*, 2016, **35**, 267-280.

265. R. K. Dubey, N. Westerveld, S. J. Eustace, E. J. R. Sudhölter, F. C. Grozema and W. F. Jager, *Org. Lett.*, 2016, **18**, 5648-5651.

266. R. Regar, R. Mishra, P. K. Mondal and J. Sankar, *J. Org. Chem.*, 2018, **83**, 9547-9552.

267. B. A. Llewellyn, E. S. Davies, C. R. Pfeiffer, M. Cooper, W. Lewis and N. R. Champness, *Chem. Comm.*, 2016, **52**, 2099-2102.

268. R. A. Cormier and B. A. Gregg, *J. Phys. Chem. B*, 1997, **101**, 11004-11006.

269. F. Wurthner and M. Stolte, *Chem. Commun.*, 2011, **47**, 5109-5115.

270. R. Schmidt, J. H. Oh, Y. S. Sun, M. Deppisch, A. M. Krause, K. Radacki, H. Braunschweig, M. Konemann, P. Erk, Z. A. Bao and F. Wurthner, *J. Amer. Chem. Soc.*, 2009, **131**, 6215-6228.

271. V. Ntziachristos and D. Razansky, *Chem. Rev.*, 2010, **110**, 2783-2794.

272. J. W. Kim, E. I. Galanzha, E. V. Shashkov, H. M. Moon and V. P. Zharov, *Nat. Nanotechnol.*, 2009, **4**, 688-694.

273. X. Xue, F. Wang and X. Liu, *J. Mater. Chem.*, 2011, **21**, 13107-13127.

274. Y. Yang, C. Fryer, J. Sharkey, A. Thomas, U. Wais, A. W. Jackson, B. Wilm, P. Murray and H. Zhang, *ACS Appl. Mater. Interfaces*, 2020, **12**, 27930-27939.

275. U. Wais, L. R. Chennamaneni, P. Thoniyot, H. Zhang and A. W. Jackson, *Polym. Chem.*, 2018, **9**, 4824-4839.

276. L. Scarfe, A. Taylor, J. Sharkey, R. Harwood, M. Barrow, J. Comenge, L. Beeken, C. Astley, I. Santeramo, C. Hutchinson, L. Ressel, J. Smythe, E. Austin, R. Levy, M. J. Rosseinsky, D. J. Adams, H. Poptani, B. K. Park, P. Murray and B. Wilm, *Stem Cell Res. Ther.*, 2018, **9**, 332.

277. A. Taylor, J. Sharkey, A. Plagge, B. Wilm and P. Murray, *Contrast Media Mol. Imaging*, 2018, **2018**, 2514796.

278. Y. Yang, University of Liverpool, 2017.

279. D. Alexander, C. B. Neal and N. Vasilis, *J. Biomed. Optics*, 2014, **19**, 1-11.

280. C. J. Martínez Rivas, M. Tarhini, W. Badri, K. Miladi, H. Greige-Gerges, Q. A. Nazari, S. A. Galindo Rodríguez, R. Á. Román, H. Fessi and A. Elaissari, *Int. J. Pharm.*, 2017, **532**, 66-81.

281. C. E. Mora-Huertas, H. Fessi and A. Elaissari, *Int. J. Pharm.*, 2010, **385**, 113-142.

282. S. Galindo-Rodriguez, E. Allemann, H. Fessi and E. Doelker, *Pharm. Res.*, 2004, **21**, 1428-1439.

283. Y. J. Wang, D. Wang, Q. Fu, D. Liu, Y. Ma, K. Racette, Z. G. He and F. Liu, *Mol. Pharm.*, 2014, **11**, 3766-3771.

284. N. G. Campbell and K. Suzuki, *J. Cardiovasc. Transl. Res.*, 2012, **5**, 713-726.

285. M. H. Amer, F. Rose, K. M. Shakesheff, M. Modo and L. J. White, *NPJ Regen. Med.*, 2017, **2**, 13.

286. B. C. Heng, S. H. Hsu, C. M. Cowan, A. Liu, J. Tai, Y. Chan, W. Sherman and S. Basu, *Cell Transplant.*, 2009, **18**, 1111-1121.

287. M. H. Amer, L. J. White and K. M. Shakesheff, *J. Pharm. Pharmacol.*, 2015, **67**, 640-650.

288. G. D. Nicodemus and S. J. Bryant, *Tissue Eng. Part B-Rev.*, 2008, **14**, 149-165.

289. J. K. Oh, R. Drumright, D. J. Siegwart and K. Matyjaszewski, *Prog. Polym. Sci.*, 2008, **33**, 448-477.

290. A. S. Hoffman, *Adv. Drug Deliv. Rev.*, 2012, **64**, 18-23.

291. B. V. Slaughter, S. S. Khurshid, O. Z. Fisher, A. Khademhosseini and N. A. Peppas, *Adv. Mater.*, 2009, **21**, 3307-3329.

292. W. E. Hennink and C. F. van Nostrum, *Adv. Drug Deliv. Rev.*, 2012, **64**, 223-236.

293. S. Ida, *Polym. J.*, 2019, **51**, 803-812.

294. L. S. Moreira Teixeira, J. Feijen, C. A. van Blitterswijk, P. J. Dijkstra and M. Karperien, *Biomaterials*, 2012, **33**, 1281-1290.

295. E. Ruel-Gariepy and J. C. Leroux, *Eur. J. Pharm. Biopharm.*, 2004, **58**, 409-426.

296. Q. V. Nguyen, D. P. Huynh, J. H. Park and D. S. Lee, *Eur. Polym. J.*, 2015, **72**, 602-619.

297. Y. Qiu and K. Park, *Adv. Drug Deliv. Rev.*, 2001, **53**, 321-339.

298. S. Jiang, S. Liu and W. Feng, *J. Mech. Behav. Biomed. Mater.*, 2011, **4**, 1228-1233.

299. A. T. Metters, K. S. Anseth and C. N. Bowman, *Polymer*, 2000, **41**, 3993-4004.

300. D. A. Gyles, L. D. Castro, J. O. C. Silva and R. M. Ribeiro-Costa, *Eur. Polym. J.*, 2017, **88**, 373-392.

301. J. A. Burdick and K. S. Anseth, *Biomater.*, 2002, **23**, 4315-4323.

302. C.-C. Lin and K. S. Anseth, *Pharm. Res.*, 2009, **26**, 631-643.

303. M. Patenaude and T. Hoare, *Biomacromolecules*, 2012, **13**, 369-378.

304. G. M. Fernandes-Cunha, K. M. Chen, F. Chen, P. Le, J. H. Han, L. A. Mahajan, H. J. Lee, K. S. Na and D. Myung, *Sci. Rep.*, 2020, **10**, 16671.

305. S. Nam, R. Stowers, J. Lou, Y. Xia and O. Chaudhuri, *Biomaterials*, 2019, **200**, 15-24.

306. L. Han, J. Xu, X. Lu, D. Gan, Z. Wang, K. Wang, H. Zhang, H. Yuan and J. Weng, *J. Mater. Chem. B*, 2017, **5**, 731-741.

307. U. S. K. Madduma-Bandarage and S. V. Madihally, *J. Appl. Polym. Sci.*, 2021, **138**, 50376.

308. T. Coviello, P. Matricardi, C. Marianecci and F. Alhaique, *J. Control. Release*, 2007, **119**, 5-24.

309. K. Y. Lee and D. J. Mooney, *Prog. Polym. Sci.*, 2012, **37**, 106-126.

310. C. K. Kuo and P. X. Ma, *Biomaterials*, 2001, **22**, 511-521.

311. A. C. Hernández-González, L. Téllez-Jurado and L. M. Rodríguez-Lorenzo, *Carbohydr. Polym.*, 2020, **229**, 115514.

312. J. Berger, M. Reist, J. M. Mayer, O. Felt, N. A. Peppas and R. Gurny, *Eur. J. Pharm. Biopharm.*, 2004, **57**, 19-34.

313. J. Fu, F. Yang and Z. Guo, *New J. Chem.*, 2018, **42**, 17162-17180.

314. F. Ahmadi, Z. Oveisi, S. M. Samani and Z. Amoozgar, *Res. Pharm. Sci.*, 2015, **10**, 1-16.

315. X. Zhang, Y. H. Yang, J. R. Yao, Z. Z. Shao and X. Chen, *ACS Sustain. Chem. Eng.*, 2014, **2**, 1318-1324.

316. D. Seliktar, *Science*, 2012, **336**, 1124-1128.

317. J. A. Rowley, G. Madlambayan and D. J. Mooney, *Biomaterials*, 1999, **20**, 45-53.

318. Y. L. Li, J. Rodrigues and H. Tomas, *Chem. Soc. Rev.*, 2012, **41**, 2193-2221.

319. J. P. Vacanti and C. A. Vacanti, in *Principles of Tissue Engineering (Fourth Edition)*, eds. R. Lanza, R. Langer and J. Vacanti, Academic Press, Boston, 2014, pp. 3-8.

320. R. E. McClelland, R. Dennis, L. M. Reid, J. P. Stegemann, B. Palsson and J. M. Macdonald, in *Introduction to Biomedical Engineering (Third Edition)*, eds. J. D. Enderle and J. D. Bronzino, Academic Press, Boston, 2012, pp. 273-357.

321. J.-H. Lee and H.-W. Kim, *J. Tissue Eng.*, 2018, **9**, 2041731418768285-2041731418768285.

322. J. I. Dawson, J. Kanczler, A. Aarvold, J. Smith and R. O. C. Oreffo, in *Comprehensive Biotechnology (Second Edition)*, ed. M. Moo-Young, Academic Press, Burlington, 2011, pp. 275-290.

323. S. Van Vlierberghe, P. Dubruel and E. Schacht, *Biomacromolecules*, 2011, **12**, 1387-1408.

324. K. Yue, G. Trujillo-de Santiago, M. M. Alvarez, A. Tamayol, N. Annabi and A. Khademhosseini, *Biomaterials*, 2015, **73**, 254-271.

325. S. R. Shin, H. Bae, J. M. Cha, J. Y. Mun, Y.-C. Chen, H. Tekin, H. Shin, S. Farshchi, M. R. Dokmeci, S. Tang and A. Khademhosseini, *ACS Nano*, 2012, **6**, 362-372.

326. S. A. Young, H. Riahinezhad and B. G. Amsden, *J. Mater. Chem. B*, 2019, **7**, 5742-5761.

327. A. Espona-Noguera, J. Ciriza, A. Cañibano-Hernández, L. Fernandez, I. Ochoa, L. Saenz del Burgo and J. L. Pedraz, *Int. J. Biol. Macromol.*, 2018, **107**, 1261-1269.

328. M. Ma, A. Chiu, G. Sahay, J. C. Doloff, N. Dholakia, R. Thakrar, J. Cohen, A. Vegas, D. Chen, K. M. Bratlie, T. Dang, R. L. York, J. Hollister-Lock, G. C. Weir and D. G. Anderson, *Adv. Healthc. Mater.*, 2013, **2**, 667-672.

329. H. K. Yang and K.-H. Yoon, *J. Diab. Complicat.*, 2015, **29**, 737-743.

330. M. Tsintou, K. Dalamagkas and A. Seifalian, *Int. J. Biomater.*, 2018, **2018**, 10.

331. D. Silva, R. A. Sousa and A. J. Salgado, *Mater. Today Bio*, 2021, **9**, 100093.

332. C. F. Adams, A. M. Delaney, D. R. Carwardine, J. Tickle, N. Granger and D. M. Chari, *Macromol. Biosci.*, 2019, **19**, 1800389.

333. A. M. Leferink, C. A. van Blitterswijk and L. Moroni, *Tissue Eng. Part B: Rev.*, 2016, **22**, 265-283.

334. C. Onofrillo, S. Duchi, S. Francis, C. D. O'Connell, L. M. Caballero Aguilar, S. Doyle, Z. Yue, G. G. Wallace, P. F. Choong and C. Di Bella, *Biomaterials*, 2021, **264**, 120383.

335. R.-M. Jin, M.-H. Yao, J. Yang, D.-H. Zhao, Y.-D. Zhao and B. Liu, *ACS Sustain. Chem. Eng.*, 2017, **5**, 9841-9847.

336. B. Liu, X. Gu, Q. Sun, S. Jiang, J. Sun, K. Liu, F. Wang and Y. Wei, *Adv. Funct. Mater.*, 2021, **n/a**, 2010779.

337. R. E. Borg and J. Rochford, *Photochem. Photobiol.*, 2018, **94**, 1175-1209.

338. F. Grinnell, *J. Cell Biol.*, 1994, **124**, 401-404.

339. S. A. Hilton, L. C. Dewberry, M. M. Hodges, J. Y. Hu, J. W. Xu, K. W. Liechty and C. Zgheib, *Plos One*, 2019, **14**, 15.

340. A. J. Holder, N. Badiei, K. Hawkins, C. Wright, P. R. Williams and D. J. Curtis, *Soft Matter*, 2018, **14**, 574-580.

341. B. Peña, M. Maldonado, A. J. Bonham, B. A. Aguado, A. Dominguez-Alfaro, M. Laughter, T. J. Rowland, J. Bardill, N. L. Farnsworth, N. Alegret Ramon, M. R. G. Taylor, K. S. Anseth, M. Prato, R. Shandas, T. A. McKinsey, D. Park and L. Mestroni, *ACS Appl. Mater. Interfaces*, 2019, **11**, 18671-18680.

342. A. Erikson, H. N. Andersen, S. N. Naess, P. Sikorski and C. d. L. Davies, *Biopolymers*, 2008, **89**, 135-143.

343. F. Burla, T. Sentjabrskaja, G. Pletikapic, J. van Beugen and G. H. Koenderink, *Soft Matter*, 2020, **16**, 1366-1376.

344. V. V. Danilenko, *Phys. Solid State*, 2004, **46**, 595-599.

345. A. M. Schrand, S. A. C. Hens and O. A. Shenderova, *Crit. Rev. Solid State Mater. Sci.*, 2009, **34**, 18-74.

346. Y. Xing and L. Dai, *Nanomedicine*, 2009, **4**, 207-218.

347. Y. Zhu, J. Li, W. Li, Y. Zhang, X. Yang, N. Chen, Y. Sun, Y. Zhao, C. Fan and Q. Huang, *Theranostics*, 2012, **2**, 302-312.

348. A. K. Geim, *Science*, 2009, **324**, 1530-1534.

349. A. K. Geim and K. S. Novoselov, *Nat. Mater.*, 2007, **6**, 183-191.

350. A. H. Castro Neto, F. Guinea, N. M. R. Peres, K. S. Novoselov and A. K. Geim, *Rev. Mod. Phys.*, 2009, **81**, 109-162.

351. S. Goenka, V. Sant and S. Sant, *J. Control. Release*, 2014, **173**, 75-88.

352. K. Yang, L. Hu, X. Ma, S. Ye, L. Cheng, X. Shi, C. Li, Y. Li and Z. Liu, *Adv. Mater.*, 2012, **24**, 1868-1872.

353. Y.-P. Sun, K. Fu, Y. Lin and W. Huang, *Acc. Chem. Res.*, 2002, **35**, 1096-1104.

354. R. H. Baughman, A. A. Zakhidov and W. A. de Heer, *Science*, 2002, **297**, 787-792.

355. K. Kokubo, K. Matsubayashi, H. Tategaki, H. Takada and T. Oshima, *ACS Nano*, 2008, **2**, 327-333.

356. P. Chaudhuri, A. Paraskar, S. Soni, R. A. Mashelkar and S. Sengupta, *ACS Nano*, 2009, **3**, 2505-2514.

357. Y. Wang and A. Hu, *J. Mater. Chem. C*, 2014, **2**, 6921-6939.

358. X. Wang, Y. Feng, P. Dong and J. Huang, *Front. Chem.*, 2019, **7**, 671.

359. V. Georgakilas, J. A. Perman, J. Tucek and R. Zboril, *Chem. Rev.*, 2015, **115**, 4744-4822.

360. J. J. Gracio, Q. H. Fan and J. C. Madaleno, *J. Phys. D: Appl. Phys.*, 2010, **43**, 374017.

361. A. Mostofizadeh, Y. W. Li, B. Song and Y. D. Huang, *J. Nanomater.*, 2011, 21.

362. J.-P. Boudou, P. A. Curmi, F. Jelezko, J. Wrachtrup, P. Aubert, M. Sennour, G. Balasubramanian, R. Reuter, A. Thorel and E. Gaffet, *Nanotechnol.*, 2009, **20**, 235602.

363. S. Osswald, G. Yushin, V. Mochalin, S. O. Kucheyev and Y. Gogotsi, *J. Am. Chem. Soc.*, 2006, **128**, 11635-11642.

364. V. Y. Dolmatov, *Russ. Chem. Rev.*, 2001, **70**, 607-626.

365. V. Pichot, M. Comet, E. Fousson, C. Baras, A. Senger, F. Le Normand and D. Spitzer, *Diam. Relat. Mater.*, 2008, **17**, 13-22.

366. I. Petrov, O. Shenderova, V. Grishko, V. Grichko, T. Tyler, G. Cunningham and G. McGuire, *Diam. Relat. Mater.*, 2007, **16**, 2098-2103.

367. O. Shenderova, A. Koscheev, N. Zaripov, I. Petrov, Y. Skryabin, P. Detkov, S. Turner and G. Van Tendeloo, *J. Phys. Chem. C*, 2011, **115**, 9827-9837.

368. T. Jiang and K. Xu, *Carbon*, 1995, **33**, 1663-1671.

369. Y.-R. Chang, H.-Y. Lee, K. Chen, C.-C. Chang, D.-S. Tsai, C.-C. Fu, T.-S. Lim, Y.-K. Tzeng, C.-Y. Fang, C.-C. Han, H.-C. Chang and W. Fann, *Nat. Nanotechnol.*, 2008, **3**, 284-288.

370. A. S. Barnard, *Analyst*, 2009, **134**, 1751-1764.

371. I. I. Vlasov, O. Shenderova, S. Turner, O. I. Lebedev, A. A. Basov, I. Sildos, M. Rähn, A. A. Shiryaev and G. Van Tendeloo, *Small*, 2010, **6**, 687-694.

372. S. L. Y. Chang, A. S. Barnard, C. Dwyer, C. B. Boothroyd, R. K. Hocking, E. Ōsawa and R. J. Nicholls, *Nanoscale*, 2016, **8**, 10548-10552.

373. S.-J. Yu, M.-W. Kang, H.-C. Chang, K.-M. Chen and Y.-C. Yu, *J. Am. Chem.l Soc.*, 2005, **127**, 17604-17605.

374. C.-C. Fu, H.-Y. Lee, K. Chen, T.-S. Lim, H.-Y. Wu, P.-K. Lin, P.-K. Wei, P.-H. Tsao, H.-C. Chang and W. Fann, *Proc. Natl. Acad. Sci.*, 2007, **104**, 727.

375. A. Kruger, F. Kataoka, M. Ozawa, T. Fujino, Y. Suzuki, A. E. Aleksenskii, A. Y. Vul and E. Osawa, *Carbon*, 2005, **43**, 1722-1730.

376. M. Ozawa, M. Inaguma, M. Takahashi, F. Kataoka, A. Kruger and E. Osawa, *Adv. Mater.*, 2007, **19**, 1201-+.

377. A. Pentecost, S. Gour, V. Mochalin, I. Knoke and Y. Gogotsi, *Acs Applied Materials & Interfaces*, 2010, **2**, 3289-3294.

378. X. Y. Zhang, C. K. Fu, L. Feng, Y. Ji, L. Tao, Q. Huang, S. X. Li and Y. Wei, *Polymer*, 2012, **53**, 3178-3184.

379. R. Kaur, J. M. Chitanda, D. Michel, J. Maley, F. Borondics, P. Yang, R. E. Verrall and I. Badea, *Int. J. Nanomed.*, 2012, **7**, 3851-3866.

380. X. Y. Zhang, S. Q. Wang, M. Y. Liu, J. F. Hui, B. Yang, L. Tao and Y. Wei, *Toxicol. Res.*, 2013, **2**, 335-342.

381. D. Wang, Y. Tong, Y. Li, Z. Tian, R. Cao and B. Yang, *Diam. Relat. Mater.*, 2013, **36**, 26-34.

382. H. B. Man, H. Kim, H. J. Kim, E. Robinson, W. K. Liu, E. K. H. Chow and D. Ho, *Nanomed. Nanotechnol. Biol. Med.*, 2014, **10**, 359-369.

383. T. B. Toh, D. K. Lee, W. X. Hou, L. N. Abdullah, J. Nguyen, D. Ho and E. K. H. Chow, *Mol. Pharm.*, 2014, **11**, 2683-2691.

384. O. Faklaris, V. Joshi, T. Irinopoulou, P. Tauc, M. Sennour, H. Girard, C. Gesset, J.-C. Arnault, A. Thorel, J.-P. Boudou, P. A. Curmi and F. Treussart, *ACS Nano*, 2009, **3**, 3955-3962.

385. A. M. Schrand, J. B. Lin, S. C. Hens and S. M. Hussain, *Nanoscale*, 2011, **3**, 435-445.

386. A. Krueger, J. Stegk, Y. Liang, L. Lu and G. Jarre, *Langmuir*, 2008, **24**, 4200-4204.

387. L. C. L. Huang and H.-C. Chang, *Langmuir*, 2004, **20**, 5879-5884.

388. X. Q. Zhang, R. Lam, X. Y. Xu, E. K. Chow, H. J. Kim and D. Ho, *Adv. Mater.*, 2011, **23**, 4770-+.

389. M. A. Zurbuchen, M. P. Lake, S. A. Kohan, B. Leung and L.-S. Bouchard, *Sci. Rep.*, 2013, **3**, 2668.

390. D. Ho, *ACS Nano*, 2009, **3**, 3825-3829.

391. X. Liu, A. Roberts, A. Ahmed, Z. Wang, X. Li and H. Zhang, *J. Mater. Chem. A*, 2015, **3**, 15513-15522.

392. M.-H. Hsu, H. Chuang, F.-Y. Cheng, Y.-P. Huang, C.-C. Han, J.-Y. Chen, S.-C. Huang, J.-K. Chen, D.-S. Wu, H.-L. Chu and C.-C. Chang, *ACS Appl. Mater. Interfaces*, 2014, **6**, 7198-7203.

393. G. T. Hermanson, in *Bioconjugate Techniques (Third Edition)*, ed. G. T. Hermanson, Academic Press, Boston, 2013, pp. 259-273.

394. W. Liu, M. Howarth, A. B. Greytak, Y. Zheng, D. G. Nocera, A. Y. Ting and M. G. Bawendi, *J. Am. Chem. Soc.*, 2008, **130**, 1274-1284.

395. D. Bartczak and A. G. Kanaras, *Langmuir*, 2011, **27**, 10119-10123.

396. F. Zhang, Y. Ma, Y. Chi, H. Yu, Y. Li, T. Jiang, X. Wei and J. Shi, *Sci. Rep.*, 2018, **8**, 8208.

397. K. M. McKinnon, *Curr. Protoc. Immunol.*, 2018, **120**, 5.1.1-5.1.11.

398. C.-Y. Fang, V. Vaijayanthimala, C.-A. Cheng, S.-H. Yeh, C.-F. Chang, C.-L. Li and H.-C. Chang, *Small*, 2011, **7**, 3363-3370.

399. S. Mukherjee, R. N. Ghosh and F. R. Maxfield, *Physiol. Rev.*, 1997, **77**, 759-803.

400. W. W.-W. Hsiao, Y. Y. Hui, P.-C. Tsai and H.-C. Chang, *Acc. Chem. Res.*, 2016, **49**, 400-407.

401. B. Woodhams, L. Ansel-Bollepalli, J. Surmacki, H. Knowles, L. Maggini, M. de Volder, M. Atatüre and S. Bohndiek, *Nanoscale*, 2018, **10**, 12169-12179.

402. The Element Six CVD Diamond Handbook, https://e6cvd.com/media/wysiwyg/pdf/E6_CVD_Diamond_Handbook.pdf, (accessed 6th January, 2021).

403. K. A. Totaro, X. Liao, K. Bhattacharya, J. I. Finneman, J. B. Sperry, M. A. Massa, J. Thorn, S. V. Ho and B. L. Pentelute, *Bioconjug. Chem.*, 2016, **27**, 994-1004.

404. G. W. Anderson, J. E. Zimmerman and F. M. Callahan, *J. Am. Chem. Soc.*, 1963, **85**, 3039-3039.

405. D. Zhang, Q. Zhao, J. Zang, Y.-J. Lu, L. Dong and C.-X. Shan, *Carbon*, 2018, **127**, 170-176.

406. Z. Xue, J. C. Vinci and L. A. Colón, *ACS Appl. Mater. Interfaces*, 2016, **8**, 4149-4157.

407. S. Chauhan, N. Jain and U. Nagaich, *J. Pharm. Anal.*, 2020, **10**, 1-12.

408. Y. Jiang, N. Krishnan, J. Heo, R. H. Fang and L. Zhang, *J. Control. Release*, 2020, **324**, 505-521.

409. J. Yang, Y. Xiao, Z. Tang, Z. Luo, D. Li, Q. Wang and X. Zhang, *J. Mater. Chem. B*, 2020, **8**, 4680-4693.

Appendix

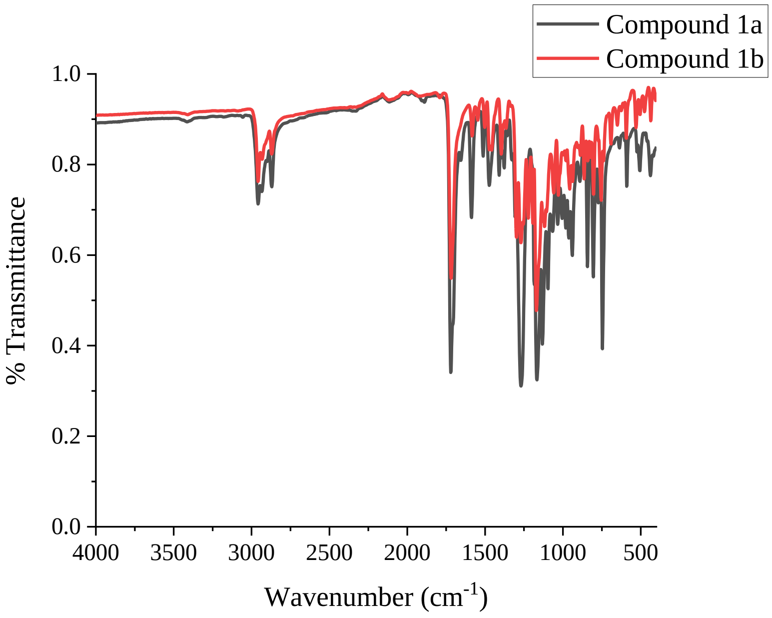

Figure A1: FTIR spectra of perylene-3,4,9,10-tetrabutylester (compound 1a) and 1,7-dibromoperylene-3,4,9,10-tetracarboxytetrabutylester (compound 1b).

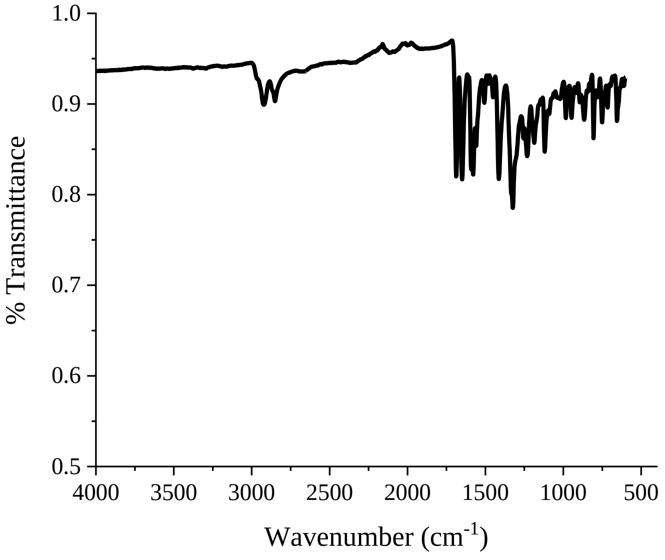

Figure A2: FTIR spectrum of *N,N'*-dicyclohexyl-1,7-di(pyrrolidinyl)perylene-3,4,9,10-tetracarboxy diimide (compound 4).

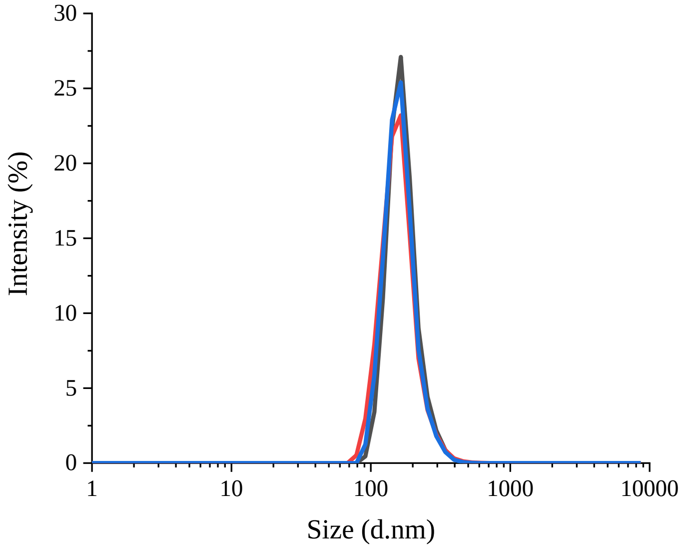

Figure A3: Number particle size distribution of PDI-SHBP nanoparticles (PDI:SHBP 2:1) measured by DLS. The different colours represent 3 measurement scans with DLS.

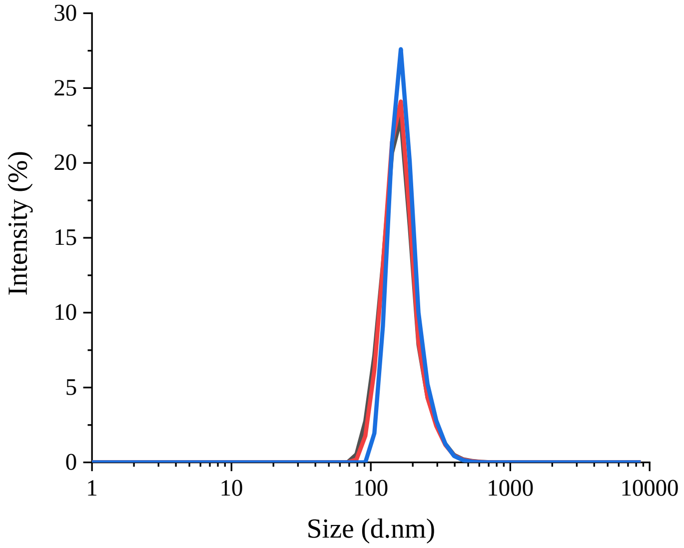

Figure A4: Number particle size distribution of PDI-SHBP nanoparticles (PDI:SHBP 3:1) measured by DLS. The different colours represent 3 measurement scans with DLS.

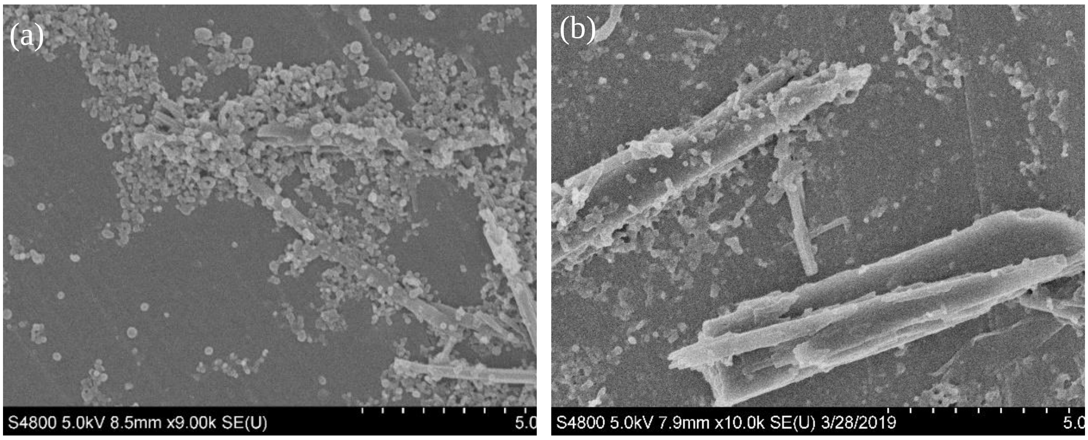

Figure A5: SEM images of PDI-SHBP nanoparticles prepared with PDI:SHBP ratios of (a) 2:1 and (b) 3:1.

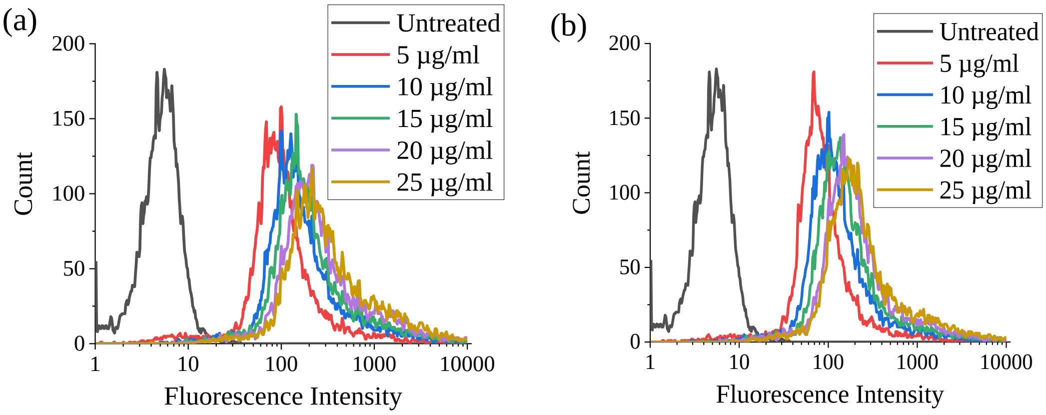

Figure A6: Live cell flow cytometry of MSCs in PBS labelled with PDI-SHBP nanoparticles with PDI:SHBP ratio of (a) 2:1 and (b) 3:1, where the percentage of cells positive was >92% for all concentrations. Fluorescence intensity was measured using FL3 filter (670 LP) and 10,000 events were counted.

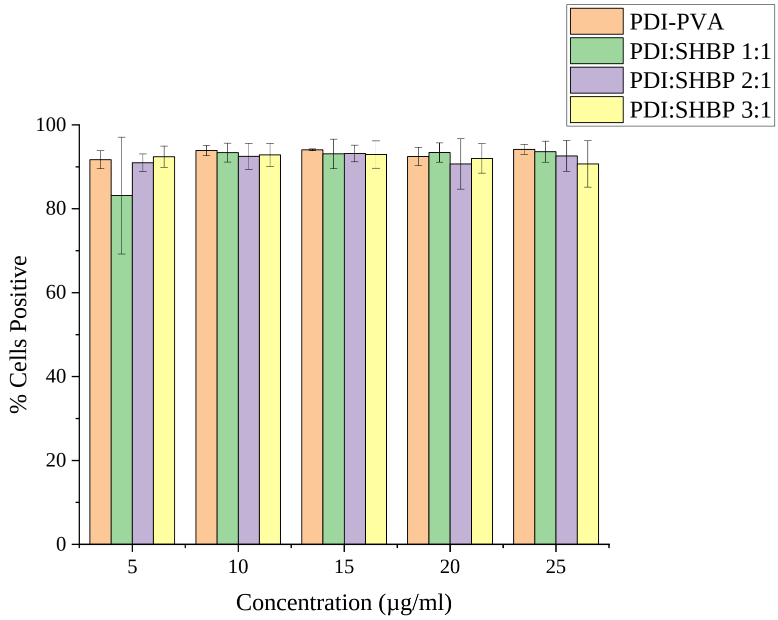

Figure A7: The percentage of cells positive with PDI nanoparticles (SHBP- and PVA-stabilised) at various concentrations using gate shown previously in Figure 11a (n=2 and the error bars represent the range).

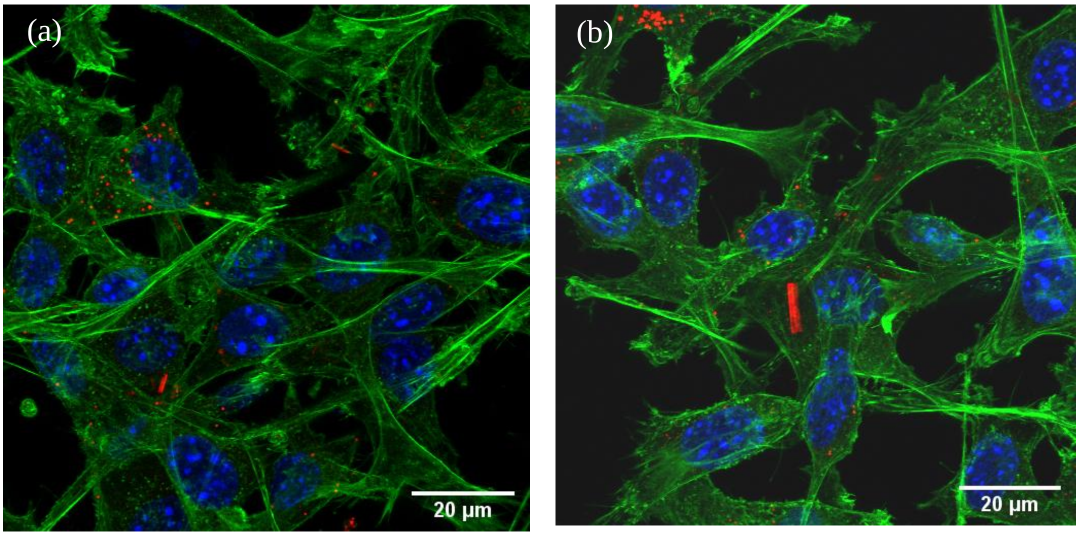

Figure A8: Confocal fluorescence microscope images of MSCs labelled with PDI-SHBP nanoparticles (a) 2:1 and (b) 3:1. Cells were fixed and stained with DAPI (blue nuclei) and AlexaFluor ® 488 phallodin (green, actin cytoskeleton).

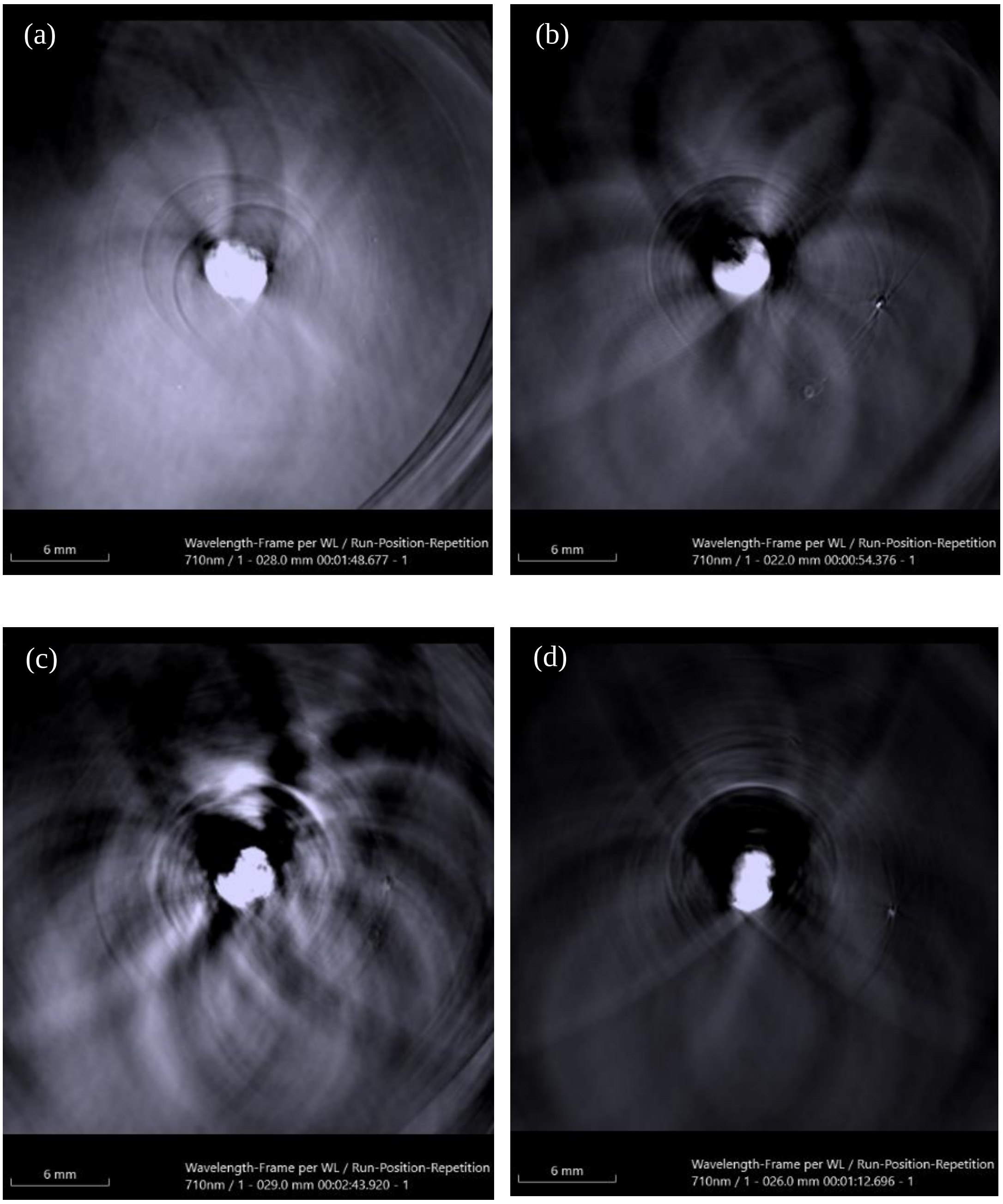

Figure A9: MSOT images at 710 nm of gels labelled with SHBP nanoparticles at concentrations of (a) 12.5, (b) 25, (c) 37.5 and (d) 50 μg/ml. Gels were fixed 1-day post-synthesis.

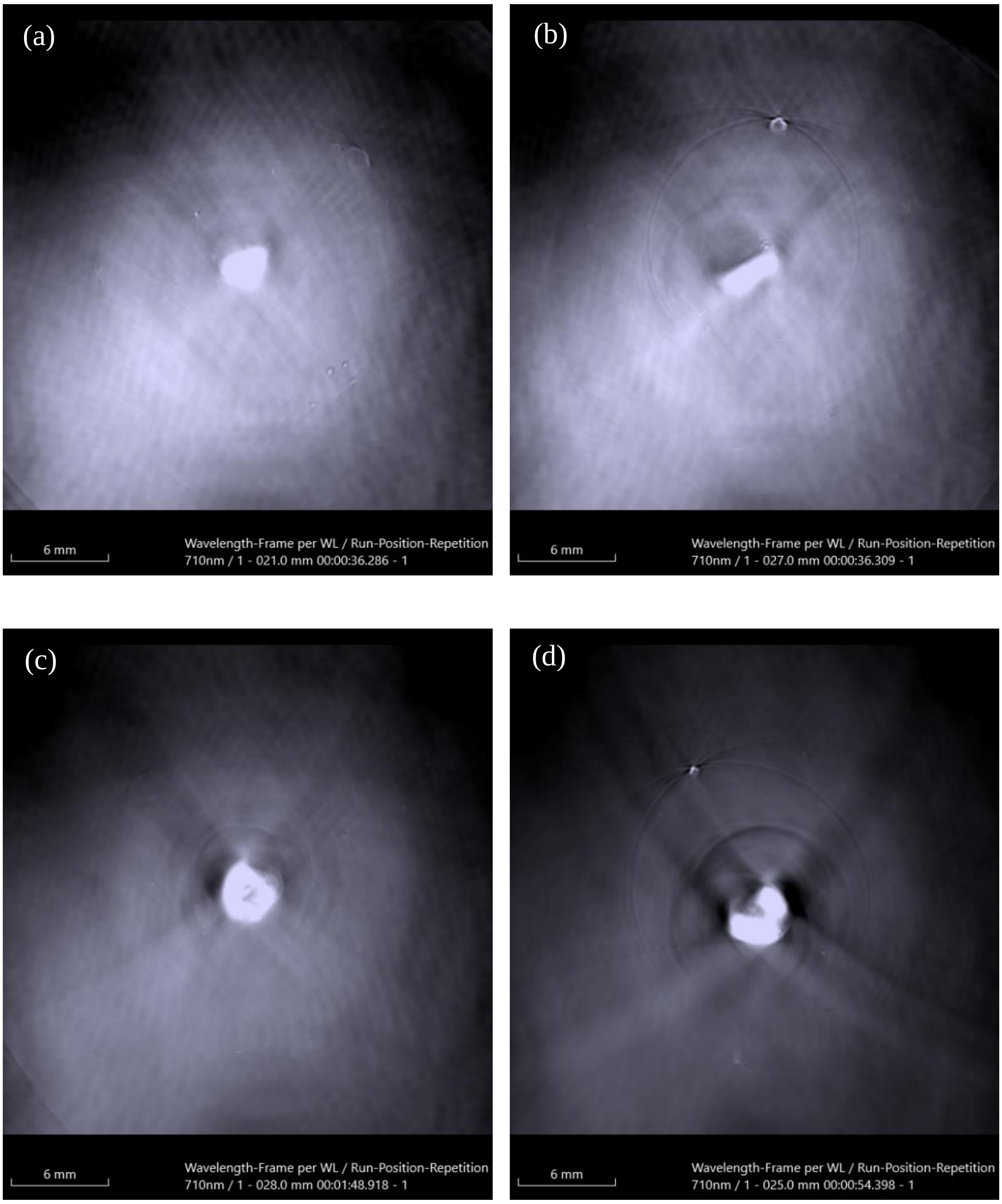

Figure A10: MSOT images at 710 nm of gels labelled with PVA nanoparticles at concentrations of (a) 12.5, (b) 25, (c) 37.5 and (d) 50 µg/ml. Gels were fixed 1-day post-synthesis.

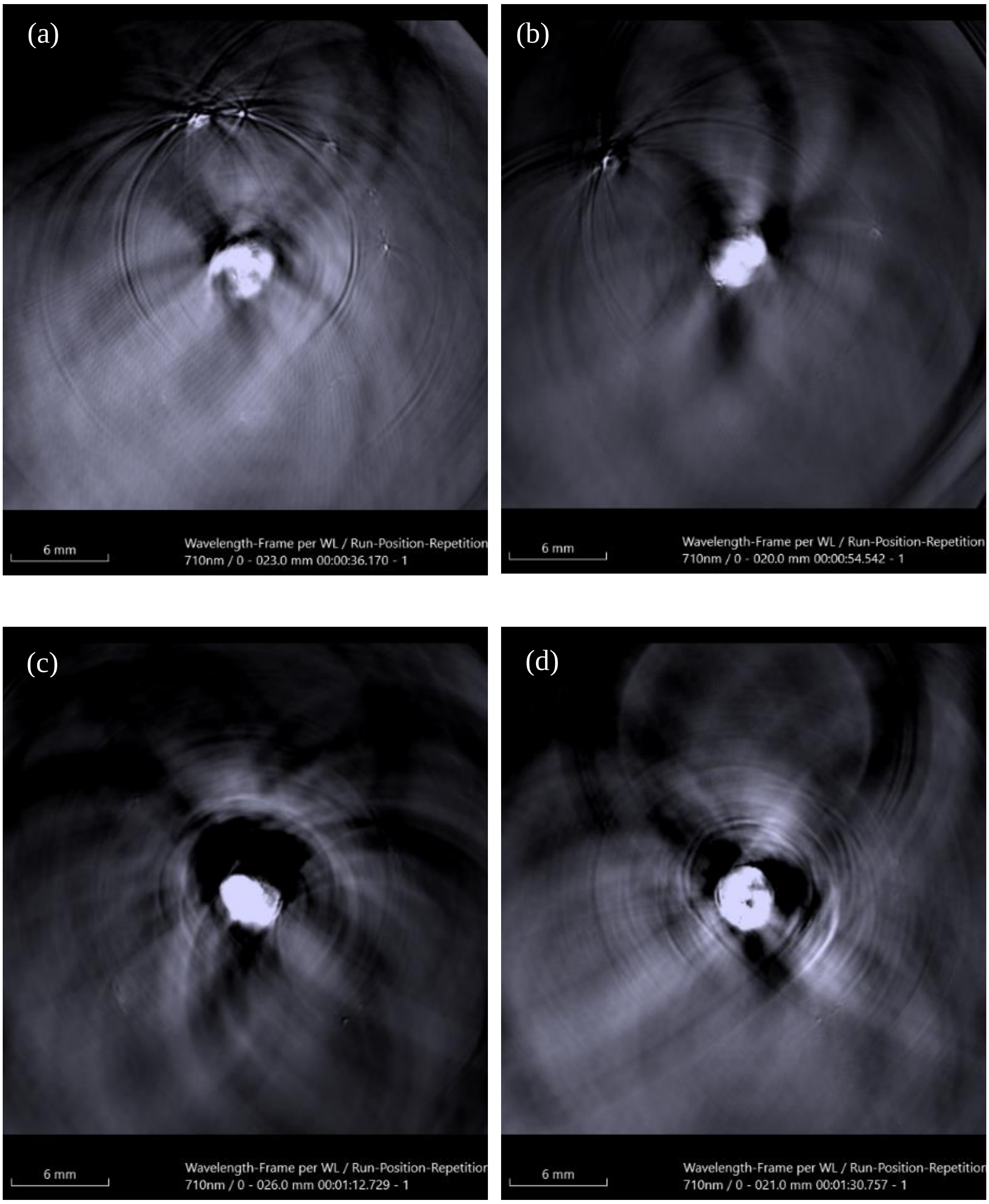

Figure A11: MSOT images at 710 nm of gels labelled with SHBP nanoparticles at concentrations of (a) 12.5, (b) 25, (c) 37.5 and (d) 50 µg/ml. Gels were fixed 1-week post-synthesis.

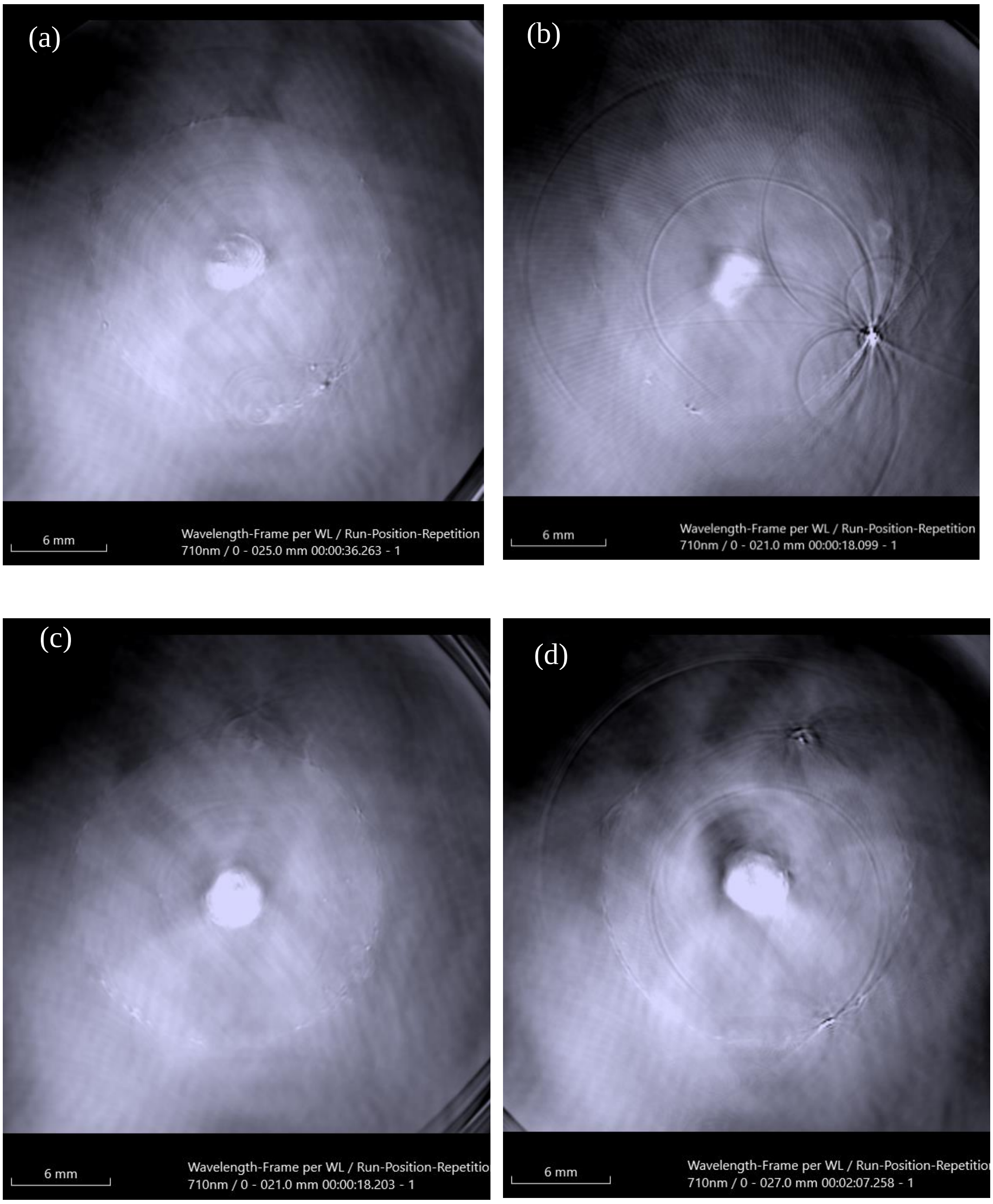

Figure A12: MSOT images at 710 nm of gels labelled with PVA nanoparticles at concentrations of (a) 12.5, (b) 25, (c) 37.5 and (d) 50 μg/ml. Gels were fixed 1-week post-synthesis.

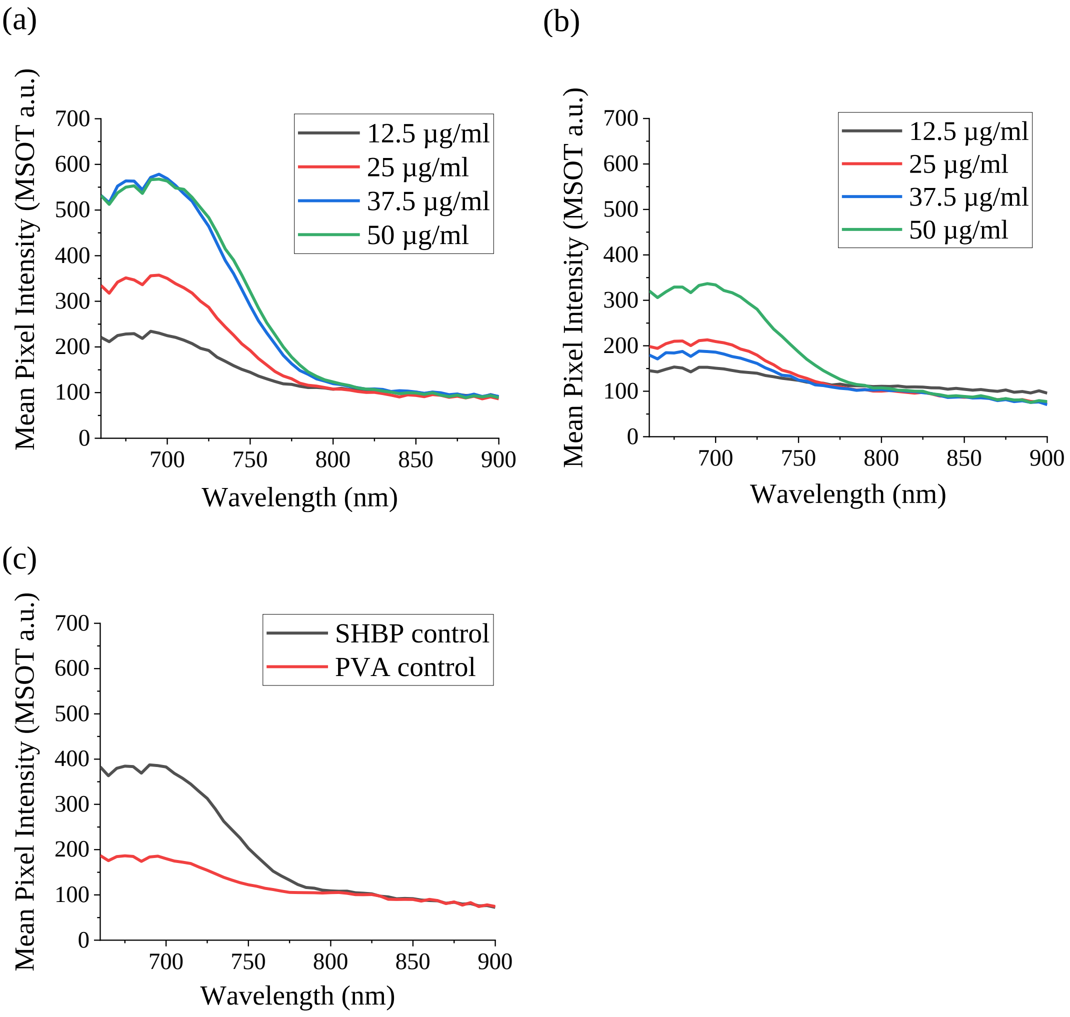

Figure A13: Repeat of MSOT of gels prepared and imaged 1-day post-synthesis, where the MSOT mean pixel intensity across a range of wavelength is shown for gels encapsulating $2x10^5$ cells and labelled with (a) PDI-SHBP and (b) PVA-nanoparticles. The control gels did not contain MSCs and are labelled at a concentration of 25 µg/ml.

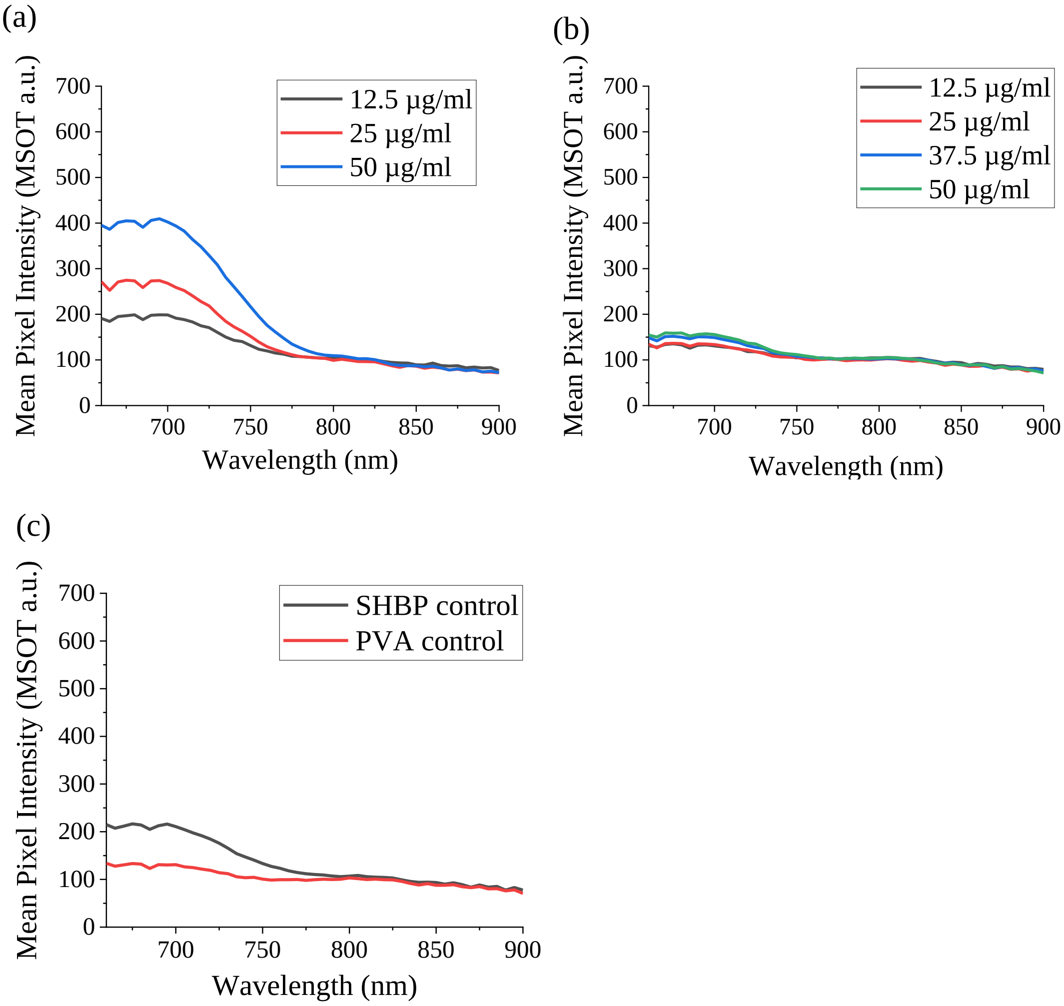

Figure A14: Repeat of MSOT of gels prepared and imaged 1-week post-synthesis, where the MSOT mean pixel intensity across a range of wavelength is shown for gels encapsulating 2x10^5 cells and labelled with (a) PDI-SHBP and (b) PVA-nanoparticles. The control gels did not contain MSCs and are labelled at a concentration of 25 µg/ml.

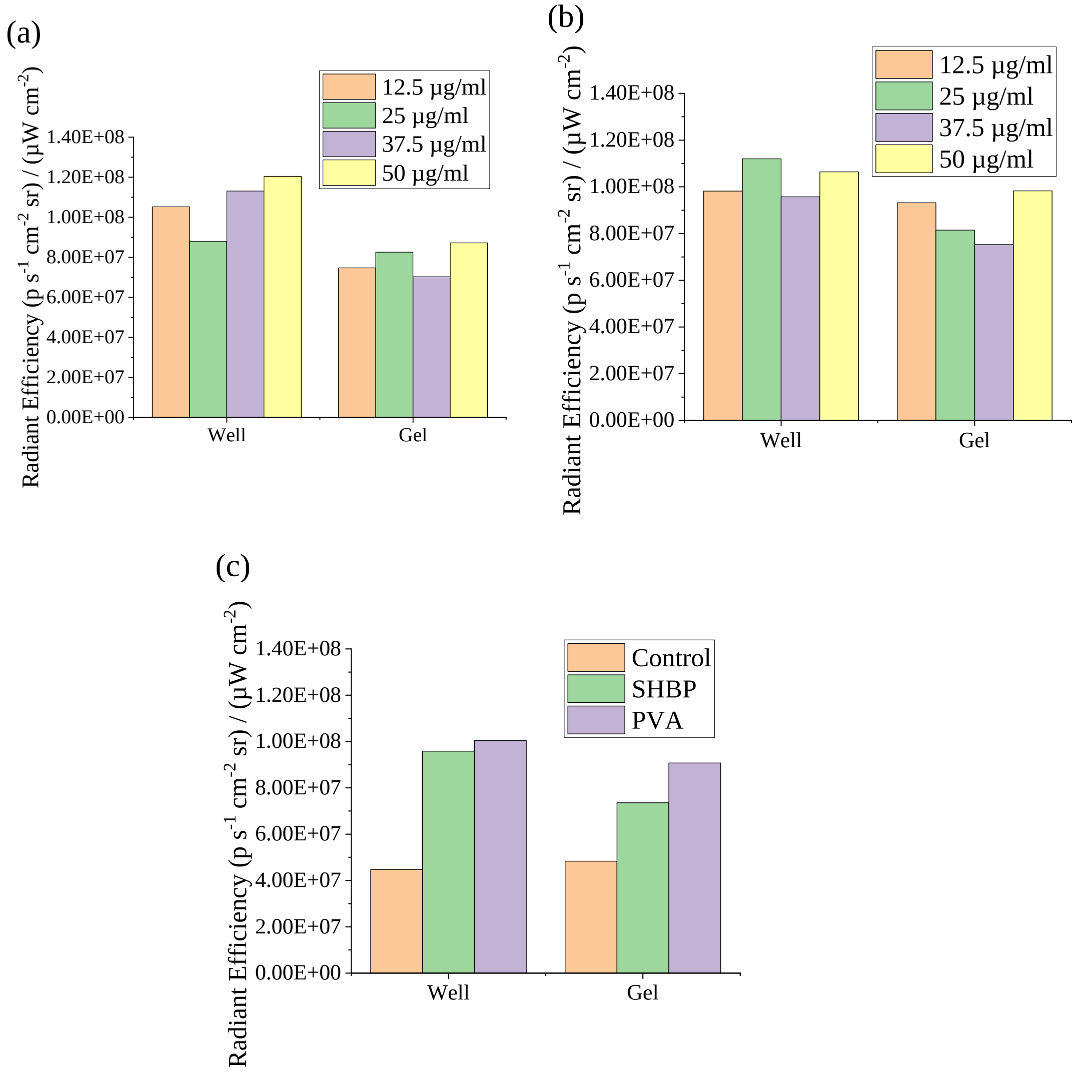

Figure A15: Quantification of the radiant efficiency of gels and wells during fluorescence imaging. Gels were labelled with (a) SHBP-stabilised and (b) PVA-stabilised PDI nanoparticles and (c) unlabelled control gel was included which contained MSCs, as well as a unlabelled gels without MSCs. Gels were moved to a new well after 24 hr and images were taken of the gel and the original well it was incubated in.

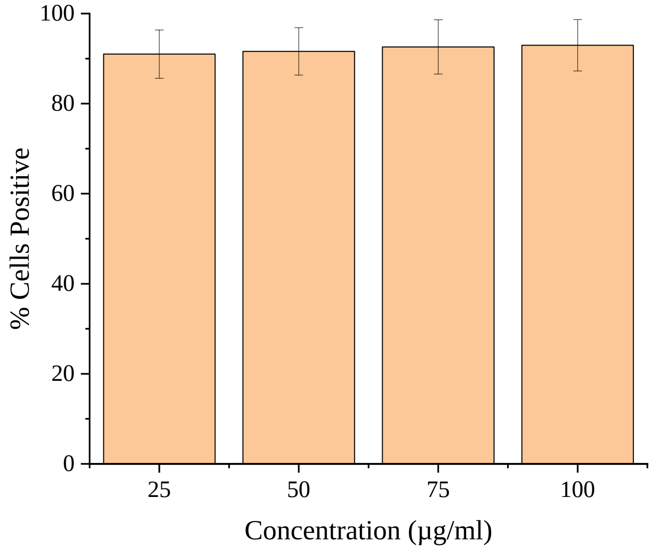

Figure A16: The percentage of cells positive with HPHT PDI-NDs at various concentrations using gate shown previously in Figure 4.11 in Chapter 4 (n=2 and the error bars represent the range).

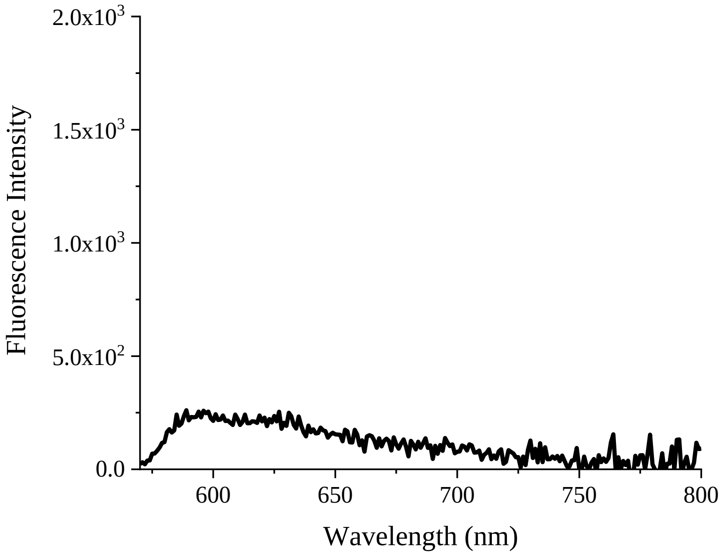

Figure A17: Emission spectrum (λex = 560 nm) of NDs (0.1 mg/ml water). An emission filter was used to block emission below 590 nm to counteract the effects of light scattering.